

May, James (2013). Investigation of fontanelle photoplethysmographs and oxygen saturations in intensive care neonates and infants utilising miniature photometric sensors. (Unpublished Doctoral thesis, City University London)



**CITY UNIVERSITY
LONDON**

[City Research Online](#)

Original citation: May, James (2013). Investigation of fontanelle photoplethysmographs and oxygen saturations in intensive care neonates and infants utilising miniature photometric sensors. (Unpublished Doctoral thesis, City University London)

Permanent City Research Online URL: <http://openaccess.city.ac.uk/2992/>

Copyright & reuse

City University London has developed City Research Online so that its users may access the research outputs of City University London's staff. Copyright © and Moral Rights for this paper are retained by the individual author(s) and/ or other copyright holders. All material in City Research Online is checked for eligibility for copyright before being made available in the live archive. URLs from City Research Online may be freely distributed and linked to from other web pages.

Versions of research

The version in City Research Online may differ from the final published version. Users are advised to check the Permanent City Research Online URL above for the status of the paper.

Enquiries

If you have any enquiries about any aspect of City Research Online, or if you wish to make contact with the author(s) of this paper, please email the team at publications@city.ac.uk.

**INVESTIGATION OF FONTANELLE
PHOTOPLETHYSMOGRAPHS AND OXYGEN SATURATIONS
IN INTENSIVE CARE NEONATES AND INFANTS UTILISING
MINIATURE PHOTOMETRIC SENSORS**

**A thesis submitted for the degree of
Doctor of Philosophy at City University London**

JAMES MICHAEL MAY

**Biomedical Engineering Research Group,
School of Engineering and Mathematical Sciences,
City University London,
Northampton Square, London, EC1V 0HB**

June 2013

Table of Contents

Table of Contents	2
List of Figures	8
List of Tables	15
Acknowledgements	17
Declaration	18
Glossary	19
Abstract	20
Chapter One	21
Introduction	21
1.1 Hypothesis	21
1.2 Thesis Outline	22
Chapter Two	25
The Neonatal Head and the Infant Oesophagus	25
2.1 The Fontanelle of the Neonate	25
2.2 Vasculature of the Head	27
2.3 The Oesophagus	29
2.4 Vasculature of the Oesophagus.....	30
2.5 The Circulatory and Respiratory System	31
2.6 The Respiratory System	31

Chapter Three	33
Photoplethysmography	33
3.1. Key Concepts of Photoplethysmography	33
3.2. History and Origin of the Photoplethysmographic Signal	36
3.3. Photoplethysmography in Pulse Oximetry and Summary	38
Chapter Four	40
Pulse Oximetry	40
4.1 A Short History of the Development of the Pulse Oximeter	40
4.2 Pulse Oximetry Principles	45
4.2.1 Beer and Lambert law	45
4.2.2 Optical properties of blood	46
4.2.3 Limitations of the Beer-Lambert law	47
4.2.4 Ratio of Ratios	47
4.2.5 Calibration of Pulse Oximeters	48
4.2.6 Technology of pulse oximeters	49
4.2.7 Pulse oximeter probes	51
4.3 Pulse oximetry applications	52
4.4 Summary of Pulse Oximetry Limitations	53
Chapter Five	54
Pulse Oximetry in Paediatric Care	54
5.1 Reliability and Accuracy of Pulse Oximeters in Paediatric Care	54
5.1.1 Intravenous Dyes	55
5.1.2 Motion Artefact	55
5.1.3 Ambient Light	55
5.1.4 Dyshaemoglobins	56
5.1.5 Hypothermia	56
5.1.6 Non Pulsatile Flow, Hypo-perfusion, Vasoconstriction and Hypotension	57
5.2 Effect of Location of Sensors in Pulse Oximetry	58
5.3 Paediatric Pulse Oximetry Summary and Proposed Research	61
Chapter Six	63
Design and Development of Multi-Wavelength	
Photoplethysmographic Sensors	63

6.1 Sensor Design and Construction	63
6.1.1 The Fontanelle Photoplethysmograph/SpO ₂ Sensor	63
6.1.2 The Oesophageal Photoplethysmograph/SpO ₂ Sensor.....	68
6.1.3 The Reference Photoplethysmograph/SpO ₂ Sensor	70
6.2 Sensor Evaluation.....	71
6.2.1 Photoplethysmographs from the Sensors.....	71
6.2.2 Thermal Safety Testing	73
6.2.3 Electrical insulation	76
6.3 Sensor Construction Summary	76

Chapter Seven 77

Dual Photoplethysmograph Instrumentation Development..... 77

7.1 System Design.....	77
7.1.1 Power Supply.....	78
7.1.2 Microcontroller / Multiplexer.....	78
7.1.3 Current Supply.....	80
7.1.4 Transimpedance Amplifier with Variable Gain.....	81
7.1.5 Demultiplexing	83
7.1.6 Filtering.....	85
7.1.7 Post Amplification	86
7.1.8 Data Acquisition and Digitisation	87
7.2 Electrical Circuit Simulation	87
7.2.1 Current Supply.....	87
7.2.2 Transimpedance Amplifier with Differential Variable Gain.....	88
7.2.3 Filtering.....	92
7.2.4 Post Amplification	94
7.3 Electrical Prototyping	94
7.3.1 Microcontroller / Multiplexer.....	96
7.3.2 Current Supply.....	96
7.3.3 Transimpedance Amplifier.....	99
7.3.4 Demultiplexing	100
7.3.5 Filtering.....	101
7.3.6 Post Amplification	103
7.3.7 Prototyping Summary.....	103
7.4 System Construction.....	104
7.5 Acquisition of PPGs and Summary	106

Chapter Eight..... 107

Photoplethysmograph Data-Logging Virtual Instrumentation	
Development	107
8.1 Virtual Instrument Design.....	107
8.1.1 LabVIEW	109
8.1.2 Data Acquisition Card Setup and Acquisition Initialisation.....	111
8.1.3 Setup PPG Data File and Continuously Save Raw Signals.....	114
8.1.4 Signal Display, Heart Rate and SpO ₂ Real-time Estimation	115
8.1.5 Time-stamping Function.....	119
8.2 Final Virtual Instrument	120
8.3 Virtual Instrumentation Development Summary.....	122
Chapter Nine.....	123
Photoplethysmograph and SpO₂ Data Analysis Methodology	123
9.1 Signal Filtering	123
9.2 Signal Normalisation.....	126
9.3 Amplitude Measurements	128
9.4 SpO ₂ Measurements.....	129
9.5 Statistics	131
9.6 Summary	133
Chapter Ten	134
Anterior Fontanelle and Foot Photoplethysmograph Analysis	
during Delivered Oxygen Concentration Change <i>In-vivo</i>.....	134
10.1 Anterior Fontanelle Clinical Procedure.....	134
10.2 Anterior Fontanelle and Foot Photoplethysmographs.....	136
10.3 Fontanelle and Foot PPG Normalised Amplitude Analysis	142
10.4 Amplitude Analysis Summary	149
Chapter Eleven	151
Anterior Fontanelle and Foot SpO₂ Analysis.....	151
11.1 Estimation of SpO ₂ during FiO ₂ increase and decrease.....	151
11.2 Fontanelle SpO ₂ compared to Blood Gas SaO ₂ Readings.....	153
11.3 Anterior Fontanelle SpO ₂ compared to Reference Foot and	
Commercial SpO ₂ Sensors.....	157
11.4 Fontanelle SpO ₂ Analysis Summary	160

Chapter Twelve..... 160

Oesophageal Photoplethysmographs and SpO₂ Analysis, Proof of Concept Demonstrations *In-vivo* 160

12.1 Clinical Methods.....	160
12.2 Oesophageal and Periphery Photoplethysmographs.....	162
12.3 Oesophageal and Periphery Normalised Amplitude Analysis	165
12.4 Estimation of SpO ₂ during FiO ₂ Increase and Decrease.....	167
12.5 Oesophageal SpO ₂ Comparison with Commercial SpO ₂ and Blood Gas SaO ₂	169
12.6 Oesophageal PPG and SpO ₂ Analysis Summary	171

Chapter Thirteen 174

Discussions, Conclusions and Future Work 174

13.1 Fontanelle PPG and SpO ₂ Monitoring	174
13.2 Oesophageal PPG and SpO ₂ Monitoring.....	179
13.3 Future Work	180

Appendices 182

Appendix A..... 182

Microcontroller Source Code	182
-----------------------------------	-----

Appendix B..... 183

Frequency Response data of Filter Circuit.....	183
<i>B.1 Low-pass Frequency Response.....</i>	<i>183</i>
<i>B.2 Band-pass Frequency Response.....</i>	<i>184</i>

Appendix C..... 185

Final Printed Circuit Board Design.....	185
<i>C.1 Final Circuit Schematics with Component Values</i>	<i>185</i>
<i>C.2 Printed Circuit Board Layout / Photo-template</i>	<i>188</i>

Appendix D..... 189

PPG data file output sample	189
-----------------------------------	-----

Appendix E..... 191

Approved Clinical Trials Protocol and Ethical Approval Confirmation	191
---	-----

Appendix F	205
Pre-Normalised AC and DC Amplitudes	205
Appendix G	208
Fontanelle Study Patient Statistics.	208
References	209
Own Publications	219

List of Figures

Figure 2.1. The Neonatal Skull, taken and adapted from (Gray 2008). Left; Side profile view of skull. Right; Top oblique view of skull.....	26
Figure 2.2: The Superficial Arteries of the Face and Scalp, Adapted from, © 2009;	27
Figure 2.3. The Sagittal Sinus, taken and adapted from (Gray, 2008). Left; Superior cut-away view. Right; Mid-sagittal view.....	28
Figure 2.4. The Route of the Oesophagus, downloaded from (training.seer.cancer.gov, 2010) June 2010.....	29
Figure 2.5. Pattern of Blood Supply to the Oesophagus, reproduced from (Liebermann-Meffert et al., 1987).....	30
Figure 2.6. The Respiratory System adapted from (www.student.loretto.org/anatomyphys/, 2013 (downloaded)).....	32
Figure 3.1. Transmission-mode photoplethysmography, source and detector are opposite.....	34
Figure 3.2. Reflection-mode photoplethysmography, source and detector are adjacent.	34
Figure 3.3. The AC-DC characteristic of the Photoplethysmographic (PPG) signal.	36
Figure 3.4. Erythrocyte orientation with systolic and diastolic action.	38
Figure 3.5. A modern pulse-oximeter, complete with with plethysmograph signal display (downloaded from www.masimo.com, 2010).	39
Figure 4.1. Principle of photoelectric colour analyser applied to haemoglobin (Millikan, 1933).....	41
Figure 4.2. Kramer's apparatus for optically recording oxygen saturation in unopened arteries of experimental animals (Severinghaus and Astrup, 1986).	42
Figure 4.3. The Millikan Oximeter (Severinghaus and Astrup 1986).....	42
Figure 4.4. Model 47201A Oximeter (left) and application of the ear probe (Merrick and Hayes, 1976).	44
Figure 4.5. The Nihon Kohden OLV-5100, the first commercially available pulse oximeter, with ear-probe (Aoyagi, 2003).	45
Figure 4.6. Absorption spectra of oxyhaemoglobin and haemoglobin, 400 – 1000 nm plotted with data from (Prahl, 1998).	46
Figure 4.7. The main components of a pulse oximeter.....	51
Figure 4.8. Transmission-type pulse oximeter probe.....	52

Figure 4.9. Reflective-type pulse oximeter probe.	52
Figure 6.1: Left KP-2012 series LED (660 nm and 940 nm). Right KPTK-2012VGC 525 nm LED	64
Figure 6.2: Vishay TEMD5010X01 broad-spectrum high speed photodiode.	65
Figure 6.3: Area of the neonatal fontanelle	65
Figure 6.4: Fontanelle PCB Layout Concept.....	66
Figure 6.5: Three-dimensional concept of flexi-pcb layout for fontanelle sensor.....	67
Figure 6.11: Final reference sensor	71
Figure 6.12a: Five second PPG capture using the fontanelle sensor on the temple of a female volunteer. Average heart rate = 84 bpm	72
Figure 6.12b: Five second PPG capture using the reference sensor on the left index finger of a female volunteer. Average heart rate = 61 bpm	72
Figure 6.12c: Five second PPG capture using the oesophageal sensor on buccal mucosa of a female volunteer. Average heart rate = 61 bpm.....	73
Figure: 6.13a: Temperature change at the tissue surface when LED driving current = 20 mA.....	75
Figure: 6.13b: Temperature change at the tissue surface when LED driving current = 40 mA.....	75
Figure: 6.13c: Temperature change at the tissue surface when LED driving current = 60 mA.....	75
Figure: 6.13d: Temperature change at the tissue surface when LED driving current = 80 mA.....	75
Figure 7.1: Instrumentation block diagram.	77
Figure 7.2: DCDC Pin-out.	78
Figure 7.3: 5 V regulator setup.....	78
Figure 7.4: Current source multiplexing routine. Three clocks (C1, C2, C3), one for each current source, are switched "ON" sequentially with an "OFF" period between to allow for the settling time of the LEDs.....	79
Figure 7.5: Pin-out diagram of the Atmel AVR MCU.....	80
Figure 7.6: Preliminary LED current supply schematic.....	81
Figure 7.7: Preliminary dual transimpedance differential amplifier schematic.....	82
Figure 7.8: Sample and hold demonstration. The three voltage amplitudes (A, B, C) represent the different light sources, each is sampled (S1, S2, S3) respectively and then held at that level (H1, H2, H3) until the next sample is taken.	84

Figure 7.9: Sample and hold IC pin out diagram.	84
Figure 7.10: Band-pass filter comprising of two Sallen-Key unity gain filters.	85
Figure 7.11: Preliminary post amplifier schematic.	86
Figure 7.12: Equivalent photodiode model used for simulation, where Ti1 and Ti2 represent the cathode and anode respectively.	89
Figure 7.13: Simulated output of transimpedance amplifier, V_1 (top) and V_2 (bottom), $C_d = 4$ pF, $C_f = 1.09$ pF.	90
Figure 7.14: Simulated output of transimpedance amplifier stages, V_1 (top) and V_2 (bottom) $C_d = 4$ pF, $C_f = 10$ pF.	91
Figure 7.15: Low-pass filter stage simulated frequency response. -3 dB cut-off at approximately 12 Hz.	92
Figure 7.16: Band-pass filter stage simulated frequency response. -3 dB cut-off at approximately 0.5 and 12.1 Hz.	93
Figure 7.17: Post Amplifier simulation. $V_{in} = 0.2$ mV (Pk – Pk), $V_{out} = 16.83$ V. Gain = 84.29	94
Figure 7.18: Single PPG sensor test circuit strip board.	95
Figure 7.19: Diagrammatic layout of the strip board.	95
Figure 7.20: The three TTL-level clocks (1, 2, 3) from the MCU. Duty cycle = 1.68 ms $\approx d = 0.166$ (16.6 %), $f = 99.92$ Hz, Amplitude = 4.8 V.	96
Figure 7.21a: Current output when $R1 = 50 \Omega$. $I_{out} = 99$ mA.	97
Figure 7.21b: Current output when $R1 = 100 \Omega$. $I_{out} = 50.6$ mA.	97
Figure 7.21c: Current output when $R1 = 150 \Omega$. $I_{out} = 32.8$ mA.	98
Figure 7.21d: Current output when $R1 = 200 \Omega$. $I_{out} = 24.8$ mA.	98
Figure 7.21e: Current output when $R1 = 250 \Omega$. $I_{out} = 20.3$ mA.	99
Figure 7.22: Digital oscilloscope capture of the voltage output from the transimpedance amplifier.	100
Figure 7.23: Digital oscilloscope capture of the output (Ch2) of one LF398 S&H chip. Input = 5 Hz sinusoid (Ch1).	101
Figure 7.24: Low-pass frequency response. The -3 dB cutoff is 11.49 Hz (0.5 Hz difference to the simulation, 7 Hz difference to calculated).	102
Figure 7.25: Band-pass frequency response. The -3 dB cut-offs are 0.6 Hz (+0.1 Hz difference to the simulated value, +0.3 Hz difference to calculated value) and 11.08 Hz (-1 Hz difference to the simulated value, -7.4 Hz difference to the calculated value).	103

Figure 7.26: Digital oscilloscope capture of AC PPG post amplifier. $V_{in}(Ch1) = 191 \text{ mV}$ (Pk – Pk), $V_{out}(Ch2) = 15.4 \text{ V}$ (Pk – Pk), Gain ≈ 81	103
Figure 7.27: Final circuit installed into instrument case.	104
Figure 7.28: Completed dual PPG instrument front panel.	105
Figure 7.29: Completed dual PPG instrument rear panel.	105
Figure 7.30: Dual channel PPG from one sensor. Visible are the red PPG signal (Ch1) and the infrared PPG signal (Ch2).....	106
Figure 8.1: Virtual instrumentation data-flow block diagram.	108
Figure 8.2: Simple LabVIEW block diagram describing the algorithm needed to add two numbers together.	109
Figure 8.3: Sample UI for the addition “calculator”.	110
Figure 8.4: Basic programming structures of LabVIEW.....	110
Figure 8.5: DAQ card setup block diagram.	111
Figure 8.6: DAQ card setup UI elements.....	112
Figure 8.7: Data file setup block diagram.....	114
Figure 8.8: Data file setup UI elements.....	115
Figure 8.9: PPG signal display and heart rate + SpO ₂ real time estimation block diagram.....	116
Figure 8.10: Signal display, heart rate, SpO ₂ and user controls UI elements.....	118
Figure 8.11: Time stamping algorithm block diagram.....	119
Figure 8.12: Time stamping UI elements.....	120
Figure 8.13: Final LabVIEW block diagram code for the dual photoplethysmographic and SpO ₂ virtual instrument.	121
Figure 8.14a: Virtual instrument UI front panel main signal display tab.	122
Figure 8.14b Virtual instrument UI front panel setup tab.	122
Figure 9.1: AC PPG signal re-sampling. The effect of the resample filter is to half the length of the signal vector and eliminate the high-frequency noise associated with $F_s = 200 \text{ Hz}$ (HF noise = $F_s/2$). The re-sampled signal (bottom plot) is notably smoother, the effect of anti-aliasing.....	124
Figure 9.2: FFT magnitude Spectrum of a PPG signal (Y) from 0 – 7 Hz. Calculating SpO ₂ relies on the amplitude information from the heart rate component frequencies, designing a digital filter with an appropriate pass-band for each patient will effectively eliminate all unwanted frequency components (Respiratory Rate + LF Noise) for that patient, thus optimizing SpO ₂ calculation.	125

Figure 9.3: AC and DC PPG separation and filtering example over 30 seconds of signal. The unfiltered mixed signal (top) has been effectively filtered and the AC component attributed to the heart rate and DC component attributed to non-pulsatile blood flow separated successfully (middle and bottom respectively).	126
Figure 9.4a: PPG signals before normalisation with their respective DC level (dotted lines). The DC magnitudes are different.....	127
Figure 9.4b: PPG signals after normalisation, each signal now has the same DC magnitude (1000 mV).	128
Figure 9.5: AC PPG amplitude calculation for a single 2-second portion of signal....	129
Figure 9.6: SpO ₂ approximation linear equation 9.5 with R value.....	131
Figure 9.7a: A sample of PPG signal with unreliable signal portions marked via time-stamps during the trial (red) and retrospectively via manual inspection (green – operator driven).	132
Figure 9.7b: Eliminated PPG amplitudes through the use of time stamps (red) and manual inspection (green – operator driven).....	132
Figure 9.7c: Eliminated SpO ₂ values through the use of time stamps (red) and manual inspection (green – operator driven).	132
Figure 10.1: AF sensor in-situ, in sterile pocket and secured with a head bandage..	136
Figure 10.2: Full recording of AC PPG waveforms from the AF (Top) and Foot (Bottom) with Time stamp markings for FiO ₂ Change (dotted horizontal lines).....	137
Figure 10.3a: Five second sample of green AF AC PPGs at the different monitoring periods.....	137
Figure 10.3b: Five second sample of infrared AF AC PPGs at the different monitoring periods.....	138
Figure 10.3c: Five second sample of red AF AC PPGs at the different monitoring periods.....	138
Figure 10.3d: Five second sample of green reference foot AC PPGs at the different monitoring periods	139
Figure 10.3e: Five second sample of infrared reference foot AC PPGs at the different monitoring periods	139
Figure 10.3f: Five second sample of red reference foot AC PPGs at the different monitoring periods	140
Figure 10.4a: Normalised amplitude measurements fro the AF sensor for the Green PPGs.....	143
Figure 10.4b: Normalised amplitude measurements fro the AF sensor for the Infrared PPGs.....	143

Figure 10.4c: Normalised amplitude measurements fro the AF sensor for the RED PPGs.....	143
Figure 10.5: Bar-graph of mean fontanelle AC PPG amplitudes across all three monitoring periods.	146
Figure 10.6: Bar-graph of mean foot AC PPG amplitudes across all three monitoring periods.....	146
Figure 10.7: Mean RED normalised PPG amplitude vs ASA score.	148
Figure 10.8: Mean IR normalised PPG amplitudes vs ASA score.	148
Figure 10.9: Mean GREEN normalised PPG amplitudes vs ASA score.	149
Figure 11.1: Custom SpO ₂ sensor readings against commercial sensor readings from one patient with trend-lines during FiO ₂ change. Commercial SpO ₂ time stamps (n) = 78.....	152
Figure 11.2: Mean bar-graph of SpO ₂ change across the three monitoring periods for the three different sensors.	153
Figure 11.3: Linear regression scatter plot of blood gas analysis (x-axis) versus the various SpO ₂ sensors (y-axis), n = 26.....	154
Figure 11.4: Blood Gas SaO ₂ verses Commercial SpO ₂ readings.....	155
Figure 11.5: Blood Gas SaO ₂ verses AF SpO ₂ readings.	155
Figure 11.6: Blood Gas SaO ₂ verses Foot SpO ₂ readings.	156
Figure 11.7: Histogram of blood gas SaO ₂ readings with superimposed normal distribution function (mean = 92.5 %) with skewness measurement.	156
Figure 11.8: AF and foot SpO ₂ /PPG sensor accuracy relative to each other.	157
Figure 11.9: AF and commercial sensor accuracy relative to each other.....	158
Figure 11.10: Reference foot and commercial sensor accuracy relative to each other.	158
Figure 11.11: Histogram of commercial SpO ₂ readings with superimposed normal distribution function (mean = 97.1 %) and skewness measurement (-3.91).	159
Figure 11.12: Histogram of fontanelle SpO ₂ readings with superimposed normal distribution function (mean = 94.9 %) and skewness measurement (-1.17).	159
Figure 11.13: Histogram of foot SpO ₂ readings with superimposed normal distribution function (mean = 93.3 %) and skewness measurement (-0.32).	160
Figure 12.1: Chest X-ray of the OES sensor in-situ of Patient 1. The head of the sensor is sitting approximately 15 cm into the oesophagus, just behind the aorta of the heart.	161

Figure 12.2: Paediatric burns Patient, Patient 2, with commercial disposable ear sensor.	162
Figure 12.3: Normalised PPG recording from Patient 1, top = OES sensor, bottom = periphery sensor on hand. Red PPGs shown in red, Infrared PPGs shown in blue.....	163
Figure 12.4: Normalised PPG recording from Patient 2, top = OES sensor, bottom = periphery sensor on temple. Red PPGs shown in red, Infrared PPGs shown in blue.....	163
Figure 12.5: Normalised and filtered PPG sample (10 seconds) from Patient 1, HR \approx – 80 BPM.....	164
Figure 12.6: Normalised and filtered PPG sample (10 seconds) from Patient 2, HR \approx 165 – 168 BPM.....	165
Figure 12.7: Red PPG amplitude changes accross the monitoring periods for each patient. Patient 1 is represented by the solid lines, Patient 2 by the dashed lines.....	166
Figure 12.8: Infrared PPG amplitude changes accross the monitoring periods for each patient. Patient 1 is represented by the solid lines, Patient 2 by the dashed lines.....	166
Figure 12.9: Mean SpO ₂ values in each monitoring period for Patient 1 from all three sensors.....	167
Figure 12.10: Mean SpO ₂ values in each monitoring period for Patient 2 from all three sensors.....	168
Figure 12.11: Linear regression plot of blood Gas SaO ₂ vs all three SpO ₂ sensors....	169
Figure 12.12: Blood Gas vs. Comercial SpO ₂ readings.	170
Figure 12.13: Blood Gas vs. Oesophageal readings	170
Figure 12.13: Blood Gas vs. reference sensor readings.....	171

List of Tables

Table 6.1: LED specifications.....	64
Table 6.2: Temperature change with changing LED supply current, all LEDs driven simultaneously.....	76
Table 7.1: Current source simulation results.....	88
Table 7.2: Transimpedance amplifier simulation results, with theoretical C_f values.....	89
Table 7.3: Transimpedance amplifier simulation results, with adjusted C_f values.....	89
Table 7.4: Effect of varying R_g on V_{out} for the desired A_v range.....	92
Table 7.5: Actual driving currents and simulated currents correlate well, suggesting that the circuit performs as expected and can handle the current range expected.....	99
Table 8.1: LabVIEW data types.....	109
Table 10.1 Kolmogorov-Smirnov normality test results (SigmaPlot, SYSTAT Software Inc).....	140
Table 10.2a: Paired t-test between periods on RED AC amplitudes from the AF sensor.....	141
Table 10.2b: Paired t-test between periods on RED DC amplitudes from the AF sensor.....	141
Table 10.2c: Paired t-test between periods on IR AC amplitudes from the AF sensor.....	141
Table 10.2d: Paired t-test between periods on IR DC amplitudes from the AF sensor.....	141
Table 10.2e: Paired t-test between periods on GREEN AC amplitudes from the AF sensor.....	141
Table 10.2f: Paired t-test between periods on GREEN DC amplitudes from the AF sensor.....	141
Table 10.2g: Paired t-test between periods on RED AC amplitudes from the FOOT sensor.....	142
Table 10.2h: Paired t-test between periods on RED DC amplitudes from the FOOT sensor.....	142
Table 10.2i: Paired t-test between periods on IR AC amplitudes from the FOOT sensor.....	142

Table 10.2j: Paired t-test between periods on IR DC amplitudes from the FOOT sensor	142
Table 10.2k: Paired t-test between periods on GREEN AC amplitudes from the FOOT sensor	142
Table 10.2l: Paired t-test between periods on GREEN DC amplitudes from the FOOT sensor	142
Table 10.3a: Mean red (660 nm) normalised AC (heart rate frequency) amplitudes..	144
Table 10.3b: Mean infrared (940 nm) normalised AC (heart rate frequency) amplitudes.	145
Table 10.3c: Mean green (525 nm) normalised AC (heart rate frequency) amplitude	145
Table 10.4: Correlation results of normalised amplitudes with age and weight.....	146
Table 10.5: Correlation results for FiO ₂ change between the foot and AF sensors....	147
Table 10.6: Amplitude differences vs ASA scores.....	147
Table 10.7: Correlation (R) of amplitude differences and ASA scores.....	149
Table 11.1: Mean SpO ₂ Values in each period for each patient.....	152
Table 11.2: Correlation of SpO ₂ values of the three sensors, computed with SpO ₂ values from the mean values at each period (pre, during and post FiO ₂ increase).....	153
Table 12.1a: Mean red (660 nm) normalised AC amplitudes for each period per patient.	165
Table 12.1b: Mean infrared (940 nm) normalised amplitudes for each period per patient.	165
Table 12.2: Correlation of PPGs accross the periods between sensors, strong correlation = R > 0.5.	166
Table 12.3: Mean SpO ₂ values in each period for both patients.	167
Table 12.4a: Correlation of SpO ₂ s between sensor locations for Patient 1.....	168
Table 12.4b: Correlation of SpO ₂ s between sensor locations for Patient 2.....	168
Table 12.5: Blood gas samples (SaO ₂) taken as part of routine clinical procedure during the time of study with corresponding SpO ₂ from all three sensors.....	169

Acknowledgements

Firstly, my thanks to my supervisor and co-supervisor Professor Panayiotis Kyriacou and Dr. Justin Phillips for their encouragement, solid advice and support throughout my studies.

I would like to extend my gratitude to Dr. Andy Petros of Great Ormond Street Hospital for Children for his support in this project, and the time spent with me during clinical trials.

An extra thanks goes to Dr. Maik Honsel and the nurses at Great Ormond Street for their added support and interest in my research.

To the parents of the Children who generously consented for the participation of their child in these studies, I extend my warmest regards and untold thanks for the contribution you have made, at a time I am sure emotions would have been high. Without you this project would not have been possible.

I would like to acknowledge the support of the Engineering and Physical Sciences Research Council for the financial assistance offered, and to the Worshipful Company of Scientific Instrument Makers and the City University Future fund for their additional contributions.

To my colleagues and friends in the Biomedical Engineering Research Group, your comradeship and times spent “drinking coffee” will never go forgotten.

My Love to my beautiful Fiancée Amanda, your patience, love and support are what encourages me to go forward.

Finally to my family and my parents, your love and encouragement to pursue my love for science can never be matched, you are the reason I am who I am.

Declaration

I certify that this project is wholly my own work and that all material extracted from other sources is clearly referenced.

I grant powers of discretion to the University Librarian to allow this thesis to be copied in whole or in part without further reference to the author. The permission covers only single copies made for study purposes, subject to normal conditions of acknowledgement.

Glossary

FiO₂ – Fraction of inspired oxygen, usually quoted as a fraction or percentage (i.e. 0.21 or 21 % is normal oxygen concentration in air), and is the parameter set in a hospital when a patient is receiving supplementary oxygen.

Hypothermia – A fall in body temperature to below 35°C. Babies have an increased risk of hypothermia they lose heat rapidly and cannot easily reverse a fall in temperature (Peters, 2007).

Hypovolaemia – An abnormally low volume of blood in the circulation, usually following blood loss due to injury, internal bleeding or surgery. It may also be due to loss of fluid from diarrhoea and vomiting (Peters, 2007).

Septicaemia – A potentially life threatening condition in which there is a rapid multiplication of bacteria and in which bacterial toxins are present in the blood (Peters, 2007).

Vasoconstriction – Narrowing of blood vessels, causing reduced blood flow to a part of the body. Vasoconstriction under the skin occurs in response to the cold and reduces heat loss from the body (Peters, 2007).

Abstract

In children and newborn babies on intensive care, information regarding blood oxygen saturation (SpO₂) is determined non-invasively by a device called a pulse oximeter. Sensors are usually placed on a hand or foot where their operation relies on the presence of pulsatile arterial blood. Light shines at two or more wavelengths (usually red and infrared) into the tissue where the pulsatile blood modulates, absorbs and scatters the different wavelengths of light in varying amounts and is detected by a photo-detector as a photoplethysmograph (PPG). The spectral information received is then processed electronically and digitally to determine the amount of haemoglobin present.

In the sickest of children blood supply can become compromised to these sensor locations and the pulsatile component of the blood may diminish and pulse oximeter readings may become unreliable, especially at times when accurate blood oxygen information would be vital. Currently the alternative is to take blood from an arterial line and run a relatively lengthy analysis (pulse oximeters are near-instantaneous in their operation) that may be unnecessary if the pulse oximeter could be relied upon at these critical moments. In the smallest of babies invasive sampling of blood becomes even more of an issue as any blood loss could lead to hypovolaemia and introduce extra sites of infection plus it causes a lot of stress to the neonate.

Since central blood flow may be preferentially preserved, the anterior fontanelle was investigated as an alternative monitoring site. Custom reflectance fontanelle and reference PPG sensors have been designed and built to investigate the fontanelle in those children at risk of peripheral supply compromise. Dedicated instrumentation and software has also been successfully developed for the control of the sensor electronics and the data-logging of PPG signals for retrospective analysis.

Sixteen neonates were recruited for fontanelle monitoring; all were ASA 1 – 3 (ASA ranges from 1 to 5 where 1 is the least sick and 5 is the most critically ill). As part of the approved protocol the delivered oxygen to the patients was artificially altered to look for corresponding changes in PPG signal amplitudes. Amplitude results reveal strong correlations ($R > 0.5$) between the reference sensor (placed on the foot) and the fontanelle sensor. This suggests that the fontanelle sensor is sensitive to changes in amplitude when oxygen in the blood alters. Correlation of the health of the child, using the ASA score, and the difference in amplitudes of PPGs between the sensors reveals that the fontanelle sensor does detect increasing fontanelle PPG amplitudes when compared to the PPGs from the reference sensor the sicker the child is, confirming that pulsatile flow is being preferentially preserved at the fontanelle in those children who are the most at risk from peripheral supply compromise. SpO₂ estimation at the fontanelle reveals a mean difference of 2.2 % to the SpO₂ as read by the commercial device and a 1.7 % difference to the blood gas results. These results confirm that the anterior fontanelle may be used as an alternative location for SpO₂ measurement in those who are at most risk of peripheral supply compromise.

Chapter One

Introduction

Paediatric and neonatal intensive care relies on constant monitoring of the vital signs of the child. Pulse oximetry has been called the “Fifth Paediatric Vital Sign” (Mower et al., 1997)

In neonates and paediatrics it has been shown that at times of periphery supply compromise, caused by the onset of hypovolaemia, hypothermia or septicaemia, the pulse oximeter can become inaccurate or fail (Kugelman et al., 2004).

The cause of these inaccuracies and failures are due to the fundamental principle on which pulse oximeters work. Pulsatile blood at the area of measurement, typically a hand or foot, is detected by a dual-wavelength light source (red and infrared light emitting diodes) and photo detector (a photodiode or phototransistor). The different wavelengths of light are absorbed differently by oxygenated haemoglobin (HbO₂) and deoxygenated haemoglobin (Hb) and the detected intensities are modulated by the pulsatile arterial blood, this modulation is then used to determine what percentage of HbO₂ is present within the arteries. This method of measurement is known as photoplethysmography (PPG). Conditions such as hypovolaemia and hypothermia can cause vasoconstriction at the limbs, which can cause a compromise of blood flow to the periphery, and thus the PPG signal needed for SpO₂ calculation diminishes, and the pulse oximeter may report an incorrect or no SpO₂ value. It is at these times that a constant SpO₂ reading would be the most beneficial, as an estimation of oxygenated blood may be useful in the treatment and diagnosis without having to run a separate invasive blood-gas analysis test, as this takes time and may be obtrusive, especially if the patient has no arterial line present.

1.1 Hypothesis

It has been proposed that the anterior fontanelle (AF), the soft area of unformed skull on a newborn, be tested as an alternative site for saturation monitoring. The hypothesis underlying this is that the blood supply is preferentially preserved at this location at times where the peripheral circulation is compromised, as the body tries to protect the most vital organs.

At the AF there is no obstruction offered by any bony material, therefore it is theorised that the AF can be used as an optical window where both red and infrared light can be used to make PPG measurements at a point below the scalp to directly monitor saturation. Other studies into SpO₂ readings from the core of the neonate would also support this (Kugelman et al., 2004) and a singular study where the AF was included as a site for PPG monitoring for the assessment of intrapartum monitoring showed that it is possible to receive PPGs in this location (Dassel et al., 1997). A second location, the infant oesophagus has also been given consideration for alternative SpO₂ monitoring, based on previous work (Kyriacou et al., 2008).

To test these hypotheses a schedule of technical work and clinical experiments has been designed to investigate these two areas for PPG monitoring. Below is an outline of this research and the work carried out.

1.2 Thesis Outline

Chapter two presents a basic description of the anatomy under investigation for alternative SpO₂ monitoring. An emphasis has been given to the localised blood supply of the head and the oesophagus and the basic structure of those organs so as to better understand the design choices made in chapter six for the construction of the PPG sensors. The circulatory and respiratory systems have also been briefly described for their role in the transport of oxygen in the body.

Chapter three introduces the concept of photoplethysmography to this research and the modalities in which it can operate. A short history of photoplethysmography and its relation with pulse oximetry has also been included.

Chapter four covers in greater detail the history of the design of the pulse oximeter and the scientific concepts that underpin its operation. The technology of the pulse oximeter has been outlined with its applications of use and a brief description of some of its limitations.

Chapter five describes in detail the use of the pulse oximeter in paediatric care. Attention has been focused on what affects the reliability and accuracy of pulse oximetry, in particular on those areas of research that have looked at improving outcomes when the pulse oximeter fails due to poor periphery blood supply. A hypothesis has been brought forward as to how to improve reliability in those neonatal and paediatric patients at risk of

periphery supply failure, by suggesting the anterior fontanelle and infant oesophagus as alternative locations of measurement for SpO₂.

Chapter six begins the technical aspect of this research by describing the design, construction and pre-trial evaluations of custom anterior fontanelle, reference and oesophageal sensors. Instrumentation and software was developed simultaneously to allow the ongoing improvement of all three technical aspects (sensors, instrumentation and software) until a satisfactory PPG monitoring setup was established.

Chapter seven describes the detailed electronic design, prototyping and testing documentation of the necessary hardware instrumentation needed to drive the custom PPG sensors and detect the returning optical signals received from the tissue.

Chapter eight finalises the technical aspect of this research by describing the design of the LabVIEW virtual instrumentation software needed to interact with the developed hardware from chapter seven. This software is responsible for data logging the recorded PPGs, and time-stamping important markers into the raw data files for synchronising with clinical events, critical to the retrospective analysis described in the following chapters.

Chapter nine presents the methodology used in the assessment of PPG signals for SpO₂ estimation, specifically how the PPGs were processed and the equations needed to compute SpO₂.

Chapter ten presents the results of amplitude analysis from 16 neonatal intensive care patients who underwent anterior fontanelle PPG investigations during delivered oxygen change. Correlations between the amplitudes of the PPG signals from the sensors and the monitoring periods have been made, as well as assessments of the amplitudes for each class of patient (ASA 1, 2 and 3).

Chapter eleven are the results of the outcome of SpO₂ calculation on the received PPGs described in chapter ten. Comparisons with clinical devices and methods of measurement have been made and the accuracy of the new sensors has been assessed.

Chapter twelve describes two in-vivo case studies utilising the oesophageal sensor described in chapter six. Two ASA – 3 patients, considered at risk of periphery supply compromise were studied. Similar amplitude and SpO₂ analysis carried out in chapter ten and eleven was performed on the data gathered from these two children.

Chapter thirteen critically discusses the results obtained from all clinical trials and makes an overall evaluation on the performance of the technology developed. Future work is suggested and final thoughts brought forward.

Chapter Two

The Neonatal Head and the Infant Oesophagus

The human body needs oxygen (O_2) in order to metabolise food and release energy, and is therefore an essential statistic that needs constant monitoring in the paediatric intensive care environment.

For continuous, non-invasive monitoring of blood O_2 levels, a device called a pulse oximeter is utilized. This device will be discussed in detail in chapter four. Various disadvantages of this technology, which are covered in the later chapters, mean that traditional monitoring locations, such as the periphery (toe, finger), are not always suitable for all patients in certain clinical situations, and most critically for this thesis, new-born babies and small children in intensive care. In an effort to overcome the limitations of current commercial pulse oximeters when applied to these populations, this thesis proposes the development of new pulse oximeter sensors designed to be applied at new anatomical areas such as the soft spot (anterior fontanelle) of a new-born's head, and the infant oesophagus. The underlying hypothesis is that such locations might be better perfused in cases where the peripheral commercial probes fail to estimate blood oxygen saturation. An overview of the related anatomy needs to be described before this technology is further discussed. This chapter provides a synopsis of the anatomy of the fontanelle and of the oesophagus and their relation with the surrounding vasculature.

2.1 The Fontanelle of the Neonate

The skull is made up of forty-four separate bones, in an adult these are fused together along rigid joints, known as sutures (Carlson, 2004). At birth these bones are not fused rigidly, between them there is a connective fibrous tissue (un-ossified mesenchyme), this results in large soft gaps between the cranial bones, where sutures intersect; these are the fontanelle, more commonly referred to as “soft spots” and are illustrated in figure 2.1. The term fontanelle comes from the Latin *fontanelles* meaning “little fountain”, as the pulsations from the brain, which can be visibly observed at these soft spots, are said to resemble the rising and falling of a fountain head (Gray, 2008). The flexibility of the skull, thanks to the presence of this connective tissue, aids in the birthing procedure by allowing the head to

distort and thus pass more comfortably along the birth canal. They also aid in later development of the child by allowing rapid growth during infancy (Graaff et al., 2009).

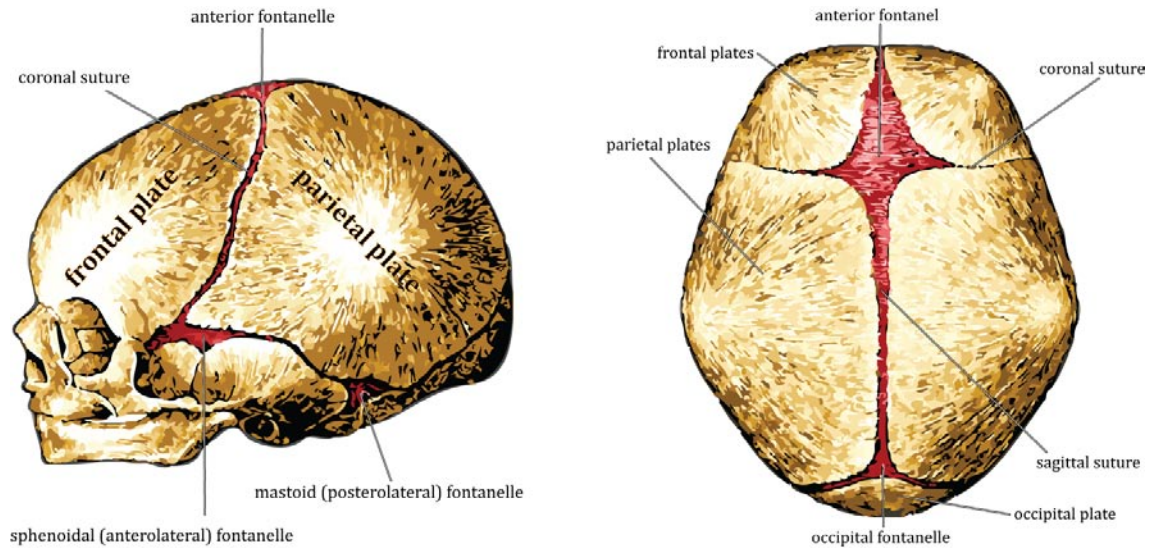


Figure 2.1. *The Neonatal Skull, taken and adapted from (Gray 2008). Left; Side profile view of skull. Right; Top oblique view of skull.*

There are six main fontanelle at birth, the largest of these is the anterior fontanelle (AF), located at the junction of the frontal and parietal plates, between the frontal, coronal and sagittal sutures. The other five include one occipital fontanelle (OF), two mastoid (posterolateral) fontanelles and two sphenoidal (anterolateral) fontanelles.

By about eight weeks the OF will close, however the large AF can persist for eighteen months, and usually by 24 months the fontanelle have ossified enough for the skull to be fully rigid, offering a protective covering for the brain (Scanlon and Sanders, 2007). Ossification is the process by which bone is formed, renewed and repaired, starting in the embryo and continuing throughout life (Peters, 2007).

Clinically the AF can be examined to note possible dehydration (the AF appears “sunken”), or a possible rise in intracranial pressure (indicated by a tense or bulging appearance). Commonly in intensive care ultrasonography is used to image the neonatal brain through either the OF or AF to aid in the diagnosis of conditions such as intracranial bleeds. The AF also serves as a landmark for withdrawal of blood for analysis from the superior sagittal sinus (Derrickson and Tortora, 2008).

2.2 Vasculature of the Head

Blood supply to the head can be split into two areas, the one that serves the face and scalp, and that one that serves the internal organs such as the brain and sensory organs.

The internal and external carotid arteries branch into five main pairs of arteries that supply the face and scalp; the ophthalmic branch from the internal carotid supplies blood to the supratrochlear and supraorbital arteries that in turn connect to the midline and lateral forehead sections of the scalp. Figure 2.2 depicts the main superficial arteries and veins of the face and scalp. The external carotid artery branches to the superficial temporal, posterior auricular and occipital arteries which supply oxygenated blood to the temporal, auricular and occipital region of the scalp respectively (Scanlon and Sanders, 2007). Venous drainage commences with respective paired veins that all drain into the internal jugular vein.

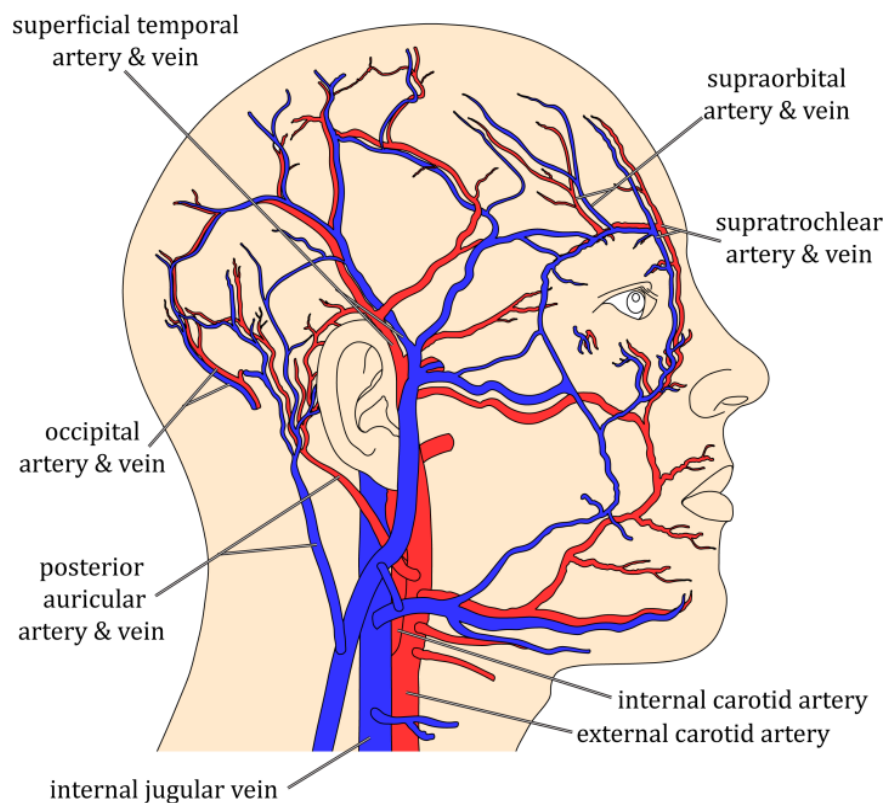


Figure 2.2: The Superficial Arteries of the Face and Scalp, Adapted from, © 2009;

The brain receives oxygenated blood from the carotid arteries, which commences from the arch of the aorta, and returns deoxygenated blood via venous drainage into the jugular vein (Scanlon and Sanders, 2007). The blood supply that communicates with the external

surfaces of the brain is the extracranial artery from the internal carotid artery. This subdivides into the anterior, posterior and middle cerebral arteries, which supply the frontal and occipital lobes, the inferior temporal lobe and the frontoparietal somatosensory cortex (Scanlon and Sanders, 2007). These three arteries subdivide even further to supply blood over the entire surface.

Venous drainage commences via the internal cerebral veins into various sinuses via veins on the dura mater. The largest of these sinuses is the sagittal sinus which runs from the anterior to the posterior between the two hemispheres within the longitudinal fissure of the brain (Scanlon and Sanders, 2007). The longitudinal fissure runs directly beneath the join between the parietal and frontal bones of the skull, and thus runs directly beneath the AF. Figure 2.3 illustrates the position of the sagittal sinus in the head.

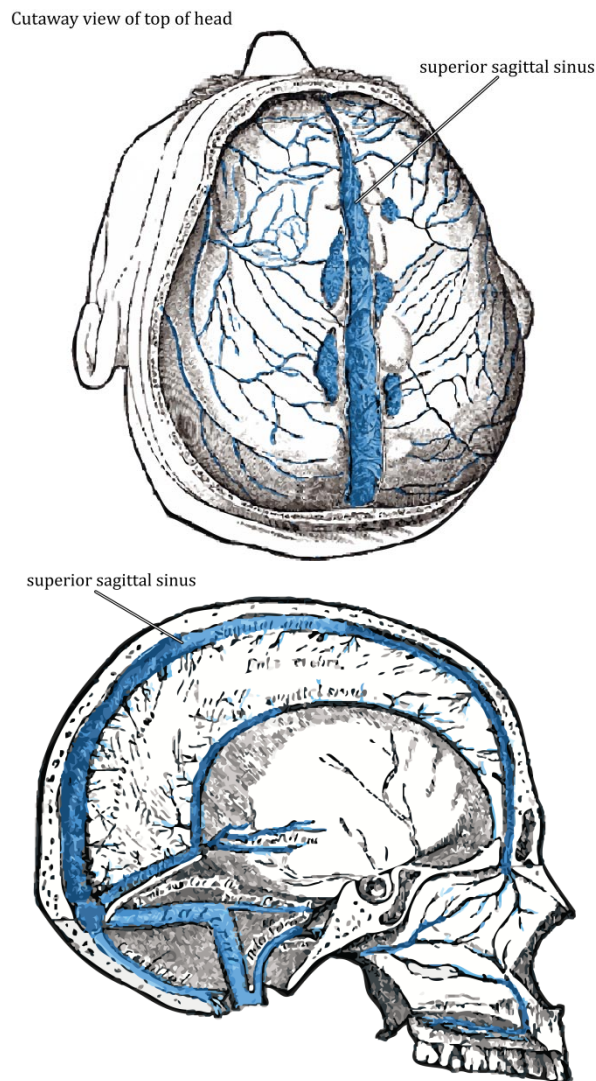


Figure 2.3. *The Sagittal Sinus, taken and adapted from (Gray, 2008). Left; Superior cut-away view. Right; Mid-sagittal view.*

2.3 The Oesophagus

The oesophagus is the muscular tube that connects the pharynx to the stomach, its' primary function is the transportation of food and liquid to the stomach, therefore it forms part of the digestive system. At birth the oesophagus has been shown to be (Jackson, 1950), approximately 10cm in length and increases by:

$$10\text{cm}(\text{length at birth}) + \frac{2 \times \text{age in years}}{3\text{cm}} \quad (2.1)$$

The route of the oesophagus, as illustrated in figure 2.4, starts at the back of the oral cavity in the neck, at approximately C5-6 vertebrae, the pharyngoesophageal junction. It descends anteriorly through the mediastinum and traverses the diaphragm, at approximately T10 of the vertebrae, at which point it then extends through the gastroesophageal junction and ends at the orifice of the stomach (Gray, 2008). On its route through the thorax the oesophagus passes behind the trachea and the pericardium, the double-walled sack that protects and encloses the heart and the roots of the great vessels, the aorta and the vena cava, and in front of the spine (Faller, 2004).

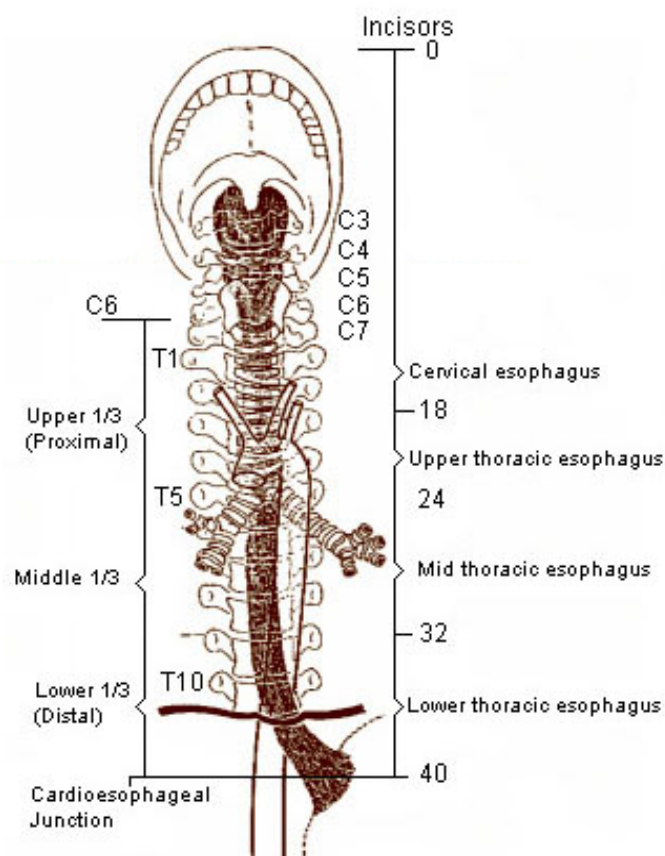


Figure 2.4. *The Route of the Oesophagus*, downloaded from (training.seer.cancer.gov, 2010) June 2010.

2.4 Vasculature of the Oesophagus

The blood supply of the oesophagus is directly supplied by the core blood supply, via vessels from the aorta and drains into the vena cava via various stem veins and the portal vein.

There have been many studies detailing the major stem vessels supplying blood to the oesophagus, all using different techniques and with varying results (Shapiro and Robillard, 1950, Swigart et al., 1950, Gloor, 1953, Tompsett, 1969, Lunderquist et al., 1983) took this previous work further and was able to visualize the microcirculation as well as the macroscopic display of the major arteries. The study concluded that the cervical portion is supplied by the superior and inferior left and right thyroid arteries, the intrathoracic by stem arteries from the caudal aspect of the aorta and the intra-abdominal supply is delivered by vessels from the left gastric artery and the splenic artery, a general pattern of blood supply from the study was constructed and illustrated in figure 2.5.

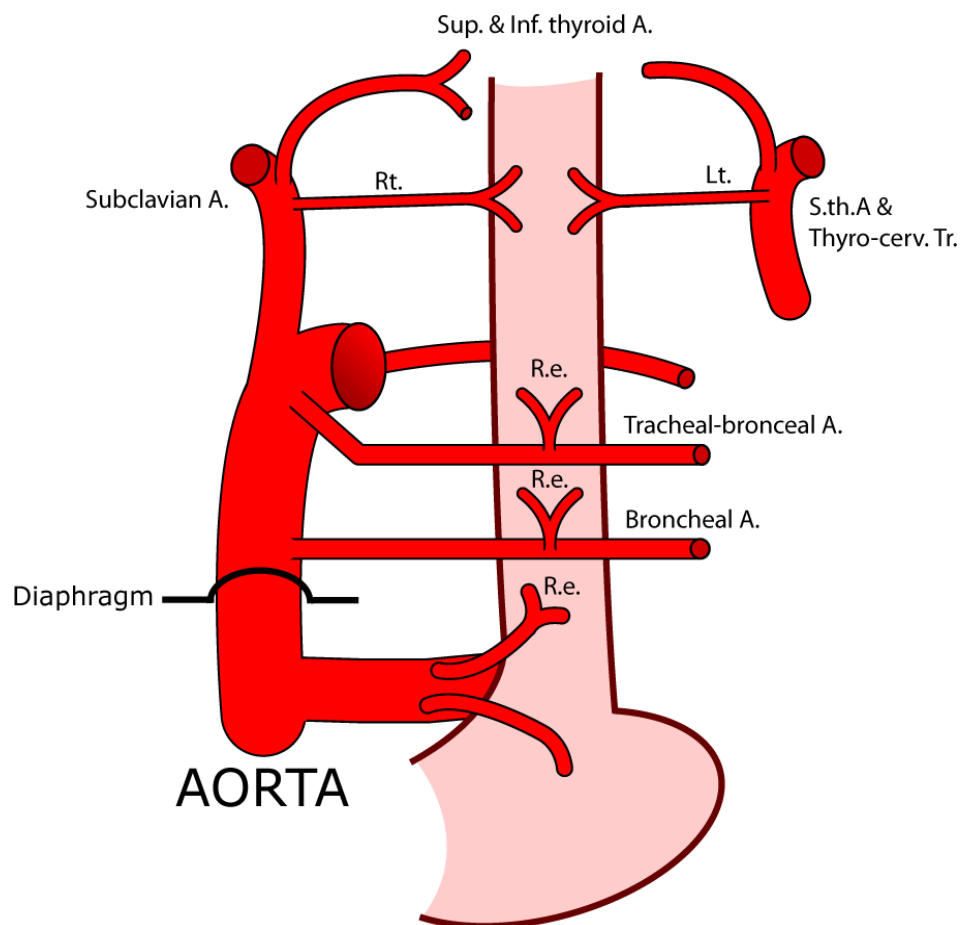


Figure 2.5. Pattern of Blood Supply to the Oesophagus, reproduced from (Liebermann-Meffert et al., 1987)

It was observed in an earlier study (Williams and Payne, 1982) that two cases in adults, long sections of oesophagus remained well perfused with blood even after being detached from their segmental blood supply. This suggested that the oesophagus complements the supply of blood to itself by a rich intramural network of arteries and veins.

Main drainage is facilitated by two major routes; the first into the superior vena cava via the azygous and hemiazygous veins for the upper portion, the second into the portal vein via branches of the left gastric vein for the lower portion (Hansen and Lambert, 2005)

2.5 The Circulatory and Respiratory System

The vasculature just described are of course part of the circulatory system, a rich network of arteries and veins that supply all the tissues of the body with the blood needed in order to receive O_2 , energy and to exchange waste products such as carbon dioxide (CO_2). The circulatory system comprises of two blood circulations, the pulmonary circulation (through the lungs) and the systemic circulation (Peters, 2007).

The pulmonary circulation carries deoxygenated blood from the systemic circulation to the lungs where it exchanges waste CO_2 with O_2 from the air at the blood-air interface (the thin barrier between individual alveoli sacks in the lung and the blood vessels which surround them) (Graaff et al., 2009). Blood is then returned to the heart where it is then passed to the systemic circulation and distributed to the body via various branches from the aorta, the major blood vessel leading from the heart. Oxygen is exchanged with the tissues in the body for waste CO_2 and the blood returns to the heart via the veins where it re-joins the pulmonary circulation to begin the process once again (Graaff et al., 2009).

2.6 The Respiratory System

The function of the circulatory system is to deliver O_2 and energy, and also remove waste (CO_2). This cannot be fully accomplished without the function of the respiratory system.

The respiratory system comprises of the lungs, airways (nasal cavity, trachea and bronchi) and the respiratory muscles (the diaphragm and intercostal muscles of the rib cage). The action of the diaphragm and the intercostal muscles draws air into the lungs where the blood-air interface aids in the transferal of O_2 from the air, and the exchange of waste CO_2 from the blood. Relaxation of these muscles expels air, and therefore the waste CO_2 from

the body (Derrickson and Tortora, 2008). Figure 2.6 illustrates all the major components of the respiratory system.

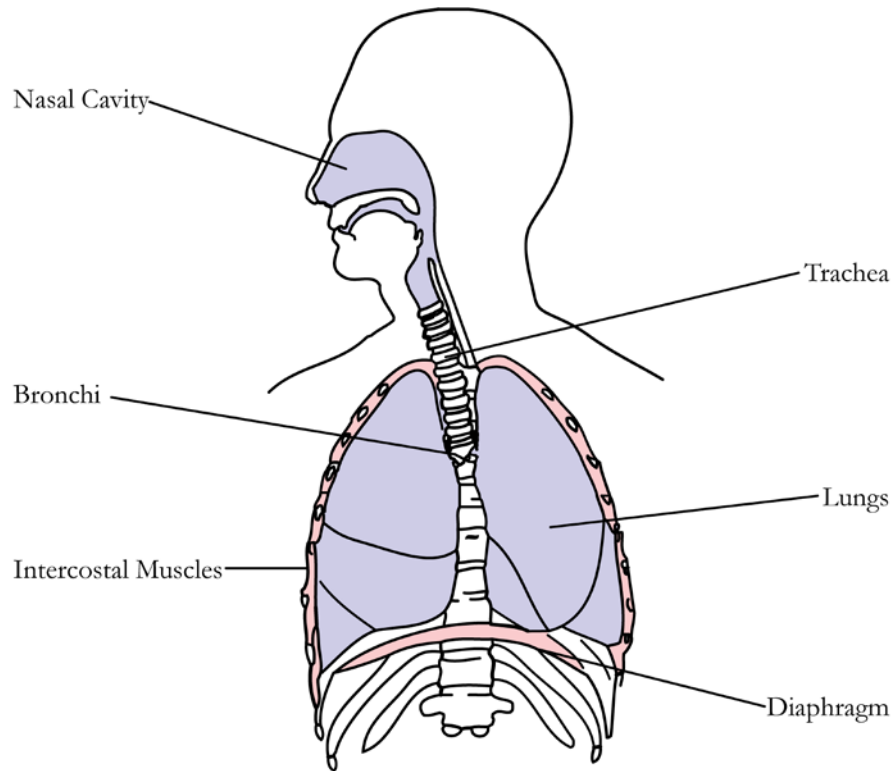


Figure 2.6. *The Respiratory System* adapted from (www.student.loretto.org/anatomyphys/, 2013 (downloaded))

Chapter Three

Photoplethysmography

First described in the 1930s (Rolfe, 1979), photoplethysmography is a photometric technique that is commonly used to monitor blood volume changes in a micro-vascular bed of tissue (Allen, 2007). This chapter describes the key concepts of photoplethysmography, the principles of operation of the technique and a brief history of its discovery and how it is used in healthcare.

3.1. Key Concepts of Photoplethysmography

Most of the studies conducted utilizing the technique of photoplethysmography have been concerned with monitoring on the peripheral parts of the body such as fingers, toes, ear lobes and other skin vascular surfaces, however there are reports that photoplethysmography has been used in the monitoring of more internal organs such as the oesophagus (Kyriacou, 2006) and other splanchnic organs (Hickey et al., 2011)

Photoplethysmography – literally meaning “measurement of volume change through the use of light” is a widely accepted term when used to describe the measurement of blood pulsations in skin and organs, utilising an optical source and a photo-detector. However, this is considered somewhat inaccurate, as alternative theories and practical experiments have revealed that the PPG waveform is far more complicated (Rolfe, 1979).

Fundamental to the idea of photoplethysmography is the fact that light is observed to pass through tissue, this can be demonstrated simply by holding a light source such as a torch against a hand and being able to discern a faint red “glow” around the torch and on the other side of the hand (Rolfe, 1979). A relatively broad-spectrum white light traverses the tissues of the hand and photons are absorbed, scattered and reflected, the faint red glow we see is a result of these processes having varyingly different amounts of effects on different wavelengths of light until only the red hues are permissible. Utilising photo-detectors, a quantitative analysis of this light shows that the light being received varies with time and in synchronicity with the beating of the heart (Allen, 2007).

The observations made with the torch reveal that detecting photons from the light source can be done with two different methods of source-detector orientation. Where light is seen to pass all the way through the hand the photo-detector can be placed opposite the source, this is called transmission-mode photoplethysmography. This is the common technique used in ambulatory or bedside monitoring where a pulse oximeter (a device used to measure blood oxygen saturation utilising the principles of photoplethysmography) uses a finger probe attached to the patient. A diagrammatic representation of transmission-mode photoplethysmography is shown in figure 3.1.

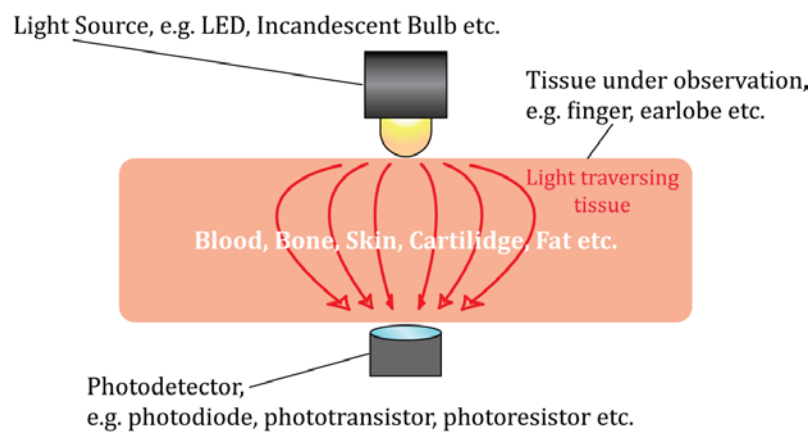


Figure 3.1. Transmission-mode photoplethysmography, source and detector are opposite.

The second method involves orientating the source and detector on the same plane, the glowing around the torch would then be detected as light is back-scattered towards the sensor, this is called reflectance-mode photoplethysmography and is illustrated in figure 3.2. Monitoring sites used are typically the forehead or the temple, however monitoring from any site is possible (Rolfe, 1979). Reflectance mode has found a use in the research of new ways of monitoring PPGs from various anatomical sites (Kyriacou, 2006, Phillips et al., 2009, Phillips et al., 2010, Hickey et al., 2011), where the usage of a transmission mode sensor is impractical.

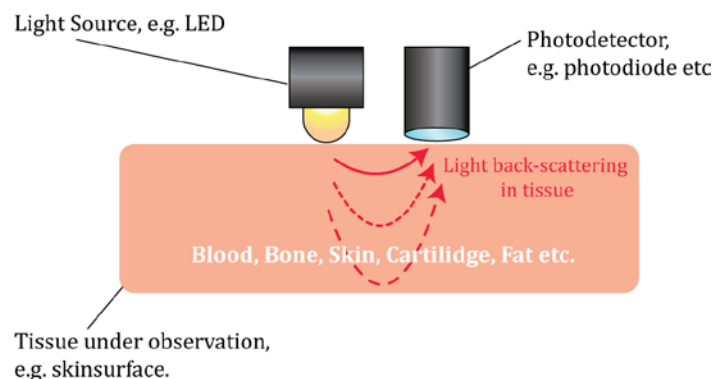


Figure 3.2. Reflection-mode photoplethysmography, source and detector are adjacent.

The properties of the PPG waveform, whether from transmission or reflectance mode, bare the same physical characteristics. As the heart contracts (systole) blood is forced through the arterial system and a pressure wave is produced, which gives rise to an increase in blood volume at sites where these “pulses” can be physically observed. During photoplethysmographic monitoring the increase in blood volume can be attributed (although it is debated that this is not the only contributory factor to the PPG waveform) by a reduction in the light intensity that is being received by the photo-detector. This in-turn represents itself as a decrease in current output from the photodetector, and therefore a decrease in electrical voltage, when observed using an oscilloscope (assuming no signal inversion). At diastole, the heart relaxes and the pressure wave diminishes and therefore so does the blood volume at the pulse sites. This manifests as a rise in electrical voltage on the oscilloscope as the amount of light penetrating through to the detector intensifies. The PPG waveform is more commonly plotted with absorption rather than voltage; these are inversely proportional, so diastole is now represented by the trough of the waveform, and systole with the peaks. The actual morphology of the signal produced has a large DC offset with a vaguely sinusoidal riding waveform. The riding waveform is indicative of the process just described and has a distinct shape, with notches and a generally steeper increase at the systolic portions of the signal, the photoplethysmographic signal (figure 3.3) can be divided into two separate components;

DC PPG – Manifests on the plot (figure 3.3) as a perceptibly consistent voltage offset. Since light is always passing through tissue, some of this light is always absorbed by the skin, bone, other various tissues and venous blood. Signal extraction techniques can extract this component for further analysis, usually with simple low-pass filters with a typical bandwidth of 0 - 0.5 Hz (Webster, 1997).

AC PPG – The pulsatile component of the signal and its’ origin comes from the beating of the heart as has been previously described. This rides on top of the DC PPG and only accounts for 1 – 2% of the entire signal. Like the DC part this can also be extracted for individual analysis using a band-pass filter with a typical bandwidth of 0.5 – 20 Hz is typical (Webster, 1997).

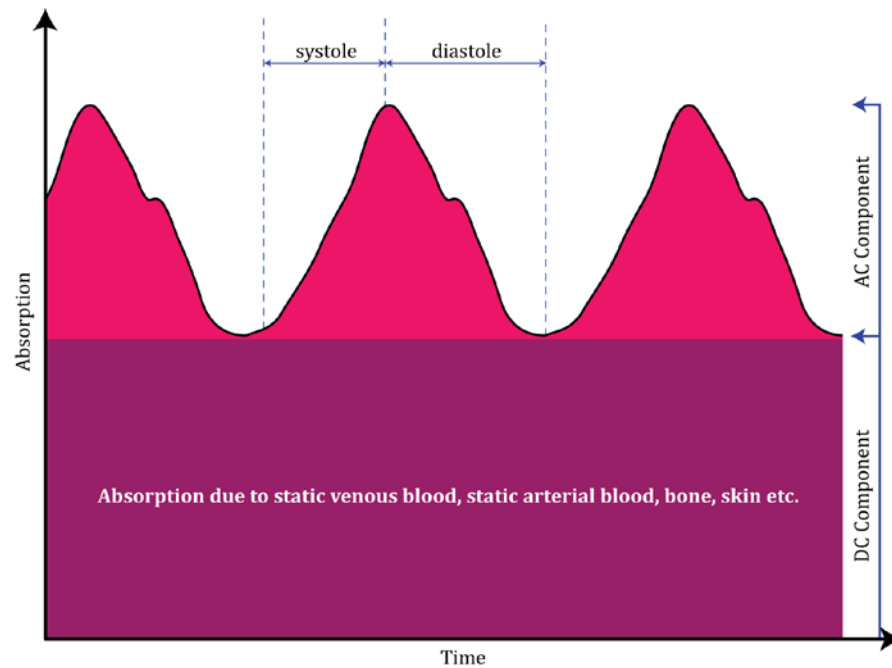


Figure 3.3. The AC-DC characteristic of the Photoplethysmographic (PPG) signal.

3.2. History and Origin of the Photoplethysmographic Signal

In 1936 Molitor & Knizazuk, and Hanzliki *et al* both described photoelectric apparatus used to measure blood volume changes in the rabbit ear where they were investigating the effects of occlusion and vasoactive drugs. Molitor & Knizazuk also described an apparatus where the photocell and light source were adjacent and a report of recordings from human fingers was made (Rolfe, 1979).

Early work in this time, which provided the greatest knowledge, was probably due to one individual and the work done by his affiliates, Alrick B. Hertzman, who conducted 30 years of experiments in this subject. His first paper on photoplethysmography was published in 1937 (Hertzman, 1937); Hertzman coined the term “photoelectric plethysmograph” and made measurements using his apparatus to show blood volume changes induced by exercise, cold, and the Valsalva manoeuvre (forceful exhalation with the mouth and nose shut) (Rolfe, 1979).

The AC and DC PPG components previously described were considered by Hertzman early on (Hertzman and Dillon, 1940), and the apparatus was modified to amplify these components separately. For the first time simultaneous measurements of both components were shown to provide more information on vasomotor changes (dilation or constriction properties of blood vessels) of the skin which was not possible previously.

The advancement of semiconductor technology reduced the size of early photo-detectors, whilst also making them more sensitive (Rolfe, 1979). New studies were conducted that were able to look at the previous findings in more detail. Senay *et al* (1960) and Hertzman and Flath (1963) (Senay *et al*, 1960, Hertzman and Flath, 1963), were able to detect the onset of cutaneous vasodilation in fingers and forearms. In 1968 and 1969, Pollard, and Weinman *et al* respectively (Pollard, 1968, Weinman *et al*, 1969) both confirmed findings from Hertzman of the Valsalva manoeuvre causing changes in blood flow in the skin.

Section 3.1 described the general formation of the photoplethysmographic signal as observed with the arterial pulse, however as stated earlier there is debate amongst scientists as to the true origin of the signal which has produced experimental results that demonstrate the PPG as a far-more complicated signal. Moyle (Moyle, 2002) describes several key factors that affect the amount of light received by the photo-detector, these include; changes in the amount of blood under the probe, erythrocyte orientation, erythrocyte concentration (hematocrit of the blood), rouleau formation, local blood velocity, separation of light source and detector, arterial inflow and venous outflow.

Notably it is the effect of the erythrocytes (red blood cells) that have produced some interesting studies. In 1967 D'Agrosa and Hertzman studied various small vessels, (frog mesentery, hamster cheek pouch and rat mesoappendix) using microscopic photoelectric photometry (D'Agrosa and Hertzman, 1967). The study looked at the varying opacity of the vessels during different inhibited situations, such as the injection of adrenalin, and they compared their results to that of others and concluded that the “opacity pulse” of arterial vessels is not volumetric in origin. A postulation was put forward that either the pulse is due to orientation of the erythrocytes, and/or a change in hematocrit (concentration of red blood cells) of the blood. In 1981 Nijboer, Dorlas and Mahieu published results from a rigid tube experiment that make suggestions that for reflectance photoplethysmography the erythrocyte orientation did have an effect on detected light intensity (*in vitro* experimentation) (Nijboer *et al*, 1981). During systole the erythrocytes would align themselves perpendicular with the flow of the blood, and in diastole the alignment would be parallel, figure 3.4. However the *in vivo* results showed that the reflection of light from surrounding tissue dominates reflection from erythrocytes, thus, *in vivo*, the reflectance PPG is dominantly an absorption measurement, and it cannot be said for certain if this mechanism is a major contributory factor.

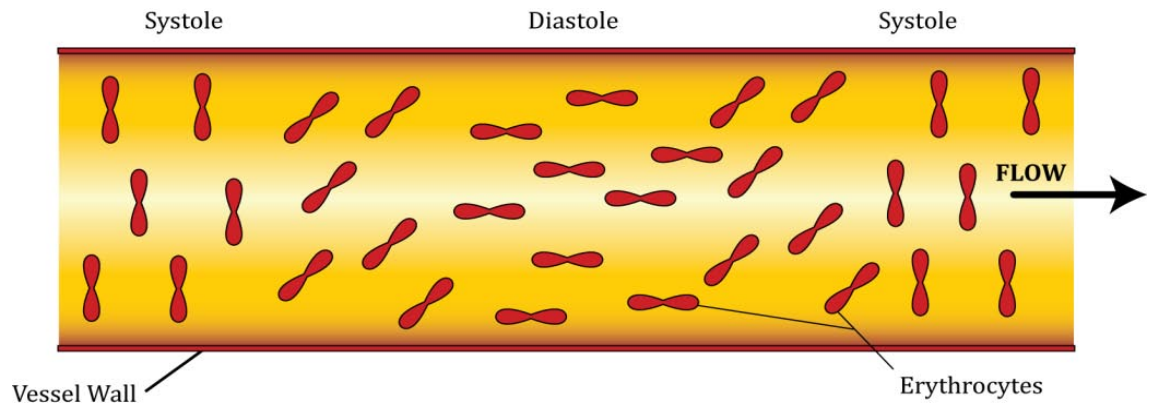


Figure 3.4. Erythrocyte orientation with systolic and diastolic action.

3.3. Photoplethysmography in Pulse Oximetry and Summary

Early bedside oximeters (such as the 1970 HP47201A) used multiple wavelengths of light and complicated computer algorithms to distinguish the oxygenated blood from the deoxygenated. Although a vast improvement and a breakthrough for early clinical non-invasive oximetry, this device required that the tissue was heated, and this presented the risk of burning, especially to infants who have sensitive skin (Webster, 1997).

The pulse oximeter challenged this method by assuming that the pulse detected via the photoplethysmogram was solely due to the arterial component of the blood supply, and therefore the oxygenated haemoglobin. This led to the invention of the pulse oximeter in 1973 by Takuo Aoyagi (Japan), a detailed history and the functionality the pulse oximeter is described in the next chapter.

Essentially a pulse oximeter shines light at two or more wavelengths through a tissue bed, e.g. the finger or earlobe, and measures the returning light signal. Differences in detected light are computed to obtain a reading for arterial blood oxygen saturation, or SpO_2 . The wavelengths chosen (usually one red and one infrared), are such that the light absorbance for oxygenated and deoxygenated haemoglobin is different enough to accommodate adequate sensitivity to each of the haemoglobin types (Webster, 1997).

Many, if not all of today's modern pulse oximeters include the ability to display a photoplethysmographic signal (figure 3.5), the use of which is used to determine whether the pulse oximeter is functioning correctly, as it is considered good practice to treat any pulse oximeter reading with caution when the photoplethysmograph signal is not displayed, or does not resemble an arterial pressure waveform, complete with a diastolic notch (Moyle, 2002).



Figure 3.5. A modern pulse-oximeter, complete with with plethysmograph signal display (downloaded from www.masimo.com, 2010).

The photoelectric plethysmograph, or photoplethysmography is a relatively simple concept to understand, however the implementations to which it can be applied to in medicine have far reaching benefits in health care. The next chapter *Pulse Oximetry* describes in detail the operation of this device and how the concepts introduced in this chapter have been effectively applied to make measurements of blood oxygen saturation (SpO_2).

Chapter Four

Pulse Oximetry

Over the period of sixty years (late 1920s to 1980), new technological advancements and scientific discoveries propelled the measurement of arterial blood oxygen saturation from an *in vitro* method (Glen A Millikan's blood oxygen saturation meter) to a real time *in vivo* method (The first commercially available pulse oximeter, Minolta OXIMET, 1980). This chapter covers a brief history of this development and looks at the key scientific discoveries that inspired the work done by the pioneers in this field. The technology and methods used, applications and limitations are also described.

4.1 A Short History of the Development of the Pulse Oximeter

The pigment that gives rise to the reddish hue in blood, haemoglobin, had been crystallized from various animals as early as the 1840s, but it wasn't until 1862 that this substance was first reported to change colour when mixed with oxygen by the biochemist Felix Hoppe-Seyler (Hoppe-Seyler, 1864). Hoppe-Seyler described the process of colour change as "beautiful" and noted two specific absorption bands, one at 560 nm and the other at 535 nm (both in the visible green band of the electromagnetic spectrum.) In 1864 a physicist, George Gabriel Stokes, was the first to report the effect of treating blood with a reducing agent, observing that the two distinct bands merge to a broader absorption band with a peak roughly half-way between the peaks for the untreated blood (Stokes, 1864). Crucially it was what Stokes did next in his experiment that demonstrated for the first time the dual-nature of the pigment, he reintroduced oxygen by shaking the blood with air, and the original bands reappeared. This process could be repeated indefinitely, and Stokes concluded that the pigment could exist in two states of oxidation, distinguished by their visible difference in colour (red for the oxygenated state, and deep red/purple for the deoxygenated state). Stokes called these two substances Scarlet Cruorine and Purple Cruorine, but it is Hoppe-Seyler's oxyhaemoglobin and haemoglobin, respectively, that we use today (Edsall, 1972).

In the late 1920s Glenn Allan Millikan from the physiological laboratory in Cambridge built and tested, as part of his graduate thesis, a simple device for measuring the oxygenation of a haemoglobin solution. His basic setup is shown in figure 4.1.

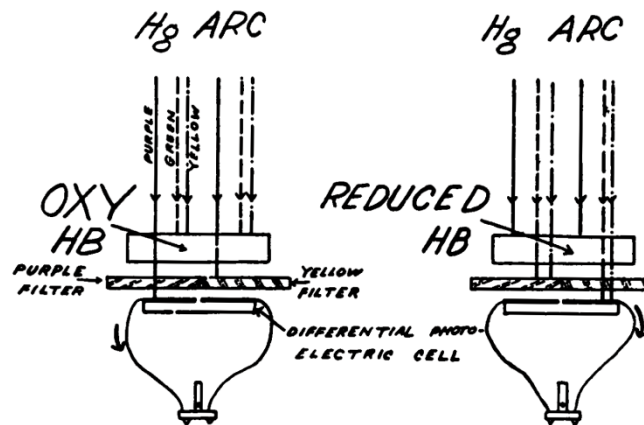


Figure 4.1. Principle of photoelectric colour analyser applied to haemoglobin (Millikan, 1933).

Light from a mercury-arc lamp passes through two filters (one purple and one yellow), so that when light goes from one end of the colour spectrum to the other there will be a significant change in the light being detected on one side of the differential photo-electric cell, the distribution of light reverses and thus so does the electric potential measured on the galvanometer. The absorption spectra for oxyhaemoglobin and haemoglobin were obtained, and calibration curves were derived. When samples of known saturation were then tested the overall accuracy of the device was approximately 4% for individual readings (Millikan, 1933, Severinghaus and Astrup, 1986).

In 1931 and 1934, Ludwig Nicolai and his associate Kurt Kramer performed the first oximeter experiments *in vivo* (Nicolai, 1932, Kramer, 1934). Nicolai's apparatus used the same Hg-ARC lamp as Millikan, and his protocol for measurement produced results that showed that the light transmitted through tissue, that had been occluded, would change linearly with time, when the logarithm was plotted. This was as expected as one would expect to see with oxygen consumption in a tissue. Kramer's experiment used the principles of the Beer and Lambert Law (see section 4.2) by fixing the optical path length (2 mm cuvette) of an exposed, unopened blood vessel in a groove (see figure 4.2). He changed his light source from the blue-green emission of the Hg-ARC lamp used by Nicolai and Millikan, and used an incandescent source with a red filter. Using a galvanometer, to make measurements, Kramer showed that saturation could be measured reproducibly and to an accuracy of $\pm 1\%$ (Severinghaus and Astrup, 1986).

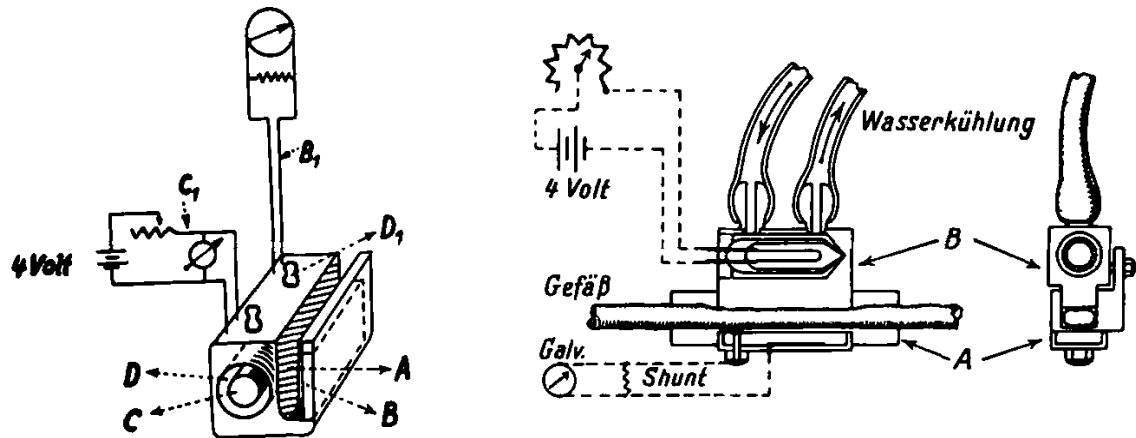


Figure 4.2. Kramer's apparatus for optically recording oxygen saturation in unopened arteries of experimental animals (Severinghaus and Astrup, 1986).

The first oximeter system to utilise two spectral regions, one not affected by the other, similar to what is seen in today's modern pulse oximeters, was developed by Karl Matthes and Franz Gross in 1939. The device was a red-infrared ear oxygen saturation meter, however it proved too large and inconvenient to use, and Matthes and Gross went back to reinvestigate the spectral properties of blood in order to improve the accuracy of their device (Severinghaus and Astrup, 1986).

The second-world war stimulated the need for an oximeter device that could be used in military aircraft in the unpressurized cabins. In 1940 Millikan had developed a working device, figure 4.3, which, according to a report by his wife, could be used to control a servo system that would control the supply of oxygen to the mask of the pilot wearing the device.



Figure 4.3. The Millikan Oximeter (Severinghaus and Astrup 1986).

Also in 1940, J R Squire from University College Hospital, London, added a new concept to the measurement procedure, by setting a zero point for the optical channels he used (one red, one infrared). By compressing the tissue in the web of the hand, and squeezing out the blood, when the compression was released the change in absorption signal seen would only be due to the blood returning, thus the surrounding tissue could be eliminated in their estimation of oxygen saturation (Squire 1940). Squire also introduced the idea of adjusting the red and infrared signal strengths, so that they would be equal with the inflow of blood, which should have made compensation perfect. This method was used by Earl Wood from the Mayo Clinic in his experiments, and anticipated the idea of the pulse oximeter (Severinghaus and Astrup, 1986).

In 1948 J E Geraci, under the guidance of Earl Wood at the Mayo Clinic, modified the Millikan ear oximeter to include an inflating balloon (Wood and Geraci, 1949). This was inflated to occlude the tissue in the ear and set a device “initial zero setting,” similar to Squire’s instrument. The balloon was deflated and the influx of blood to the tissue was used to determine the saturation reading. By 1950 the Mayo group had reported use of the new oximeter in newborn infants, thoracic surgical operations, cardiac diagnostic procedures and exercise testing (Severinghaus and Astrup, 1986).

In the Hewlett Packard Journal of October 1976 (Merrick and Hayes, 1976), a review of the methods of oximetry, and a new multi-wavelength device were discussed. In this they highlighted the key limitations on the work done by Wood and those before him on ear oximetry. With regard to the ear oximetry technique they noted these points; The bloodless ear is not truly bloodless; The optical characteristics of the compressed ear differ from those of the ear in the normal state; The optical path in the compressed state differs from that of the relaxed state; Any movement of the earpiece changes the measuring circumstances, requiring a re-measurement of the bloodless state; The forces required to secure the earpiece could interfere with the flow of blood.

It was Robert Shaw, an M.D. from the Presbyterian Hospital in San Francisco that went to Hewlett Packard and showed that using a combination of measurements from several wavelengths it was possible to overcome these limitations. Feasibility studies were conducted, a product was designed and finally the achievement was the Hewlett Packard Model 47201A Oximeter (Figure 4.4) (Merrick and Hayes, 1976). In operation the device used a Tungsten-Iodine lamp with a rotating wheel of optical filters that cut the beam sequentially. This light was carried by a fibre-optic bundle to the emitting window of the

earpiece. A returning bundle of fibres carried the transmitted light back to the instrument where a silicon photo-detector and amplifier was used to measure the returning light. The rotating filter was used to synchronise reference and ear measurements so that the difference in each measurement for each wavelength could be compared, measured and digitised by an on-board analogue to digital converter. An on-board computer then made the calculation of oxygen saturation.



Figure 4.4. Model 47201A Oximeter (left) and application of the ear probe (Merrick and Hayes, 1976).

The pulse oximeter, as we know it today, was conceived in December 1972 by Takuo Aoyagi (Nihon Kohden Corporation, Japan). In a review of his discovery (Aoyagi, 2003), Aoyagi makes it clear that the majority of his research was based on work done by the likes of Wood and Squire, even going as far as obtaining a Wood ear oximeter that they could study. The principles of operation of the pulse oximeter are detailed below, however it was in 1974 that the invention of the pulse oximeter was disclosed to the Japanese Society of Medical Electronics, and the OLV-5100 (figure 4.5) went to market, however this was somewhat unsuccessful commercially. In 1979 the patent for the Pulse Oximeter was granted with Aoyagi named as inventor. Aoyagi left his research group for a period of eight years and it was in this time that the first commercially successful pulse oximeter hit the market, the Minolta OXIMET-1471 (1980), which used a conventional lamp + filters + optical fibres for the delivery of light to the tissue. In 1983 Nellcor Developed the N-100, which had replaced the light source and detector with LED's and photodiode that could be mounted directly in the probe where the measurement was taking place. Aoyagi gives his thanks to Minolta and Nellcor for their development of the pulse oximeter, without them he says “the idea of pulse oximetry would have been buried” (Aoyagi, 2003).

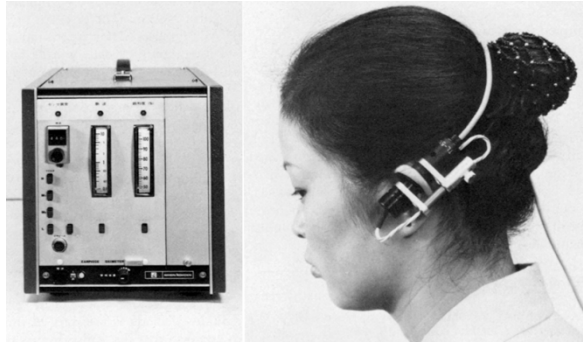


Figure 4.5. The Nihon Kohden OLV-5100, the first commercially available pulse oximeter, with ear-probe (Aoyagi, 2003).

4.2 Pulse Oximetry Principles

4.2.1 Beer and Lambert law

The principles of the Beer-Lambert law underpin spectrophotometry, a scientific method used to measure concentrations of transparent substances in a solution. The work done by Kramer, for example, attempted to use spectrophotometry on living animals by fixing the path length by mounting the artery in a clamp (figure 4.2). Monochromatic light, I_0 , entering a medium will be partly absorbed, and the intensity, I , of this light will diminish exponentially with increasing distance:

$$I = I_0 e^{-\varepsilon(\lambda)cd} \quad (4.1)$$

where the molar extinction coefficient, $\varepsilon(\lambda)$ ($\text{L mmol}^{-1}\text{cm}^{-1}$), is specific for a given wavelength, c is the concentration of the absorbing substance (mmol L^{-1}) and d is the optical path length. To give this measurement a meaning in terms of “absorbance” transmittance, T , first needs to be calculated:

$$T = \frac{I}{I_0} = e^{-\varepsilon(\lambda)cd} \quad (4.2)$$

then absorbance, A , is defined as:

$$A = -\ln T = \varepsilon(\lambda)cd \quad (4.3)$$

In reality any solution is itself an absorber, as well as the substance being measured, and there may also be other absorbers present, therefore the total absorbance, A_t , is the sum of all the independent absorbencies:

$$A_t = \sum_{i=1}^n \epsilon_i(\lambda) c_i d \quad (4.4)$$

By measuring the absorbance through a medium at several wavelengths, and knowing the coefficients for the multiple absorbers, then by simultaneous equations the absorbance due to each component, and hence the concentration can be calculated.

4.2.2 Optical properties of blood

Blood is a substance of multiple absorbers, and although it appears opaque in fact transmits light over a broad range of wavelengths, and is especially reflective in the red to infrared region. When talking about pulse oximetry the principle absorbers we are interested in are oxyhaemoglobin (HbO_2) and haemoglobin (Hb). When Stokes first observed the separate bands of absorption for Hb and HbO_2 , it was in the visible green part of the spectrum (535 – 560 nm) (Edsall 1972). Visualising this on a modern absorption spectra (figure 4.6) we observe these bands fairly clearly.

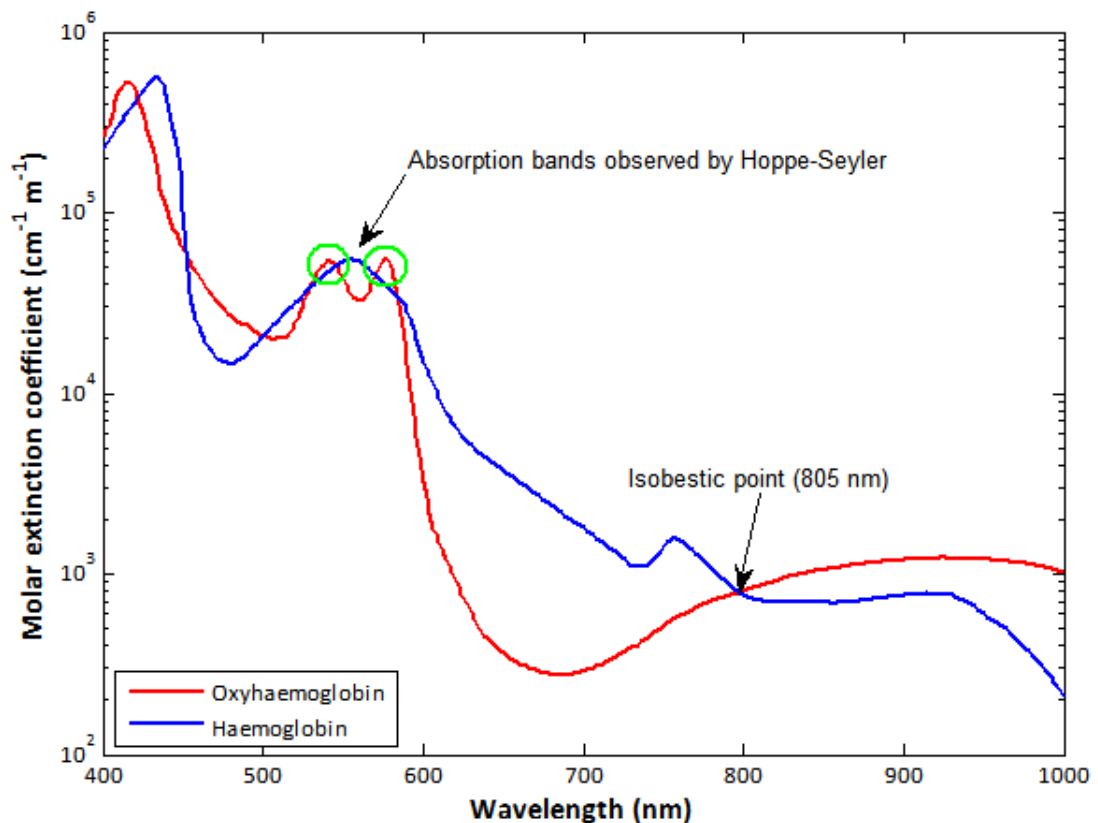


Figure 4.6. Absorption spectra of oxyhaemoglobin and haemoglobin, 400 – 1000 nm plotted with data from (Prahl, 1998).

Modern pulse oximeters take advantage of the coefficients in the red-near infrared region (630 – 950 nm). In his original experiments and developmental work of the pulse oximeter Aoyagi had selected 630 nm and 900 nm filters for his light sources. Light absorption at 630 nm was found to be most sensitive for oxygen saturation (Severinghaus, 2007), and 900 nm was chosen, because at the time Aoyagi was utilising the injection of a dye to measure cardiac output, which did not absorb this wavelength. In this region it is also observed that at approximately 805 nm the coefficients become equal, the isobestic point.

4.2.3 Limitations of the Beer-Lambert law

When calculating the concentration of a singular substance in a solution, in a cuvette of a fixed length, and assuming that light is either transmitted or absorbed only, then the Beer-Lambert law is valid. Unfortunately in the case of pulse oximeters, and early oximeters, the measuring “cuvette” is the tissue under investigation, whether it is the web of the hand or an ear lobe, etc. This presents several problems: Firstly the compressible nature of tissue means that the path length can never truly be fixed, and therefore when measuring the attenuation of light through such thin tissue the minute differences that may arise from the natural swelling, or pulsations (caused by expanding and contracting of the arteries and arterioles) in the tissue will have a significant impact. Figure 3.1 in chapter 3 demonstrates this pulsation as seen in photoplethysmography. Secondly the Beer-Lambert law does not take into account the effect of light scattering. When a photon enters a medium it is either scattered by a surface (a cell wall for example), and scattered in a different direction, or it is absorbed by the tissue. Transmission of any remaining photons in a medium with multiple absorbers will be a combination of these two phenomena, and the actual path length travelled will be longer than the distance between the entrance and exit points.

4.2.4 Ratio of Ratios

Takuo Aoyagi’s “Eureka!” moment was when he was observing his cardiac output experiments and noticing the pulsation of the photoplethysmographic trace from his detector. Aoyagi realised that by computing the ratio of the pulsating, AC, and non-pulsating, DC, portions at two wavelengths (Red and Infrared) he could achieve the same ratio that Wood used in his oximeter when he occluded blood from the ear to obtain a reference point. In other words the pulsatile portion of the photoplethysmograph, which is attributable only by the arterial blood as it is pumped by the heart, could be separated electronically from the rest of the blood and the surrounding tissue (Webster, 1997). This would also mean that the measurement site was not restricted to the ear, as the pulsations

observed could be obtained from anywhere, and for each pulse, so any momentary shift of the probe would cause a small artefact before the measurements returned to normal. Aoyagi termed this as the ratio of ratios (Aoyagi, 2003):

$$R = \frac{AC_{RED}/DC_{RED}}{AC_{IR}/DC_{IR}} \quad (4.5)$$

A new method for obtaining a ratio with which to calculate oxygen saturation was now available, however this also did not account for light scattering, and calibration based on the Beer-Lambert law is unreliable for these reasons (Moyle, 2002). Reliable methods of calibration were needed that could be used to derive equations and calibration curves so that saturation could be calculated.

4.2.5 Calibration of Pulse Oximeters

In Moyle's "Pulse Oximetry" (Moyle, 2002), it is stated that it is important to know what the pulse oximeter is actually measuring, and thus what they are calibrated to measure. There are two major definitions, functional oxygen saturation and fractional oxygen saturation.

Functional saturation is defined as the amount of oxygen carrying content of the blood, i.e. the total percentage of whole blood that is oxyhaemoglobin and not haemoglobin, and is defined as;

$$Functional SaO_2 = \frac{HbO_2}{HbO_2 + Hb} \times 100\% \quad (4.6)$$

Fractional saturation still measures the amount of oxygen carrying content, but takes into account the other two main species of haemoglobin, and is considered far more accurate. The other two species, carboxyhaemoglobin (HbCO) and methaemoglobin (MetHb) are now included in the total blood content;

$$Fractional SaO_2 = \frac{HbO_2}{HbO_2 + Hb + HbCO + MetHb} \times 100\% \quad (4.7)$$

Pulse oximeters that measure SaO_2 will state what they measure, either functional or fractional, whereas those pulse oximeters which state neither and use the conventional two wavelengths will measure SpO_2 , which is defined as oxygen saturation measured by a pulse oximeter (Moyle, 2002).

The “gold standard” for calibration of pulse oximeters is the CO-oximeter. The CO-oximeter uses the standard spectrophotometric techniques, utilising wavelengths in the visible part of the spectrum. Depending on the model of the CO-oximeter a sample of blood somewhere between 35 µl and 100 µl is introduced to the input port. The blood is haemolysed with ultrasound and a tungsten-halogen lamp is used to illuminate the sample at a number of wavelengths (which is usually determined by the number of constituents the machine is capable of measuring). Light is detected using a photodiode; the measurement is converted to a digital number for a microprocessor, which then calculates the measurements needed (Moyle, 2002).

Pulse oximeters that have been calibrated *in vivo*, i.e. a healthy human volunteer has had blood samples taken at different oxygen saturations whilst having their saturation artificially lowered have only needed to be calibrated during the developmental stages, the values obtained are stored in a lookup table that the pulse oximeter then uses to correlate the ratio with the appropriate SaO₂ level. The only calibration needed after this stage is a two-point check of the wavelength of the LEDs, slight deviations from the appropriate wavelength of either LED are compensated for by the calibration data for that specific wavelength. It has to be understood, however that the ethical implications of artificially lowering a person’s oxygen saturation is considered dangerous, and guidelines state that the saturation level being investigated should not drop below 85%, otherwise the risk of hypoxic brain damage is too high, therefore values below this have to be extrapolated, and may not be accurate (Webster, 1997; Moyle, 2002).

4.2.6 Technology of pulse oximeters

Light sources

The Nihon OLV-5100 and the Minolta OXIMET-1471 both used conventional lamps with filters and fibre-optic bundles to transmit the monochromatic light required for measurements, however this had always proved bulky and expensive. The Nellcor N-100 demonstrated that there was a new method for delivering the light needed the light emitting diode (LED).

The LED has the ideal characteristics to be used as the near-ideal light source for pulse oximeters. They are small in size and can be mounted directly in the probe at the sight of measurement. They have excellent drive characteristics with a large output in a very narrow bandwidth. Also, they have become so cheap that the LEDs used in multi-use probes can

be the same as the ones used in the one-time probes, i.e. ones used in neonatal care that are incorporated into sticky plasters, thus no disadvantage in terms of light output can be determined between the different types of probe.

The choice of LED wavelength is an important consideration. Typically 660 nm and 940 nm are chosen for the red and infrared LEDs respectively. At 660 nm it is observed (figure 4.6) that there is a large difference in coefficients for Hb and HbO₂. At 940 nm the spectras of the coefficients have overlapped and there is a small difference in their values (Mendelson and Ochs, 1988).

Photo detectors

All modern pulse oximeters use photodiodes as their choice of photo detector. The historical reasons that lead to virtually all modern pulse oximeters using this form of detector are largely unimportant, but their main characteristics that certainly contributed to their use are; Relatively low cost; Linear output current response to incident light, no need for complicated linearization circuitry; Response speed can be increased by applying a reverse bias voltage (although largely unused for pulse oximeter applications); Low dark current, as the ambient temperature increases so does the dark current, having low dark current ensures that the transimpedance amplifier stage after the photodiode has less chance of over-amplifying the signal that may lead to the circuit becoming saturated and the signals become useless; Good sensitivity, important to achieve good signal to noise ratio for the signal, as less amplification is needed; Spectral response can be broad over the desired wavelengths, typically 80 – 100% relative response from 660 – 940 nm. Specially treated photodiodes can even respond with a relatively good response to lower or higher wavelengths, facilitating the use of more than one wavelength of light, i.e. green or even blue; Available in a wide variety of packaging which makes their use widely adaptable.

Instrumentation

The instrumentation involved in driving the LEDs and detecting the output current from the photodiode is relatively simple, an outline of the main typical components are illustrated in figure 4.7; Low-cost microcontrollers used to control a constant current source for the LEDs; Current source drives the LEDs with the desired current; A transimpedance amplifier amplifies and converts the small current signal from the photodiode to a large voltage signal; Demultiplexing circuitry separates the signal for the individual wavelengths; Analogue filters split the signal into AC and DC components;

Optional amplification of the AC components may be utilised with another gain-stage; The signals are sent to an analogue to digital converter (ADC) where they can then be sent to the microcontroller for SpO₂ calculation, or externally to a computer for off-line storage for further analysis.

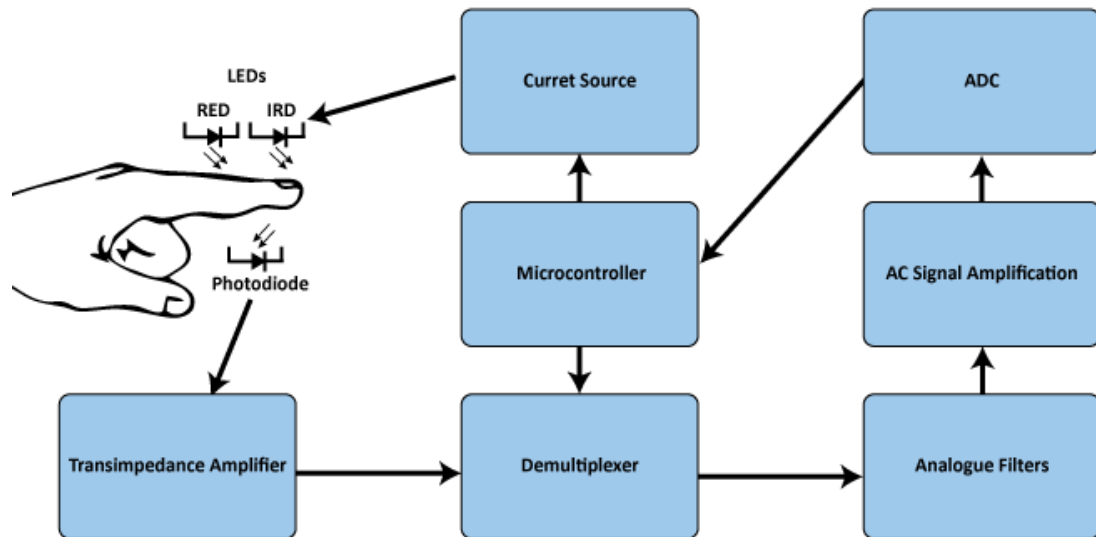


Figure 4.7. The main components of a pulse oximeter.

4.2.7 Pulse oximeter probes

The placement of the emitting components, the LEDs, relative to the photo-detector, the photodiode, can be set up in one of two ways, and although the finger is a common site, the methods of component orientation about to be described can be applied to various measurement sites.

Transmission-type pulse oximeter probes (figure 4.8) have the LEDs and photodiode mounted opposite each other. In this configuration the light is made to transverse the entire length of the tissue before reaching the detector. This is most common in areas such as the finger or earlobe where the distance travelled by the light is minimal and where a mechanical clip can be securely fastened to the patient without causing much discomfort.

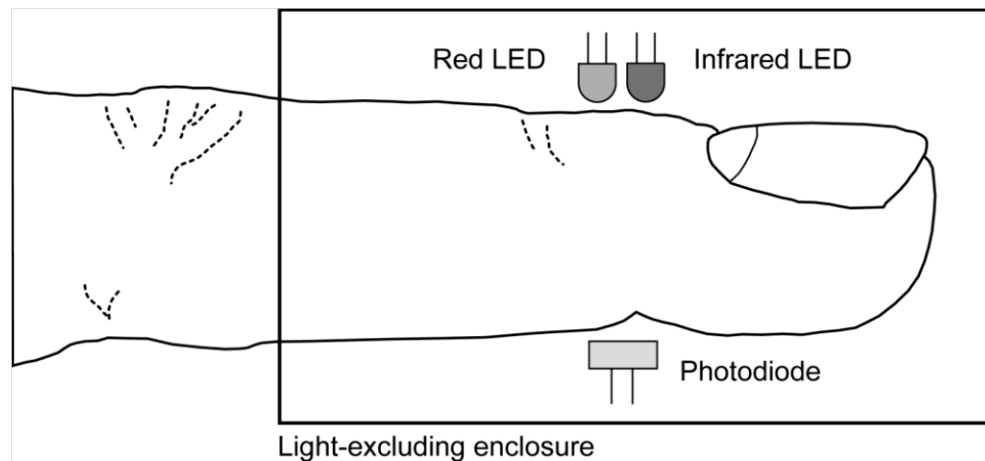


Figure 4.8. Transmission-type pulse oximeter probe.

Reflective-type pulse oximeter probes (figure 4.9) have the source and detector mounted next to each other. In this configuration the light must reach the detector by back-scattering from the underlying blood vessels and surrounding tissue. This offers the advantage that it may be used anywhere on the skin surface (Mendelson and Ochs, 1988), but offers lower signal to noise ratio (Webster, 1997).

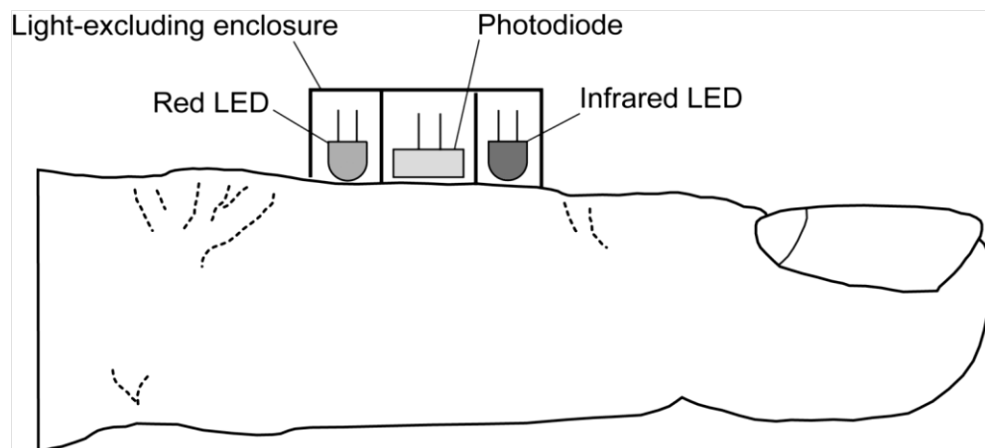


Figure 4.9. Reflective-type pulse oximeter probe.

4.3 Pulse oximetry applications

Its' common presence in hospitals, on ambulances and in other health care settings demonstrate that the pulse oximeter is a versatile and robust instrument. The use for which it has found a place include;

1. As an indicator of arterial oxygen saturation, alerting medical professionals to rapidly-occurring hypoxic events.

2. All modern pulse oximeters will display the pulse of the patient, an indicator of heart rate.
3. Perfusion index indicators may detect a change in the circulation in the skin, often an indication that circulation is deteriorating, which can be a symptom of an infection or that the patient is beginning to “shut down” (patients with mild to severe systemic disturbance).
4. The latest pulse oximeters from makers such as Masimo are able to display the values for the other haemoglobin species, HbCO and MetHb, useful when assessing accident and emergency patients who have suffered smoke inhalation from fires or gas poisoning.

4.4 Summary of Pulse Oximetry Limitations

A summary of the main reported limitations of pulse oximetry is presented below:

1. *In vivo* calibration, as previously stated, is limited by ethical concerns about artificially inducing a hypoxic event in the human being. Severinghaus and Koh have shown that there is indeed an inaccuracy at low readings, especially in cases of anaemia (Severinghaus and Koh, 1990).
2. Over or under-estimation of saturation levels has also been reported where there are high levels of skin pigmentation (Adler et al., 1998, Feiner et al., 2007).
3. Dyshaemoglobinaemias, non-functional haemoglobins such as HbCO and MetHb, have been known to cause false readings where patients have suffered excessive inhalation of smoke or poisonous gas (James, 1999), however recent advancements in pulse oximeter technology mean that these non-functional haemoglobins may be measured as well, or simply taken into account when SpO₂ is measured (Masimo, 2007, Masimo, 2008), this issue is described some more in Chapter 5.
4. Problems arising from a low peripheral perfusion when a patient becomes cold due to illness or surgery can bring the accuracy of the pulse oximeter into question, and has been shown to occur in neonates and infants, as well as adults undergoing certain forms of surgery (Iyer et al., 1996), this issue is described some more in Chapter 5.

Chapter Five

Pulse Oximetry in Paediatric Care

If we consider the modern pulse oximeter as the device which utilises light emitting diodes (LEDs) as the light source, rather than conventional filament lamps, as in the Nihon Kohden pulse oximeter of 1974, then the first reviews we started seeing of the reliability and accuracy of pulse oximeters appear in the early 1980's. Such devices had started making their way into hospitals, thanks largely to the reduction in cost attributed to the switch from expensive filament bulb and fibre optic bundle combinations to the low cost LEDs and photodiodes we are familiar with today. This chapter concentrates on the review of pulse oximeter technology, specifically in neonatal and paediatric care.

5.1 Reliability and Accuracy of Pulse Oximeters in Paediatric Care

In the 1980s pulse oximetry was largely seen as an “alternative” measurement technique, rather than the *de facto* (Deckardt and Steward, 1984, Fanconi et al., 1985, Jennis and Peabody, 1987). In 1986 there was a case from Birmingham Maternity Hospital, UK, that reported the use of the Ohmeda BIOX 3700 pulse oximeter on a 620g 25 week-old baby who had moist friable skin (Morgan and Durbin, 1986). The use of ECG electrodes caused trauma to the superficial layers of skin and the risk of sepsis and fluid loss was deemed too high for continued use of the ECG monitor, and also of a transcutaneous oxygen (O₂) sensor. The decision was taken to monitor the heart rate and O₂ saturation entirely with the pulse oximeter, and was done successfully for two weeks without any complications whilst simultaneously reducing the need to handle the infant. It was noted, however, that in order to detect hypoxaemia the use of an indwelling arterial line was needed for partial pressure monitoring. This was an early demonstration of the advantages of pulse oximetry over other well established procedures.

Dedicated researchers persisted in their investigations of the devices at the time, one review detailing the reliability of one device was made by Hay and associates in 1989 (Hay et al., 1989). The device in question, an Ohmeda BIOX 3700, was determined to have sufficient accuracy of SpO₂ (89% - 95% range) that it could be used reliably to predict PaO₂, however it was noted that at low and high SpO₂ readings (SpO₂ < 89% and SpO₂ > 95%) the device

could not be relied upon as an accurate indicator of PaO₂. The causes of these inaccuracies needed to be investigated.

A number of sources of error, both from the point of view of the ability of the pulse oximeter and clinical situations had been identified. These include;

- The use of intravenous dyes
- Motion artefact
- Ambient light
- Dyshaemoglobins
- Hypothermia
- Non Pulsatile Flow, hypo-perfusion, vasoconstriction and hypotension

5.1.1 Intravenous Dyes

Methylene blue, indocyanine green and indigo carmine have all been shown to lower SpO₂ readings (Sinex, 1999). In these cases other methods should be used to determine the oxygen saturation. The MasimoSET line of pulse oximeters warn in their guides that the presence of dyes may cause erroneous SpO₂ readings (Masimo, 2006).

5.1.2 Motion Artefact

Pulse oximetry relies on a good signal to noise ratio, and being able to extract the signal due to the absorption of light by pulsatile arterial blood in order to make calculations for SpO₂. When there is heavy movement by the patient this portion of the signal can become lost and the result is erroneous readings, loss of readings and false alarms (Trivedi et al., 1997). While this may have been a major contention for pulse oximeters in the past there now exists various technologies that are designed to read through the motion and reduce false alarms and improve reliability (Petterson et al., 2007).

5.1.3 Ambient Light

The specific wavelengths of light, commonly 660 nm (Red) and 940 nm (Infrared), used in pulse oximetry are, unfortunately, common bands that exist in the environment in typical clinical setups. Interference has been shown to come from fluorescent lights, infrared heaters, other medical devices, and daylight (Poets and Southall, 1994). Where this may have once been quite a common occurrence, it was realised early on that using optical shields around the probes and positioning them properly eliminated many of the errors

once seen (Poets and Southall, 1994). A controlled study (Fluck et al., 2003), set out to study the effect of different light sources in a darkened environment, utilising the Nellcor N200 transmission finger pulse oximeter. The study concluded that light sources common in the clinical setting had no clinically important effect on the ability of the pulse oximeter.

5.1.4 Dyshaemoglobins

As described in chapter 4, there are two ways that pulse oximeters present SpO₂ readings. The values given are either functional oxygen saturation values (only takes into account oxyhaemoglobin and deoxyhaemoglobin) or fractional oxygen saturation (accounts for the four main haemoglobin species, oxyhaemoglobin, deoxyhaemoglobin, carboxyhaemoglobin and methaemoglobin). In monitors that measure functional saturation errors can occur in cases where there are unusually high concentrations of the other two haemoglobin types (carboxyhaemoglobin and methaemoglobin). This happens because the different species interact and absorb light at specific wavelengths at different rates, and pulse oximeters usually only rely on two wavelengths to make their measurements, so when there is a contamination of another absorber that absorbs in the same region as the species of interest then readings can become falsely high or low. Emergency patients who have suffered some sort of gas poisoning often present this problem (Eisenkraft, 1988, Ralston et al., 1991, Reynolds et al., 1993).

A new generation of pulse oximeter (The MasimoSET with Masimo RAD-57 sensors) which utilises up to eight wavelengths of light, has been shown independently to successfully measure carboxyhaemoglobin within $\pm 2\%$ in a range of 0 – 15% and methaemoglobin with a confidence limit of 0.5% in the range of 0 – 12% (Barker, 2006, Barker and Badal, 2008).

5.1.5 Hypothermia

Neonates and infants who have undergone hypothermic cardiothoracic surgery will have a period of time where they recover from hypothermic shock. This presents a unique opportunity to study the effect of skin temperature on pulse oximetry readings in the neonate or infant that would otherwise be unethical to induce. A study (Iyer et al., 1996) examining pulse oximetry in a set of twenty-five infants who had undergone hypothermic cardiopulmonary bypass surgery demonstrated that for 95% of the cases a peripheral temperature greater than 29°C yielded saturation values that were in good agreement with hemoximeter oxygen saturation (SaO₂) (within 3%), below a peripheral temperature of

27°C caution was recommended as it was found that less than half (45%) agreed within the same limits.

5.1.6 Non Pulsatile Flow, Hypo-perfusion, Vasoconstriction and Hypotension

It has been shown that various conditions of the tissue where a pulse oximeter is placed can have an effect on the ability of a pulse oximeter to function (Lawson et al., 1987, Morris et al., 1989, Severinghaus and Spellman, 1990, Trivedi et al., 1997). In these reviews the ability of the devices under investigation to detect an arterial pulse varied, and even went as far as to point out that some oximeters were in fact very good at detecting pulses of small amplitude (Lawson et al., 1987) when the arm was occluded up to 93% of systolic pressure. Most, if not all, of the studies were performed on adults receiving hospital care or on volunteers.

There is a serious lack of knowledge from the paediatric or neonatal populations. Villanueva (Villanueva et al., 1999) from the department of Anaesthesiology Yale Medical School, USA, set out to assess a selection of pulse oximetry failure criteria in 19 children of 10 years of age or less including blood flow and pulse pressure. The main results concluded that low blood flow, induced artificially by increasing cuff pressure has little effect on the ability of the pulse oximeter to perform its functions, however it was noted that artificial inducement would not necessarily induce systemic vasoconstriction and therefore arterial pulsations at the periphery were still detectable. The end of Villanueva's study noted that it took at least two factors to affect the pulse oximeter significantly, particularly the combination of low skin temperature and low haemoglobin concentration, thus giving support that systemic vasoconstriction, induced by cold periods or hypovolaemia does significantly affect pulse oximeter function. It would be unethical to induce vasoconstriction on the human infant or neonate in order to see what affect this has. Therefore more efforts need to be made to look for opportunities to study infants in critical care who are already at risk of peripheral shutdown.

There remains the question of what effect sensor placement has on the reliability and accuracy of pulse oximetry, as the architecture of the tissue at any one location can differ greatly. The location chosen has a bearing on what type of sensor technology to use, transmission or reflectance mode, and because this is more of a technical limitation/problem it cannot easily fall into the same category as measurements made

during specific clinical situations. It is the focus of the following section to look at the effect of the differences in these two modalities.

5.2 Effect of Location of Sensors in Pulse Oximetry

Chapter four described the two different modes of pulse oximetry, transmission mode and reflectance mode. The vast majority of sensors are configured for transmission, placed on the finger, ear or foot where source and detector can easily be arranged either side a sample of tissue (finger ear lobe or toe). This has the major disadvantage that when a patient has poor or no periphery blood flow then the pulse oximeter has been known to fail.

A number of researchers and manufacturers have described their efforts to overcome these problems by designing various reflectance mode sensors for use in locations where it has been theorised that perfusion is preserved at times when the periphery has failed, including in the paediatric and neonatal populations. These include oesophageal sensors (Kyriacou, 2006, Kyriacou et al., 2008), and head/scalp/trunk sensors (Faisst et al., 1995, Dassel et al., 1997, Faisst et al., 1997, Berkenbosch and Tobias, 2006).

A pilot study on ten adult volunteers (Mendelson et al., 2006) demonstrated that it was possible to acquire SpO₂ readings from the forehead using a reflectance sensor. The sensor was setup against a conventional finger sensor with only a small difference in mean and standard deviation of the values between sites.

Research into pulse oximetry from the head, whether from paediatrics or adults, was prone to giving falsely high or low readings when compared against readings from a peripheral location. Six adults and seven neonates were selected for a study in 1995 (Nijland et al., 1995) to compare the effect of pulsating arteries on reflectance pulse oximetry. To make the comparison the sensor was placed either on the forehead or the temple (temporal area of head), where the effect of the superficial temporal artery on pulse oximetry could be studied closely and without any invasive intervention. The orientation of the sensor on the temple was varied between having either the LEDs or the photodiode directly over the blood vessel. When the photodiode was placed over the artery SpO₂s were shown to be lower in both populations (7.5% and 5.8% for neonates and adults respectively) than the reading from the forehead. When re-orientated, so that the LEDs were over the artery, there was an insignificant change in SpO₂, however the plethysmograph signals were larger than at the forehead.

Another investigation into erroneous SpO₂ readings at the forehead was made with twenty-five general anaesthetic patients, ASA category I and II scheduled for gynaecological and urological procedures (Shelley et al., 2005). The patients were assessed with pulse oximeters placed on the finger, ear and forehead. The study set out to investigate reports of erroneously low SpO₂s and signal instability from commercial forehead pulse oximeter sensors. The findings from the investigation suggest that the problems previously reported were due to complex waveforms at the forehead. The complex waveforms showed morphology that was consistent with a central venous trace, and therefore that the presence of venous signals was the source of the problems experienced previously.

These two studies suggest that the superficial vessels in the head/scalp may have a bearing on SpO₂ and photoplethysmography results, and all efforts should be made to include their effect when analysing results from any new studies.

It is either the forehead or temple that seems to be the main focus for reflectance pulse oximetry at the head; this is probably suggestive of the fact that these two locations are generally easy to locate a sensor since there is no obstruction that may be caused by hair. In neonates, who are often born with little or no hair there exists the opportunity to locate the sensor in other scalp locations where SpO₂ monitoring may be unaffected by the phenomena previously described. Two studies of reflectance pulse oximetry in neonates describe at least one other location selected for sensor placement (Faisst et al., 1995, Dassel et al., 1997).

Faisst (Faisst et al, 1995) recruited thirty-one neonates from an ICU who had a reflectance sensor placed on the forehead, cheek, occiput (back of the head) and back, in turn, to determine optimal positioning of the sensor. Dassel (Dassel, Graaff et al, 1997) solely concentrated on placing the sensor only on the scalp (eight separate locations) of seven healthy infants. Faisst reported close agreements for the reflectance sensor versus a transmission sensor placed simultaneously on the hand for SpO₂ and heart rate. It was noted that the reflectance sensor placed on the back was unreliable and susceptible to breathing artefacts, but this is unimportant to this review as it is the head locations which are of interest.

Dassel's efforts seem to be unique in these studies as the methods used include the use of a dedicated photoplethysmography system capable of analysing the individual red and infrared PPG waveforms, as well as the usual SpO₂ and heart rate values. From the plethysmograph signals recorded it was observed that there was a clear difference in the

effect of location, with up to a 13% difference in SpO_2s . Dassel states that the differences observed can be explained by the optical differences of different tissues at each of the locations. Interestingly it is when there is a space in the skull (over the anterior fontanelle) where the largest red/infrared values are observed, which again can be attributed by specific optical properties of the underlying tissues, and in this case the specific lack of any solid material, i.e. skull. Dassel reports that underlying pulsations from the sagittal sinus at the fontanelle may have been the cause for inaccurate readings. Although a source of error for global saturation, these pulsations may help in determining local saturation values at/under the fontanelle, a hypothesis yet to be investigated.

The latest advancements in reflectance pulse oximetry have led to sensors such as the Max-Fast forehead sensor from Nellcor, independently assessed for use in patients with poor perfusion (Bebout et al., 2001, MacLeod et al., 2005). Berkenbosch (Berkenbosch and Tobias, 2006) reported the use of the Max-Fast sensor in twenty-eight paediatric patients, comparing against a conventional transmission digit sensor. Results from all three studies suggest a faster response time to changing oxygen levels. Berkenbosch did comment on the lack of data in the paediatric population regarding that perfusion is preferentially preserved at the forehead than in the periphery at times of poor perfusion. There was some indication, however, that the paediatric patients receiving vasoactive medicine did exhibit better precision from the forehead sensor. The suggestion here being that forehead perfusion may well be better preserved than the periphery, but without a case of peripheral shut-down this is difficult to substantiate.

Because of the adaptability of reflectance mode pulse oximetry there were also efforts to develop reflectance pulse oximeters for the oesophagus (Kyriacou, 2006). In the topical review by Kyriacou 2006, he first presented the work by a number of groups who recorded SpO_2s from the upper oesophagus, but quickly noted that there were no efforts made to study the signal morphology directly. Following development of a custom PPG system with customized oesophageal sensors (Kyriacou et al., 1999), a batch of clinical investigations were carried out to assess oesophageal pulse oximetry from anaesthetised patients (Kyriacou et al., 1999, Kyriacou et al., 2001, Kyriacou et al., 2002b, Kyriacou et al., 2002a, Pal et al., 2005). Reflectance pulse oximetry from the oesophagus in the adult population presents as a reliable and accurate method for SpO_2 monitoring at times when periphery pulse oximetry may fail. In the paediatric population there is less supportive evidence, however a pilot study carried out at Great Ormond Street Hospital for Children, UK (Kyriacou et al., 2008) has demonstrated successfully that the neonatal oesophagus is

viable for PPG and saturation monitoring. This study was unable to gather simultaneous readings from a finger or foot (either from a commercial or customised sensor) so it is unclear whether the oesophagus in neonates and paediatrics exhibits similar behaviour to the adult at times of peripheral compromise.

There may also other reasons to pursue alternative locations for SpO₂ monitoring. It has been demonstrated (Sedaghat-Yazdi et al., 2008) that some transmission-based sensors are less accurate when placed on the sole or palm, as opposed to the finger or toe when SpO₂ < 90%. In neonatal a paediatric critical care the smaller dimensions of the infant toe or finger make them inadequate for proper attachment of the sensors, and so accuracy and precision may be affected when the sensor is alternatively placed.

5.3 Paediatric Pulse Oximetry Summary and Proposed Research

Over the course of its thirty year life, pulse oximetry has undergone significant developments and improvements and is, by some “...more than the fifth vital sign” (Hay, 2005). In nearly every clinical setting, including monitoring new-borns, it is the principle measurement used for early detection of oxygen saturation problems and general heart rate monitoring.

Since its conception, and by its nature, the pulse oximeter is a true multi-parameter monitoring technology (SpO₂, heart rate and perfusion index are at least the minimal parameters expected to be found on the majority of bedside devices today), an ability afforded to virtually no other medical device, costing relatively little. At the time of writing this thesis portable pulse oximeters for use in the home can be bought for as little as £20. Monitoring oxygen saturation is dependent on being able to detect the human pulse, from which an accurate measure of heart rate can be obtained.

Advancements in device manufacture have seen the pulse oximeter sensor migrate from the finger to the neonatal oesophagus and utilise new microprocessor technology to become ever more accurate and reliable. The efforts by individual companies have meant that pulse oximetry has gone beyond O₂ saturation measurements, and can function in scenarios where it was once impossible to use such devices.

Reflectance pulse oximetry, along with continued research, may offer us new methods of monitoring the critically ill, especially at times when the periphery is unavailable, especially

in the most vulnerable of patients, the neonate and the infant, and this will be the focus of this research.

In summary it is proposed that two monitoring sites are explored for the purpose of PPG and SpO₂ investigations, the neonatal anterior fontanelle and the infant oesophagus. Custom sensors will be constructed along with instrumentation and software that will be able to simultaneously monitor two anatomical locations together; the fontanelle or oesophagus and a reference location that is prone to periphery supply failure (either a hand or foot). In this manner a true comparative study can be performed, where PPGs and SpO₂s can be directly compared and tested for accuracy with commercial devices and “gold standard” blood-gas analysis.

Chapter Six

Design and Development of Multi-Wavelength Photoplethysmographic Sensors

Chapter four and chapter five introduced the concept and history of arterial oxygen saturation (SpO_2) monitoring from the head and the oesophagus. A hypothesis has been proposed that aims to study the photoplethysmograph (PPG) signal from the head and the oesophagus in an effort to estimate SpO_2 at times of periphery supply compromise. This chapter describes the design and development of custom fontanelle, oesophageal and foot reflectance PPG sensors specifically for this purpose.

6.1 Sensor Design and Construction

Acquisition of either fontanelle or oesophageal PPGs needs to be simultaneously compared with PPGs from a traditional sensor location so that a true comparative study can be made on the raw signals being acquired. For this reason a sensor has been designed and constructed that can be placed on either the hand or foot. This sensor will have the same electrical and optical specifications as the separate fontanelle and oesophageal sensors.

General construction for all three sensors will be based around the concept of reusability; this eliminates any sensor construction flaws that may influence the data between individual studies. In order to be reusable all outer materials (any part of the sensor that may come in contact with a patient) will be medical-grade, non-conducting (electrically) and able to be sanitized with standard sanitization fluids/wipes available in the hospital.

6.1.1 The Fontanelle Photoplethysmograph/ SpO_2 Sensor

LED Selection

Webster (Webster 1997) describes the two wavelengths traditionally used for SpO_2 monitoring, red (660 nm) and infrared (940 nm). A third wavelength in the green part of the visible spectrum (525 nm) will also be incorporated into the sensor. This would allow the possibility of additional PPG investigations that may go beyond standard SpO_2 measurement. There have been a number of studies investigating the use of green light

PPGs (Stack et al., 1998, Futran et al., 2000, Sandberg et al., 2005, Näslund et al., 2006, Maeda et al., 2008, Maeda et al., 2010). The range of wavelengths documented in these were all in the range of 510 – 565 nm, and were primarily used to look at the flow of blood or perfusion of specific tissues in an attempt to assess the health of that tissue following a surgical procedure. Work done, by Maeda *et al* (Maeda et al., 2008, Maeda et al., 2010) used green light PPG in an attempt to measure heart rate more precisely, for example. The three LEDs chosen for the sensor are summarised in table 6.1 and shown in figure 6.1.

Table 6.1: LED specifications.

Parameter	LED 1	LED 2	LED 3	Units
Manufacturer	Kingbright	Kingbright	Kingbright	-
Part Number	KP-2012SRC	KP-2012F3C	KPTK-2012VGC	-
Colour	Red	Infrared	Green	-
Peak Wavelength	660	940	525	nm
Dimensions (HxWxL)	1.1 x 1.25 x 2.0	1.1 x 1.25 x 2.0	0.75 x 1.25 x 2.0	mm
V _f @ 20 mA I _f	1.85	1.2	3.2	V
Max Peak I _f	150 @ 0.1 ms pulse width	1200 @ 10 μ s pulse width	100 @ 0.1 ms pulse width	mA

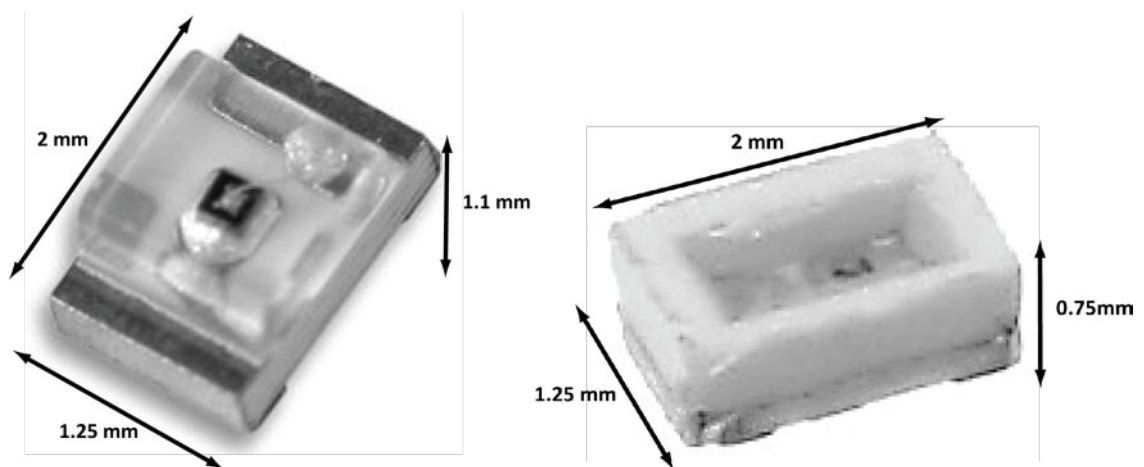


Figure 6.1: Left KP-2012 series LED (660 nm and 940 nm). Right KPTK-2012VGC 525 nm LED

Photo-detector Selection

The LEDs have to be switched on and off simultaneously at a rate of approximately 100 Hz. The LEDs cover a spectral bandwidth in the range 525 – 940 nm. A high-speed (rise and fall time = 100 ns), wide-bandwidth (410 – 1100 nm), large photo-sensitive area (7.5 mm²) photodiode (TEMD5010X01, Vishay Intertechnology Inc, USA) was selected as

the photo-detector (see figure 6.2). Other specifications of the photo-diode are; has a peak sensitivity at 940 nm, matching the peak output from the infrared LED, and a reverse dark current (I_{r0}) of 2 – 30 nA. Reverse light current (I_{ra}) is 45 – 55 μ A.

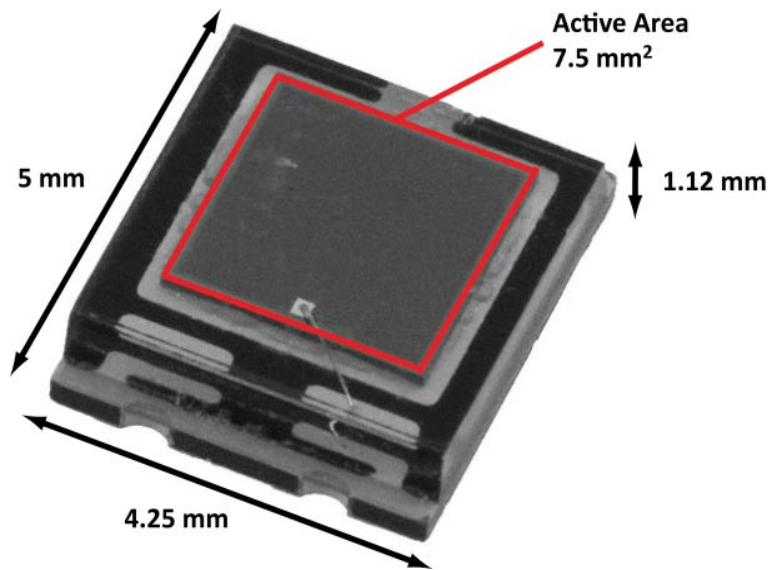


Figure 6.2: Vishay TEMD5010X01 broad-spectrum high speed photodiode.

Geometry

Previous studies (Davies et al., 1975) revealed the mean size of the AF to be 220 mm², treating the AF as an irregular quadrilateral diamond with four points of reference (see figure 6.3). These mean dimensions served as a primary reference for the optical component layout in figure 6.4.

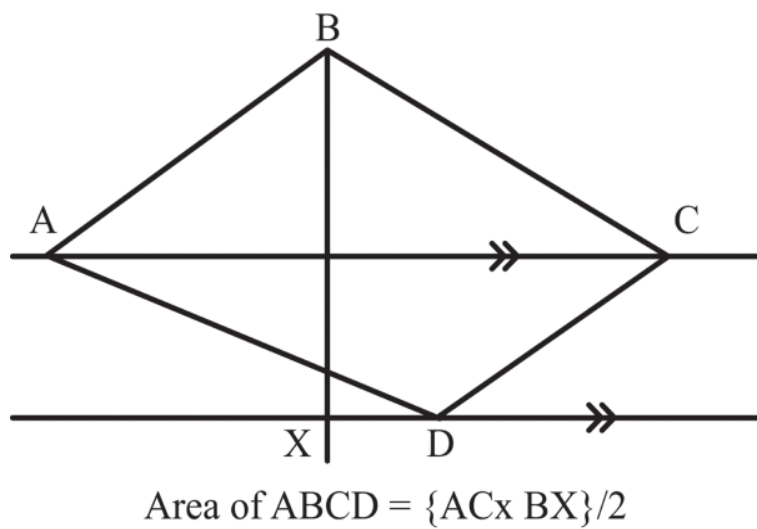


Figure 6.3: Area of the neonatal fontanelle

Line BX intersects line AC at point bx and by treating an area within triangle BC(bx) as a placement for the photodiode it was determined that the LEDs can be placed around the photo-detector, which will be optically isolated, at a distance of 5 mm from the centre of the photodiode. To account for any curvature or irregularity of the shape of the head, and the AF, the sensor will be made to be semi-flexible, allowing slight distortion so that the active components of the sensor lay flat against the head during monitoring.

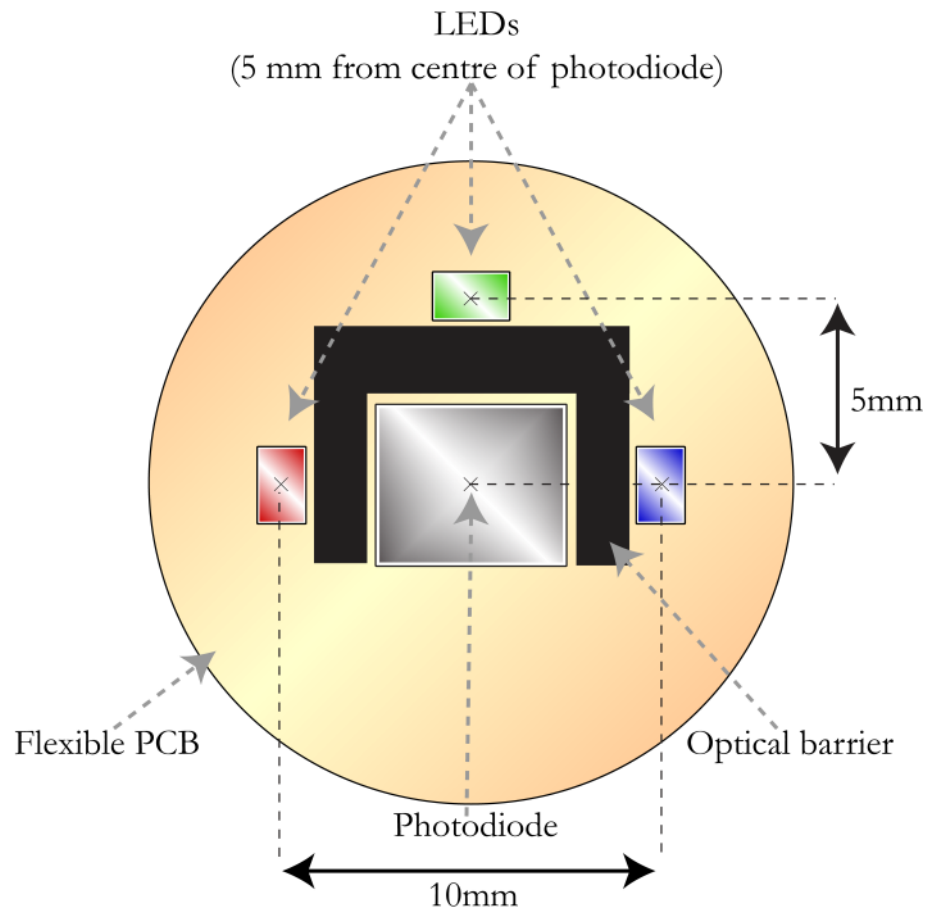


Figure 6.4: Fontanelle PCB Layout Concept

Sensor construction

With sensor geometry and component selection specified, a PCB layout was drawn in Altium (Sydney, Australia), a three-dimensional PCB layout is shown in figure 6.5. This design has space for the planned LEDs, including an arrangement of pads that would allow the LEDs to be arranged opposite, as in figure 6.4, or next to each other as is found in commercial sensors. The design was chemically etched onto a flexible copper substrate (Pyrulux, DuPont, USA). Components were manually soldered onto the circuit with a six-strand ribbon cable. An ECG electrode (Ambu® Blue, Ambu A/S, Denmark) was deconstructed which then had the PPG sensor circuit encased into it and sealed with medical-

grade epoxy resin (Dymax Corporation, USA). This would help ensure electrical insulation and a safe cleaning surface when cleaned between studies during the planned clinical trials. Figure 6.6 is the final construction of the fontanelle sensor.

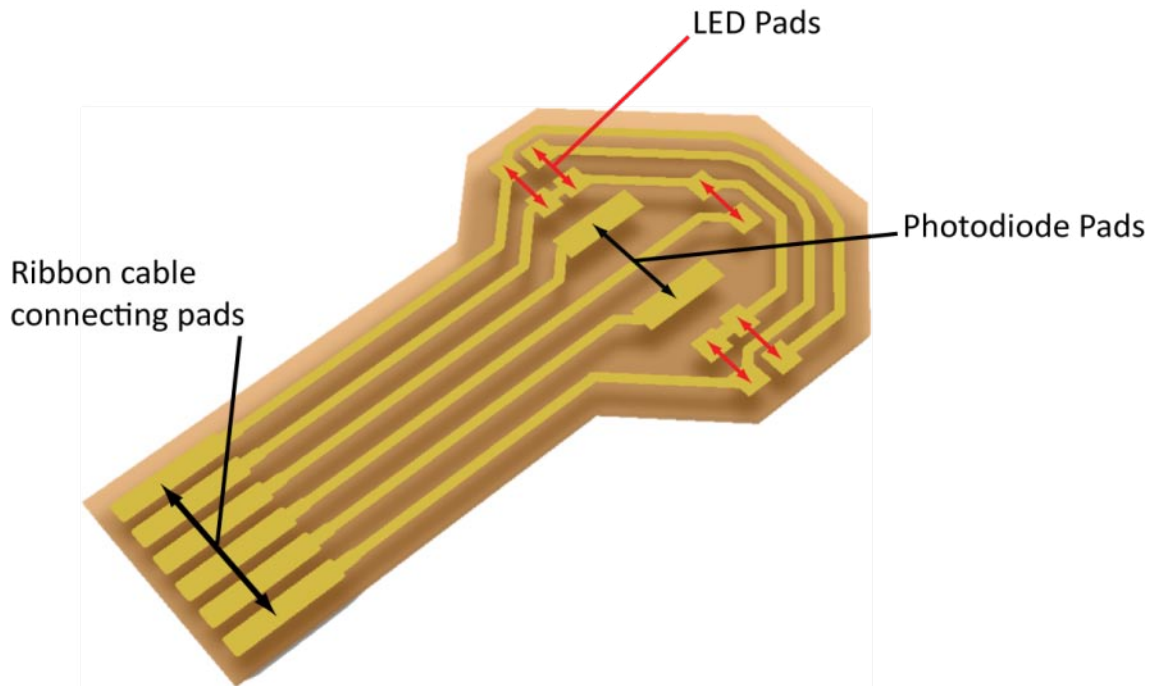


Figure 6.5: Three-dimensional concept of flexi-pcb layout for fontanelle sensor.

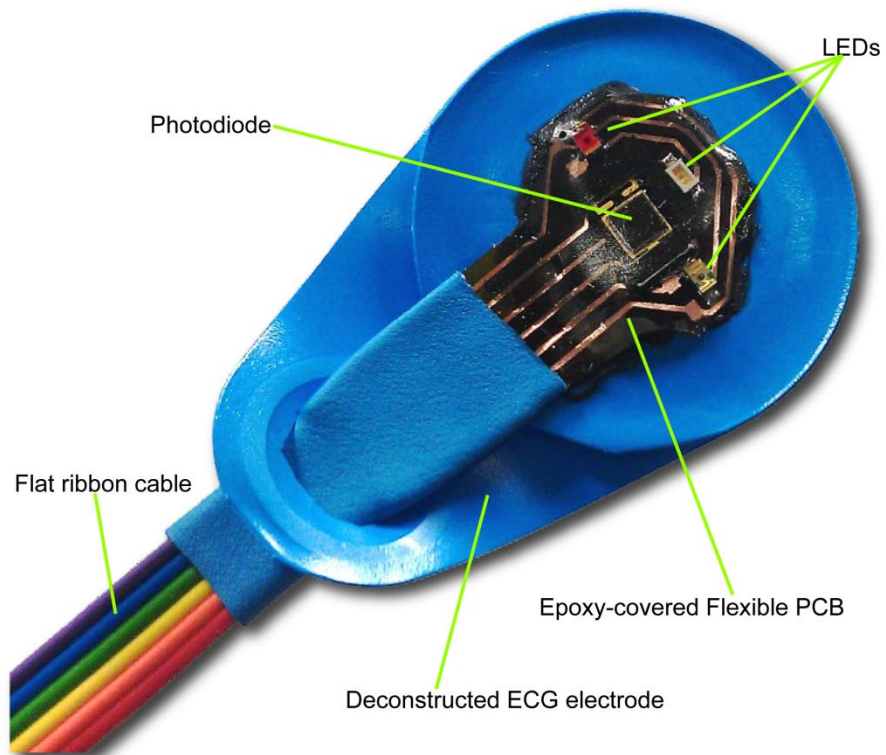


Figure 6.6: Final reflectance fontanelle PPG/SpO₂ sensor.

6.1.2 The Oesophageal Photoplethysmograph/SpO₂ Sensor

An effective design for a neonatal/paediatric oesophageal PPG sensor was demonstrated by Kyriacou *et al* (Kyriacou et al., 2008) based on designs done for the adult (Kyriacou et al., 1999). The size restrictions encountered meant that the original photodiode had to be replaced so that the sensor could be threaded into an oesophageal feeding tube.

LED selection

The red and infrared LEDs chosen for the oesophageal sensor were the same as in section 6.1.1. Due to size constrictions of placing the sensor in a feeding tube with an inner diameter ≈ 1.5 mm there was no configuration of LED and photodiode that meant that all components were evenly spaced, for this reason the green LED was omitted and PPGs from green light within the oesophagus will not be explored.

Photodiode

The photodiode selected (TEMD7000X01, Vishay Intertechnology Inc, USA) has an active area of 0.23 mm^2 and almost identical dimensions to the red and infrared LEDs ($2 \times 1.25 \times 0.85$ mm), see figure 6.7. The standard specifications of the photodiode are; spectral bandwidth = $430 - 1100$ nm; peak sensitivity = 900 nm; reverse dark current = $1 - 3$ nA; reverse light current = $2.4 - 3.6$ μA ; rise and fall time = 100 ns.

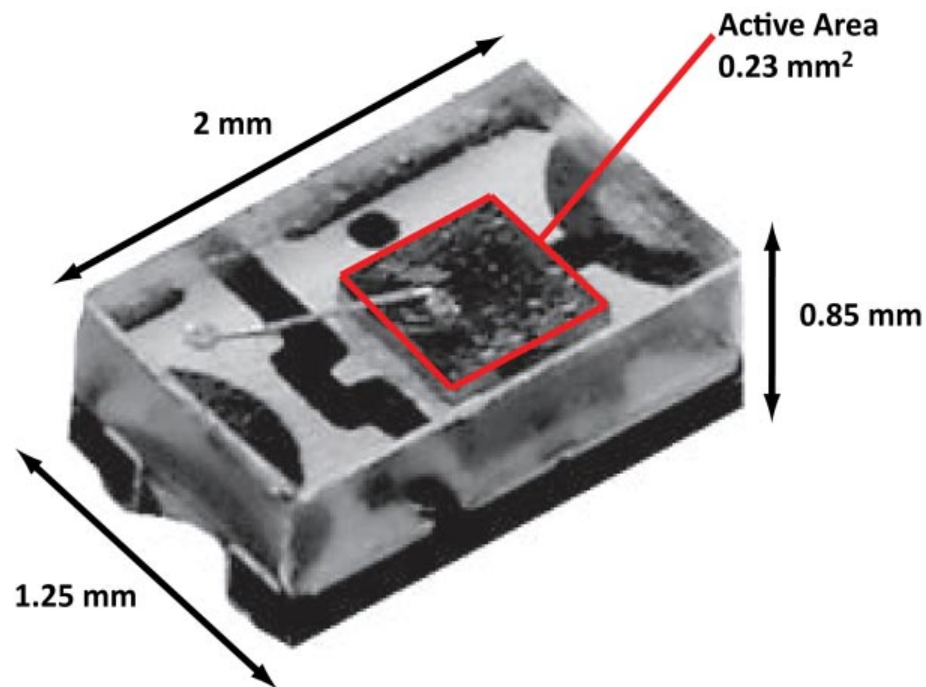


Figure 6.7: Vishay TEMD7000X01 broad-spectrum high speed photodiode.

Connecting wire

The developed neonatal oesophageal probe was connected to custom multi-core cable which was constructed in the laboratory utilising ultra-thin insulated (enamel-coated) single core wires (0.15 mm). Five cores were needed for the sensor and were wrapped in a PVC heat shrink to provide strength and additional insulation.

Construction

A design was drawn (figure 6.8) that emphasised on reducing sensor head width, to allow for the insertion into feeding/nasogastric tubes with an inner diameter of 1.5 mm. LEDs were soldered into place with their centre's 5 mm from the centre of the photodiode on to a thin fibreglass-backed copper board. The ends of the cores from the custom cable were attached and the end of the sensor head incorporated into the end of the heat shrink surrounding the cable. A thin layer of medical-grade epoxy resin was then applied to the head to add strength, rigidity and a final layer of electrical insulation. Figure 6.9 is the final oesophageal sensor construction.

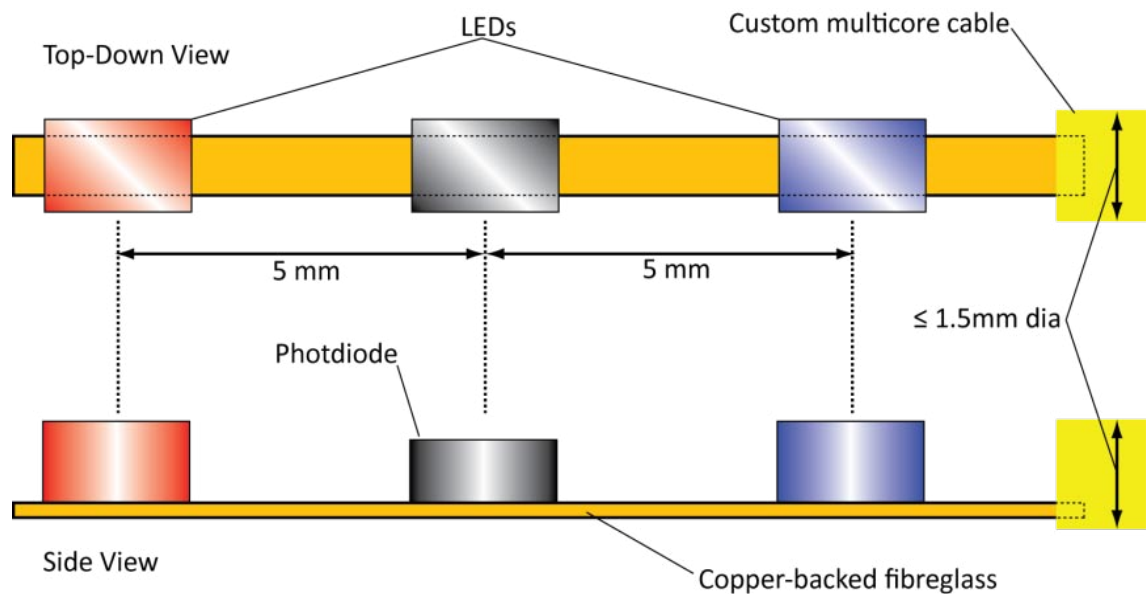


Figure 6.8: Oesophageal sensor construction drawing

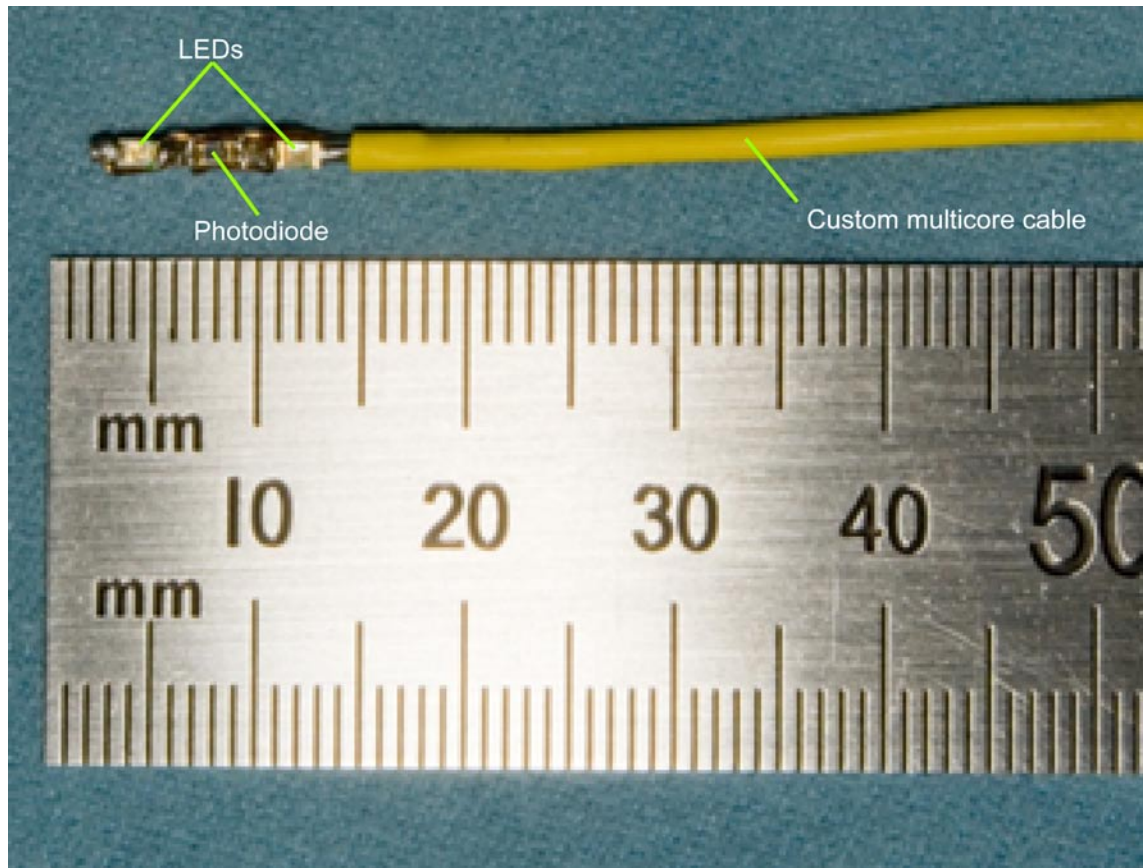


Figure 6.9: Final reflectance oesophageal PPG/SpO₂ sensor.

6.1.3 The Reference Photoplethysmograph/SpO₂ Sensor

The reference sensor was designed to be optically identical to the fontanelle sensor. A slightly modified PCB layout (figure 6.10) was employed in this design as it closely resembles the way commercial sensors have their components arranged. Photodiode to LED distance was identical to the fontanelle sensor. Figure 6.11 is the final foot sensor construction.

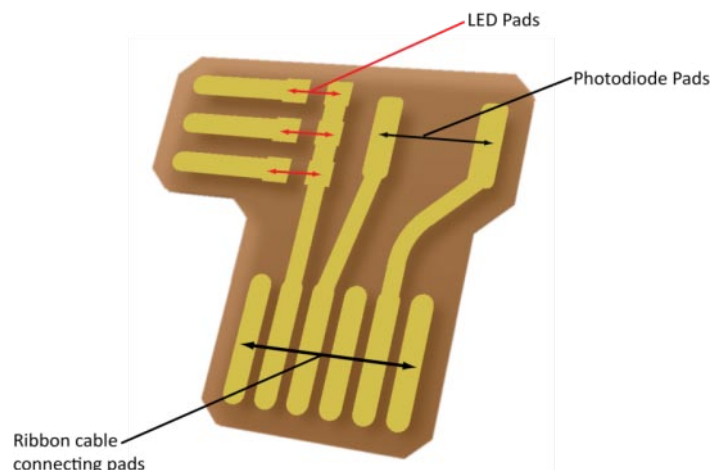


Figure 6.10: Three-dimensional concept of flexi-pcb layout for the reference sensor

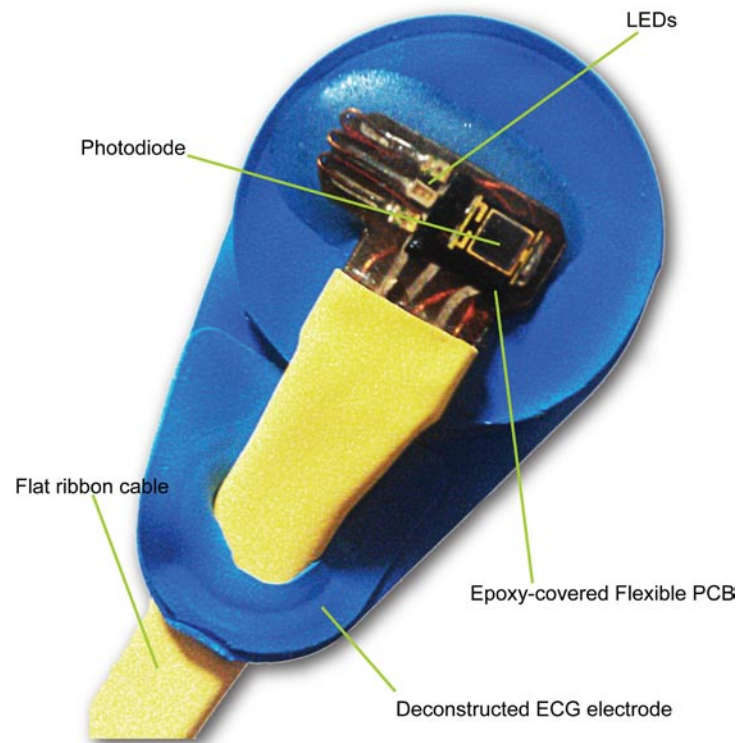


Figure 6.11: Final reference sensor

6.2 Sensor Evaluation

Development of instrumentation and software of the described sensors is covered in the chapters *Dual Photoplethysmograph Instrumentation Development* (Chapter 7), and *Virtual Instrumentation Development* (Chapter 8). The following evaluations were conducted with the instrumentation and software in those chapters.

6.2.1 Photoplethysmographs from the Sensors

Utilising the instrumentation and software, discussed in the following chapters, the sensors were tested to assess their operability. The sensors were tested by placing the fontanelle sensor on the temple of a healthy adult volunteer, the oesophageal was place in the mouth (held against the buccal mucosa) of a healthy adult volunteer and the reference sensor was placed on the finger of an adult healthy volunteer. Figure 6.12a-c shows PPG signals from all three developed sensors at all available wavelengths.

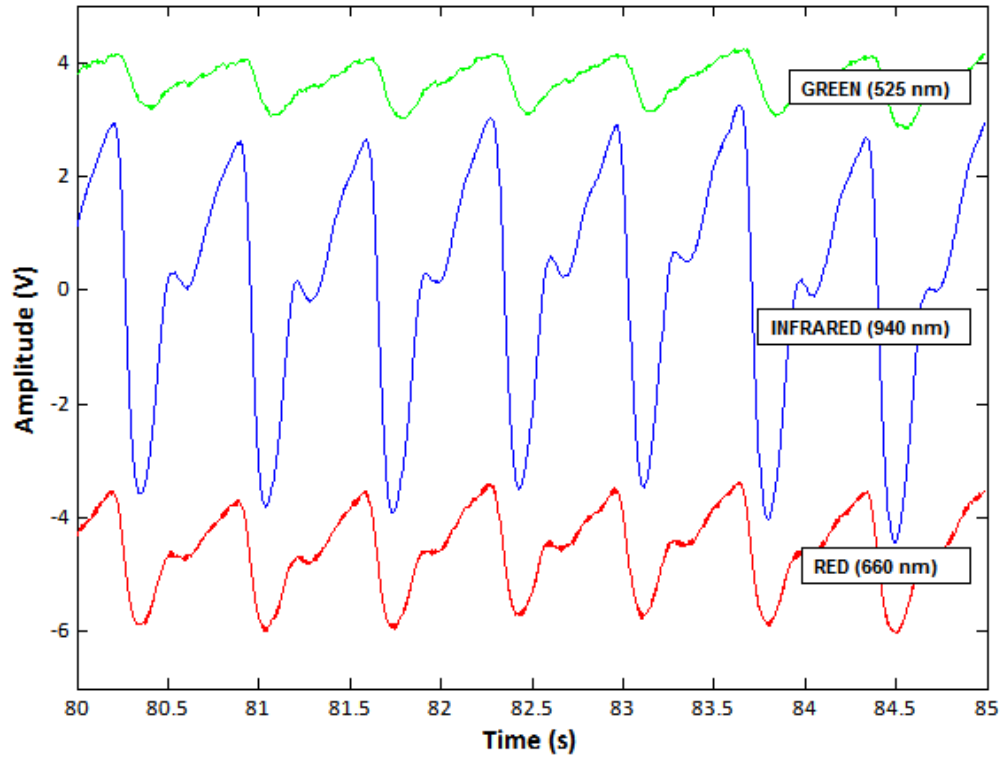


Figure 6.12a: Five second PPG capture using the fontanelle sensor on the temple of a female volunteer. Average heart rate = 84 bpm

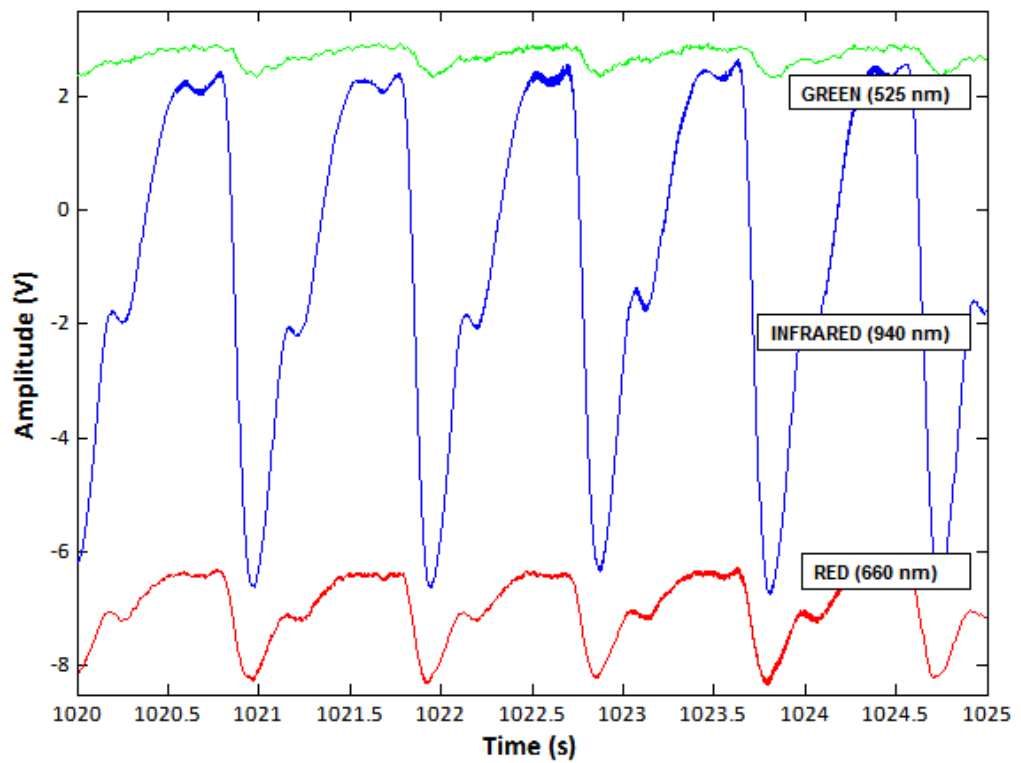


Figure 6.12b: Five second PPG capture using the reference sensor on the left index finger of a female volunteer. Average heart rate = 61 bpm

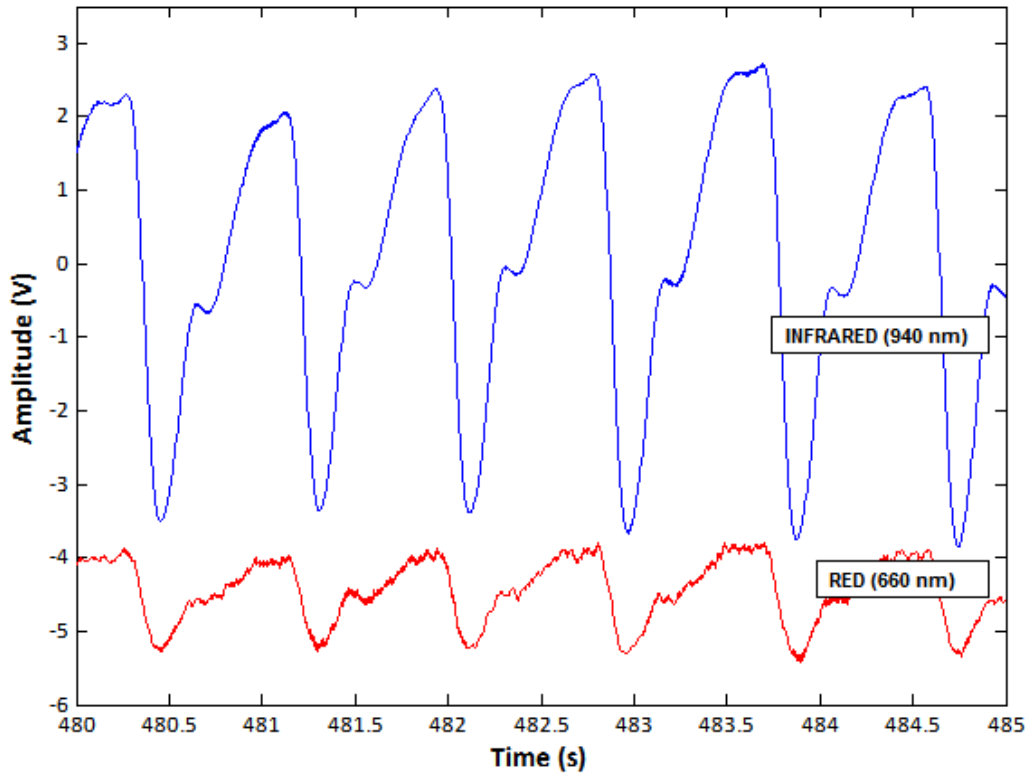


Figure 6.12c: Five second PPG capture using the oesophageal sensor on buccal mucosa of a female volunteer. Average heart rate = 61 bpm

6.2.2 Thermal Safety Testing

As an active sensor technology PPG and SpO₂ sensors interact with their environment by illuminating the tissue with non-ionising radiation. It is important to consider this thermal radiation as heating effects to the tissue could cause thermal damage.

Thermal Safety Test Method

Thermal safety testing was carried out only on the fontanelle sensor as the active components (the LEDs) were electrically identical to the foot sensor. The oesophageal sensor has one less LED, however as already described has identical LED specifications also. The fontanelle sensor was connected to the PPG sensor test circuit described in section 7.3 (Chapter 7) which could drive each LED simultaneously. Each LED was driven with a 0 – 5 V square wave at 100 Hz with a duty cycle of 1/6. The epoxy layer thickness is similar across all sensors and should act as an effective thermal insulator.

Four LED currents were selected for testing (20, 40, 60 and 80 mA). The current was varied by changing the resistor R1 in the LED current driver circuit figure 7.6, section 7.1.3, (Chapter 7).

An *in vivo* experiment was carried out on the forearm of a male volunteer. The sensor was placed face down onto the skin, with an LM35 temperature sensor (National Semiconductor, USA) directly adjacent on the tissue next to the LEDs. This was connected to one analogue input of a data acquisition card (USB 6009, National Instruments, USA). The output of the sensor was 10 mV/°C in the range of -55°C - 150°C, and had a resolution of 0.1°C, accurate to 0.5°C. Data was recorded at a rate of 100 Hz by the use of a virtual instrument implemented in LabVIEW (National Instruments, USA). Data was processed offline in Matlab (The Mathworks, USA).

For each LED current setting a baseline of two minutes of temperature recording was taken before the LED current was switched on. All three LEDs were driven simultaneously. At commencement of the LEDs being switched on temperature recording continued for ten additional minutes before the LEDs were then switched off and temperature recording continued for a further ten minutes to allow the skin on the forearm to cool. The experiment was repeated twice more to confirm and average out results.

Results

Successful temperature rise and fall data was gathered and is displayed in figures 6.13a – 6.13d, where steps in temperature can clearly be seen in the 60 and 80 mA settings. By taking the mean temperature in each on and off period for each LED current setting the average tissue temperature rise could be determined. It was found that at 20 and 40 mA the temperature rise seen was below the precision of the temperature sensor, suggesting that temperature rise was not significant. At 60 and 80 mA the temperature rise was 0.5 °C. This temperature step is clearly visible in the graphs in figure 6.13b – 6.13c and can therefore certainly be attributable to the operation of the LEDs. All temperatures recorded were below average human core body temperature (37 °C) and would unlikely cause any thermal damage. A summary of the temperature rises is shown in table 6.2.

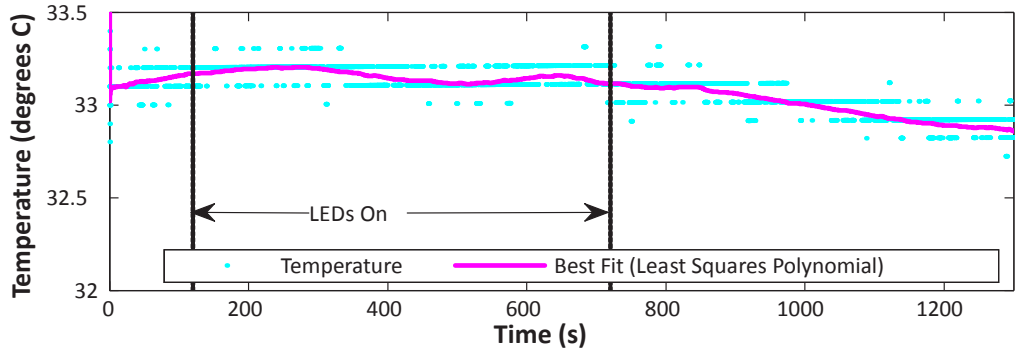


Figure 6.13a: Temperature change at the tissue surface when LED driving current = 20 mA

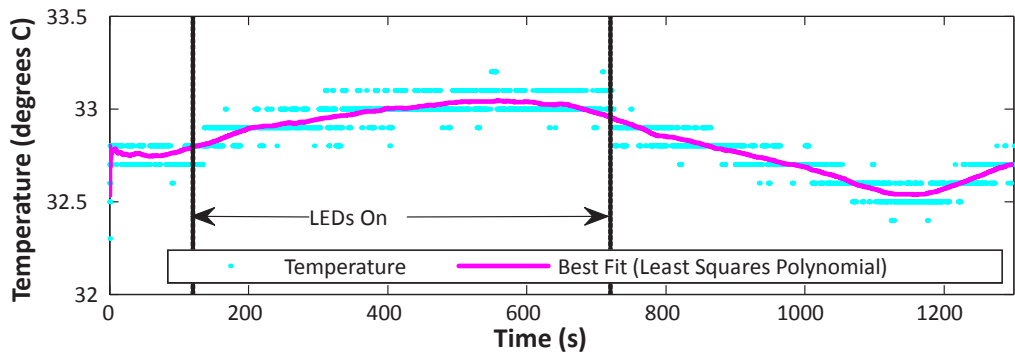


Figure 6.13b: Temperature change at the tissue surface when LED driving current = 40 mA

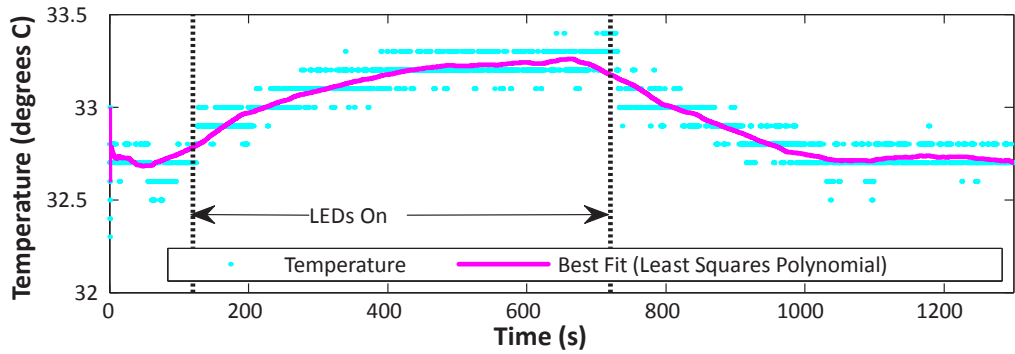


Figure 6.13c: Temperature change at the tissue surface when LED driving current = 60 mA

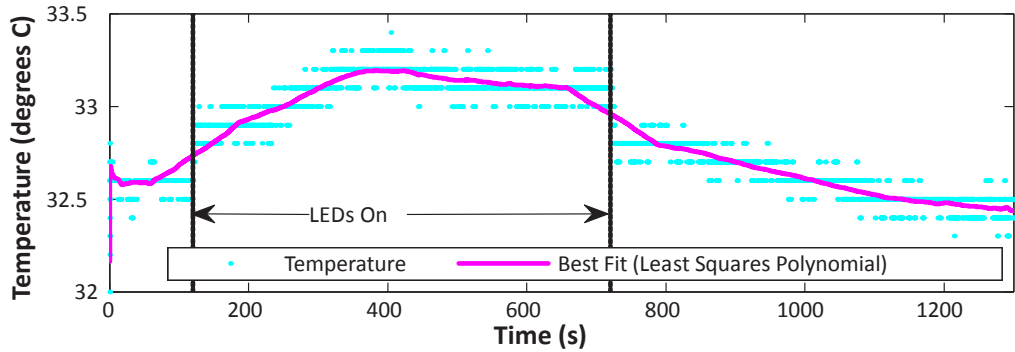


Figure 6.13d: Temperature change at the tissue surface when LED driving current = 80 mA

Table 6.2: Temperature change with changing LED supply current, all LEDs driven simultaneously.

LED status	Mean Temperature (°C)			
	LEDs @ 20 mA	LEDs @ 40 mA	LEDs @ 60 mA	LEDs @ 80 mA
LEDs off 2 minute baseline	33.1	32.7	32.6	32.5
LEDs on 10 minutes	33.1 (+ 0.0)	32.9 (+ 0.2)	33.1 (+ 0.5)	33.0 (+ 0.5)
LEDs off 10 minutes	32.9 (- 0.2)	32.6 (- 0.3)	32.8 (- 0.3)	32.6 (- 0.4)

6.2.3 Electrical insulation

A simple continuity test done on each PPG sensor between the termination connector and the sensor face revealed no flow of any current or any potential difference (measured in Ohms). When the sensor was connected to the test circuit used for the thermal evaluation and switched on, a volt-meter could not read any potential across the components or on any part of the sensor where insulation was applied (either epoxy resin or PVC heat shrink).

6.3 Sensor Construction Summary

Design and construction of the three PPG/SpO₂ sensors has been successfully and fully realised, meeting the specifications set out in the introduction and conforming to the layout and design considerations. A thermal and electrical test of the sensors has determined that the use of such sensors is unlikely to cause thermal or electrical injury during the *in vivo* investigations.

Chapter Seven

Dual Photoplethysmograph Instrumentation Development

Chapter six described the design and manufacture of three photoplethysmograph (PPG) sensors for the monitoring of pulsatile blood in different locations of the neonate or infant. A custom made hardware PPG processing system was also developed to drive the optical probes, multiplex the three wavelengths of the sensors, de-multiplex the photodiode current and convert it into a voltage signal, condition (filtering and amplification) of all acquired physiological signals and prepare them for digitisation and retrospective analysis. Software to handle data acquisition, online signal processing and offline analysis is covered in chapter eight.

7.1 System Design

Design and testing of the instrumentation was split into several separate electronic design stages, as shown in the block diagram in figure 7.1.

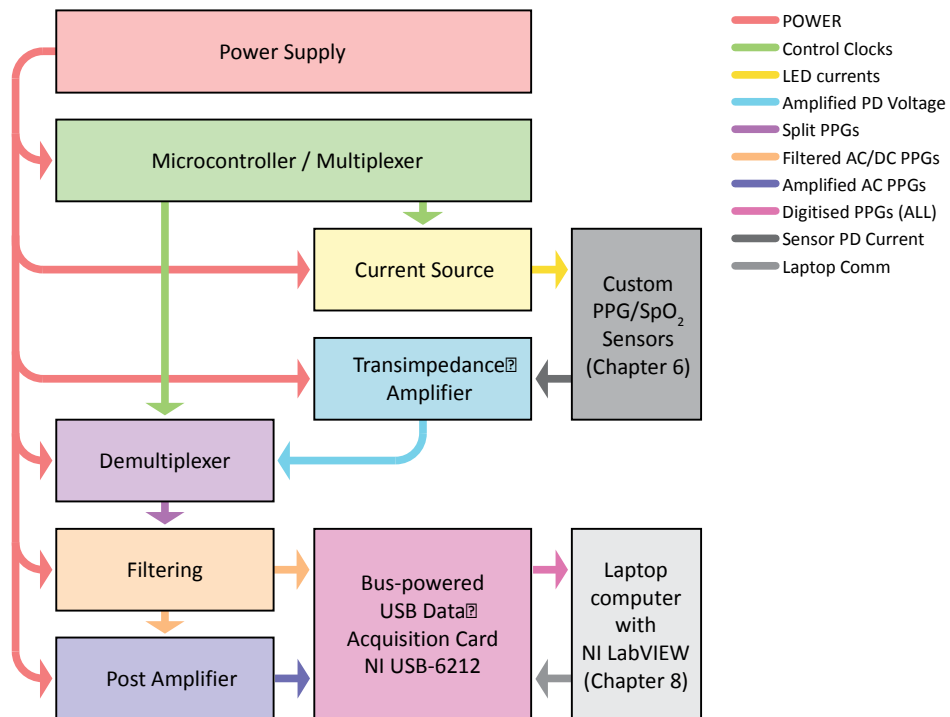


Figure 7.1: Instrumentation block diagram.

7.1.1 Power Supply

The instrument runs off two 12 V lead acid batteries (SONNENSCHNEIN - A512/2.0S, EXIDE Technologies, Bidingen, Germany) with a 2 Ah capacity. These have been set in a parallel configuration to give a 4 Ah capacity charge and were used to supply a ± 12 V DC-DC converter (THD101222, Traco Power, Zurich, Switzerland) (Figure 7.2 for DCDC Pin Out). The ± 12 V from the DC-DC powered the analogue circuitry (current supplies, transimpedance amplifiers, filters and post amplifiers and the 5 V regulator). The 5 V regulator (LM7805CT, Fairchild Semiconductor Corp, CA, USA) supplied the power for the microcontroller. It required two capacitors for stability, $0.33 \mu\text{F}$ on the input, and $0.1 \mu\text{F}$ on the output. Figure 7.3 is a schematic of the 5 V regulator setup.

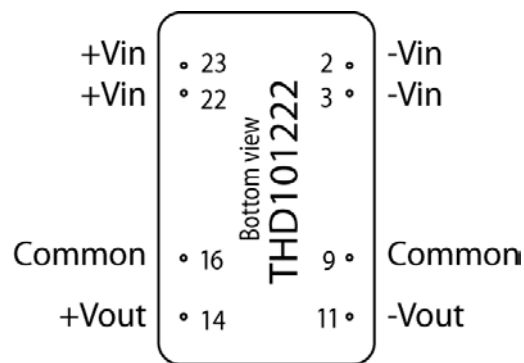


Figure 7.2: DCDC Pin-out.

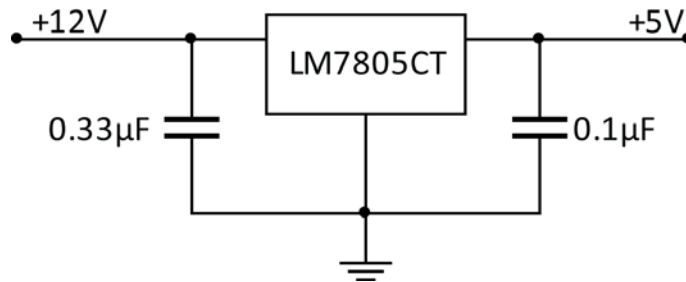


Figure 7.3: 5 V regulator setup.

7.1.2 Microcontroller / Multiplexer

The multiplexer is responsible for the fast and accurate switching of current sources that activate the specific LEDs on the sensors. This switching was achieved with multiple TTL-level (+5 V) square waves operating at approximately 100 Hz. The multiple square waves were sequenced as such to produce a cycle where only one LED is activated at any one moment, and there was an off period between the activation of each LED to allow time for the LEDs to settle between their on and off states. The duty cycle (d) was determined by:

$$d = 1/2n \tag{7.1}$$

where n is the number of current sources to be multiplexed. For a rate of 100 Hz each duty cycle's time duration (t) was determined by:

$$t (s) = 1/f \times d \tag{7.2}$$

where f is the desired frequency. When $n = 6$, $d = 0.166$ (16.6 %) and $t = 1.66$ ms. The system then multiplexed three current sources in the manner shown in figure 7.4. This is based on a similar routine described in Webster (Webster, 1997).

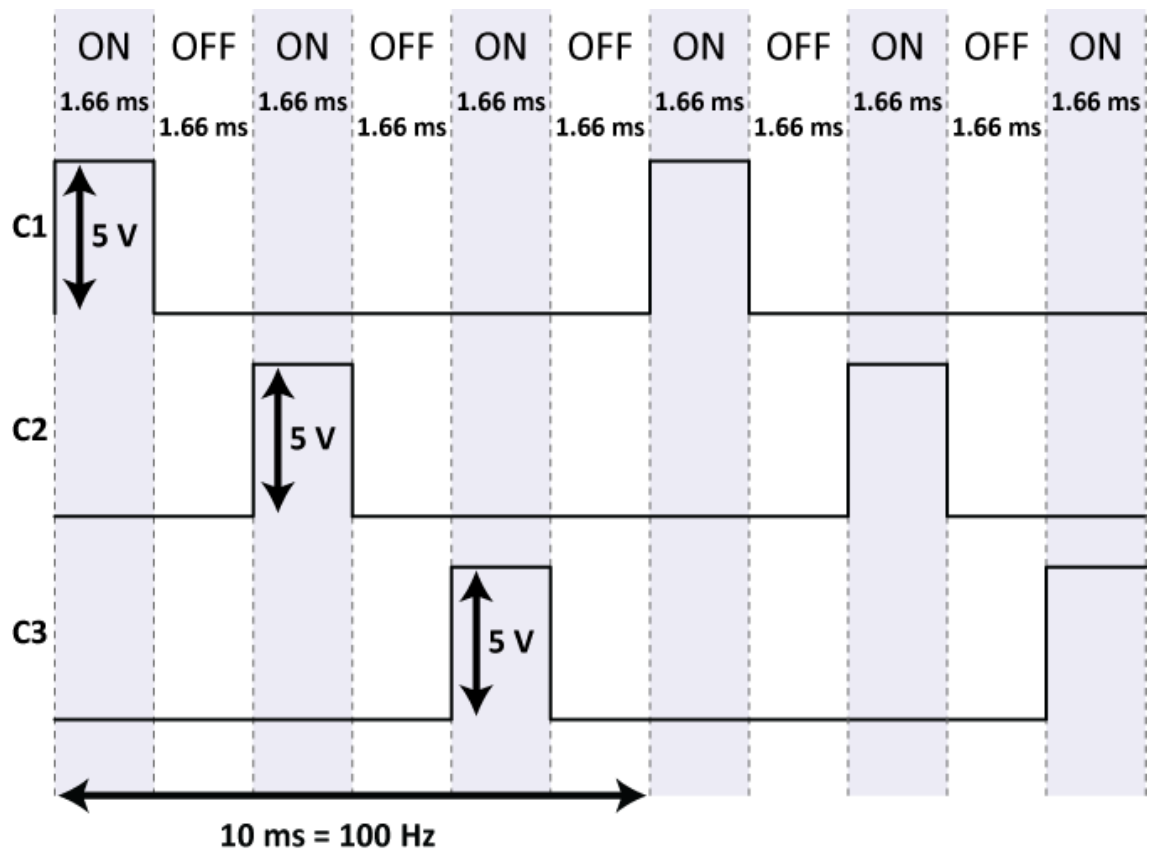


Figure 7.4: Current source multiplexing routine. Three clocks (C1, C2, C3), one for each current source, are switched “ON” sequentially with an “OFF” period between to allow for the settling time of the LEDs.

The hardware component chosen for this task was a 20 MHz Atmel AVR micro-control-unit (MCU) (ATTiny2313-20PU, Atmel Corp, CA, USA). Its low cost, relative ease to program and robust specifications, without the need to use an external oscillator mean that it is less reliant on other components and less likely to fail due to other circuit problems. The MCU will be flash-programmed from a C-source code file created in Win-AVR studio

(Atmel Corp, CA, USA) (Appendix A). The MCU drew current and power from the +5 V regulator. Figure 7.5 is a pin-out representation of the chosen MCU. Port B, channels 0 – 2 (pins 12 – 14), was programmed with the three output clocks.

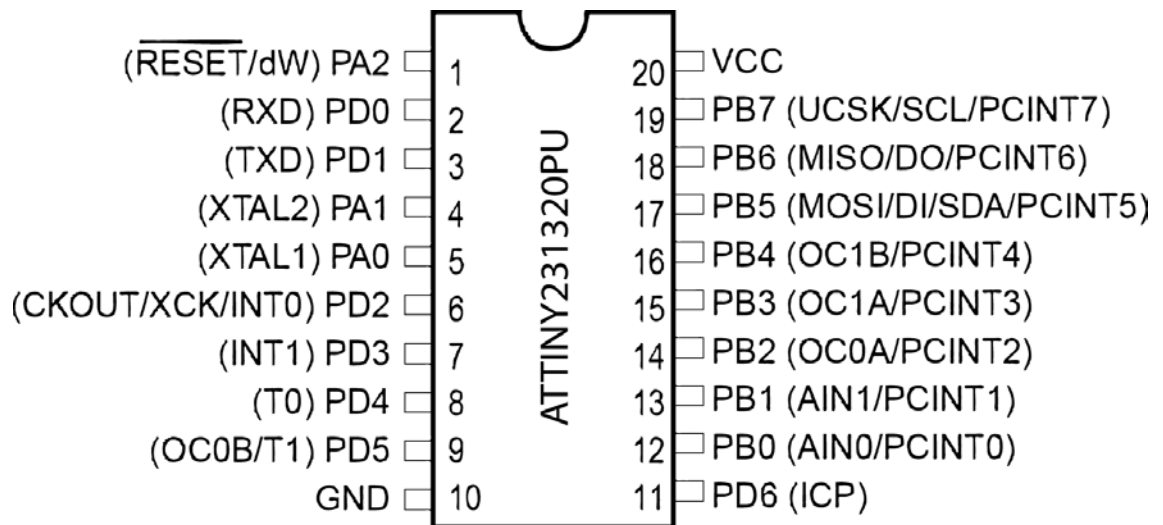


Figure 7.5: Pin-out diagram of the Atmel AVR MCU.

7.1.3 Current Supply

Most LEDs operate in a given range of 20 – 100 mA. From Ohm's law we know the relationship of current and voltage is determined thus;

$$V = IR \quad (7.3)$$

By combining a single operational amplifier with a bipolar transistor and wiring in a negative feedback we can cause the voltage at the emitter (V_e) to be equal to the voltage at the input to the operational amplifier (V_{in}) (See figure 7.6). Thus, by selecting an appropriate resistance value at the emitter we can set any desired current value, simply by;

$$I_e = V_e / R_1 \quad (7.4)$$

For this design it was assumed that the collector current (I_c) is equal to the emitter current (I_e) and the current at the base (I_b) is negligible, and so did not affect the final current output. In reality $I_c = I_e + I_b$, but I_b is often a great deal smaller than I_e and for simple current supply implementations, this value can be ignored.

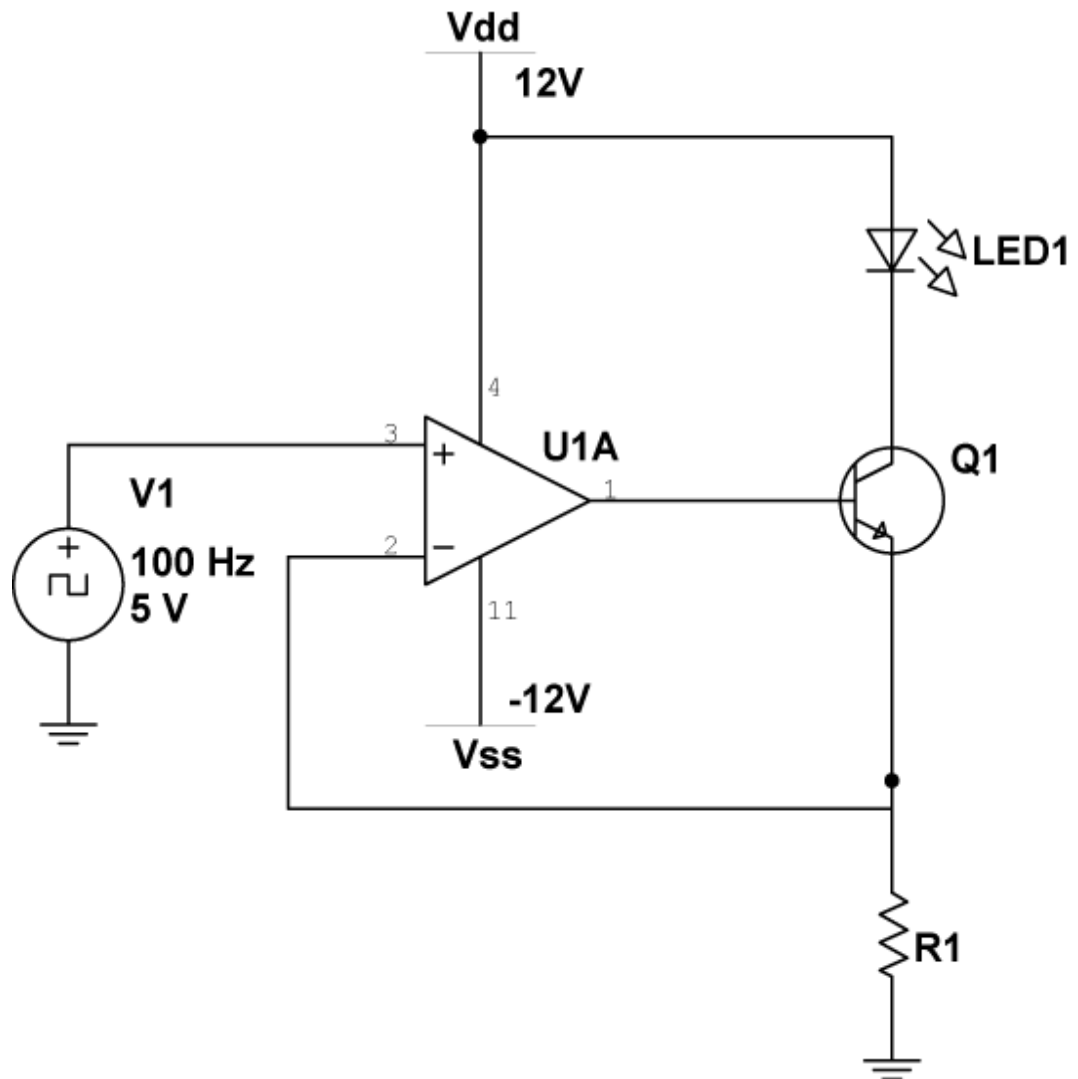


Figure 7.6: Preliminary LED current supply schematic

The input to the operational amplifier non-inverting pin was a 5 V square wave, with the same routine as calculated in 7.1.2. By equation 7.4 we can see that an appropriate range for R_i is 250Ω (20 mA) - 50Ω (100 mA). During circuit prototyping this was accomplished by the use of swap sockets for the resistors, and eventually became a variable resistor.

7.1.4 Transimpedance Amplifier with Variable Gain

To convert the current of the photodiode into a voltage ready for digitisation at the last stage of the circuit required the use of a transimpedance amplifier. The design chosen for this application was in the form of a dual transimpedance configuration as the photodiode is a current source and can therefore drive two inputs simultaneously at opposing polarities. The two outputs then became the inputs to a differential amplifier with an adjustable gain, see figure 7.7 for the preliminary design.

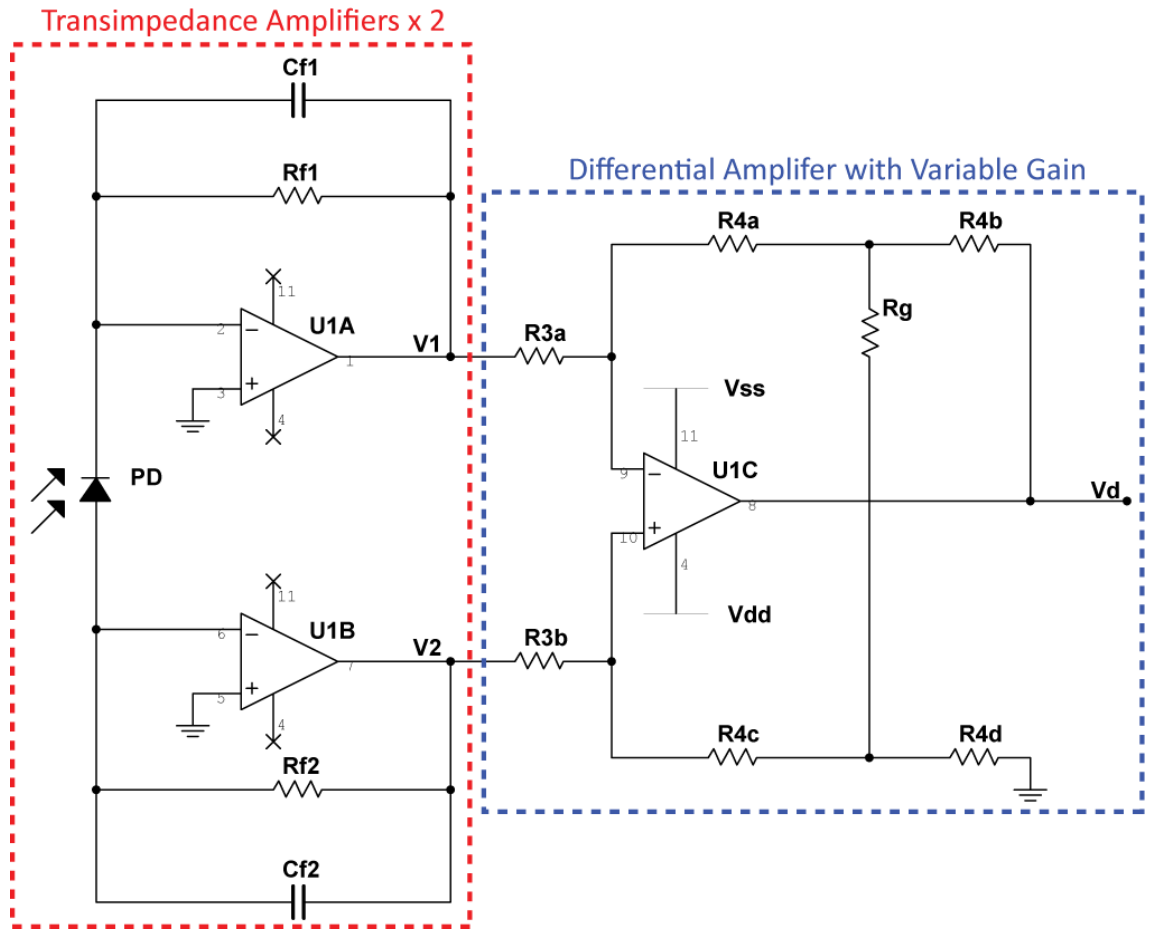


Figure 7.7: Preliminary dual transimpedance differential amplifier schematic.

The transimpedance stage consists of a feedback resistor (R_f) and feedback capacitor (C_f). R_f is responsible for the voltage gain (V_{out}) of the transimpedance by:

$$-V_{out} = I_{in}R_f \tag{7.5}$$

V_{out} is identical for V_1 and V_2 in figure 7.7. The value of C_f can be determined by:

$$C_f = \frac{1}{4\pi R_f GBW} \left\{ 1 + \sqrt{(1 + 8\pi R_f C_d GBW)} \right\} \tag{7.6}$$

where GBW was the bandwidth gain product of the specific operational amplifier, and C_d was the capacitance of the photodiode (see chapter 6). C_f was responsible for stabilising the transimpedance stage, by helping reduce overshooting artefacts arising from the capacitance across the photodiode in the sensor.

Variable gain (A_v) on the amplifier was controlled by R_g on the differential input stage, and was determined by:

$$A_v = \frac{V_d}{(V_2 - V_1)} = \frac{2R_4}{R_3} \left(1 + \frac{R_4}{R_g} \right) \quad (7.7)$$

where V_1 and V_2 are the V_{out} of the two transimpedance amplifiers from equation 7.5, and V_d is the output voltage of the differential amplifier. The photodiodes described in chapter 6 have different specifications regarding their typical reverse light current (expected current flow at a given amount of light). The variable resistor, R_g , in this amplifier will allow for adjustment of the gain of the circuit to suit the diodes in each sensor; however the fixed components still needed to be calculated. Selecting the extremes of these specifications from the photodiode data sheets allowed an informed design choice. Photodiode TEMD7000X01 had the smallest reverse light current (2.4 μ A), whilst photodiode TEMD5080X01 had the largest reverse light current (60 μ A). Selecting a desired output of 10 V peak-to-peak amplitude meant that A_v from equation 7.7 had a maximum value of approximately 4.2 million.

7.1.5 Demultiplexing

The output of the transimpedance amplifier (V_d) was a mixed (multiplexed) signal, since light from all three LEDs is sensed by one photodiode. To recover the amplitude information belonging to the individual wavelengths it was necessary to split V_d into three parts that were then passed to the filters and the AC post-amplifier. In 7.1.2 it was illustrated that the LEDs are switched on and off sequentially with periods where all LEDs are off between each LED switching on (Figure 7.4). Using the same timing clocks (C1 – C3) it was possible to “sample” V_d at specific intervals so that the signal being passed to the filters for each light source only received the amplitude level for individual wavelengths. Whilst the LEDs are off it was necessary to “hold” the sampled voltage until the next clock pulse triggers a new acquisition. Figure 7.8 demonstrates this “sample and hold” routine.

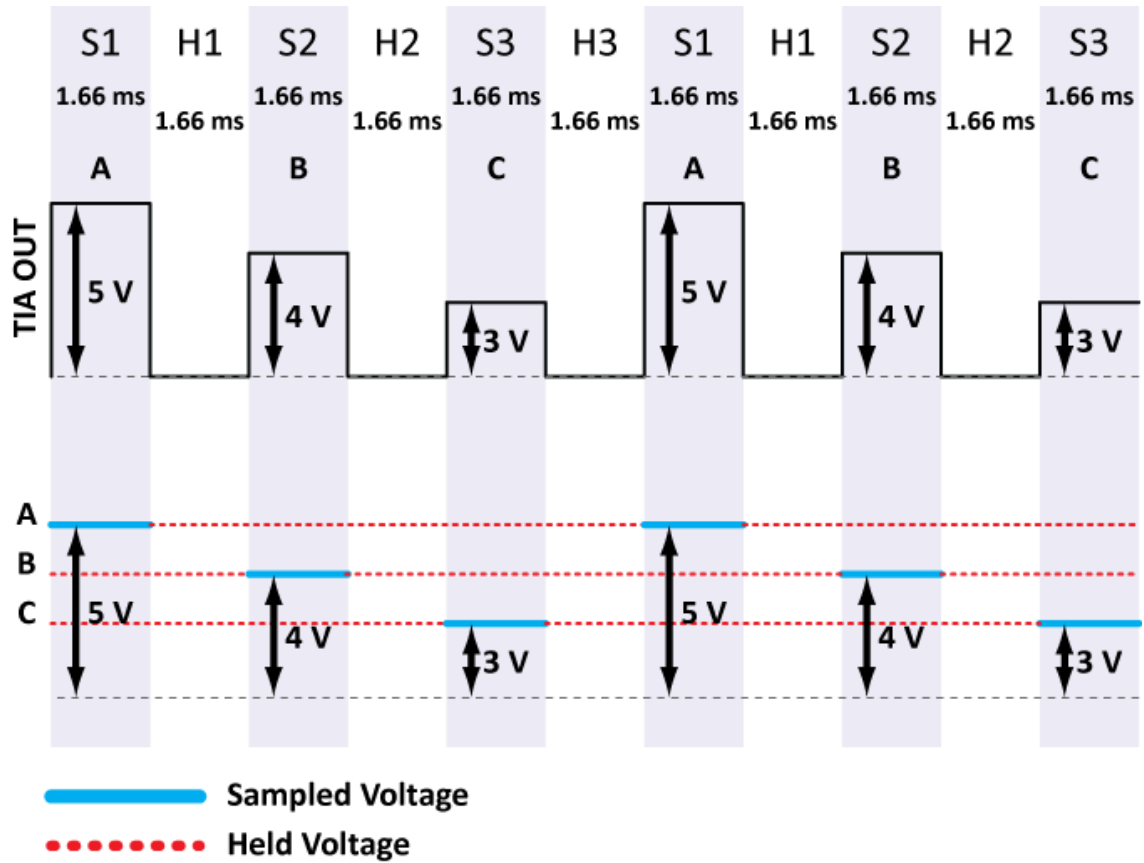


Figure 7.8: Sample and hold demonstration. The three voltage amplitudes (A, B, C) represent the different light sources, each is sampled (S1, S2, S3) respectively and then held at that level (H1, H2, H3) until the next sample is taken.

Electronically this was implemented with the use of a purpose-built sample and hold (S&H) IC (LF398AN, Texas Instruments, TX, USA). The chip required a power source (± 12 V), a sampling clock (either C1, C2 or C3 depending on what channel to sample), the input signal to be sampled (V_d) and an external capacitor to stabilise the hold routine operation of the chip. Figure 7.9 is a pin-out diagram of the Sample and Hold (S&H) chip.

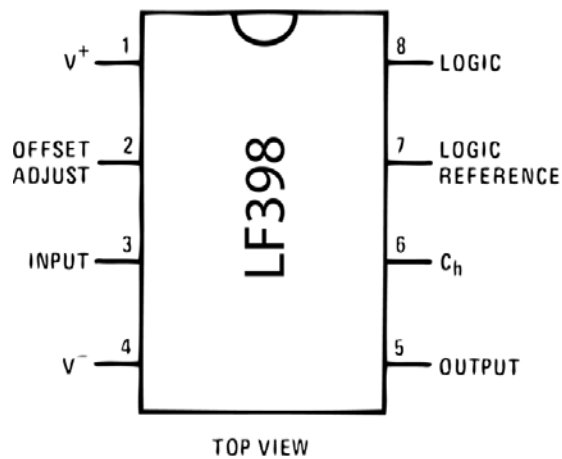


Figure 7.9: Sample and hold IC pin out diagram.

7.1.6 Filtering

The raw signals obtained after the demultiplexing stage were passed through filters to remove unwanted high frequencies and any “step” (aliasing) artefacts caused by the sample and hold circuits. This anti-aliasing filter is a low-pass filter with a cut off of approximately 20 Hz, sufficient bandwidth to pass all PPG information, whilst staying well below the 100 Hz of the demultiplexing cycle that causes the aliasing. This signal is then passed simultaneously to the data acquisition card for immediate digitisation of the raw signals, containing both the DC and AC portion of the signal, and to a high-pass filter. The high-pass filter is implemented to remove the DC portion and therefore extract the AC portion of the signal before it was passed to a post-amplification and digitisation stages. This cascade of filters is in effect a band-pass filter.

The topology chosen to implement the band-pass filter is of two separate Sallen-Key 2nd – order filters. The preliminary schematic of the filter is shown in figure 7.10.

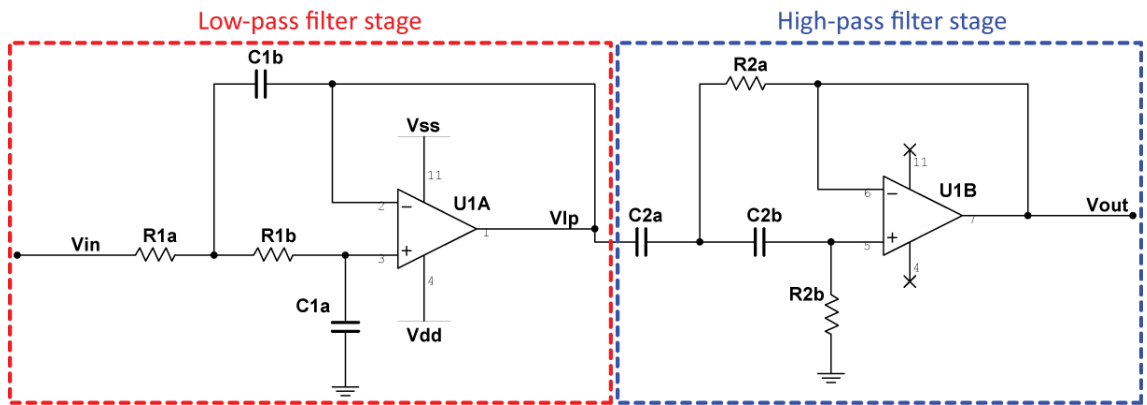


Figure 7.10: Band-pass filter comprising of two Sallen-Key unity gain filters.

V_{lp} on the schematic is where the two filters couple, and where the raw signal (AC+DC) will be digitised. The low-pass stage of the amplifier can be described by:

$$2\pi f_{cl} = \frac{1}{\sqrt{R_{1a}R_{1b}C_{1a}C_{1b}}} \quad (7.8)$$

where f_{cl} is the desired cut-off frequency of the low-pass filter. Rearranging and equating $R_{1a} = R_{1b} (R_1)$ and $C_{1a} = C_{1b} (C_1)$ yields:

$$f_{cl} = \frac{1}{2\pi R_1 C_1} \quad (7.9)$$

The high pass stage can be dealt with in the same manner giving:

$$f_{ch} = \frac{1}{2\pi R_2 C_2} \quad (7.10)$$

where f_{ch} is the desired cut-off of the high-pass filter.

7.1.7 Post Amplification

SpO₂ calculation relies on the ability to measure the AC and DC component of the red and infrared PPGs. To make maximum use of the digitisation process in the final stage of the instrument it was desirable to amplify the AC component separately. An inverting amplifier (figure 7.11) was implemented to amplify this signal until the output is within ± 10 V, the range of the data acquisition device.

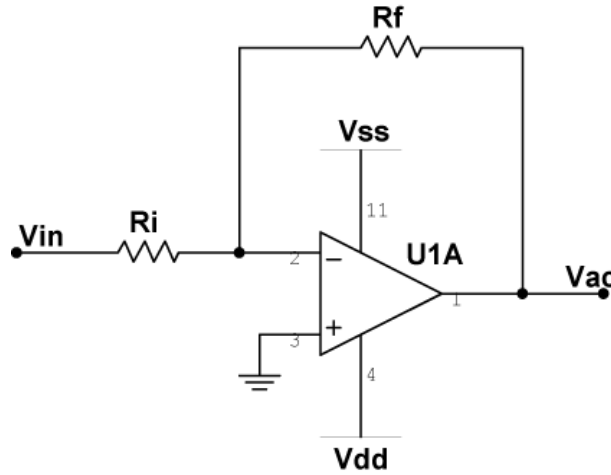


Figure 7.11: Preliminary post amplifier schematic

The amplification was selectable with two resistors, R_f and R_i :

$$V_{ac} = \frac{-R_f}{R_i} V_{in} \quad (7.11)$$

where V_{ac} is the amplified AC signal and V_{in} is the AC signal from the band-pass filter. The AC signal of the PPG is typically as much as 2% or less of the total PPG signal, therefore if a maximum peak at the TIA stage of 10 V is observed then only 0.1 – 0.2 V (Pk – Pk) will be the AC portion. In this range a simple gain of 100 would mean that by eqn. 7.11 $V_{ac} = 10 - 20$ V (Pk – Pk). Issues may arise at the data-acquisition stage with Pk – Pk values of 20 V, as this will be maximum range of the card (typically ± 10 V), and some clipping may occur and some data may be lost. For this reason lowering the gain to 85

would give $P_k - P_k$ values of 8.5 – 17 V, good large amplitudes that still make use of most of the range of the card. From standard resistor values and by eqn. 7.11, $R_f = 330 \text{ k}\Omega$, $R_i = 3.9 \text{ k}\Omega$. Gain = 84.6.

7.1.8 Data Acquisition and Digitisation

All mixed PPG signals (AC/DC) and separately amplified AC PPG signals were passed onto a 16-bit data acquisition card (USB6212, National Instruments, TX, USA). This card has selectable voltage resolutions ranging from $\pm 250 \text{ mV}$ to $\pm 10 \text{ V}$. It is a bus-powered device, drawing its operational current directly from the attached laptop computer via USB cable. Software controlling the operation of the card is covered in chapter 8.

7.2 Electrical Circuit Simulation

To assess all stages of the circuit before prototyping and final construction it was necessary to model the circuits on a personal computer to identify any potential problems that may occur. All simulations were performed in Multisim (National Instruments, TX, USA).

The operational amplifier used in the simulations was the OPA4137PA (Burr Brown, Texas Instruments, TX, USA), chosen for its' high performance characteristics (slew rate = $3.5 \text{ V}/\mu\text{s}$ and wide bandwidth = 1 MHz) and suitability for various applications that include photodetector amplifier, precision integrator, active filters and battery-powered instruments. The NPN transistor was a 2N3904 (Fairchild Semiconductor Corp, CA, USA). Resistors were simulated from a generic model with component tolerances taken into account. Capacitors were similarly modelled with tolerances and lead polarisation if appropriate.

7.2.1 Current Supply

From section 7.1.3 suitable limiting resistors, R_i , were calculated to be in the range of 50 – 250 Ω . A simulation was constructed, and a transient analysis performed for a range of R_i . The data was then saved and analysed in MATLAB. The multiplexing signal was a simulated square wave with matching characteristics to the output of the MCU, (100 Hz square wave with a 17 % duty cycle). Table 7.1 shows the simulation setup parameters with the results of the simulation. Note that the expected duty cycle is 17 % as opposed to 16.6 %, as calculated by eqn. 7.1; this was due to a limitation of Multisim where the input parameter “duty cycle” would only accept whole integers.

Table 7.1: Current source simulation results.

R1 (Ω)	Current (mA)		Duty Cycle (%)	
	Expected	Simulated	Expected	Simulated
50	100	100.60 (+ 0.6 %)	17	17.3 (+ 1.76 %)
100	50	49.66 (- 0.68 %)	17	17.3 (+ 1.76 %)
150	33	33.98 (+ 2.96 %)	17	17.4 (+ 2.35 %)
200	25	25.83 (+ 3.32 %)	17	17.4 (+ 2.35 %)
250	20	19.98 (-0.1 %)	17	17.2 (+ 1.18 %)

Through simulation it was observed that both the desired LED driving current and the duty cycle was maintained to within 3 % or better of the desired values between the maximum and minimum R_f .

7.2.2 Transimpedance Amplifier with Differential Variable Gain

The photodiodes TEMD7000X01 and TEMD5080X01 have a C_d of 4 pF and 90 pF respectively. Due to the variable nature of the gain on this circuit it is not necessary to choose such a high R_f value at the transimpedance stages. A resistor of value 680 k Ω (a common value), would mean that the gain of the differential stage need only vary between 1 and 3.09 for the desired gain calculated in 7.1.4.

By eqn. 7.6; when $C_d = 4$ pF, $R_f = 680$ k Ω and $GBW = 1,000,000$ the feedback capacitor, C_f needed on the transimpedance stages = 1.09 pF. When $C_d = 90$ pF and all other values remain the same, $C_f = 4.7$ pF.

A simulation was constructed using the above values for R_f and C_f and the photodiode was modelled as a current source with a parallel capacitance equal to C_d , see figure 7.12. The photodiode receives light from all 3 LEDs sequentially, meaning that the resulting photodiode output will have 3 distinct on and off periods, each representing one LED wavelength. With a multiplexing rate of approximately 100 Hz per LED with a duty cycle of approximately 17 %, the combined photodiode output will produce a square wave of 300 Hz with a duty cycle of 50 %. This will be the routine used in the photodiode model during simulation. The current level for the routine will be set at 1 μ A for both simulated photodiodes. Data from the simulation was saved and analysed in MATLAB. Table 7.2 is the simulation setup parameters with simulation results.

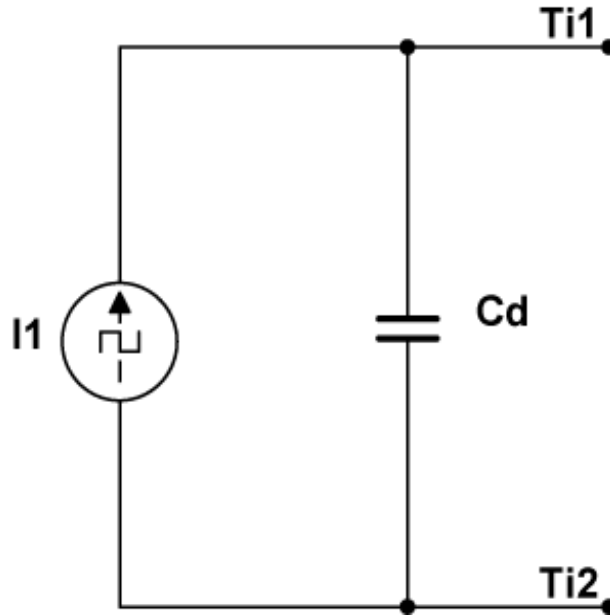


Figure 7.12: Equivalent photodiode model used for simulation, where Ti1 and Ti2 represent the cathode and anode respectively.

Table 7.2: Transimpedance amplifier simulation results, with theoretical C_f values.

Capacitance		Voltage (mV)							
Cd (pF)	Cf (pF)	V2 peak		V1 peak		+ Overshoot		- Overshoot	
		Expect	Sim (± % diff)	Expect	Sim (± % diff)	V2	V1	V2	V1
4	1.09	680	673 (-1.04 %)	-680	-672 (+1.19 %)	+533	+119	-137	-356
90	4.7	680	677 (-0.44 %)	-680	-677 (+0.44 %)	+271	+203	-209	-273

Both photodiodes showed considerable overshoot, with their calculated C_f values, see figure 7.13. The final circuit will use a single value of C_f regardless of the photodiode present on the sensor, therefore it was only necessary to find an appropriate value that would eliminate these overshoots for both photodiodes. The C_f value was changed to 10 pF and the simulation re-run, see Table 7.3 and Figure 7.14.

Table 7.3: Transimpedance amplifier simulation results, with adjusted C_f values.

Capacitance		Voltage (mV)							
Cd (pF)	Cf (pF)	V2 peak		V1 peak		+ Overshoot		- Overshoot	
		Expect	Sim (± % diff)	Expect	Sim (± % diff)	V2	V1	V2	V1
4	10	680	649 (-4.78 %)	-680	-646 (-5.26 %)	+33	+8	-12	-29
90	10	680	664 (-2.41 %)	-680	-667 (-1.95 %)	+20	+17	-47	-20

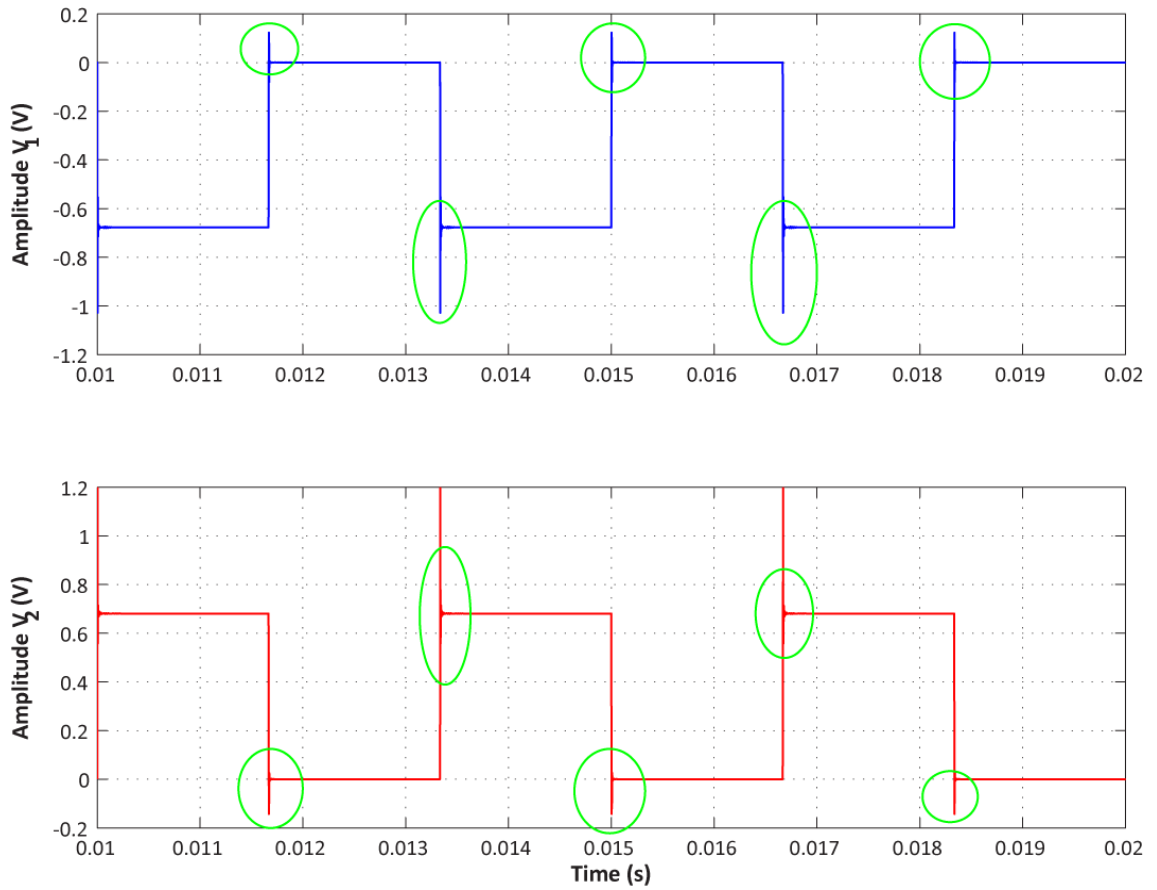


Figure 7.13: Simulated output of transimpedance amplifier, V_1 (top) and V_2 (bottom), $C_d = 4 \text{ pF}$, $C_f = 1.09 \text{ pF}$.

Clearly visible in figure 7.13 (highlighted) are the positive and negative overshoots that may cause distortion in the signal when it is sampled by the demultiplexing stage. This phenomenon was observed when $C_d = 90 \text{ pF}$ and $C_f = 4.7 \text{ pF}$ also.

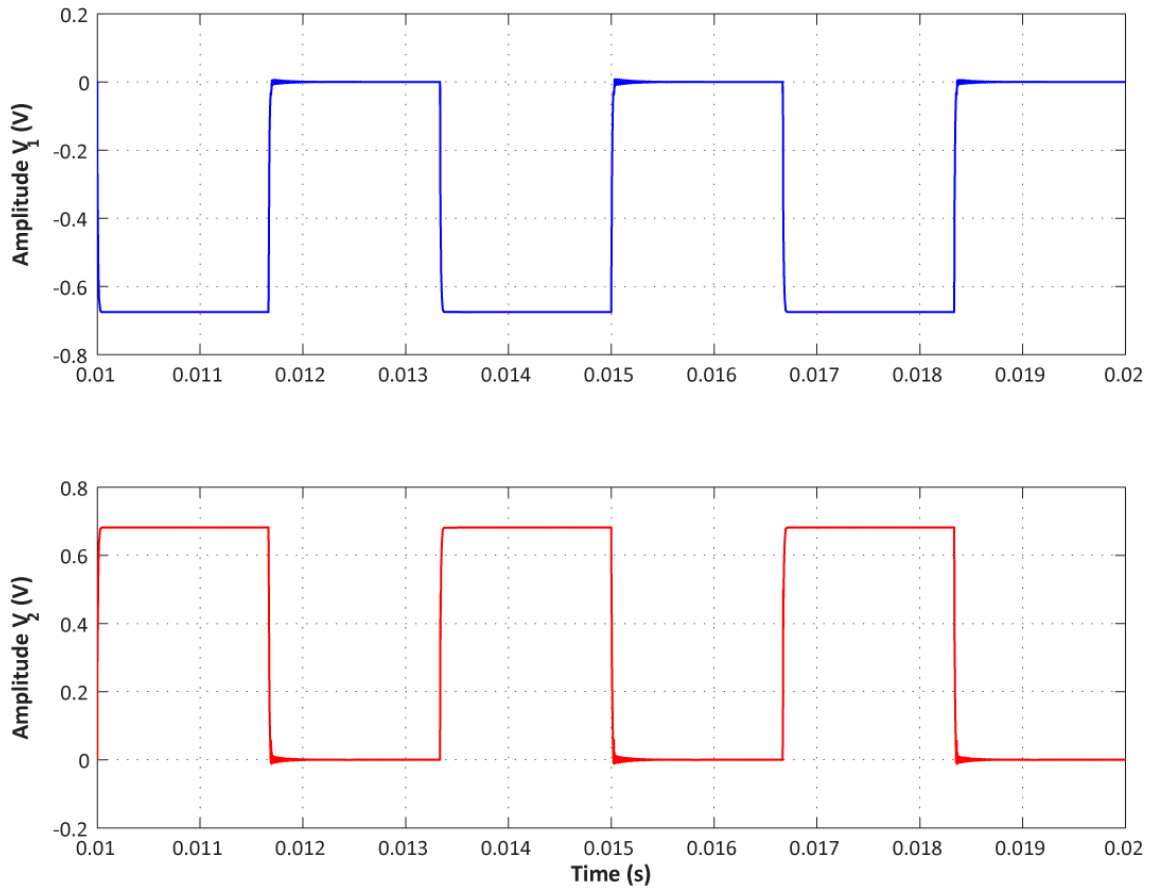


Figure 7.14: Simulated output of transimpedance amplifier stages, V_1 (top) and V_2 (bottom) $C_d = 4 \text{ pF}$, $C_f = 10 \text{ pF}$.

Figure 7.14 effectively demonstrates the almost complete elimination of the positive and negative overshoots illustrated in figure 7.13, again the same effect was observed when $C_d = 90 \text{ pF}$ and $C_f = 10 \text{ pF}$.

Design of the differential amplifier stage began by building the balanced differential bridge (R_{Aa-d} figure 7.7). A value of 560Ω ($\pm 1\%$) was selected. The input resistors (R_{3a+b} figure 7.7) were set at $1.2 \text{ k}\Omega$ ($\pm 1\%$), which are responsible for maintaining a high input impedance to the operational amplifier and helping to set the overall gain (eqn. 7.7). The variable gain resistor (R_g figure 7.7) was calculated by solving 7.7 when $1 \leq A_v \leq 3.09$. When $A_v = 1$, $R_g = 7839 \Omega$, and when $A_v = 3.09$ $R_g = 243 \Omega$. A simulation of the differential stage was run where the inputs, V_1 and V_2 , were driven by the expected outputs of the dual transimpedance amplifiers, as already demonstrated. Table 7.4 is the simulation results for the differential stage.

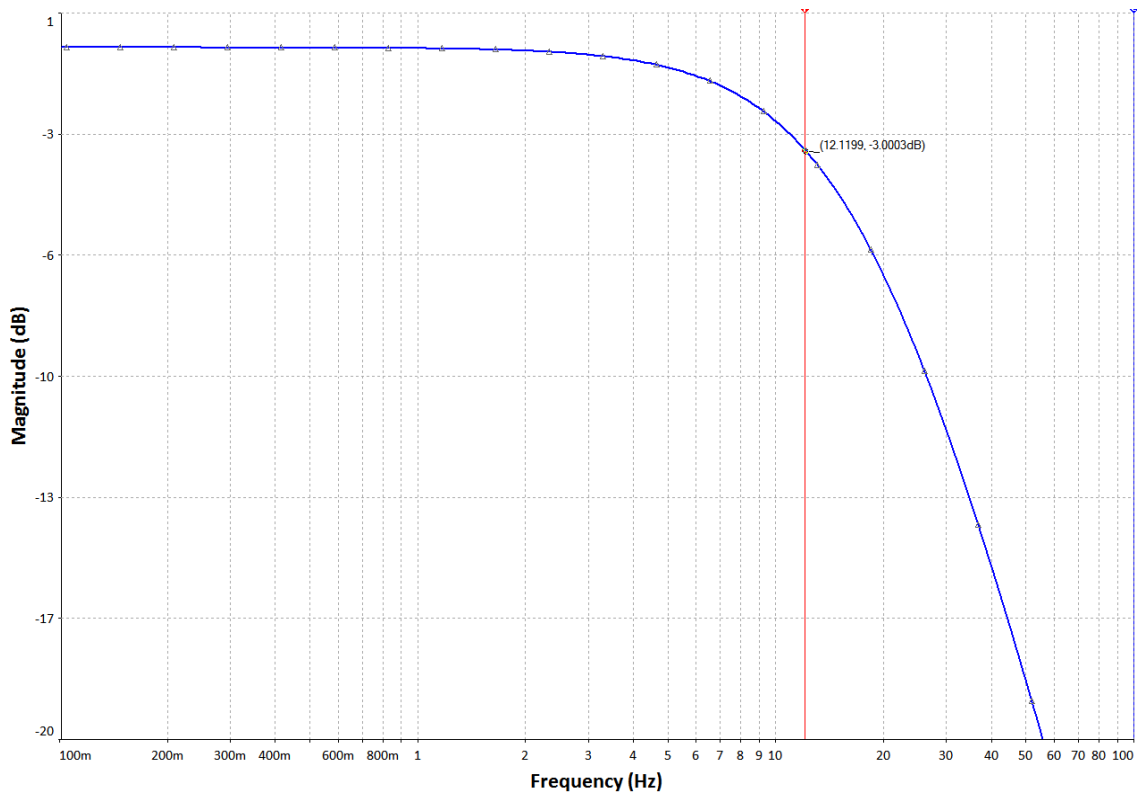
Table 7.4: Effect of varying R_g on V_{out} for the desired A_v range.

R_g (Ω)	Voltage (V)			V_{out} Sim (\pm % diff)
	V_1 Peak (V)	V_2 Peak (V)	V_{out} Expect	
243	-0.680	0.680	4.195	4.225 (+0.715 %)
7839	-0.680	0.680	1.360	1.396 (+2.647 %)

7.2.3 Filtering

Setting $f_{cl} = 20$ Hz, $f_{cb} = 0.3$ Hz, $C_1 = 22$ nF and $C_2 = 100$ nF then solving equations 7.9 and 7.10 $R_1 = 361715 \Omega$ and $R_2 = 5305165 \Omega$. The closest standard resistors are 390 k Ω and 4.7 M Ω for R_1 and R_2 respectively. Recalculating f_{cl} and f_{cb} gives theoretical values of 0.33 Hz and 18.5 Hz respectively for the pass band of the filter.

A frequency response for the low-pass filter stage in figure 7.10 was first simulated in Multisim with the derived values for R_1 and C_1 and is shown in figure 7.15. As can be seen the -3 dB cut off, the point at which the input power is reduced by half, the cut-off is found to be approximately 12.1 Hz, 5.9 Hz below the calculated and 7.9 Hz below the desired.

Figure 7.15: Low-pass filter stage simulated frequency response. -3 dB cut-off at approximately 12 Hz.

This simulation was repeated with the addition of the high-pass pass filter, with $R_2 = 4.7 \text{ M}\Omega$, $C_2 = 100 \text{ nF}$, to simulate the band-pass filter. Figure 7.16 is the simulated frequency response of the filter. The cut-off frequencies were found to be approximately 0.5 and 12.1 Hz.

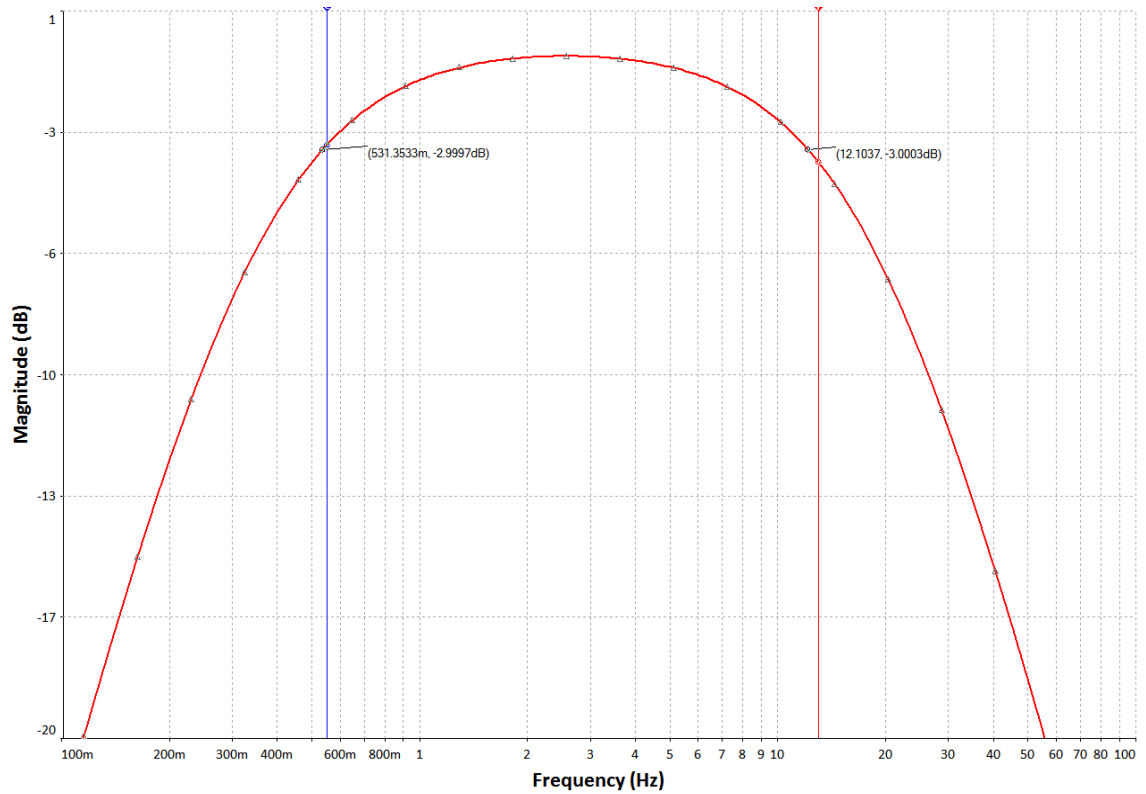


Figure 7.16: Band-pass filter stage simulated frequency response. -3 dB cut-off at approximately 0.5 and 12.1 Hz.

The low pass and band-pass cut-off frequencies were below the expected and desired cut off frequencies, and may be explained by component tolerances used in the simulation. However the bandwidth remained sufficient wide enough to accommodate the frequencies associated with normal and abnormal heart rates. The 0.5 Hz cut-off introduced by the high pass stage into the band-pass filter will allow the post amplification stage before analogue to digital conversion to digitise only the AC portion of the signal.

7.2.4 Post Amplification

A simulation of the post amplifier described in 7.1.7 with $R_f = 330 \text{ k}\Omega$, $R_i = 3.9 \text{ k}\Omega$, and a 5 Hz 0.2 V (Pk – Pk) sine wave generates the plot in figure 7.17.

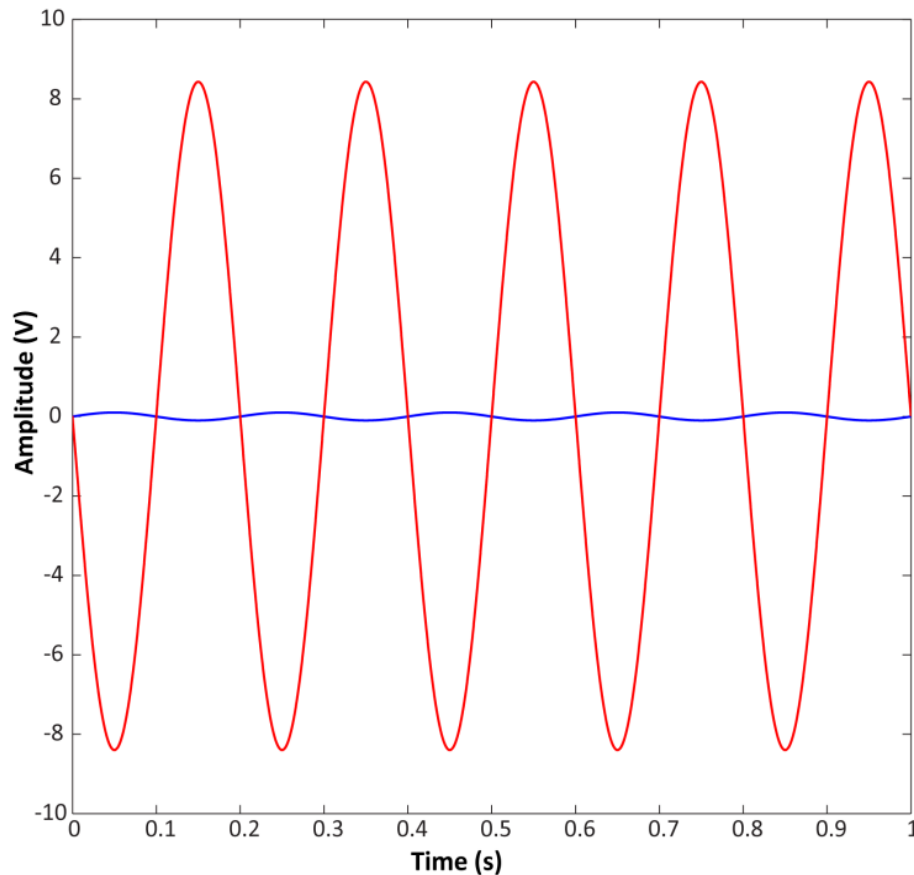


Figure 7.17: Post Amplifier simulation. $V_{in} = 0.2 \text{ mV (Pk - Pk)}$, $V_{out} = 16.83 \text{ V}$. Gain = 84.29

Simulated response for the post-amplifier shows a gain of 84.29 (-0.4 % from theoretical). The simulation also shows the inversion of the test signal due to the inverting configuration of the circuit.

7.3 Electrical Prototyping

Full electronic testing was achieved by implementing the circuits from section 7.1 onto a prototyping strip board (Figure 7.18), utilising all the component values calculated in section 7.2. Electrical testing was done with the use of a bench-top DC power supply (GPS-4303, GW INSTRUK ,Taiwan), digital waveform generator (TGA1241, AimTTi, Cambridgeshire, UK), multi-meter (FLUKE187, Fluke Corp, WA, USA) and two digital oscilloscopes (TDS3012B, and TDS3014B, Tektronix, OR, USA). Figure 7.19 is a diagrammatic layout of the strip board. This is a single PPG sensor set-up; a full dual

sensor design has been implemented as the final circuit construction (Section 7.4). All operational amplifiers used were the Burr Brown OPAX137PA (Texas Instruments, TX, USA) (Dual OPA2137PA or Quad OPA4137PA).

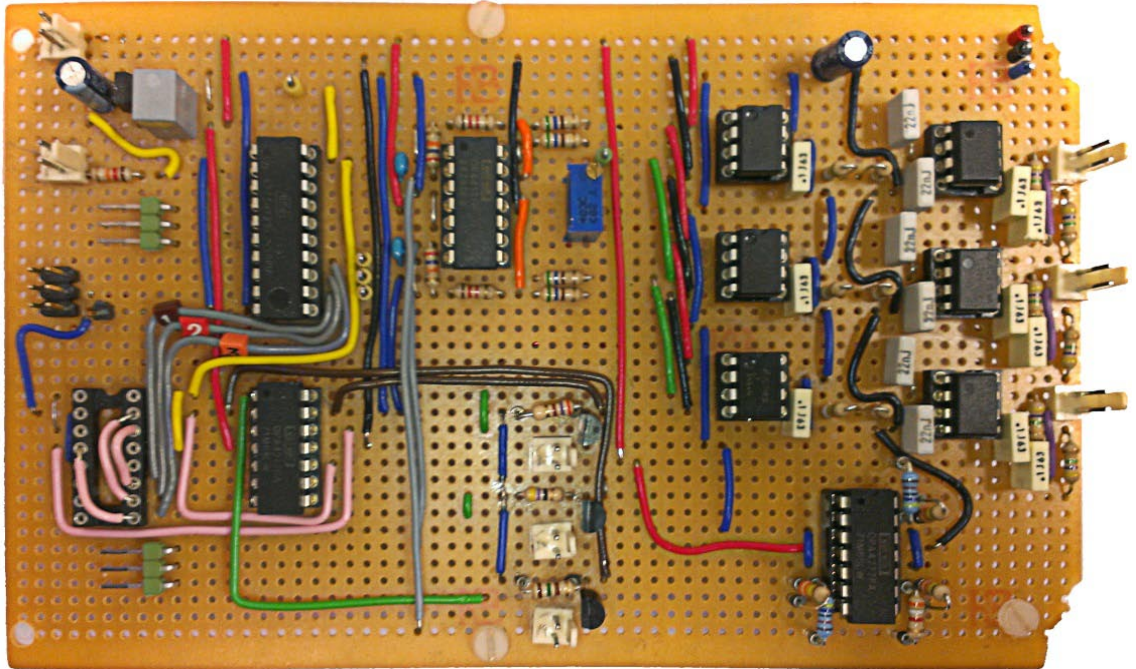


Figure 7.18: Single PPG sensor test circuit strip board.

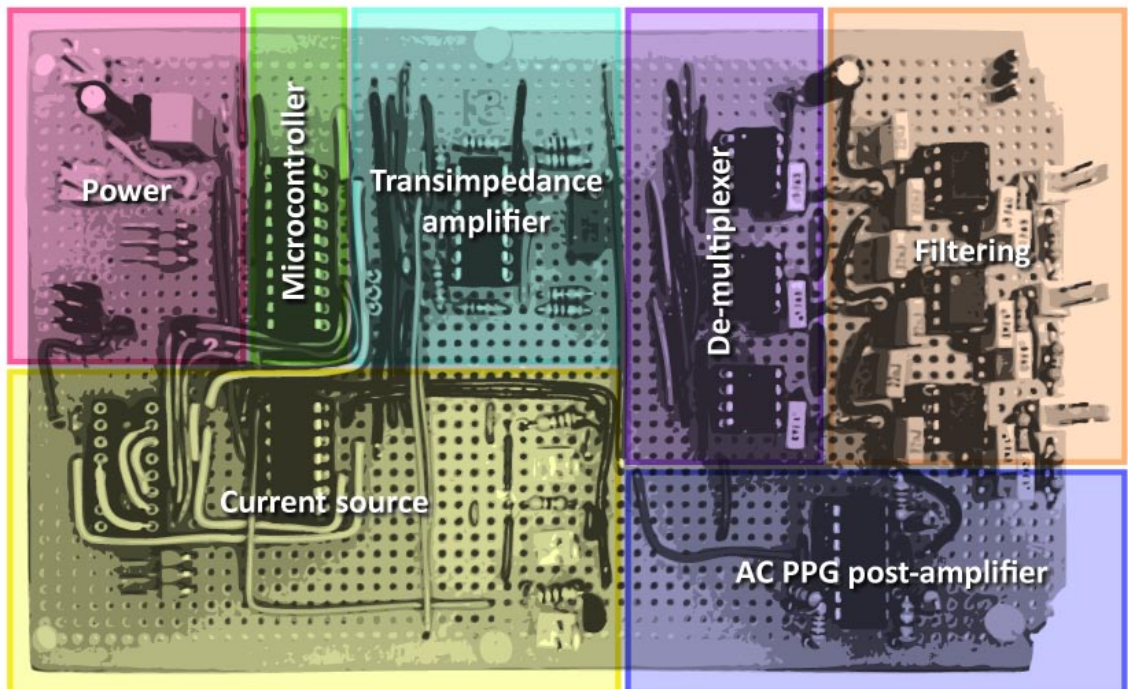


Figure 7.19: Diagrammatic layout of the strip board.

7.3.1 Microcontroller / Multiplexer

The microcontroller (MCU) was flashed with the c-code in Appendix A using an AVR STK 500 programming board (Atmel Corp, CA, USA). The MCU was then placed into the circuit (Figure 7.19), and using a bench-top power source, switched on. Pins 12 – 14 were the output pins for the Clocks (C1 - C3) and were monitored on the digital oscilloscope. The duty cycle (measured using the DO vertical cursors), frequency and amplitude were all recorded via the screen capture function on the DO (Figure 7.20)

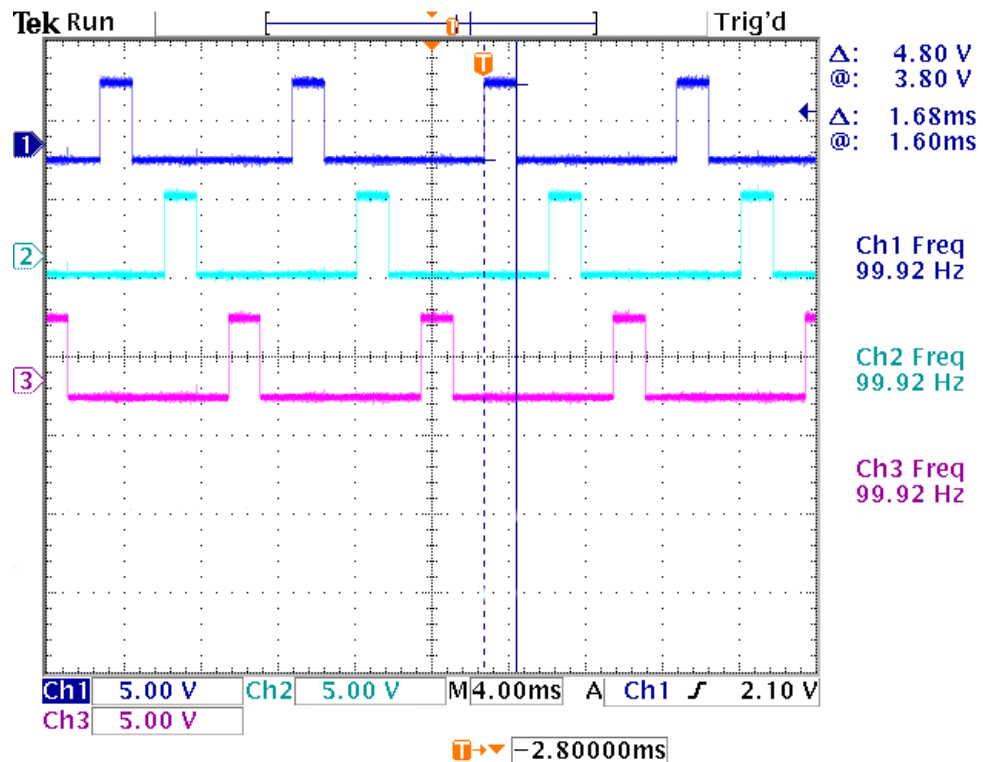


Figure 7.20: The three TTL-level clocks (1, 2, 3) from the MCU. Duty cycle = 1.68 ms $\approx d = 0.166$ (16.6 %), $f = 99.92\text{ Hz}$, Amplitude = 4.8 V.

7.3.2 Current Supply

The R1 values tested in the simulation in 7.2.1 were tested in the prototype circuit by systematically swapping out the resistors at each current source utilising pin sockets. Once again the screen capture and various measuring utilities on the digital oscilloscope were utilised (Figure 7.21a – 7.21e). Table 7.5 compares the expected, simulated and actual outputs of the current driver circuit.

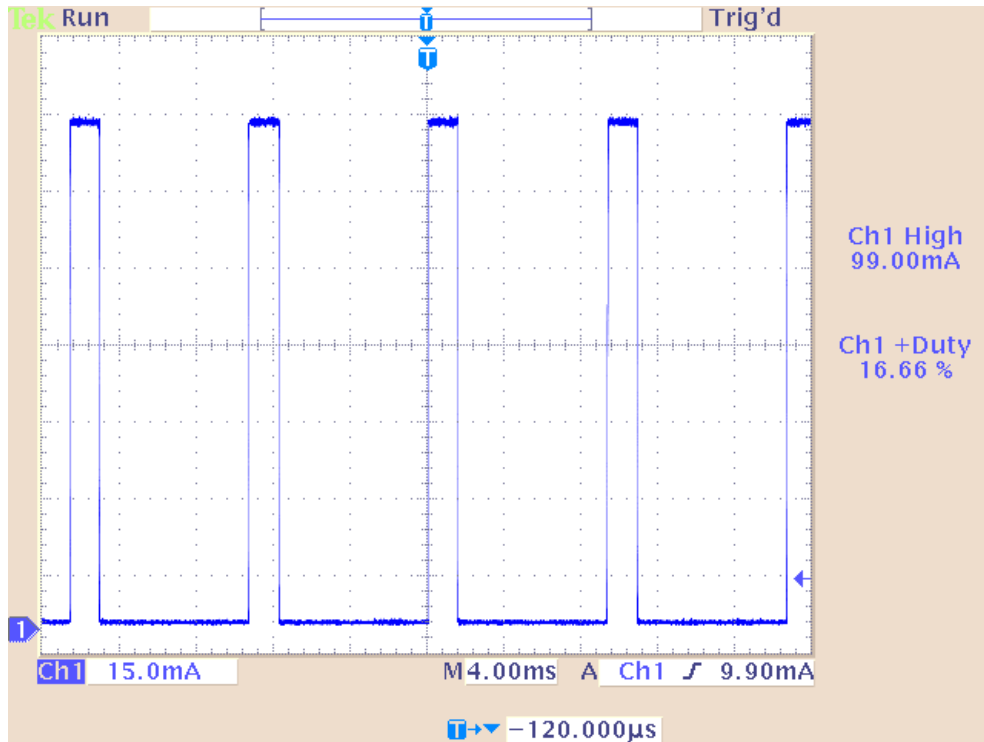


Figure 7.21a: Current output when $R1 = 50 \Omega$. $I_{out} = 99 \text{ mA}$

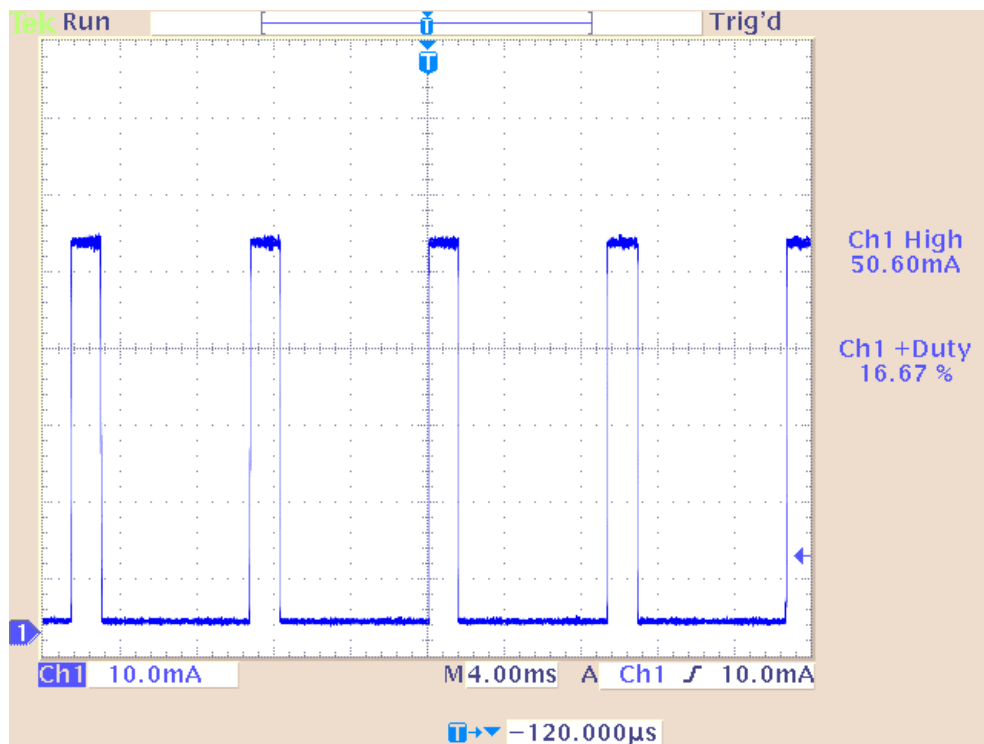


Figure 7.21b: Current output when $R1 = 100 \Omega$. $I_{out} = 50.6 \text{ mA}$

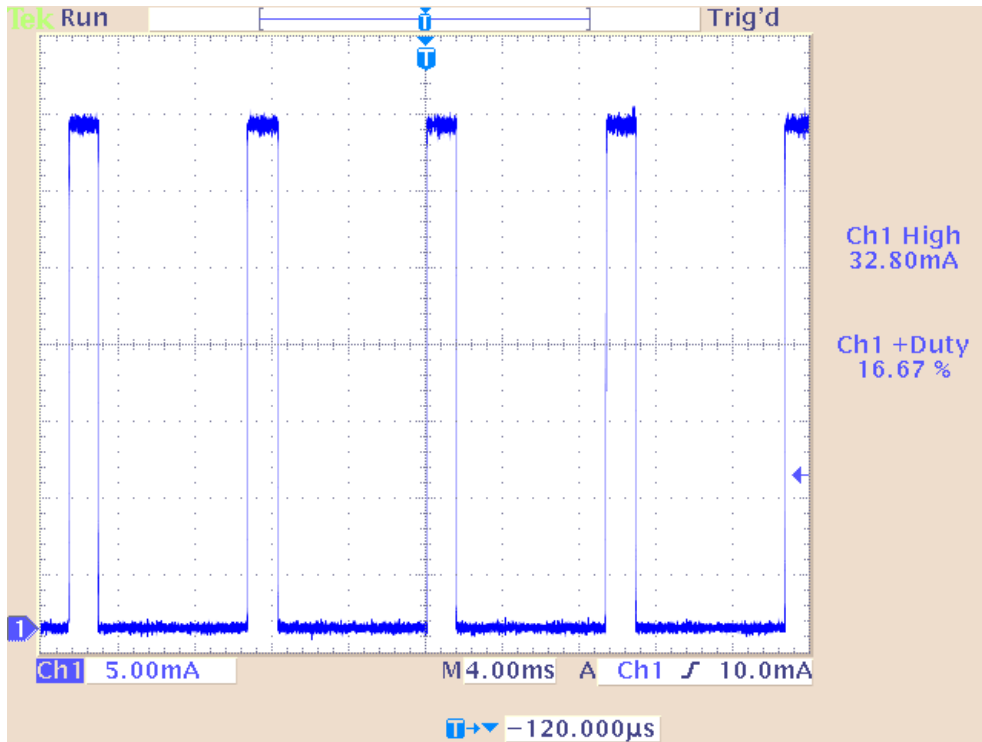


Figure 7.21c: Current output when $R1 = 150 \Omega$. $I_{out} = 32.8 \text{ mA}$

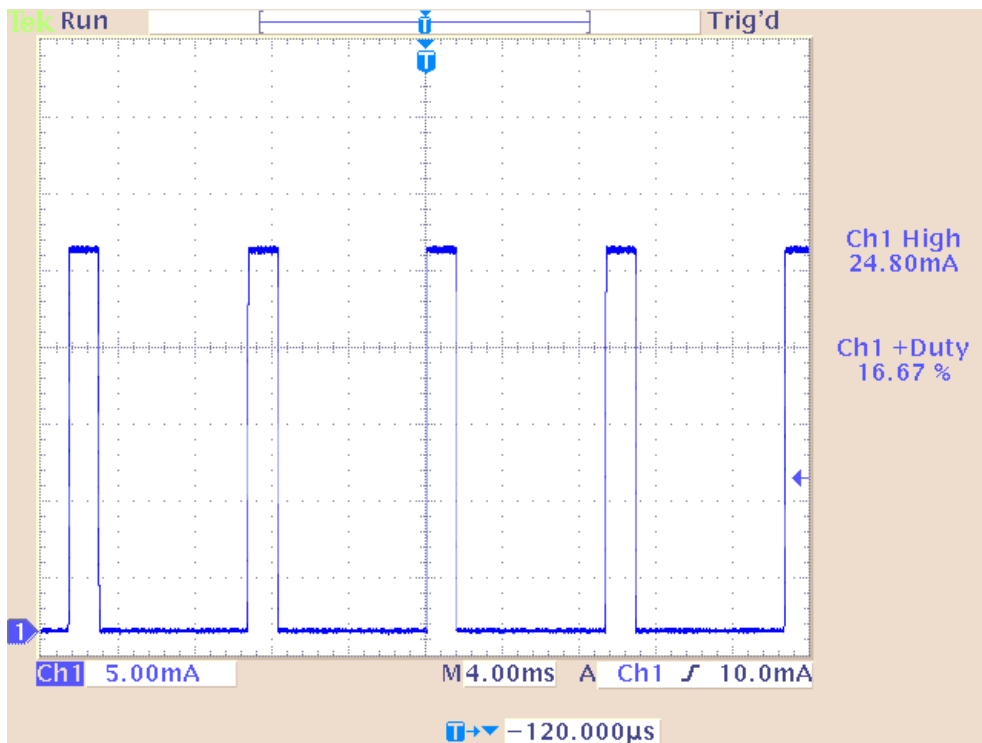


Figure 7.21d: Current output when $R1 = 200 \Omega$. $I_{out} = 24.8 \text{ mA}$

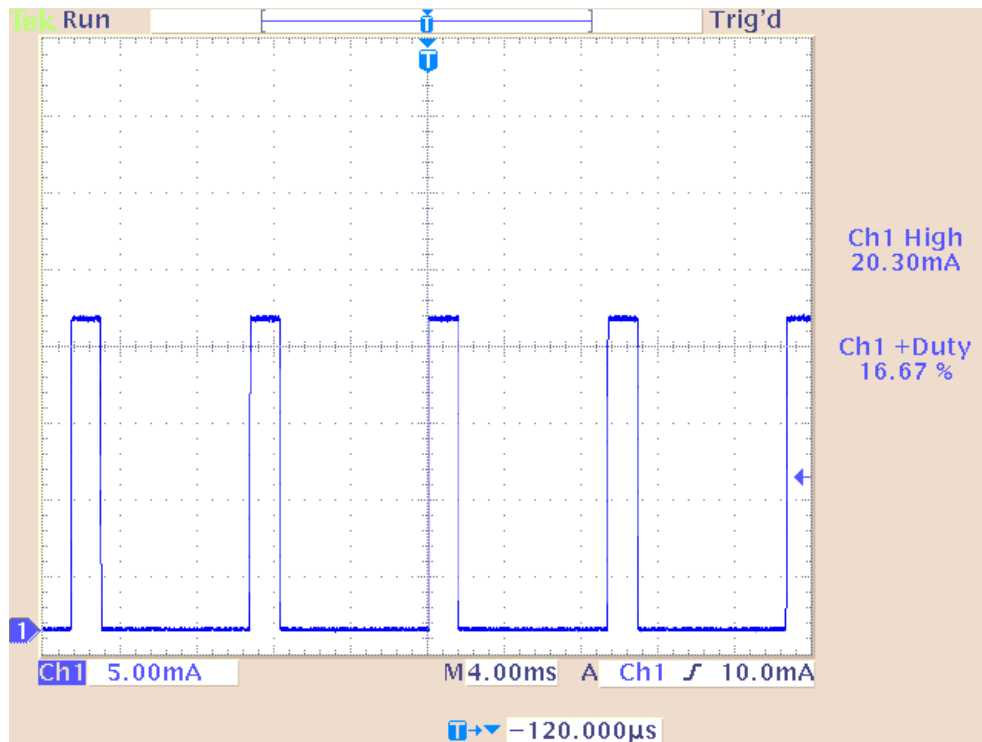


Figure 7.21e: Current output when $R1 = 250 \Omega$. $I_{out} = 20.3 \text{ mA}$

Table 7.5: Actual driving currents and simulated currents correlate well, suggesting that the circuit performs as expected and can handle the current range expected.

R1 (Ω)	Expect	Current (mA)	
		Sim (\pm % diff)	Actual (\pm % diff)
50	100	100.60 (+ 0.6 %)	99.0 (- 1.00 %)
100	50	49.66 (- 0.68 %)	50.6 (+ 1.2 %)
150	33	33.98 (+ 2.96 %)	32.8 (- 0.6 %)
200	25	25.83 (+ 3.32 %)	24.8 (- 0.8 %)
250	20	19.98 (-0.1 %)	20.3 (+ 1.5 %)

7.3.3 Transimpedance Amplifier

A prototype reflectance PPG sensor, placed on the left index finger, was used to test the transimpedance amplifier circuit. The component values from 7.2.2 were kept, and the LED currents set to 40 mA. Figure 7.22 is the output of the amplifier before the demultiplexing stage. Overshoots and undershoots are kept to a minimum, and the maximum voltage does not clip the voltage supply rails, ensuring full signal integrity. The three different level flat peaks are clearly identifiable arise from the PD's ability to capture the different intensities of the different wavelengths of light as they are absorbed differently by the tissues of the in the area being monitored.

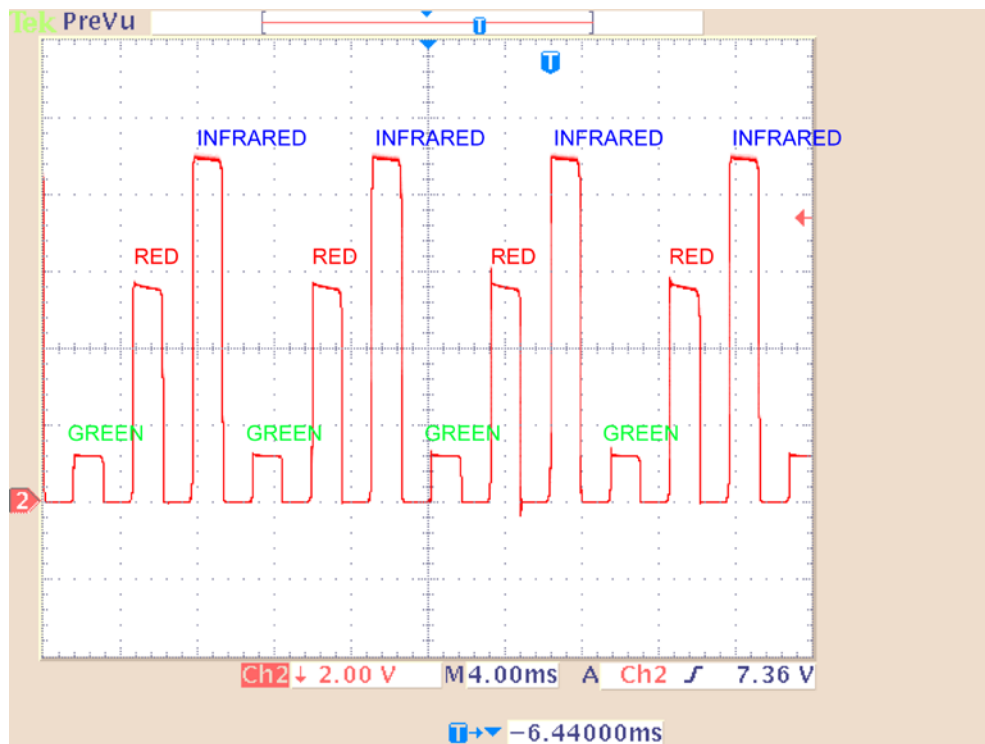


Figure 7.22: Digital oscilloscope capture of the voltage output from the transimpedance amplifier.

7.3.4 Demultiplexing

To test the demultiplexing stage of the circuit, the TIA was driven with a $0.15 \mu\text{V}$ (achieved with a voltage divider circuit after the output of the function generator), 5 Hz sinusoid. TIA overall gain was set to 4.2 M ($R_g = 243 \Omega$). This produced $V_d \approx 630 \text{ mV}$ (Pk – Pk). Figure 7.23 is a DO screen shot of one LF398AN IC performing the sample and hold function on the test signal.

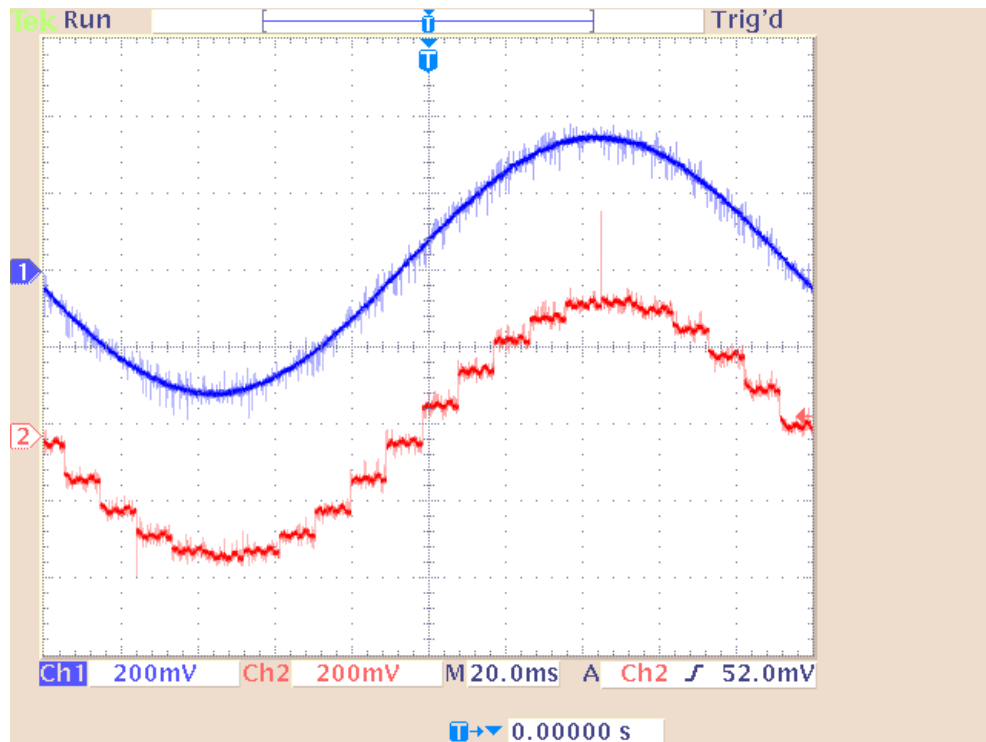


Figure 7.23: Digital oscilloscope capture of the output (Ch2) of one LF398 S&H chip. Input = 5 Hz sinusoid (Ch1).

The stepping artefact (aliasing) seen in Ch2 is caused by the chip “holding” the voltage level at the previous sample before a new one is made. This will be smoothed out by the low-pass filter (anti-aliasing filter) in the next stage of the circuit.

7.3.5 Filtering

An experimental frequency response was carried out separately on the low-pass and band-pass points of the filter (V_{lp} and V_{out} respectively). The tabulated data can be found in Appendix B. Figure 7.24 and 7.25 are the experimental frequency response graphs for the low-pass and band-pass filter stage respectively.

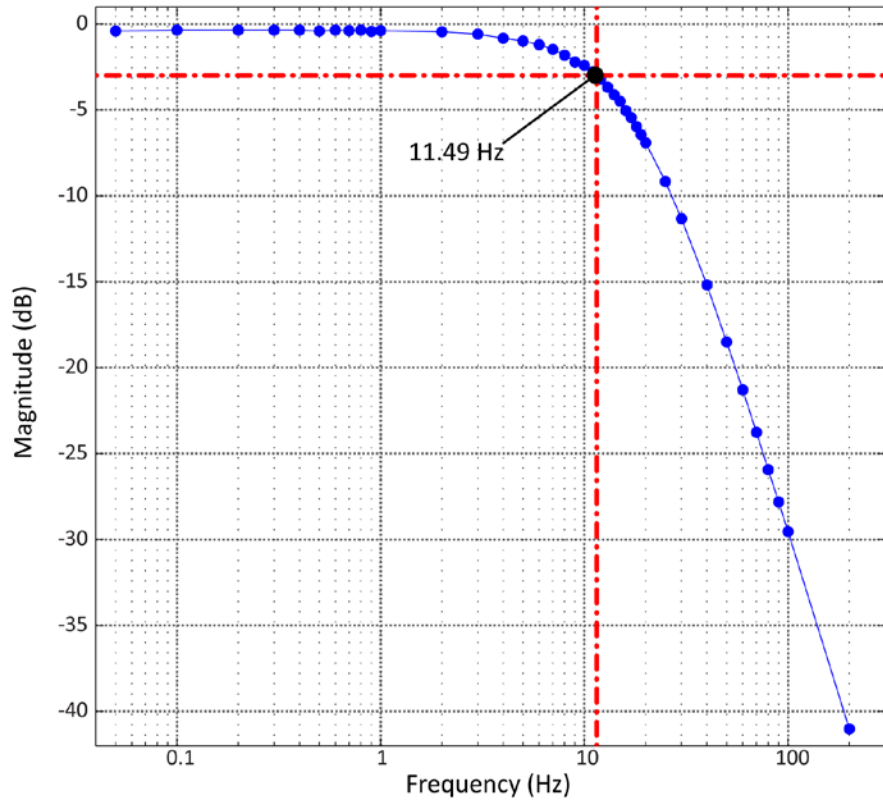


Figure 7.24: Low-pass frequency response. The -3 dB cutoff is 11.49 Hz (0.5 Hz difference to the simulation, 7 Hz difference to calculated).

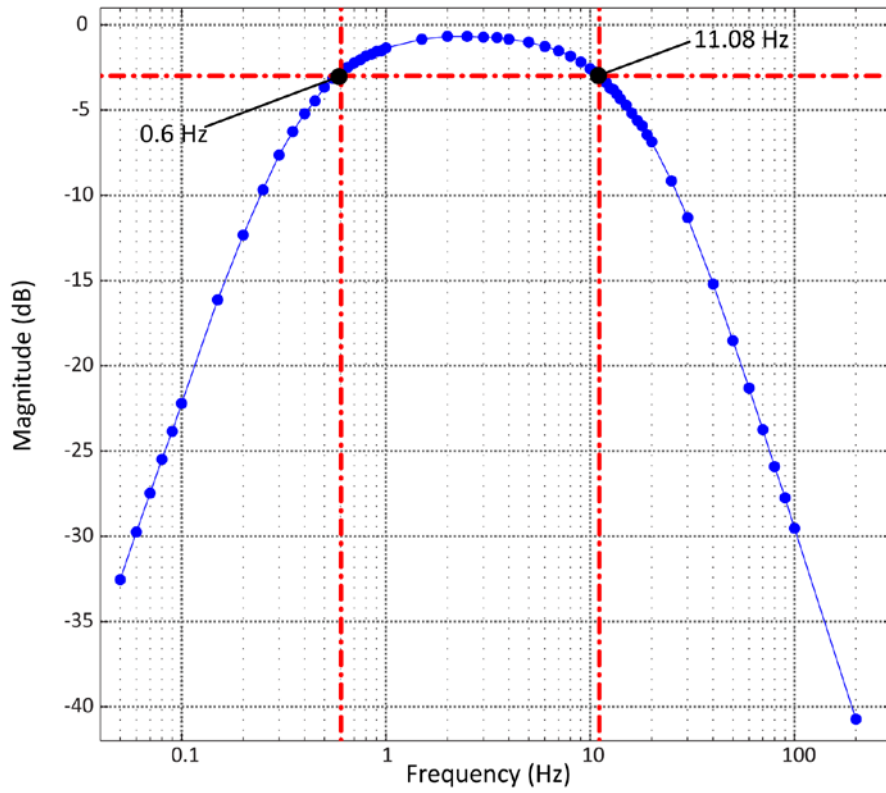


Figure 7.25: Band-pass frequency response. The -3 dB cut-offs are 0.6 Hz (+0.1 Hz difference to the simulated value, +0.3 Hz difference to calculated value) and 11.08 Hz (-1 Hz difference to the simulated value, -7.4 Hz difference to the calculated value)

7.3.6 Post Amplification

Set-up parameters from the simulation (7.2.4) were repeated for the PA on the prototyping circuit. A 5 Hz sine wave with approximate 0.2 V (Pk – Pk) amplitude was applied to V_{in} and the output observed on the DO. Figure 7.26 is a screen capture and direct measurement of the input and out signals.

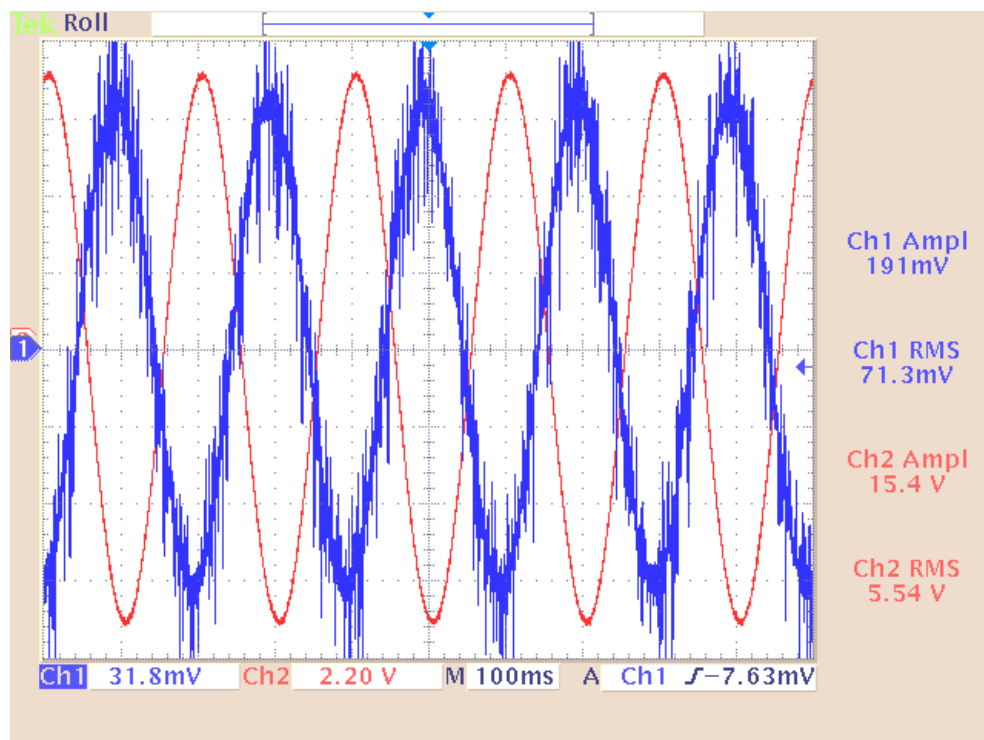


Figure 7.26: Digital oscilloscope capture of AC PPG post amplifier. $V_{in}(Ch1) = 191 \text{ mV (Pk - Pk)}$, $V_{out}(Ch2) = 15.4 \text{ V (Pk - Pk)}$, Gain ≈ 81 .

The gain achieved with the prototype circuit (≈ 81), was -4 % below the theoretical gain and -3.9 % below the simulated gain. As with the simulation the effect of the inverting nature of the PA is observed clearly.

7.3.7 Prototyping Summary

All stages of the electronic prototyping correlated well with calculated values and with the simulations. The current supply for the final circuit will use components that allow for the ability to dynamically adjust the currents between 100 mA and 20 mA. Stable control clocks were observed, and all amplification stages (transimpedance amplifier + post amplifier) performed within acceptable limits. The transimpedance amplifier stage will

incorporate a variable R_g to allow the use of different photodiodes on different sensors, or simply to adjust the gain of the signal during clinical trials on a patient-by-patient basis.

Filtering has a narrower bandwidth than calculated in 7.1.6. However, the bandwidth achieved is sufficient enough to pass the signals of interest and will not be altered for the final circuit construction.

7.4 System Construction

A schematic of the final circuit incorporating repeated circuitry to allow the operation of two PPG/ SpO_2 sensors simultaneously was finalised (Appendix C.1). From this a printed circuit board layout was generated (Appendix C.2), and using in-house manufacturing facilities a final circuit board was manufactured and populated and installed into a shielded steel instrument case (SA series instrument case, RS Components, Northants, UK), figure 7.27. Included into the box also was the data acquisition card and lead acid batteries (not shown).

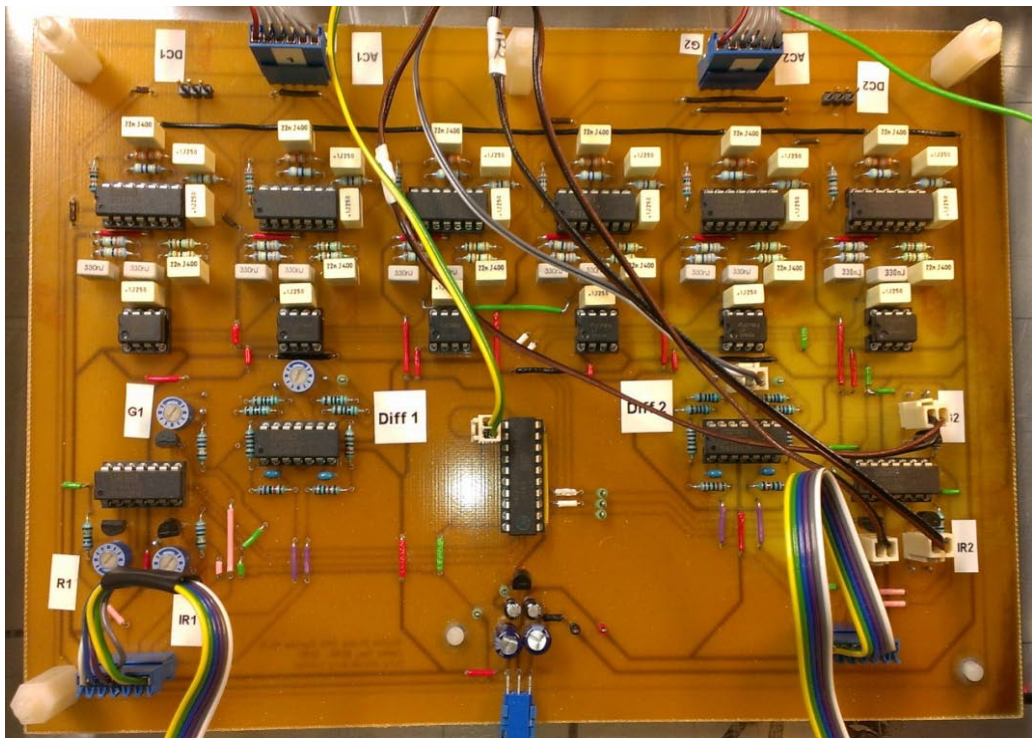


Figure 7.27: Final circuit installed into instrument case.

The circuitry can be switched on and off with a panel mount power switch and an LED indicator notifies the user of circuit operation. Two keyed panel-mount sockets for the PPG/ SpO_2 sensors (Lemo Redel, Ecublens, Switzerland), have also been incorporated onto the front panel for the sensors described in chapter 6 (See figure 7.28).



Figure 7.28: Completed dual PPG instrument front panel.

Access to the data-acquisition card USB terminal has been facilitated by a USB-B connector on the rear panel. Control of the LED currents for the exploratory sensor (the fontanelle or oesophageal sensor) as well as control for the transimpedance amplifier gain for the same sensor have been facilitated by panel mount potentiometers (P16 series, Vishay, PA, USA). LED currents and transimpedance gain for the reference sensor (the foot sensor) can also be set by potentiometers, but these are located internally and will be set to standard values for the majority of the clinical trials. An MCU reset switch (connected to the reset pin of the MCU), has also been included should the need arise to restart the circuit quickly and safely. Figure 7.29 shows the rear panel of the completed instrument.



Figure 7.29: Completed dual PPG instrument rear panel.

7.5 Acquisition of PPGs and Summary

A short test using a reflectance PPG/SpO₂ sensor placed on the left index finger was observed on the DO at the output of the post amplifier on all channels. Little to no noise or aliasing was observed on the PPGs, and they demonstrated large amplification with no clipping or distortion. Figure 7.30 is a short (4 seconds) DO capture of PPGs from two channels on one sensor.

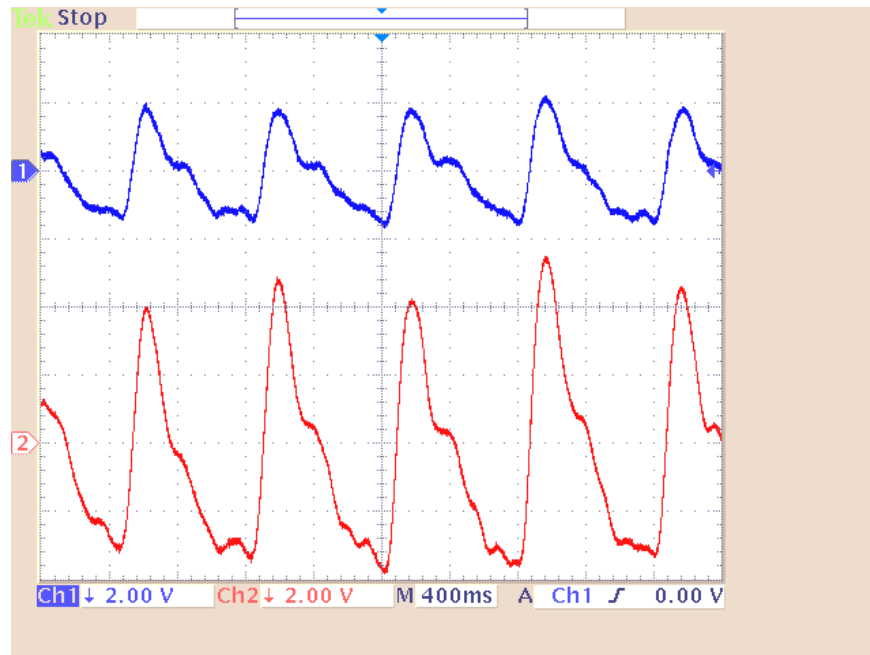


Figure 7.30: Dual channel PPG from one sensor. Visible are the red PPG signal (Ch1) and the infrared PPG signal (Ch2).

PPGs with definable features (peak and dicrotic notch) are clearly observable as a raw waveform direct from the circuit. This tiered design process (circuit design, circuit simulation, circuit testing and final construction) has produced a high quality instrument adequate for the acquisition of raw PPGs. The final stage, digitisation and offline storage of PPGs, is covered in the next chapter.

Chapter Eight

Photoplethysmograph Data-Logging Virtual Instrumentation Development

In chapter seven instrumentation was developed to acquire the raw photoplethysmographic signals (PPGs) from the sensors described in chapter six. The analogue signals that were digitised by the data acquisition device in the instrumentation now have to be stored offline for retrospective analysis. This chapter describes the development of a virtual instrument (VI) created in LabVIEW (National Instruments, TX, USA), for displaying all acquired physiological signals in real time plus archiving all raw data for further offline analysis. Also, algorithms have been developed to enable the real time calculation of heart rate and blood oxygen saturation (SpO_2) from the individual sensors. A time-stamping function has also been implemented that allows the researcher to synchronise hand written notes regarding clinical events/observations directly into the raw signal data file, i.e. readings from commercial monitors regarding vital signs.

8.1 Virtual Instrument Design

A data flow diagram describing the path of the PPG signals was constructed to help with the VI program development. Figure 8.1 shows the flow diagram.

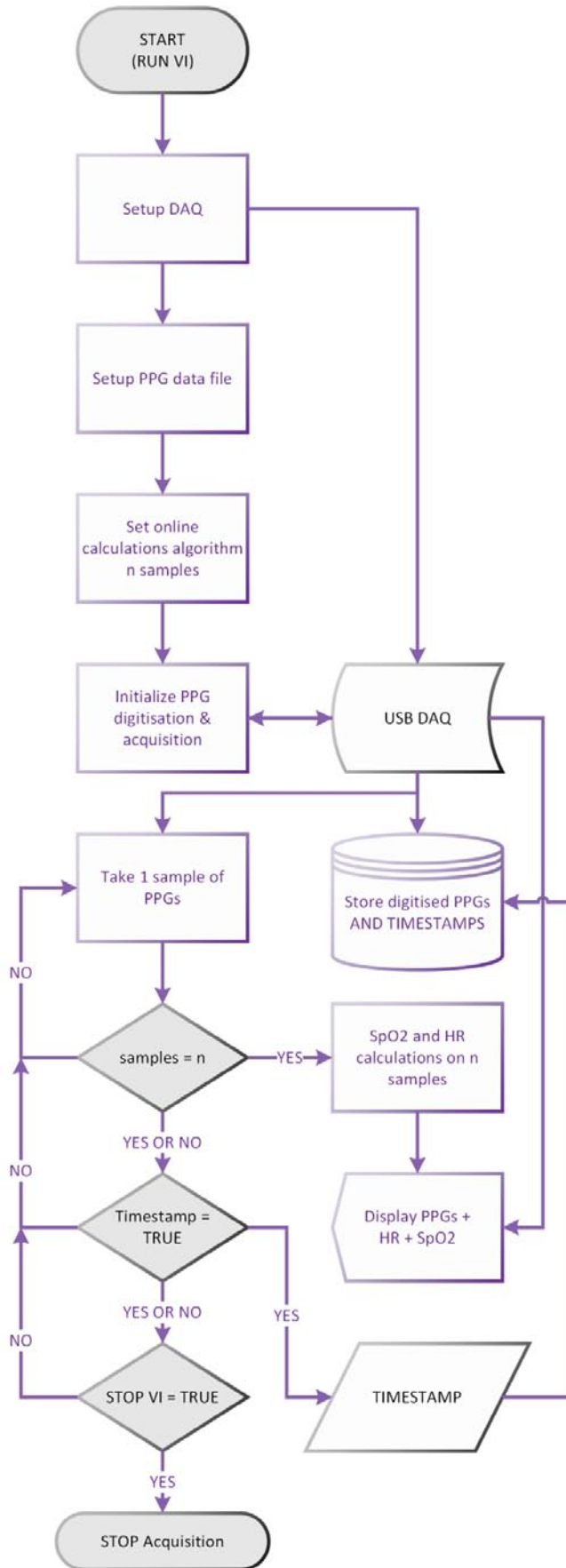

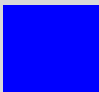




Figure 8.1: Virtual instrumentation data-flow block diagram.

8.1.1 LabVIEW

The programming environment chosen for the VI development was LabVIEW (LV) (National Instruments, USA), short for *Laboratory Virtual Instrumentation Engineering Workbench*. This is an environment with a graphical programming language known as “G”. When designing programs using the data-flow method as illustrated in figure 8.1, LV is uniquely suited, as the concept of data-flow is the heart of operation, with the flow of data provided by an end user, or external component, driving the various steps in the VI’s core algorithms. Various data types can be handled by LV, and are represented by coloured icons and connecting wires that illustrate the flow of data and various operations. Table 8.1 illustrates the key data-types and their associated colour coding. Figure 8.2 is a sample LV “block diagram” describing the process of a simple addition “calculator”.

Table 8.1: LabVIEW data types.

Colour Key	Data Type	Description
 Orange	Floating Point	Any number represented as a single-precision floating-point to complex extended-precision, floating-point imaginary or real.
 Blue	Integer	Any whole number represented as byte (8-bit) signed integer to quad (64-bit) unsigned integer.
 Pink	String	ASCII characters that can represent data or function calls that can be manipulated by LV.
 Green	Boolean	True or False (0 or 1).

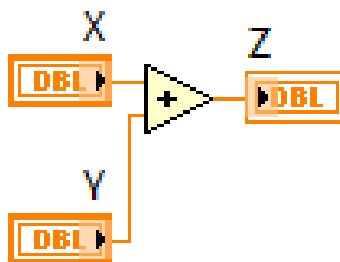


Figure 8.2: Simple LabVIEW block diagram describing the algorithm needed to add two numbers together.

LV also has the ability of user interface (UI) design, or “Front Panel”, where end users may interact and observe the operations as they are happening in real-time. Various UI elements such as numerical controls and graph displays have a corresponding icon in the block diagram so that inputs and outputs from the main code can be easily connected to an appropriate feature on the UI. Figure 8.3 is the UI associated with the G code shown in figure 8.2.

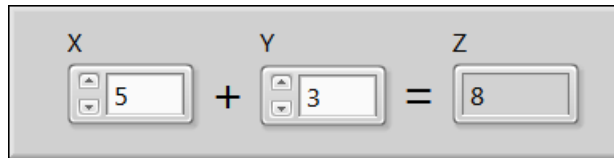


Figure 8.3: Sample UI for the addition “calculator”.

Traditional programming structures such as for-loops, while-loops case structures and sequences can all be programmed in a similar way, and are also represented by their own unique iconographic symbols. Figure 8.4 shows the types of program structures available in LV.

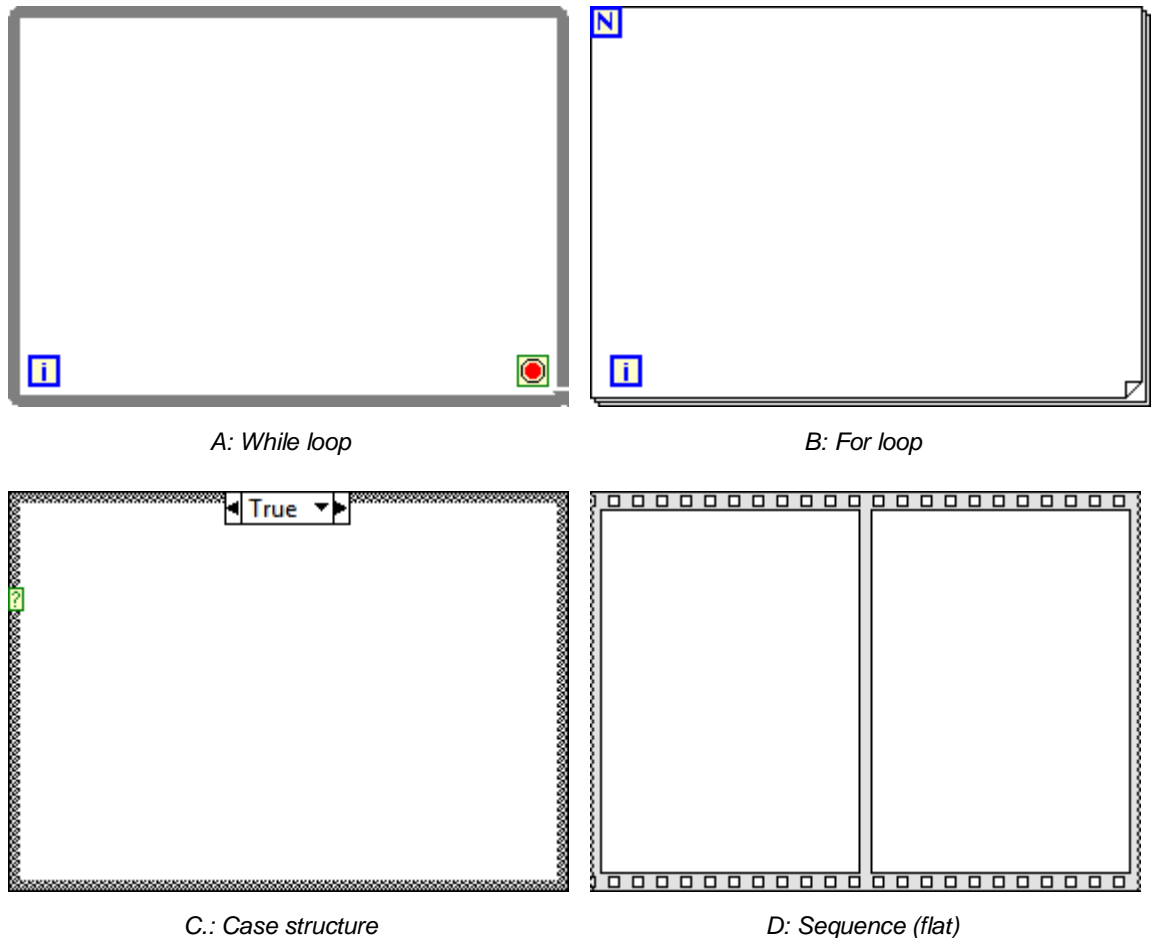


Figure 8.4: Basic programming structures of LabVIEW

The while-loop (Figure 8.4 A) will continuously execute all code within it until its conditional terminal (small red circle in green box) receives a Boolean “true” command. At this point the while-loop will finish executing all code within it. It also has an iteration terminal (blue “i” in a blue square) that can be used to call the number of iterations the while loop has made. The for-loop (Figure 8.4 B) executes the code within it N times. This is determined by wiring a control or constant to the loop’s blue “N” terminal. It also has an iteration terminal used for calling loop iterations. A case structure (Figure 8.4 C) can execute either of many codes within its’ frames, determined by a condition (usually true or false) that is wired to its selector terminal. It ONLY executes one code, not all. A sequence structure (Figure 8.4 D) (flat or stacked) will execute the code within its’ frames sequentially so that operations can be forced or made to wait until a preceding piece of code has been executed. It executes all code within ALL its’ frames, not one, unlike the case structure.

8.1.2 Data Acquisition Card Setup and Acquisition Initialisation

The data acquisition card (DAQ) described in the previous chapter (USB-6212, National Instruments, TX, USA), communicates with a PC or laptop via a set of drivers called NI-DAQmx. In LV all the function calls, commands and analogue to digital converter (ADC) output can be directly accessed via block diagram elements. Figure 8.5 is the basic DAQ card commands needed to set sampling rate, buffer size, starting the ADC conversion, reading the samples taken and stopping the DAQ card before clearing the parameters before the card is used again.

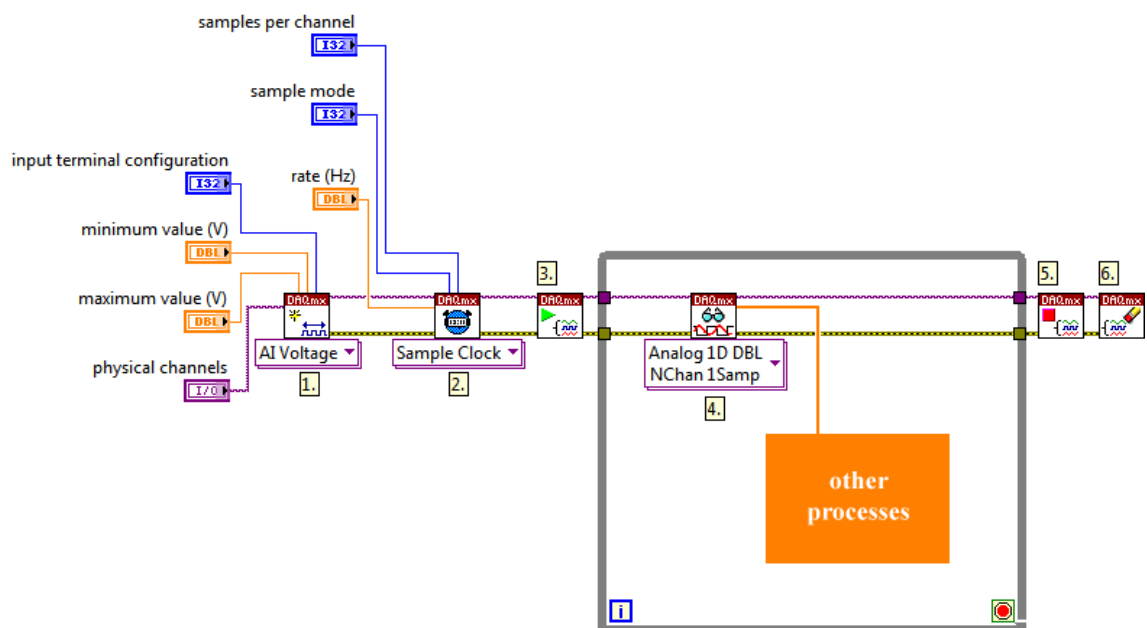


Figure 8.5: DAQ card setup block diagram.

The commands in figure 8.5 can be summarised as follows:

1. The DAQ card is called and given the commands to set up the analogue in (AI Voltage) parameters. This includes what channels should be sampled, the maximum and minimum input range of the signal, and the terminal configuration.
2. The sample clock speed (rate) is set in Hertz, and what type of sampling should take place (i.e. continuous or finite sampling). The input buffer is determined by the samples per channel terminal.
3. The DAQ card is told to run (start acquiring samples).
4. Within a while-loop the AI voltages that have been sampled by the DAQ card are read to the size of the buffer set in the step 2. To continuously read the input voltage at the AI terminals the loop will re-execute once all the code in the loop has been run once. As long as the execution time of one loop does not exceed the time it takes to fill the buffer on the DAQ card all the “other processes” will execute in time to show their outputs to the researcher. The “other processes” illustrated in the figure will include writing to file, and calculations on the input signals for heart rate and SpO₂. When the while-loop receives a “true” condition at its conditional terminal it will finish executing all the code before step 5.
5. The DAQ card is commanded to stop its current operation
6. The DAQ card is cleared of its previous setup parameters ready for a new set of instructions.

A number of input terminals in the block diagram at stages 1 and 2 require user-defined parameters. These are set via the corresponding UI elements shown in figure 8.6.

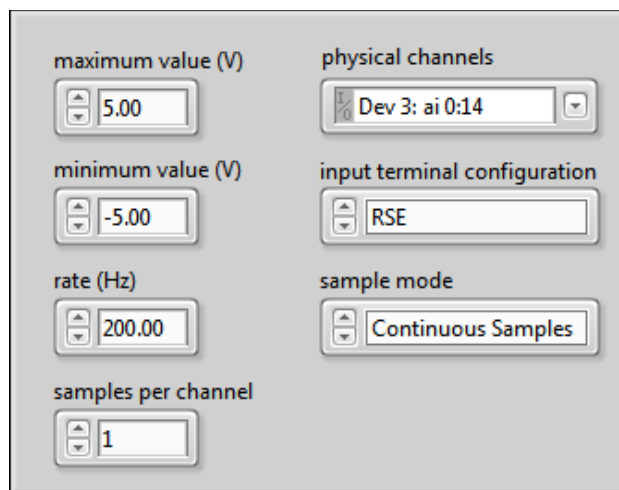


Figure 8.6: DAQ card setup UI elements.

The parameters required by the NI-DAQmx elements are:

- *maximum value (V)* – The maximum voltage input to the DAQ card.
- *minimum value (V)* – The minimum voltage input to the DAQ card.
- *rate (Hz)* – The sampling rate per channel on the card.
- *samples per channel* – The buffer size per channel when the DAQ card sampling mode is set to ‘continuous samples’.
- *physical channels* – A string data-type command that can be read by LV to determine what card to select and what channels must be used.
- *input terminal configuration* – This is the form in which samples are measured. There are several choices:
 - *RSE* – reference single ended, voltages are read with respect to the ground terminal of the DAQ card.
 - *NRSE* – non-reference single ended, voltages are read with respect to a dedicated terminal on the DAQ card.
 - *Differential* – two channels are read simultaneously with respect to each other.
- *sample mode* – how the card acquires samples from the AI terminals, again there a number of choices:
 - *continuous samples* – samples are acquired continuously until the card is told to stop.
 - *finite samples* – a set number of samples are taken, set by the “samples per channel” parameter.
 - *hardware timed single point* – one sample is taken per channel when the card receives a command from an external source.

The parameters chosen as the default settings for the final PPG VI will be:

- ± 10 V max and min input range to closely match the output from the instrumentation (approximately ± 5 -9 V)
- 200 Hz sampling rate, to ensure that all fundamental frequencies of the PPG and their residual harmonics are sampled adequately according to the Nyquist criteria.
- 1 sample per channel buffer size, chosen because the sampling rate chosen is relatively low compared to the maximum rate the card can run 12 channels

simultaneously (33.33 kHz per channel), and data manipulation will be made simple when performing heart rate and SpO₂ calculations.

- RSE terminal configuration, the instrumentation ground line will be directly connected to the DAQ card AI GND input.
- 12 channels input physical channel setup (2 sensors x (3(AC) + 3 (mixed))).
- Continuous sampling as the length of any clinical trial is unknown.

8.1.3 Setup PPG Data File and Continuously Save Raw Signals

Saving the digitised raw PPG signals continuously to a tab-delimited spreadsheet is easily realised using the “File I/O” blocks. Figure 8.7 is the setup utilised to allow the user to be prompted for appropriate save location, setting some header information into the file and then continuously saving to the file in a spreadsheet format.

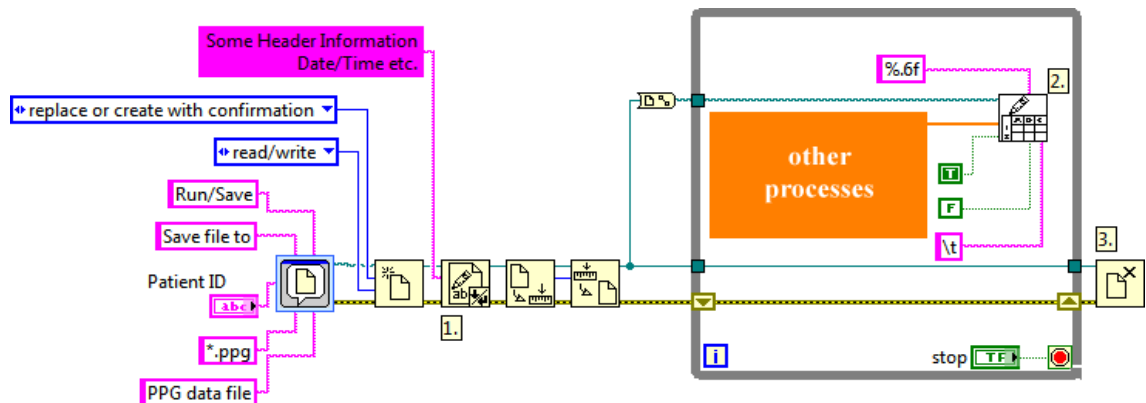


Figure 8.7: Data file setup block diagram

The stages involved in setting the appropriate parameters for the raw PPG data file can be summarised into three separate stages:

1. Setting a custom file type (.ppg) and using “Patient ID” as the file name to be used as the file to be saved to. The user is prompted via a system dialogue to confirm save location, and if a file already exists with the same name will be given the opportunity to change it. Header information regarding time, date patient information will also be added at the beginning of the file so that each data-file is easily identifiable and unique. A singular UI element “Patient ID” is used to name the output file.
2. Data is written then appended to the file continuously in an ASCII formatted spreadsheet, directly to the hard disk, where “other processes” is the output from the DAQ card and time stamping function. Data is written in the “tab de-limited” method with an accuracy of 6 decimal places. This while-loop is the same one

from the DAQ card setup, therefore it can be said that data acquisition and file writing is occurring simultaneously. Writing to the file is continuous until the while-loop receives a true input to its' conditional terminal.

3. At the commencement of the while-loop ending its' last iteration the file is closed in system memory.

The file setup routine only contains one unique UI element and one shared element that is global to the whole VI program. These are illustrated in figure 8.8.

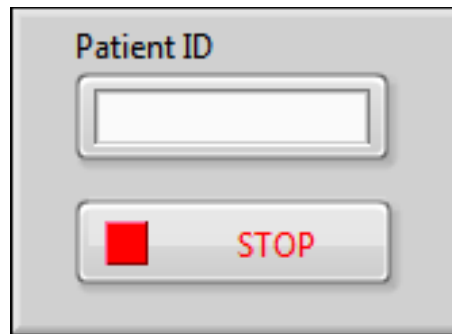


Figure 8.8: Data file setup UI elements

The UI elements for this routine are primarily the Patient ID input string, which is used as the file output name, and the stop button. Although the stop button is global to the entire functioning of the VI it is described here because it is important that when used that all data read from the DAQ card and any time stamps logged by the user are successfully recorded into the data file. Therefore, the final VI will incorporate coding into “other processes” that checks that this condition is met.

8.1.4 Signal Display, Heart Rate and SpO₂ Real-time Estimation

To ensure that the instrumentation is functioning and that the signals being received are of use for retrospective analysis, an algorithm was developed that calculates heart rate, SpO₂ and displays the raw signals in real time. Figure 8.9 is the developed algorithm for one sensor; the second sensor algorithm is a direct copy of this code.

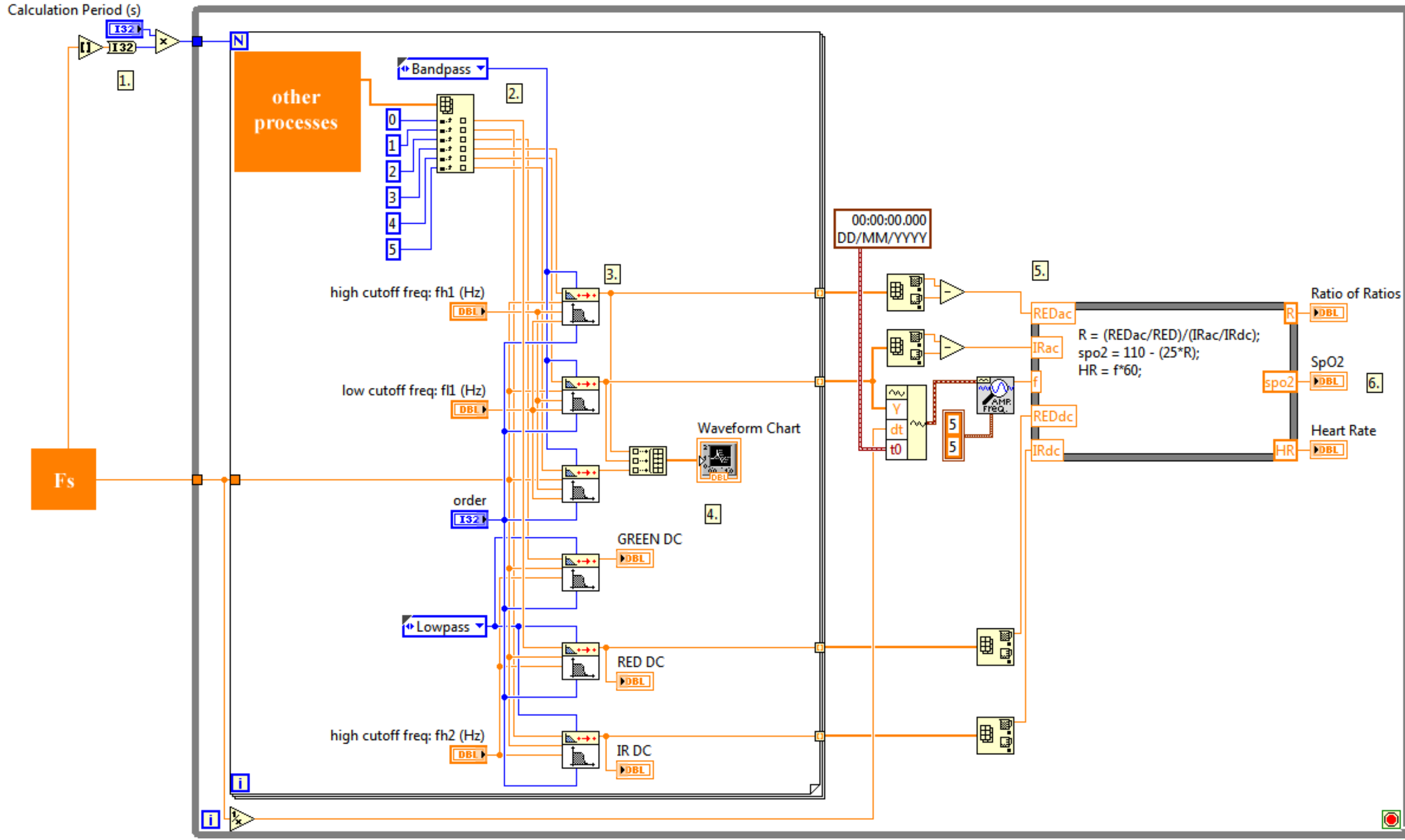




Figure 8.9: PPG signal display and heart rate + SpO2 real time estimation block diagram

To calculate heart rate and SpO₂ it was necessary to process the incoming raw PPG signals and extract certain parameters so that appropriate equations could be applied.

The steps (1 – 6) figure 8.9 summarise this process:

1. A calculation period (determined via a UI element) is set. This value is the amount of time between successive calculations of the heart rate and SpO₂. This is multiplied with the sampling frequency (Fs) from the DAQ card setup. This forms the “N” input to the for-loop inside the main program while-loop. In this manner if the period is 2 seconds and Fs = 200 Hz, then N = 400. This instructs the for-loop to run this many times for every one iteration of the while loop.
2. In the DAQ card setup the sampling size was set to 1, within the for-loop every loop iteration produces 1 sample per PPG channel which are then passed on to steps 3 and 4. An array function (index array) splits the output from the DAQ card into the separate samples from the individual channels.
3. The block diagram element “Butterworth filter point by point” , is used simultaneously on each channel to eliminate noise and aliasing that may affect the final calculation. Three band-pass filters for the AC component and three low-pass filters for the DC component of the signal are utilised.
4. Before all the filtered values are sent to the indexing function at the output of the loop they are simultaneously displayed on the chart display UI element (AC signals) and on numerical displays (DC signals).
5. When the for-loop has run N times all N data points are sent to various array functions to extract the amplitude of the AC signals (REDac + IRac) and the mean of the DC signals (REDdc + IRdc). One AC signal is also processed by the tone extractor block element , to look for the dominant frequency (f) within the sampled data this will be used to calculate the instantaneous heart rate at that period. All outputs from the array functions and tone extractor (REDac, IRac, REDdc, IRdc and f) are then sent into a formula node where the equations (8.1 - 8.3) are implemented:

$$R = \frac{REDac/REDdc}{IRac/IRdc} \quad (8.1)$$

$$SpO_2 = 110 - 25R \quad (8.2)$$

$$HR = 60f \quad (8.3)$$

- The outputs of the formula node are displayed on UI numerical displays and the while-loop reiterates, sending the next N samples into the for-loop which are processed identically. This process continues indefinitely until the while-loop receives a true value at its' conditional terminal sent from the UI stop button described in the file set-up routine.

At this stage a number of UI elements are present on the front panel, used to display the outputs being calculated and setting various parameters needed to ensure successful calculations. The UI elements are shown in figure 8.10.

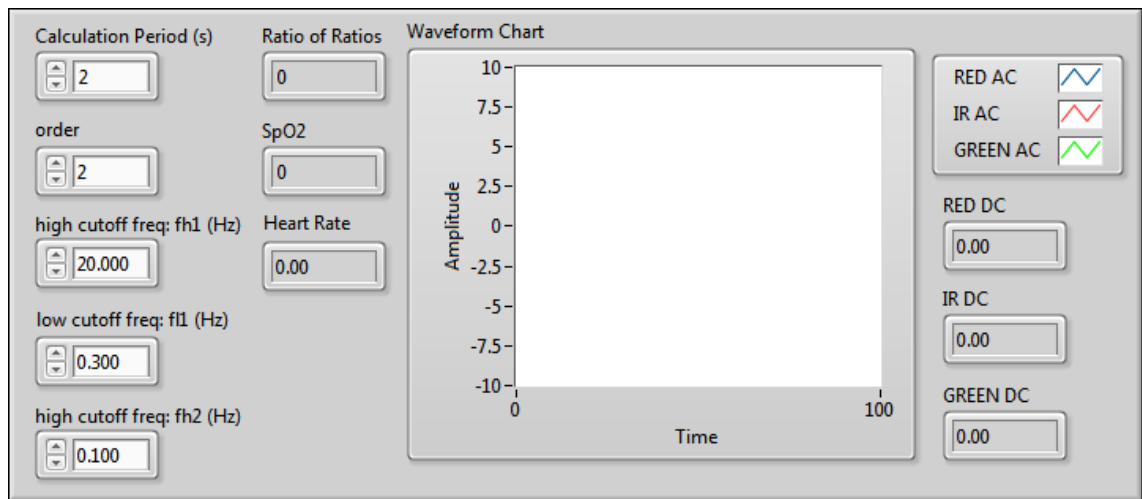


Figure 8.10: Signal display, heart rate, SpO₂ and user controls UI elements.

The UI elements shown in figure 8.10 can be described in two categories;

- Numerical controls

- Calculation Period* – The time period over which to calculate each successive value of heart rate and SpO₂.
- order* – The order of the Butterworth filters.
- high cutoff freq:fh1* – the upper bandwidth limit of the band-pass filter for the AC signals.
- low cutoff freq:fl1* – the lower bandwidth limit of the band-pass filter for the AC signals.
- high cutoff freq:fh2* – the upper limit of the low-pass filter for the DC signals.

- Numerical Displays

- *Ratio of Ratios, SpO2, Heart Rate, RED DC, IR DC and GREEN DC* – corresponding outputs from the block diagram.
- *Waveform Chart* – A graphical representation of the output from RED AC, IR AC and GREEN AC to display the PPG signals.

8.1.5 Time-stamping Function

The use of a time stamping function within the main VI will allow notes made during clinical trials to be synchronised easily with the raw data file. Figure 8.11 describes the algorithm needed to mark the raw data file with the time information every time a UI control is activated.

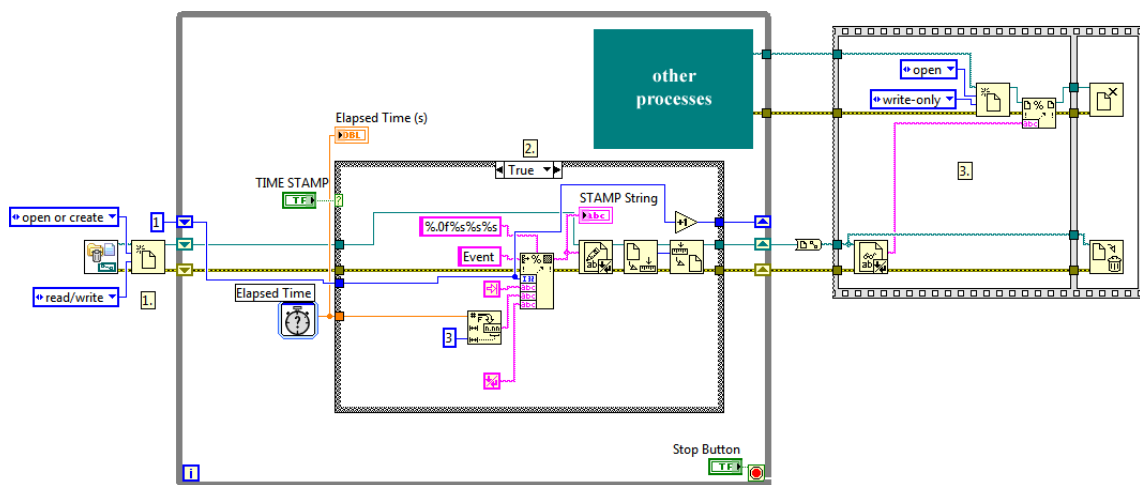


Figure 8.11: Time stamping algorithm block diagram.

To time stamp the main data file at random intervals involves three main steps:

1. Create a temporary file where information can be written before it is committed to the main data file.
2. When the user interacts with the UI element “TIME STAMP” a case structure executes some code that writes the current elapsed time and event number into the temporary file. At all other times the temporary file remains unwritten to. Each successive time stamp interaction appends the created string to the file. The string is displayed in “STAMP string” for the benefit of UI interaction.
3. When the main program while-loop is terminated the temporary file is merged into the main PPG data file from “other processes”. The temporary file is then deleted from the hard disk and the raw PPG data file is updated and closed.

For the time stamping algorithm three new UI elements are introduced, and are shown in figure 8.12, the stop button of the main program loop is also shown as this is a critical element that allows the functioning of the code.

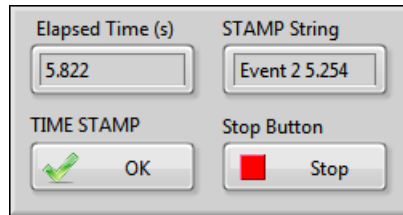


Figure 8.12: Time stamping UI elements.

The main time stamp UI elements are:

- *Elapsed Time (s)* - Shows the current elapsed time that the VI has been running
- *TIME STAMP* – this is the action used to insert the current elapsed time into the data file.
- *STAMP String* – Shows the last event # and the time that it was recorded.

8.2 Final Virtual Instrument

The code from sections 8.1.2 – 5 was combined to form the final code in figure 8.13

The design of the user interface uses all the same UI elements previously described, but using the various design tools available in LV the final UI developed is that seen in figure 8.14a and figure 8.14b.

A number of visual differences to that which was described during development have been made. The underlying code remains identical. The setup parameters have been moved to a separate tab (figure 8.14b) to the signal displays. On the signal display tab the numerical indicators used for DC value display have been changed to bar indicators, this gives a quick and easy visual interpretation of the DC levels in the PPG signals. The “STAMP String” has been renamed as “Event Index and Time” and now displays as a list of events rather than just the last recorded time. The PPG signal display has been made to accommodate as much of the screen as possible and the heart rate and SpO₂ indicators are also in a large font to be easily read.

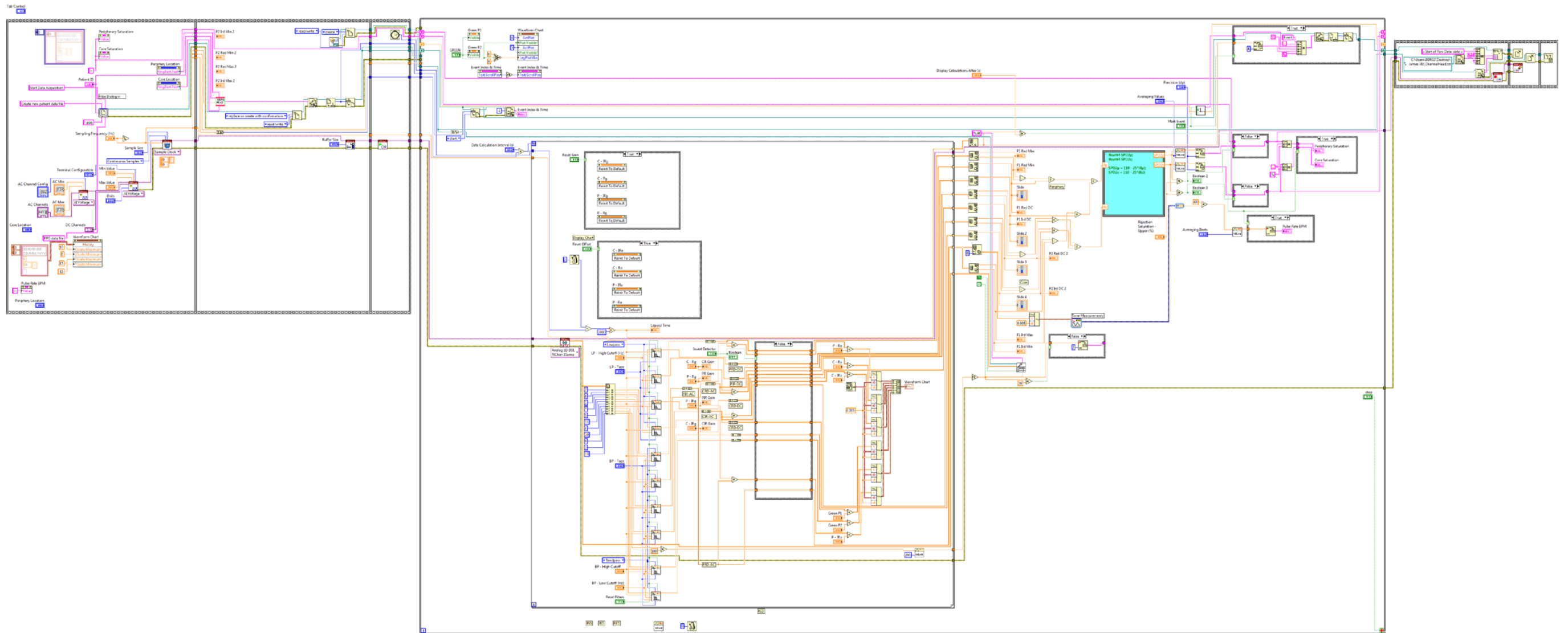


Figure 8.13: Final LabVIEW block diagram code for the dual photoplethysmographic and SpO₂ virtual instrument.

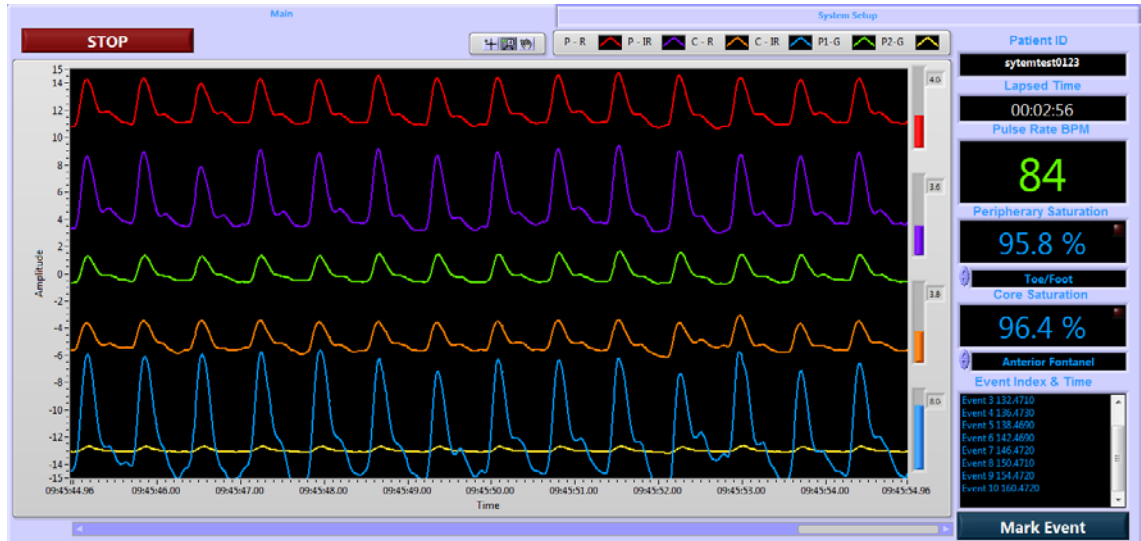


Figure 8.14a: Virtual instrument UI front panel main signal display tab.



Figure 8.14b Virtual instrument UI front panel setup tab.

The VI setup tab accommodates all the parameters used to set up the DAQ card, filters and to adjust some display properties on the main PPG signal display. The numerical indicators previously described for DC values have also been retained and placed here for reference. A sample of the output files (*somename.ppg*) created by this VI is shown in Appendix D.

8.3 Virtual Instrumentation Development Summary

A virtual instrument has been successfully implemented using LV. During tests the VI was not observed to slow down or crash unexpectedly and the output PPG files, when viewed offline in MATLAB (The Mathworks Inc, USA) show all the time stamps recorded, as well as all the raw PPG signals.

Chapter Nine

Photoplethysmograph and SpO₂ Data Analysis

Methodology

Raw photoplethysmograph (PPG) waveforms captured from clinical trials with the sensors and instrumentation described in chapter six and seven respectively were saved to hard-disk via the software described in chapter eight. Retrospective analysis was needed to quantify and interpret this data to help reveal meaningful information that was used to assess the ability of the new sensors to estimate blood oxygen saturation (SpO₂). This chapter presents the methods used to convert the raw unfiltered PPG waveforms into SpO₂ values and introduces the statistical processes that helped assess whether these new sensors are viable alternatives to the traditional sensors already used.

9.1 Signal Filtering

To eliminate unwanted noise and condition the raw signals ready for SpO₂ calculation the PPGs have been put through various stages of filtering. The first filter used was a re-sampling finite impulse response (FIR) anti-aliasing filter set to half the original sampling rate (Fs) from 200 Hz to 100 Hz. This was implemented using the ‘resample’ function in MATLAB (The MathWorks, USA). The form of the function used was $y = \text{resample}(x,p,q,n)$, where x was the original signal, p and q were the numerator and denominator of the resample multiplication factor (p/q) and n was the length of the FIR filter. Figure 9.1 is an example of the re-sampling filter. The re-sampling was performed on all signals before additional filtering routines.

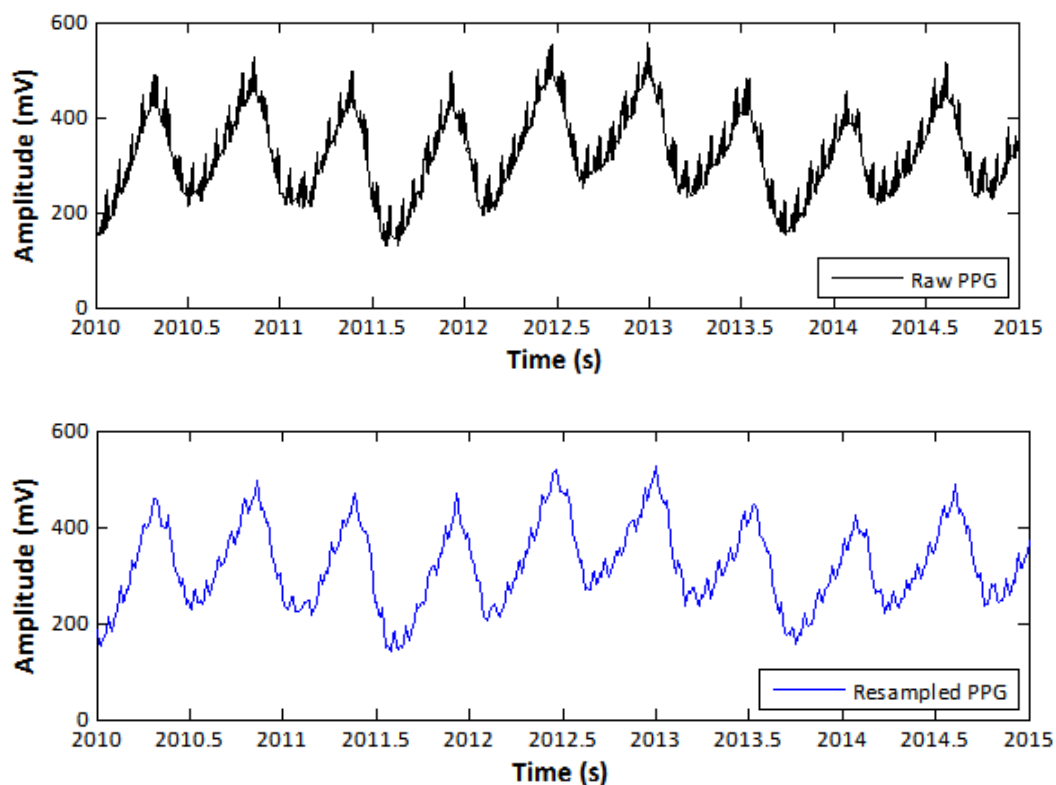


Figure 9.1: AC PPG signal re-sampling. The effect of the resample filter is to half the length of the signal vector and eliminate the high-frequency noise associated with $F_s = 200$ Hz ($HF\ noise = F_s/2$). The re-sampled signal (bottom plot) is notably smoother, the effect of anti-aliasing

Re-sampling to half the original sampling rate was performed on all signals from all clinical trials. The next stage of filtering was to separate the AC and DC components using a band-pass and low-pass filter respectively. The filter for DC separation was identical for all sets of data; it was designed using the filter design and analysis toolbox in MATLAB (The MathWorks, USA). The parameters used were a low-pass equiripple FIR filter with a pass-band of 0 – 0.15 Hz and a stop-band point of 0.1 Hz. Attenuation beyond the pass-band was set to 40 dB. This resulted in a 2835th order low-pass digital filter. The filter coefficients were exported into the MATLAB workspace and used with the ‘filtfilt’ function to separate the DC signal from the re-sampled PPG. The ‘filtfilt’ function is a zero-phase digital filter that preserves signal features in the filtered time waveform exactly where the original feature appeared in the unfiltered waveform, i.e. there is zero-phase distortion. The filter used to separate the AC component was designed in the same manner, except the filter chosen was a band-pass filter, and the pass-band and stop-band parameters were determined individually for each set of signals by inspection of an amplitude spectrum: To make the AC filter efficient at eliminating unwanted movement artefact and respiration/ventilator modulation all signals were subject to a fast-Fourier

transform (FFT) algorithm. This helped visualise the main frequency components of the PPG signals and hence determine the appropriate parameters for the filter design. With attenuation set to 40 dB for every AC filter, and the pass and stop-band parameters set with a resolution of 0.05 Hz the resulting band-pass filter had an order of 2835 also. The filter coefficients were similarly exported and used with the 'filtfilt' function. Figure 9.2 is an FFT amplitude spectrum from one patient in the clinical trials, and figure 9.3 is the result of filtering the AC and DC components from the original PPG signal.

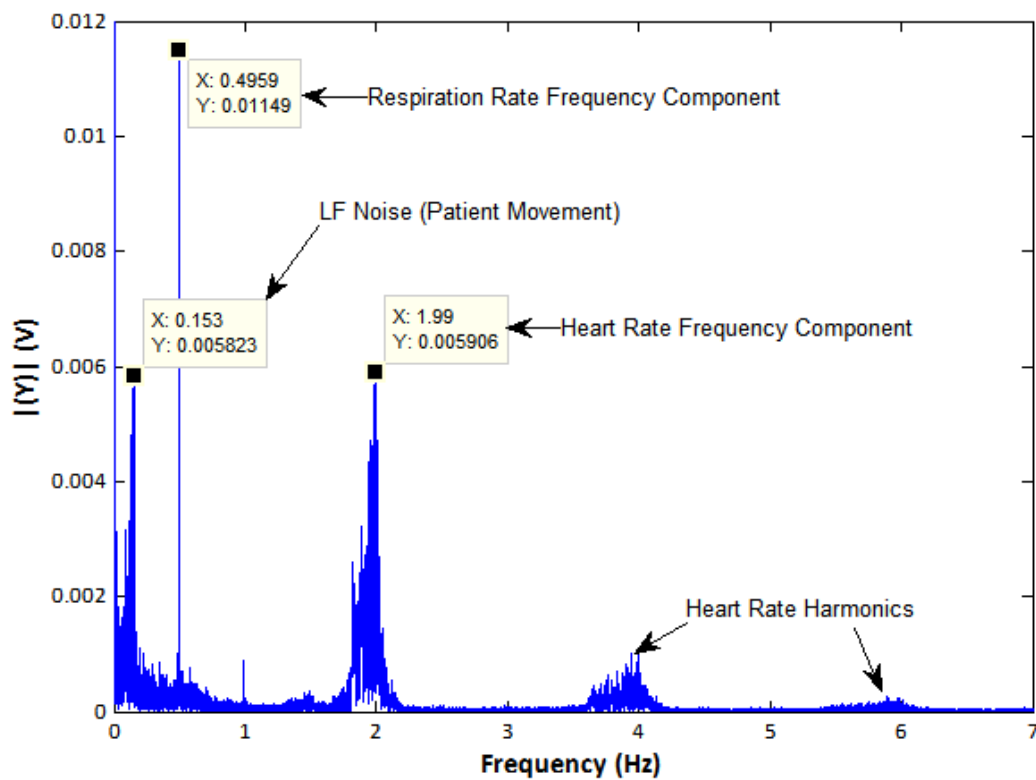


Figure 9.2: FFT magnitude Spectrum of a PPG signal (Y) from 0 – 7 Hz. Calculating SpO_2 relies on the amplitude information from the heart rate component frequencies, designing a digital filter with an appropriate pass-band for each patient will effectively eliminate all unwanted frequency components (Respiratory Rate + LF Noise) for that patient, thus optimizing SpO_2 calculation.

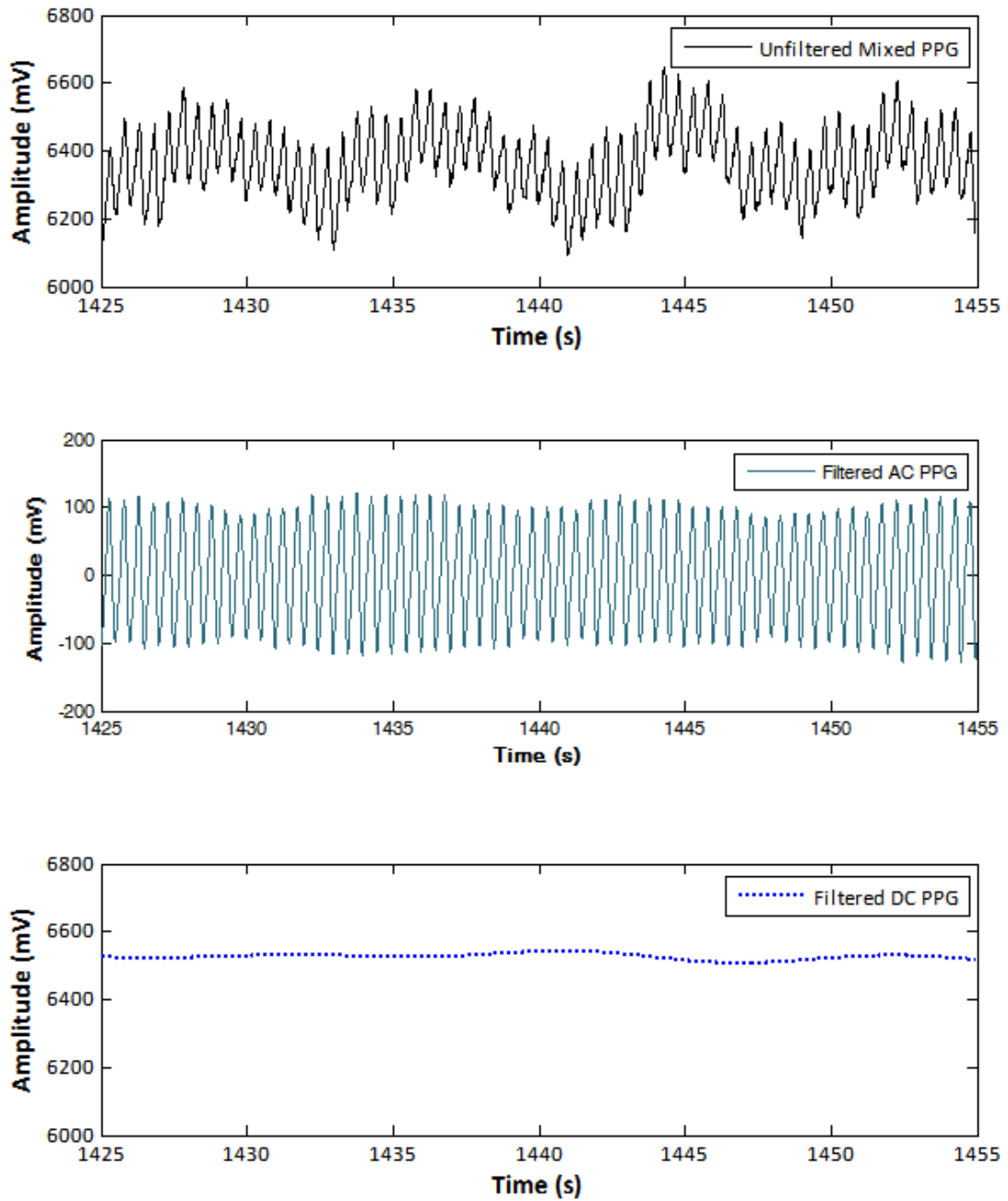


Figure 9.3: AC and DC PPG separation and filtering example over 30 seconds of signal. The unfiltered mixed signal (top) has been effectively filtered and the AC component attributed to the heart rate and DC component attributed to non-pulsatile blood flow separated successfully (middle and bottom respectively).

9.2 Signal Normalisation

In order to compare different wavelengths of light for the calculation of SpO_2 all the PPG signals were divided by their respective DC component. A PPG signal is formed of two constituent parts, the AC portion (attributed to the pulsatile arterial blood) and the DC portion (attributed to the tissue and non-pulsatile blood flow from veins). This process is

necessary as the measured light intensities at the different wavelengths will be different for the different LEDs. The absorbing characteristics of the DC components and the sensitivity of the photodetector also differ for different wavelengths and the tissue absorption and path length will vary widely from patient to patient (Webster, 1997). Normalisation (N) is done by dividing the PPG signal (AC + DC) at each wavelength with its individual DC component given by equation 9.1

$$N_{\lambda} = \text{PPG}_{\lambda} / \text{DC}_{\lambda} \quad (9.1)$$

where λ is the wavelength of light of the signal being normalised and $\text{PPG}_{\lambda} = \text{AC}_{\lambda} + \text{DC}_{\lambda}$. Figure 9.4a and 9.4b are an illustration of this process for two wavelengths (red and infrared).

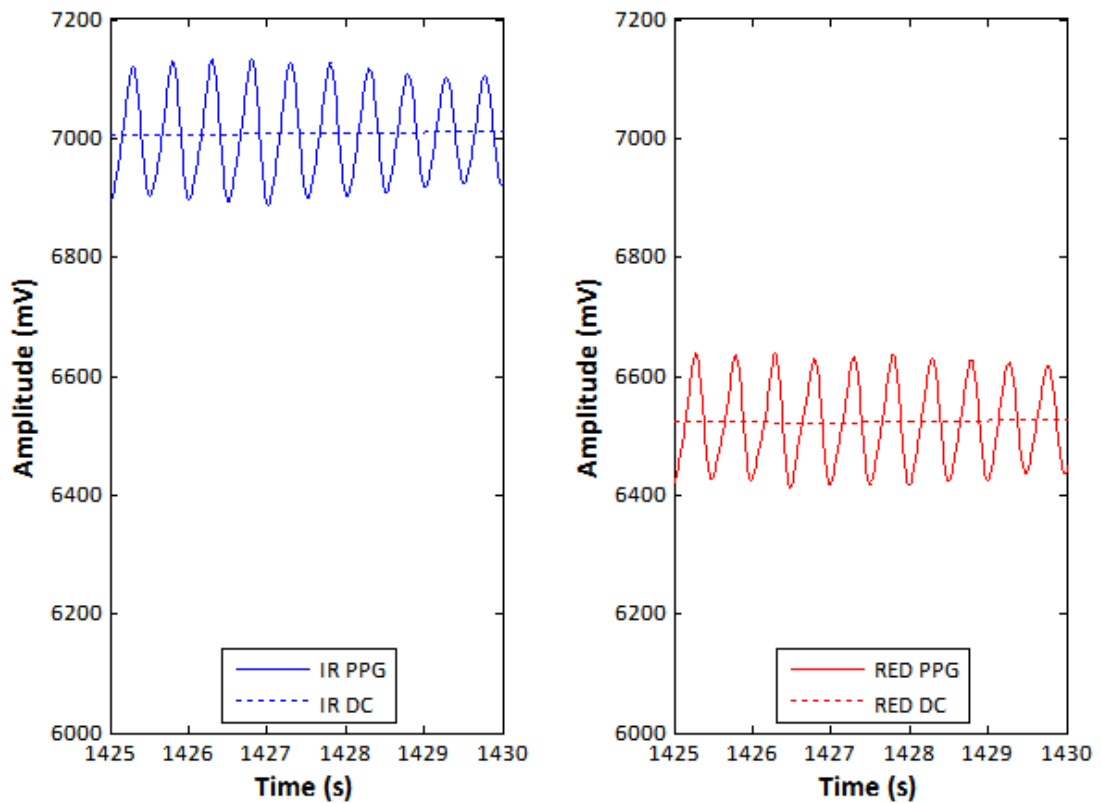


Figure 9.4a: PPG signals before normalisation with their respective DC level (dotted lines). The DC magnitudes are different.

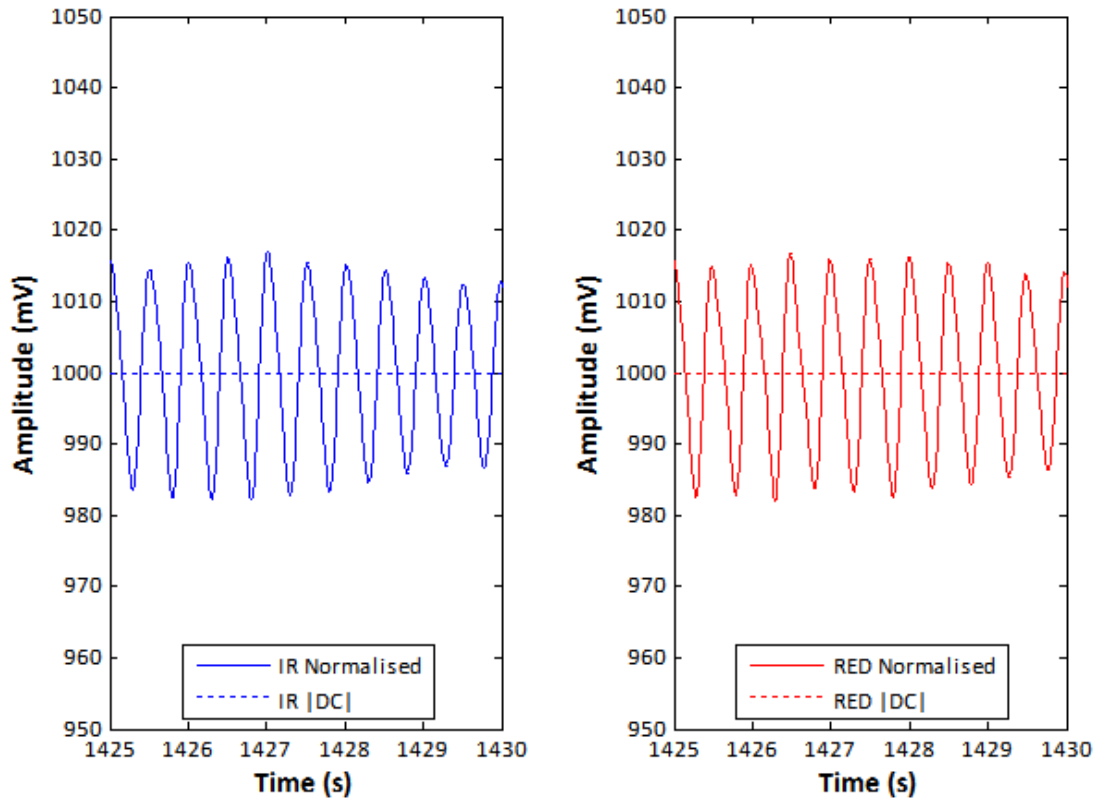


Figure 9.4b: PPG signals after normalisation, each signal now has the same DC magnitude (1000 mV).

9.3 Amplitude Measurements

Calculation of SpO_2 required the information from the measurement of the amplitude of the PPG signals at different wavelengths in order to determine the amount each source of light is absorbed by the blood and tissue. Since it is the AC component of the signal, attributed to the pulsatile arterial blood, which is said to be representative of blood oxygen concentration when measured at more than one wavelength it is necessary to measure this amplitude (A_{ac}). The algorithm used, written in MATLAB (The MathWorks, USA), implements equation 9.2 on the normalised PPG signals; it takes each set of PPG signals and divides the length of the signal (L) into two-second portions (s). For every two seconds the amplitude is simply calculated by subtracting the lowest detected amplitude value (A_L) (usually the trough of a PPG waveform) away from the highest detected amplitude value (A_H) (usually the peak of the PPG waveform);

$${}^nA_{ac} = {}^nS_{AH} - {}^nS_{AL} \quad (9.2)$$

where n is a number from 1 to $(L/2)$ and represents the portion of PPG signal where A_{ac} is being calculated. Figure 9.5 illustrates this method.

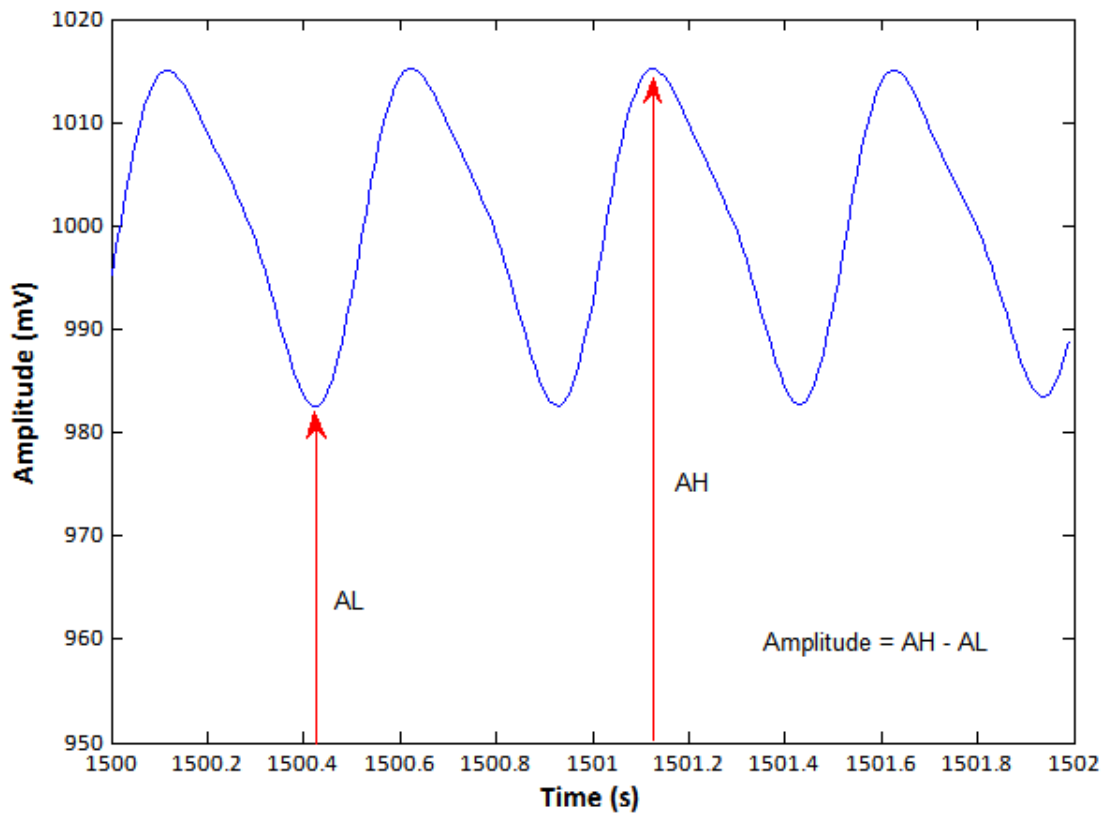


Figure 9.5: AC PPG amplitude calculation for a single 2-second portion of signal.

9.4 SpO_2 Measurements

For comparison of SpO_2 values from the new sensors with the commercial pulse oximetry devices the amplitude measurements made by the method in section 9.4 were converted into meaningful values that were compared directly with SpO_2 . The first stage of conversion was to derive an arbitrary value from the separate PPGs (red and infrared). Traditionally this value is known as ‘R’ and several methods of calculating it exist. The method chosen for this thesis is described in *Design of Pulse Oximeters* (Webster, 1997), and is known as the derivative method, and is calculated using the separated AC and DC components that we have already computed. By equation 9.3 the amplitudes from the AC and DC components for each wavelength (red and infrared) is used to compute R;

$$R = \frac{AC_{RED}/DC_{RED}}{AC_{IR}/DC_{IR}} \quad (9.3)$$

When using the normalised signals, calculated in section 9.3, $DC_{RED} = DC_{IR}$; therefore eqn. 9.3 becomes;

$$R = N_{RED}/N_{IR} \quad (9.4)$$

This 'R' value, or ratio of ratios as it is commonly referred to, was then used with a calibration equation to estimate SpO₂. Again there are several equations in existence and many are described in both *Design of Pulse Oximeters* (Webster, 1997) and in *Pulse Oximetry* (Moyle, 2002). However since a degree of calibration would be required to calibrate these new sensors with actual blood-gas analysis values for accurate operation, and since the protocol for the clinical experiments (described in Chapter 10) is looking for changes in SpO₂ rather than accurate SpO₂ scores, the SpO₂ approximation chosen is equation 9.5, and is described briefly in *Design of Pulse Oximeters* (Webster, 1997);

$$SpO_2 = 110 - 25R \quad (9.5)$$

This is a linear equation and can be represented graphically as shown in figure 9.6.

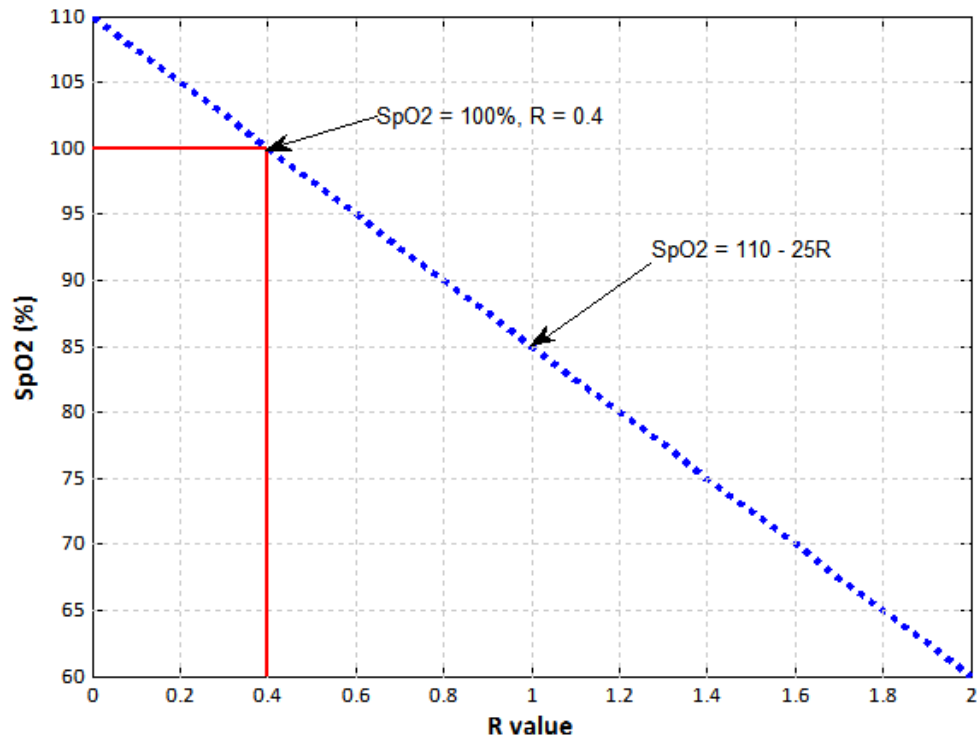


Figure 9.6: SpO_2 approximation linear equation 9.5 with R value.

9.5 Statistics

Following computation of amplitudes and SpO_2 values, various statistical analyses and tests were performed on the sets of data to make the appropriate comparisons between the computed values and the actual observations made in the hospital. Prior to the statistical analysis the amplitudes and SpO_2 values obtained were inspected to eliminate those values which were calculated during any heavy movement artefact or clinical procedure which caused portions of the signals to become unreliable. A signal portion was specified by this researcher to be unreliable when either the characteristic AC pulsatile signal ceased, or if a time stamp indicated a clinical procedure which caused unwanted movement in the patient. Figure 9.7a , 9.7b and 9.7c are an example of one PPG signal with unreliable signal portions and the elimination process on the corresponding amplitudes and SpO_2 values.

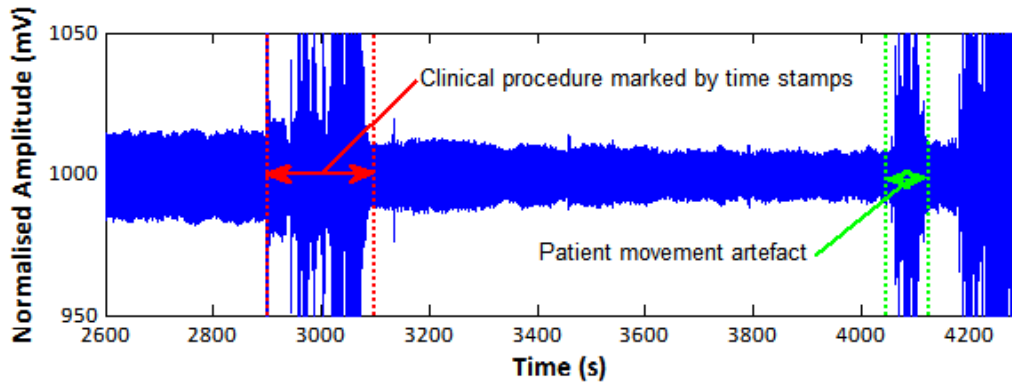


Figure 9.7a: A sample of PPG signal with unreliable signal portions marked via time-stamps during the trial (red) and retrospectively via manual inspection (green – operator driven).

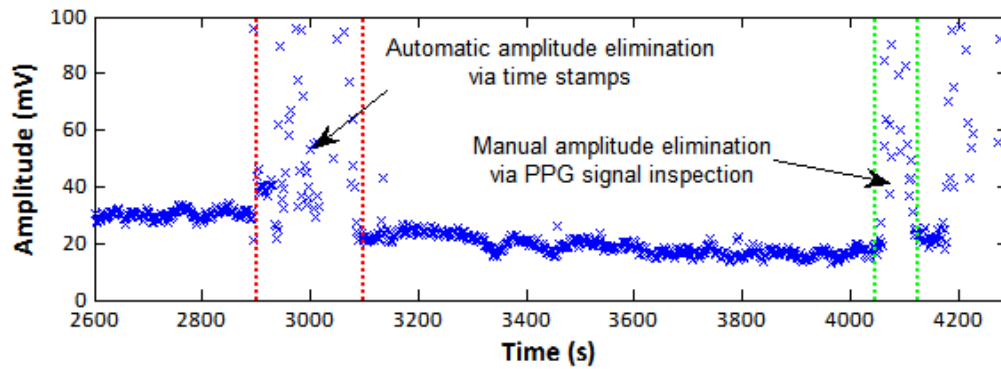


Figure 9.7b: Eliminated PPG amplitudes through the use of time stamps (red) and manual inspection (green – operator driven).

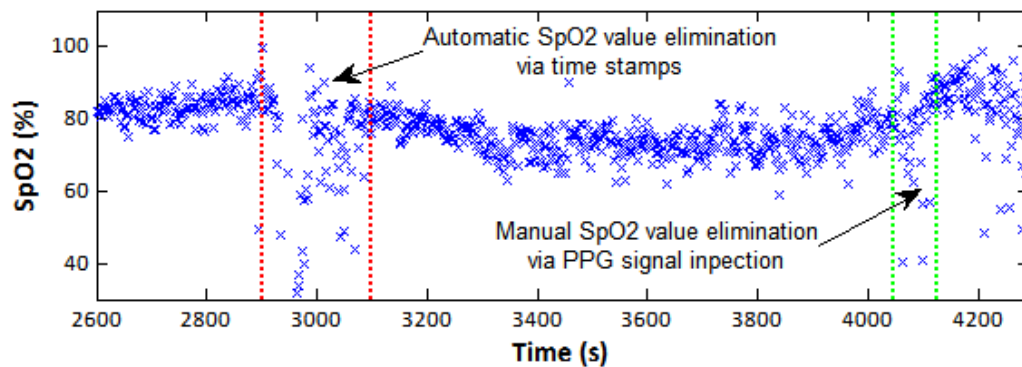


Figure 9.7c: Eliminated SpO_2 values through the use of time stamps (red) and manual inspection (green – operator driven).

With the amplitude and SpO_2 data now conditioned to remove unwanted erroneous readings, a series of statistical tests were performed. These included mean and standard deviation, correlation, “Bland and Altman” agreement analysis (Bland and Altman, 1986)

and paired distribution t-tests. The pre-normalised data (AC and DC) was also tested using the t-test to look for changes in the signals before normalisation. The details of how each of these tests was performed on the sets of data are covered in the following chapters. Results from the commercial sensors and blood gas tests were pooled into tables and analysed with the same statistical algorithms and compared accordingly. All statistical computations were performed in MATLAB (The MathWorks, USA).

9.6 Summary

The methods outlined here have been used to derive the results in the following chapters, Chapter 10 – *Anterior Fontanelle and Foot Photoplethysmography Analysis During Delivered Oxygen Concentration Change In-vivo* , Chapter 11 – *Anterior Fontanelle and Foot SpO_2 Analysis*, and Chapter 12 - *Oesophageal Photoplethysmographs and SpO_2 Analysis, a Proof of Concept Demonstration In-vivo*. Appropriate referencing to this chapter is cited.

Chapter Ten

Anterior Fontanelle and Foot

Photoplethysmograph Analysis during Delivered Oxygen Concentration Change *In-vivo*

Chapter five summarised that at times of peripheral blood supply compromise in neonates and infants a core location such as the anterior fontanelle (AF) or the oesophagus may be better suited as an oxygen saturation monitoring (SpO_2) location. A clinical protocol was written and approved by a local ethics committee (Appendix E) to investigate whether these locations could yield the necessary raw photoplethysmographic waveforms (PPGs) needed for SpO_2 calculation. All instrumentation was tested and passed for electrical safety by the participating hospital's biomedical engineering department as part of the local ethic committee's requirements. This chapter presents the details of the clinical trials (from the fontanelle) including all the analysis on multi-wavelength PPGs from the AF and the foot of 16 neonates (9 male, 7 female) on an intensive care unit at Great Ormond Street Hospital for Children.

10.1 Anterior Fontanelle Clinical Procedure

Candidates for AF PPG monitoring were selected on ward rounds by the lead clinician against the list of inclusion/exclusion criteria specified in the protocol. All patients were categorized as either ASA 1, 2 or 3 (American Society of Anaesthesiologists physical status classification system), where 1 is the least critical and the patient wasn't on respiratory support and 3 was more severe and the patient was on an oscillator, a high frequency (typically 4 times greater than normal respiratory rate) mechanical ventilator that utilises small tidal volumes to effectively ventilate a patient with reduced risk of ventilator-associated lung injury. Category 2 patients were on regular ventilator support.

In these pilot studies utilisation of the fontanelle sensor was carried out on 16 intensive care neonates (9 male, 7 female) with a mean age of 36.5 days (SD = 46.8 days) and a mean weight of 3.07 kg (SD = 0.93 kg). All patients were assessed by the lead clinician as suitable for study (ASA score 1 – 3) where those with an ASA of 3 were considered to be

most at risk of periphery supply shutdown. All patients were sedated and receiving delivered oxygen. ASA 1 patients were not on mechanical respiratory support (5 cases), ASA 2 patients were on ventilator respiratory support (8 cases) and ASA 3 patients were on oscillatory respiratory support (3 cases). One ASA 1 patient (Patient 3, Appendix G) failed to yield adequate PPGs for study from the AF, and the data was eliminated from further overall analysis. For this patient it was commented by the clinician that the AF felt smaller than usual, suggesting that observations of PPGs through the AF were hindered by the presence of underlying tissue.

Following informed consent from parents the procedure to look for PPG signal changes at the AF commenced; A routine blood gas test was scheduled and both sensors (foot and AF) were cleaned with alcohol wipes and placed into clear adhesive sterile pockets (Tegadern™, 3M, MN, USA). The reference PPGs were established by placing and securing the foot sensor on the sole of the foot with standard medical tape. The lead clinician then manoeuvred the AF sensor over the fontanelle until PPGs with good amplitude and signal to noise ratio were observed on the laptop monitor. The AF sensor was then secured in position with a bandage that was wrapped around the back of the head or jaw-line. Figure 10.1 shows the AF sensor *in situ* on a male patient, photographic consent was obtained from the parent for the use of this image in publications related to this work. At this time the routine blood sample was taken for blood-gas analysis, and marked as a time stamp in the data file with the time-stamp function of the virtual instrument (VI). Recording of PPGs was continued for a maximum length of 30 minutes before the baseline of delivered oxygen concentration (FiO_2) was increased by 50 %, .e.g. 30 % to 45 %. The time of FiO_2 changes were marked as time stamps. Continued monitoring was maintained for a maximum time of one hour before the FiO_2 was decreased back to the initial baseline value and PPGs were further monitored for 30 minutes before the trial ended.

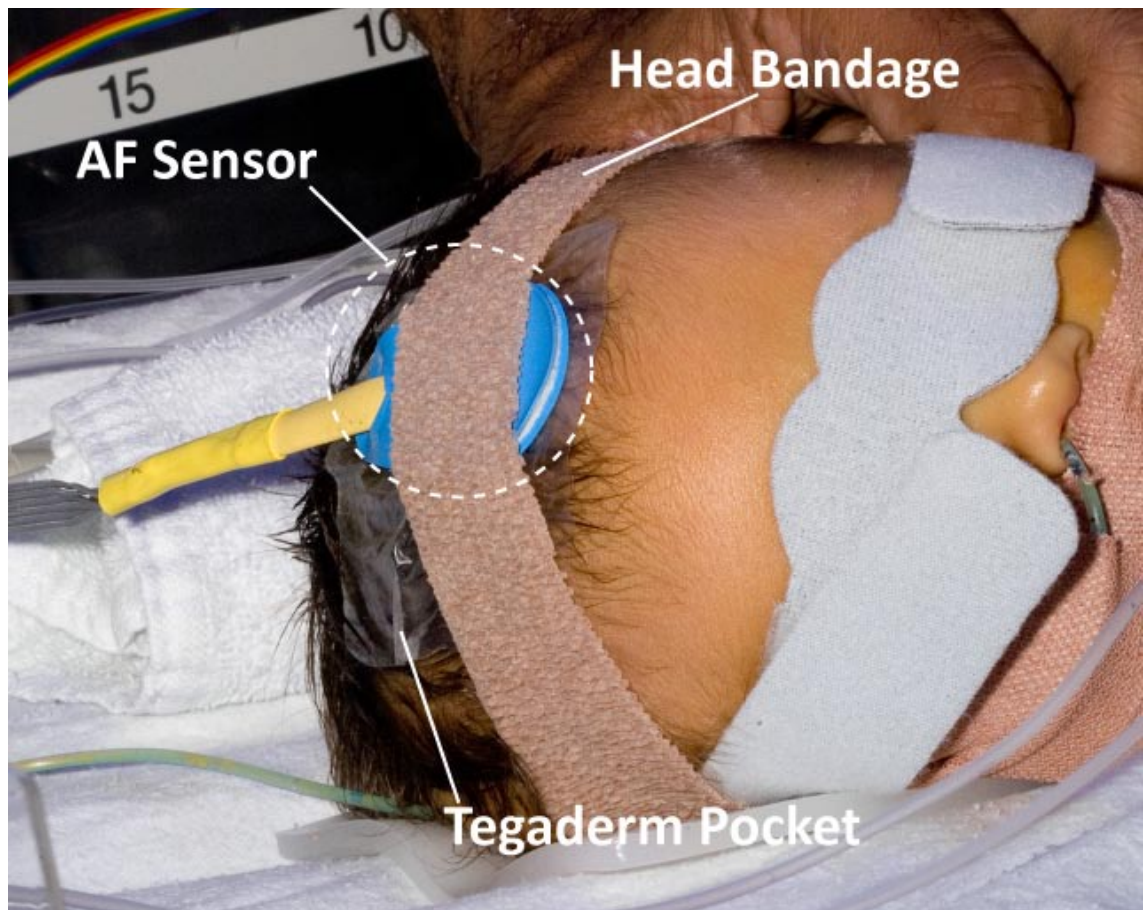


Figure 10.1: AF sensor in-situ, in sterile pocket and secured with a head bandage.

10.2 Anterior Fontanelle and Foot Photoplethysmographs

The raw data was inspected before post processing was applied. Figure 10.2 is an example of the raw PPG recording at all three wavelengths from the AF and foot sensors over the entire duration of a trial, with FiO_2 change time stamps depicted. The pre-normalised amplitudes (AC and DC) were calculated and are tabulated in Appendix F.

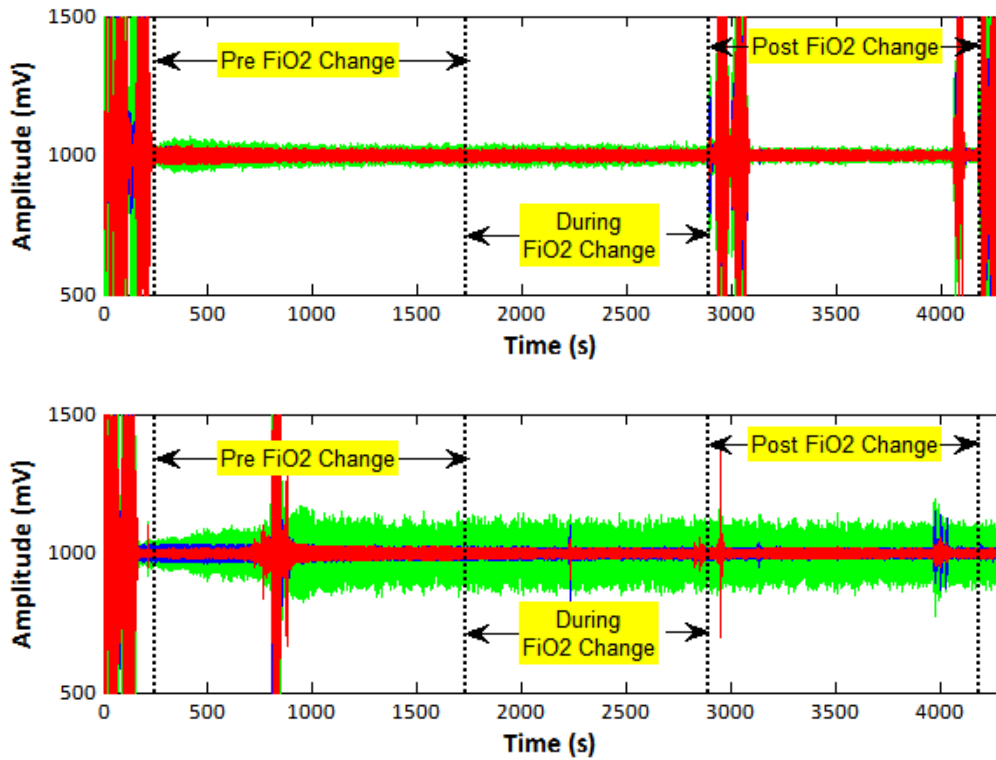


Figure 10.2: Full recording of AC PPG waveforms from the AF (Top) and Foot (Bottom) with Time stamp markings for FiO₂ Change (dotted horizontal lines).

Figures 10.3a – 10.3f illustrate typical AC PPGs from the AF fontanelle and reference sensor placed on the foot at all wavelengths during all three periods of monitoring.

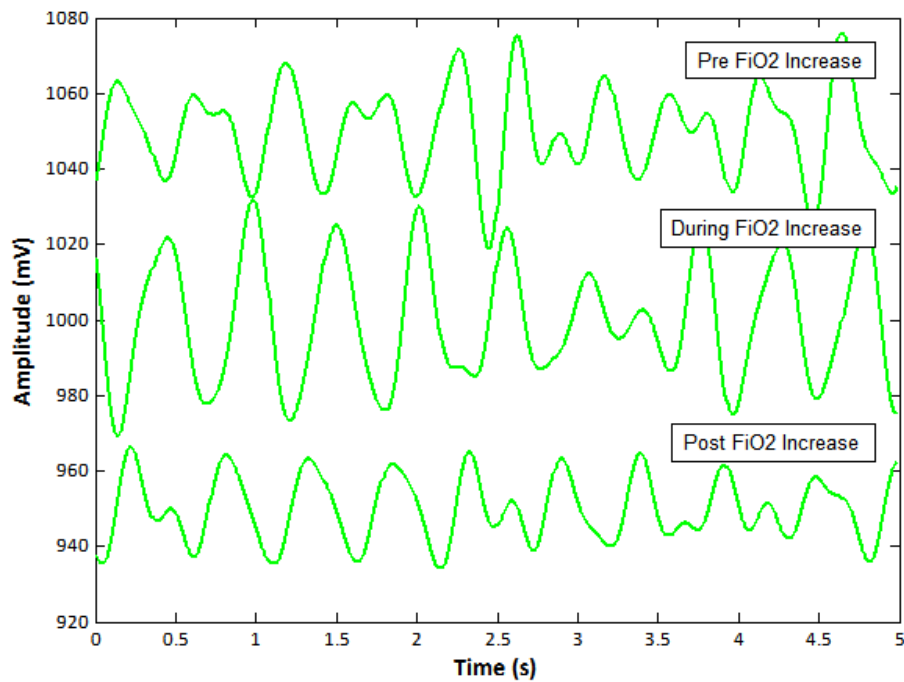


Figure 10.3a: Five second sample of green AF AC PPGs at the different monitoring periods

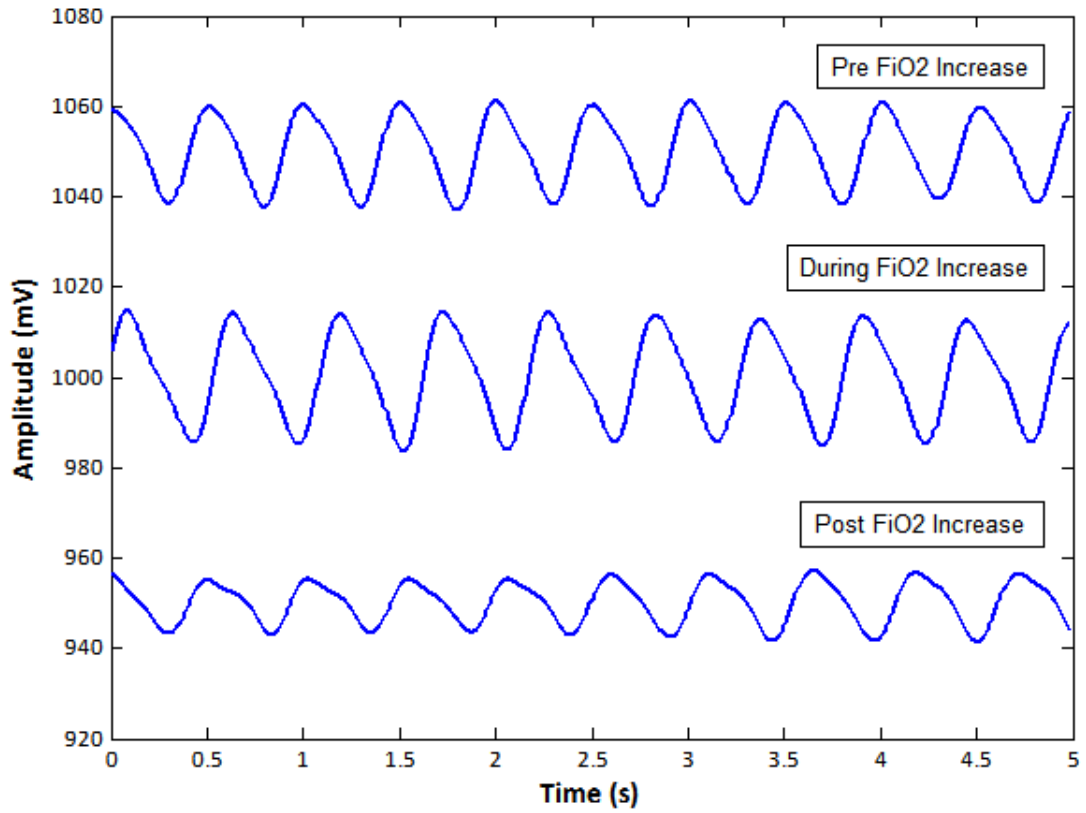


Figure 10.3b: Five second sample of infrared AF AC PPGs at the different monitoring periods

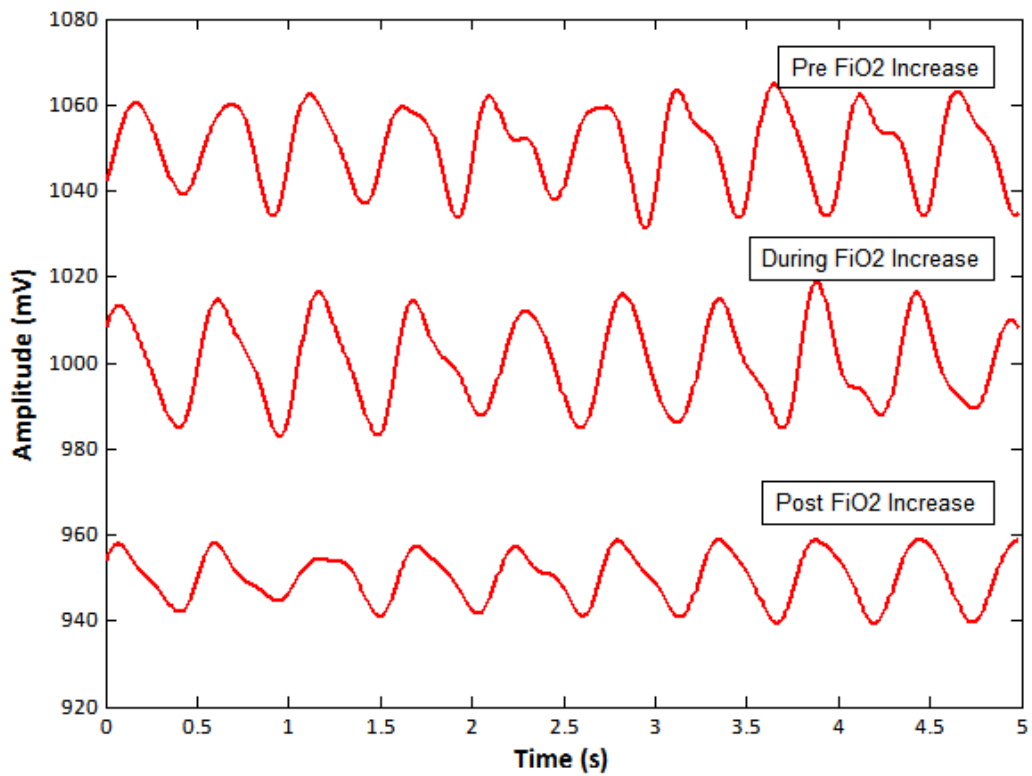


Figure 10.3c: Five second sample of red AF AC PPGs at the different monitoring periods

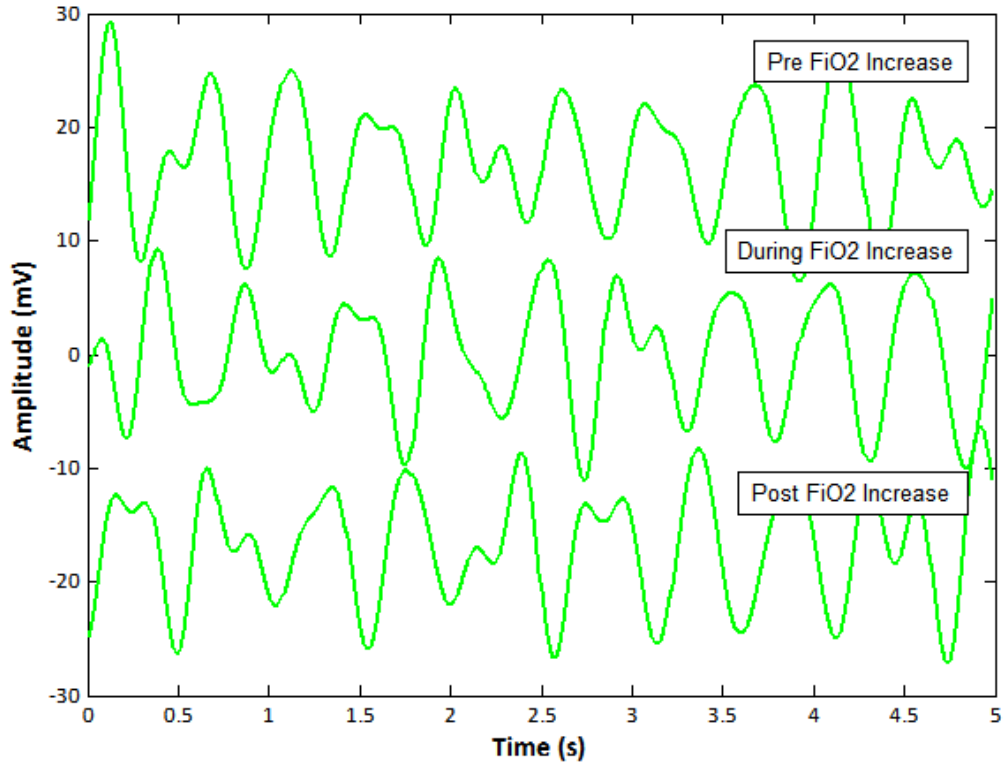


Figure 10.3d: Five second sample of green reference foot AC PPGs at the different monitoring periods

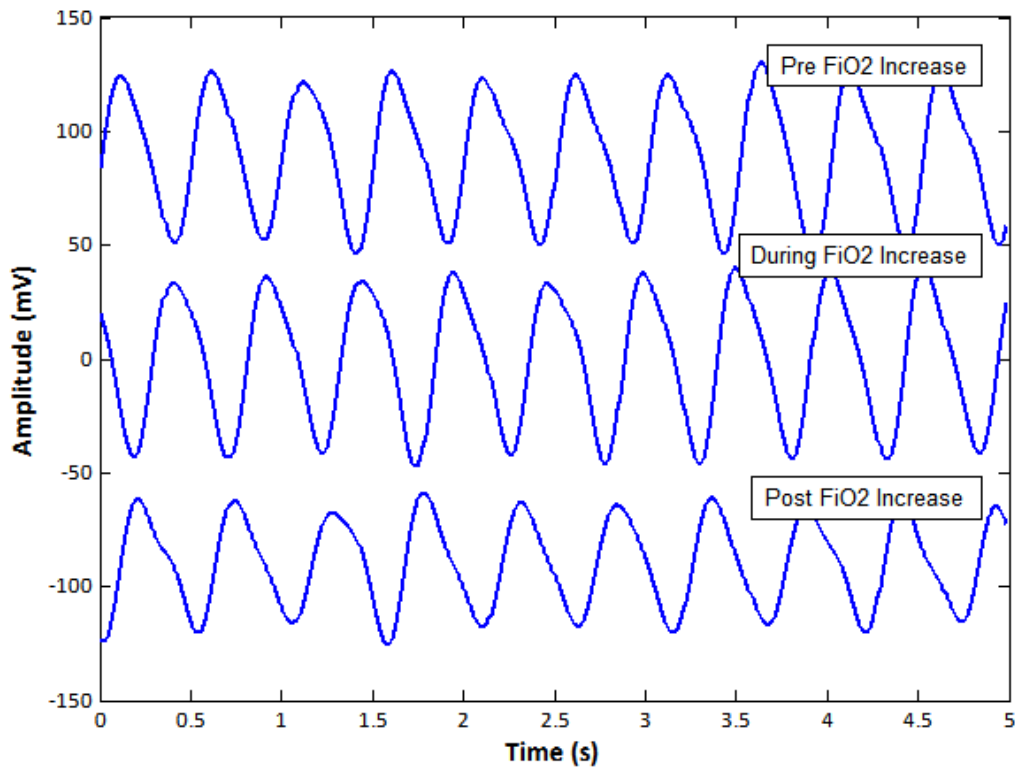


Figure 10.3e: Five second sample of infrared reference foot AC PPGs at the different monitoring periods

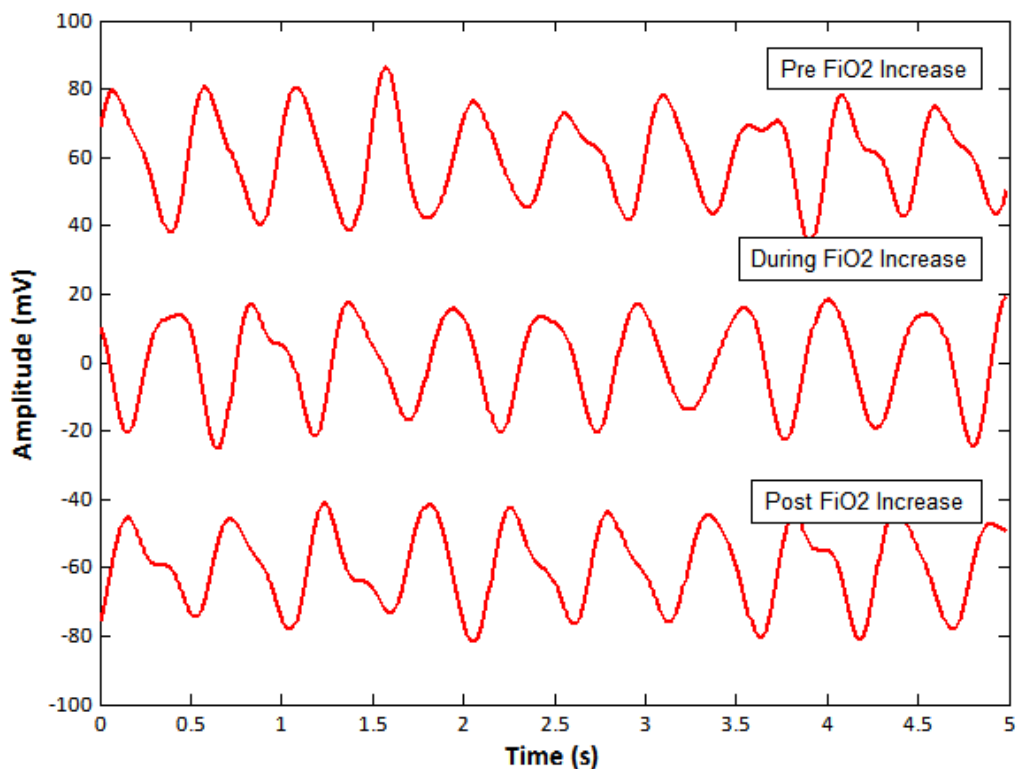


Figure 10.3f: Five second sample of red reference foot AC PPGs at the different monitoring periods

SigmaPlot (SYSTAT Software Inc, USA) was used to test the PPG amplitudes for normality (Kolmogorov-Smirnov Test) prior to any further statistical tests. The results from the normality test are tabulated in table 10.1.

Table 10.1 Kolmogorov-Smirnov normality test results (SigmaPlot, SYSTAT Software Inc)

Wavelength	Period	Sensor	AC Amplitudes		DC Amplitudes	
			p-score	Result	p-score	Result
660 nm RED	Pre FiO ₂	Foot AF	P = 0.064	Passed	P = 0.107	Passed
			P > 0.200	Passed	P = 0.199	Passed
	During FiO ₂	Foot AF	P = 0.057	Passed	P = 0.100	Passed
940 nm IR	Pre FiO ₂	Foot AF	P = 0.167	Passed	P = 0.098	Passed
			P > 0.200	Passed	P = 0.157	Passed
	Post FiO ₂	Foot AF	P > 0.200	Passed	P = 0.048	Failed
525 nm GREEN	Pre FiO ₂	Foot AF	P = 0.020	Failed	P > 0.200	Passed
			P = 0.124	Passed	P > 0.200	Passed
	During FiO ₂	Foot AF	P = 0.009	Failed	P > 0.200	Passed
525 nm GREEN	Pre FiO ₂	Foot AF	P > 0.200	Passed	P > 0.200	Passed
			P = 0.023	Failed	P = 0.149	Passed
	Post FiO ₂	Foot AF	P > 0.200	Passed	P > 0.200	Passed
525 nm GREEN	Pre FiO ₂	Foot AF	P = 0.006	Failed	P = 0.107	Passed
			P > 0.200	Passed	P > 0.200	Passed
	During FiO ₂	Foot AF	P = 0.163	Passed	P = 0.126	Passed
525 nm GREEN	Pre FiO ₂	Foot AF	P > 0.200	Passed	P = 0.093	Passed
			P > 0.200	Passed	P > 0.200	Passed
	Post FiO ₂	Foot AF	P > 0.200	Passed	P > 0.200	Passed

A two-tailed paired t-test was then performed to test whether or not the change in FiO₂ caused a significant change in the resulting AC or DC amplitudes between monitoring periods for each sensor (P < 0.05 was used as the limit at which FiO₂ was considered to have an effect on the PPG amplitudes). These results are shown in tables 10.2a – 10.2f, with highlighted significant results.

Table 10.2a: Paired t-test between periods on RED AC amplitudes from the AF sensor

Paired T-test	Pre FiO ₂ increase	During FiO ₂ increase	Post FiO ₂ increase
Pre FiO ₂ increase	-	0.643	0.677
During FiO ₂ increase	0.643	-	0.355
Post FiO ₂ increase	0.677	0.355	-

Table 10.2b: Paired t-test between periods on RED DC amplitudes from the AF sensor

Paired T-test	Pre FiO ₂ increase	During FiO ₂ increase	Post FiO ₂ increase
Pre FiO ₂ increase	-	0.014	0.977
During FiO ₂ increase	0.014	-	0.425
Post FiO ₂ increase	0.977	0.425	-

Table 10.2c: Paired t-test between periods on IR AC amplitudes from the AF sensor

Paired T-test	Pre FiO ₂ increase	During FiO ₂ increase	Post FiO ₂ increase
Pre FiO ₂ increase	-	0.225	0.761
During FiO ₂ increase	0.225	-	0.305
Post FiO ₂ increase	0.761	0.305	-

Table 10.2d: Paired t-test between periods on IR DC amplitudes from the AF sensor

Paired T-test	Pre FiO ₂ increase	During FiO ₂ increase	Post FiO ₂ increase
Pre FiO ₂ increase	-	0.031	0.139
During FiO ₂ increase	0.031	-	0.884
Post FiO ₂ increase	0.139	0.884	-

Table 10.2e: Paired t-test between periods on GREEN AC amplitudes from the AF sensor

Paired T-test	Pre FiO ₂ increase	During FiO ₂ increase	Post FiO ₂ increase
Pre FiO ₂ increase	-	0.191	0.352
During FiO ₂ increase	0.191	-	0.136
Post FiO ₂ increase	0.352	0.136	-

Table 10.2f: Paired t-test between periods on GREEN DC amplitudes from the AF sensor

Paired T-test	Pre FiO ₂ increase	During FiO ₂ increase	Post FiO ₂ increase
Pre FiO ₂ increase	-	0.871	0.407
During FiO ₂ increase	0.871	-	0.484
Post FiO ₂ increase	0.407	0.484	-

Table 10.2g: Paired t-test between periods on RED AC amplitudes from the FOOT sensor

Paired T-test	Pre FiO ₂ increase	During FiO ₂ increase	Post FiO ₂ increase
Pre FiO ₂ increase	-	0.355	0.694
During FiO ₂ increase	0.355	-	0.442
Post FiO ₂ increase	0.694	0.442	-

Table 10.2h: Paired t-test between periods on RED DC amplitudes from the FOOT sensor

Paired T-test	Pre FiO ₂ increase	During FiO ₂ increase	Post FiO ₂ increase
Pre FiO ₂ increase	-	0.003	0.033
During FiO ₂ increase	0.003	-	0.576
Post FiO ₂ increase	0.033	0.576	-

Table 10.2i: Paired t-test between periods on IR AC amplitudes from the FOOT sensor

Paired T-test	Pre FiO ₂ increase	During FiO ₂ increase	Post FiO ₂ increase
Pre FiO ₂ increase	-	0.661	0.921
During FiO ₂ increase	0.661	-	0.912
Post FiO ₂ increase	0.921	0.912	-

Table 10.2j: Paired t-test between periods on IR DC amplitudes from the FOOT sensor

Paired T-test	Pre FiO ₂ increase	During FiO ₂ increase	Post FiO ₂ increase
Pre FiO ₂ increase	-	0.256	0.244
During FiO ₂ increase	0.256	-	0.309
Post FiO ₂ increase	0.244	0.309	-

Table 10.2k: Paired t-test between periods on GREEN AC amplitudes from the FOOT sensor

Paired T-test	Pre FiO ₂ increase	During FiO ₂ increase	Post FiO ₂ increase
Pre FiO ₂ increase	-	0.802	0.482
During FiO ₂ increase	0.802	-	0.355
Post FiO ₂ increase	0.482	0.355	-

Table 10.2l: Paired t-test between periods on GREEN DC amplitudes from the FOOT sensor

Paired T-test	Pre FiO ₂ increase	During FiO ₂ increase	Post FiO ₂ increase
Pre FiO ₂ increase	-	0.943	0.643
During FiO ₂ increase	0.943	-	0.124
Post FiO ₂ increase	0.643	0.124	-

10.3 Fontanelle and Foot PPG Normalised Amplitude Analysis

The methods of filtering and normalisation described chapter 9 section 9.1 – 9.2 were applied to the raw signals. Amplitudes were calculated by the method described in section 9.3 (Chapter 9), and erroneous readings identified and removed from further calculations by the method given in section 9.5 (Chapter 9). Figures 10.4a 10.4c are examples of

normalised amplitude traces across the three monitoring periods for the three wavelengths from the AF sensor.

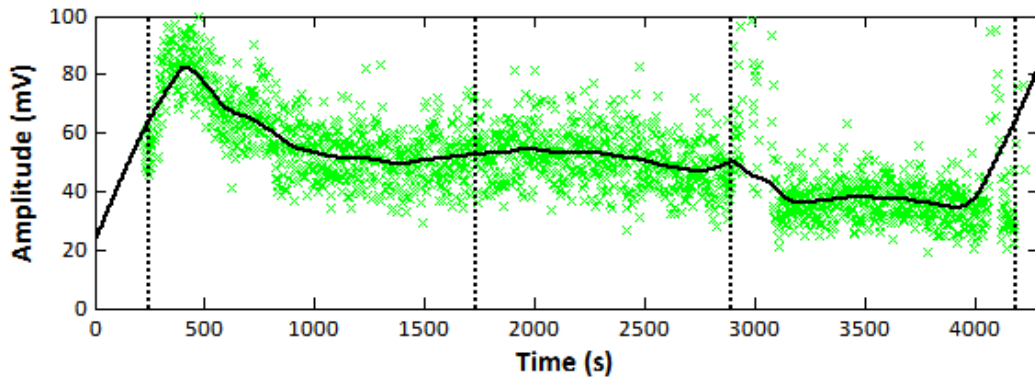


Figure 10.4a: Normalised amplitude measurements from the AF sensor for the Green PPGs.

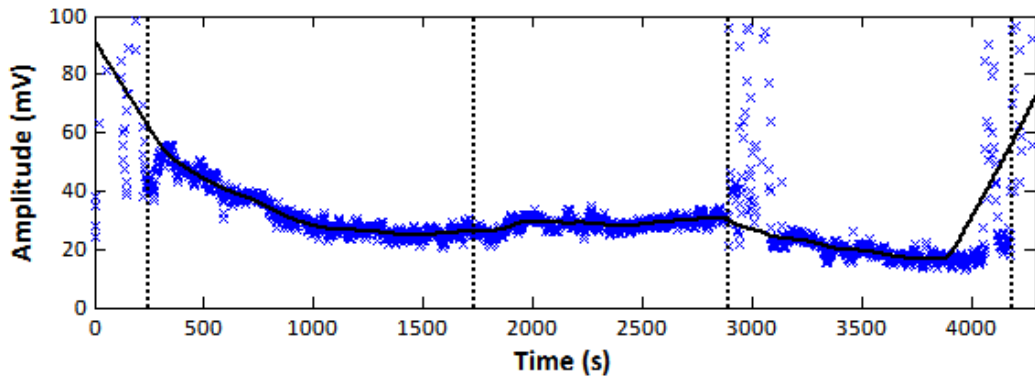


Figure 10.4b: Normalised amplitude measurements from the AF sensor for the Infrared PPGs.

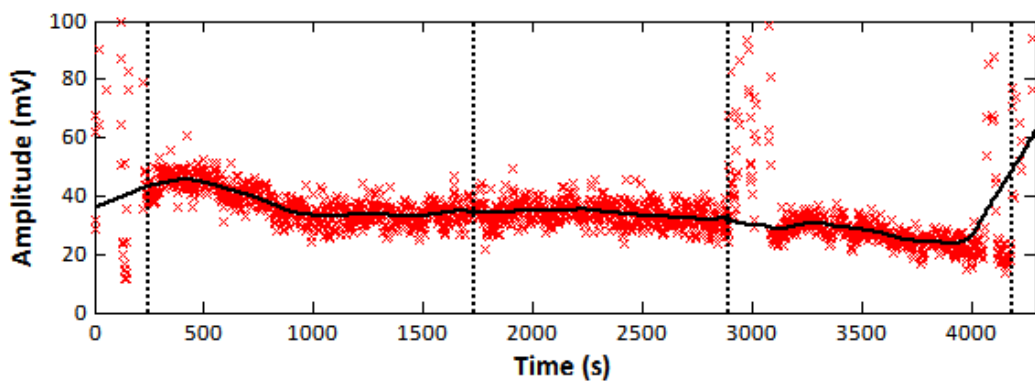


Figure 10.4c: Normalised amplitude measurements from the AF sensor for the RED PPGs.

From the sixteen clinical trials 1 case (Patient #3) failed to yield adequate PPGs from the AF for any length of time, and has been completely omitted from the following results. The clinician’s observation about the AF noted that it was “smaller than usual” and may have been the contributing factor to the failure, and it was noted by the researcher that

although infrared signals from the AF were seen, because the red signals failed the trial was aborted as the primary goal of the experiment is to assess PPGs for the estimation of SpO₂; Two cases (Patient #4 and #16) were receiving an FiO₂ of 100 %, and hence there was no FiO₂ increase or decrease, a further 2 cases posed technical difficulties where the trial procedure was interrupted and only partially completed (Patients #12 and #15).

Four patients (#5, #7, #10 and #13) exhibited green PPGs from the AF, and only three of those (#5, #7 and #13) had green PPG traces across all three monitoring periods. This will be discussed in the final chapter *Discussions, Conclusions and Future Work*.

Amplitude analysis was conducted for each wavelength separately and individually for each sensor and during the three monitoring periods specified in the protocol, (Pre-FiO₂ increase, During-FiO₂ increase and Post-FiO₂ increase). Figure 10.4a – 10.4c are normalised PPG traces from the AF from one individual at the three wavelengths at the different monitoring periods. The normalised amplitude results for all patients are shown in tables 10.3a – 10.3c, and displayed as a bar-graph in figures 10.5 and 10.6.

A statistical test to explore the correlation (R) of age and weight (Appendix G) against the mean amplitudes for each patient was performed and is shown in table 10.4.

Table 10.3a: Mean red (660 nm) normalised AC (heart rate frequency) amplitudes.

Patient #	RED Normalised Amplitudes (mV)					
	Pre FiO ₂ increase		During FiO ₂ increase		Post FiO ₂ increase	
	Foot	AF	Foot	AF	Foot	AF
1	122.7	66.8	115.8	74.3	110.8	87.0
2	48.9	33.8	35.1	29.5	38.9	22.2
4	25.9	30.6				
5	142.6	36.2	122.6	35.9	125.1	30.4
6	143.5	29.7	90.2	36.9	92.3	31.8
7	38.8	33.6	25.5	33.8	23.7	25.8
8	17.5	27.0	16.5	36.5	26.5	33.7
9	53.5	29.4	22.6	29.4	39.5	22.6
10	137.4	34.4	119.6	29.0	83.9	31.2
11	156.8	50.3	131.3	52.5	122.0	51.6
12	16.5	19.8	18.1	27.8		
13	14.9	24.7	17.1	16.7	13.7	16.5
14	156.5	40.8	196.6	28.1	259.2	38.2
15	217.0	17.5				
16	65.5	10.0				
Mean	90.5	32.3	75.9	35.9	85.0	35.6
SD	65.8	13.6	61.0	14.7	71.0	19.4
Measurements (n)	15	15	12	12	11	11

Table 10.3b: Mean infrared (940 nm) normalised AC (heart rate frequency) amplitudes.

Patient #	IR Normalised Amplitudes (mV)					
	Pre FiO ₂ increase		During FiO ₂ increase		Post FiO ₂ increase	
	Foot	AF	Foot	AF	Foot	AF
1	49.9	96.2	47.5	140.2	45.7	166.9
2	87.7	100.0	82.3	77.2	73.0	77.2
4	25.3	43.1				
5	271.7	152.4	252.1	135.8	241.3	117.4
6	224.8	24.3	180.6	25.4	149.0	22.0
7	37.4	26.3	29.4	29.0	25.6	22.6
8	21.1	36.5	25.4	50.1	31.6	51.5
9	58.9	56.0	56.1	35.2	60.1	34.0
10	316.4	91.8	325.2	58.2	188.1	64.6
11	174.7	99.6	175.7	122.1	155.2	101.3
12	23.8	39.8	27.1	38.0		
13	35.4	50.7	38.3	43.0	31.9	38.7
14	211.0	46.1	257.1	49.8	305.2	77.1
15	190.3	37.4				
16	127.8	17.1				
Mean	123.7	61.1	124.7	67.0	118.8	70.3
SD	100.1	38.1	107.9	42.1	95.7	44.6
Measurements (n)	15	15	12	12	11	11

Table 10.3c: Mean green (525 nm) normalised AC (heart rate frequency) amplitude

Patient #	GREEN Normalised Amplitudes (mV)					
	Pre FiO ₂ increase		During FiO ₂ increase		Post FiO ₂ increase	
	Foot	Font	Foot	Font	Foot	Font
1	369.7		345.3		333.2	
2	54.1		52.9		45.9	
4	49.9					
5	563.0	104.4	552.9	97.8	570.7	90.9
6	603.9		569.9		581.5	
7	161.9	51.9	144.8	51.2	126.5	38.5
8	37.1		48.0		58.2	
9	70.1		51.6		61.1	
10	495.4	125.4	393.1		239.0	
11	390.3		390.9		350.2	
12	154.9		180.2			
13	39.7	98.5	51.3	65.3	38.5	74.7
14	627.8		809.8		889.7	
15	627.4					
16	50.3					
Mean	286.4	95.0	299.2	71.5	299.5	68.0
SD	244.9	31.0	252.7	23.9	280.4	26.8
Measurements (n)	15	4	12	3	11	3

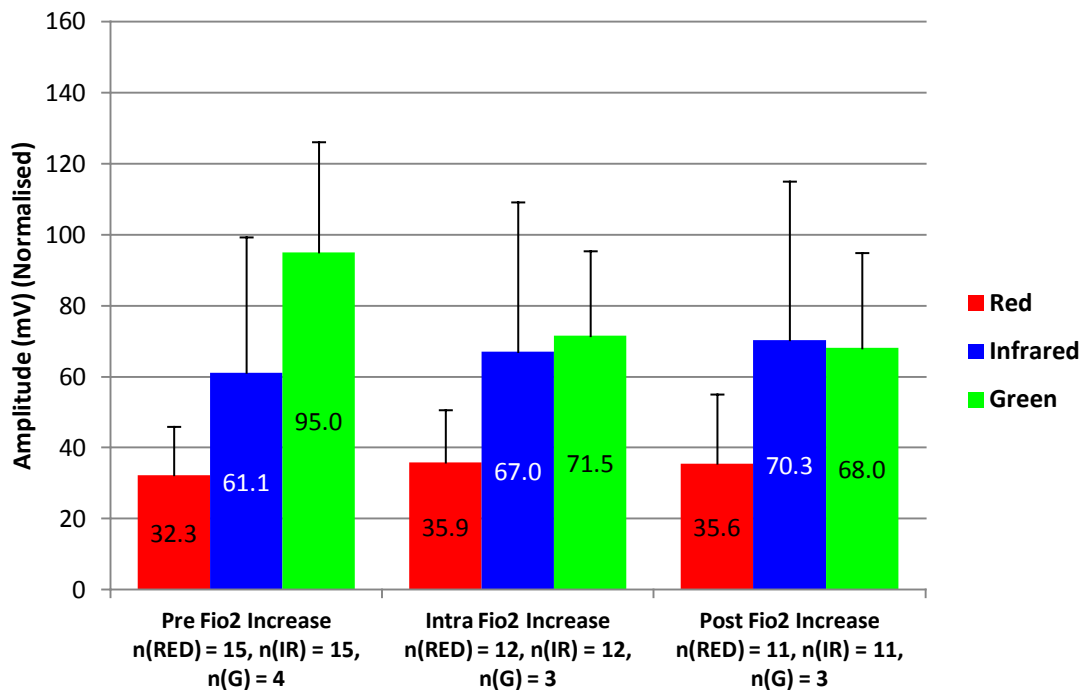


Figure 10.5: Bar-graph of mean fontanelle AC PPG amplitudes across all three monitoring periods.

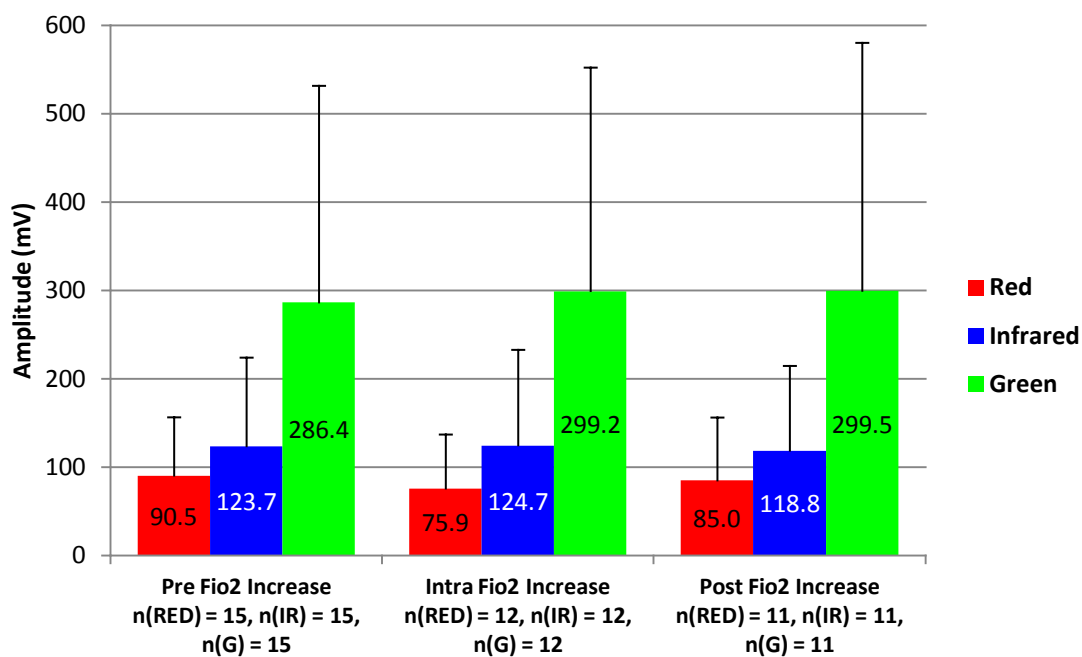


Figure 10.6: Bar-graph of mean foot AC PPG amplitudes across all three monitoring periods.

Table 10.4: Correlation results of normalised amplitudes with age and weight

Correlation (R)	Mean Normalised Amplitude					
	RED Foot	RED AF	IR Foot	IR AF	GR Foot	GR AF
Age	0.02	0.16	0.14	0.25	-0.13	0.81
Weight	0.24	0.25	0.15	0.44	0.18	0.97

The mean values for the individual wavelengths of both sensors were correlated against one another to look at the overall relationship of amplitudes between the foot and the AF, the results are displayed in table 10.5.

Table 10.5: Correlation results for FiO₂ change between the foot and AF sensors.

Period	Mean Normalised Amplitudes (mV)					
	RED (660 nm)		IR (940 nm)		GR (525 nm)	
	Foot	AF	Foot	AF	Foot	AF
Pre FiO ₂	90.5	32.3	123.7	61.1	286.4	95.0
During FiO ₂	75.9	35.9	124.7	67.0	299.2	71.5
Post FiO ₂	85.0	35.6	118.8	70.3	299.5	68.0
Correlation (R)	-0.833		-0.669		-0.995	

Finally an analysis was performed to search for a trend in PPG amplitudes against the relative health of the patient, assessed by the patient’s individual ASA score (Appendix G). This was done by computing the difference between foot and AF PPGs at each wavelength and at each monitoring period, then plotting the results against the relative ASA score (1 – 3). The tabulated results are displayed in table 10.6 and illustrated in figures 10.7 – 10.9.

Table 10.6: Amplitude differences vs ASA scores

#	ASA	Amplitude Difference (AF - Foot) (mV)								
		Pre FiO ₂ increase			During FiO ₂ increase			Post FiO ₂ increase		
		RED	IR	GR	RED	IR	GR	RED	IR	GR
1	2	-55.9	46.3		-41.5	92.7		-23.8	121.2	
2	3	-15.1	12.3		-5.6	-5.1		-16.7	4.2	
4	3	4.7	17.8							
5	1	-106.4	-119.3	-458.6	-86.7	-116.3	-455.1	-94.7	-123.9	-479.8
6	2	-113.8	-200.5		-53.3	-155.2		-60.5	-127.0	
7	2	-5.2	-11.1	-110.0	8.3	-0.4	-93.6	2.1	-3.0	-88.0
8	3	9.5	15.4		20	24.7		7.2	19.9	
9	2	-24.1	-2.9		6.8	-20.9		-16.9	-26.1	
10	1	-103	-224.6	-370.0	-90.6	-267		-52.7	-123.5	
11	1	-106.5	-75.1		-78.8	-53.6		-70.4	-53.9	
12	2	3.3	16.0		9.7	10.9				
13	2	9.8	15.3	58.8	-0.4	4.7	14.0	2.8	6.8	36.2
14	1	-115.7	-164.9		-168.5	-207.3		-221	-228.1	
15	2	-199.5	-152.9							
16	2	-55.5	-110.7							
n		15	15	4	12	12	3	11	11	4

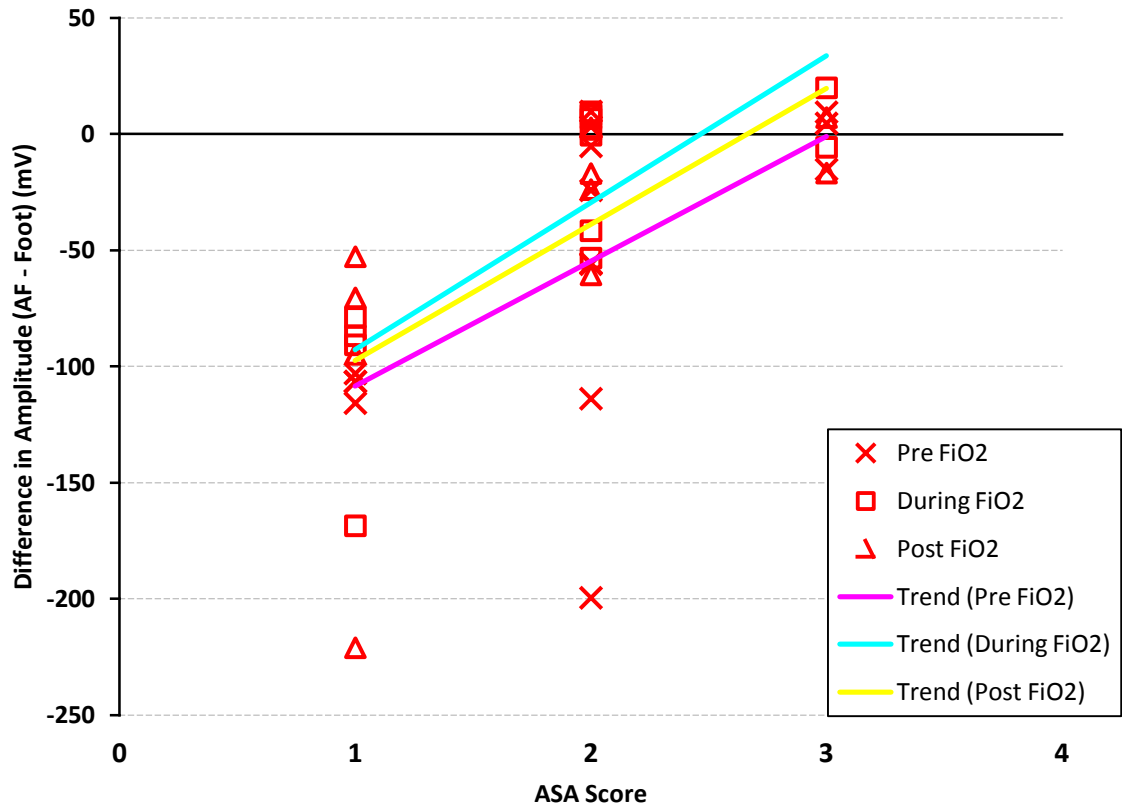


Figure 10.7: Mean RED normalised PPG amplitude vs ASA score.

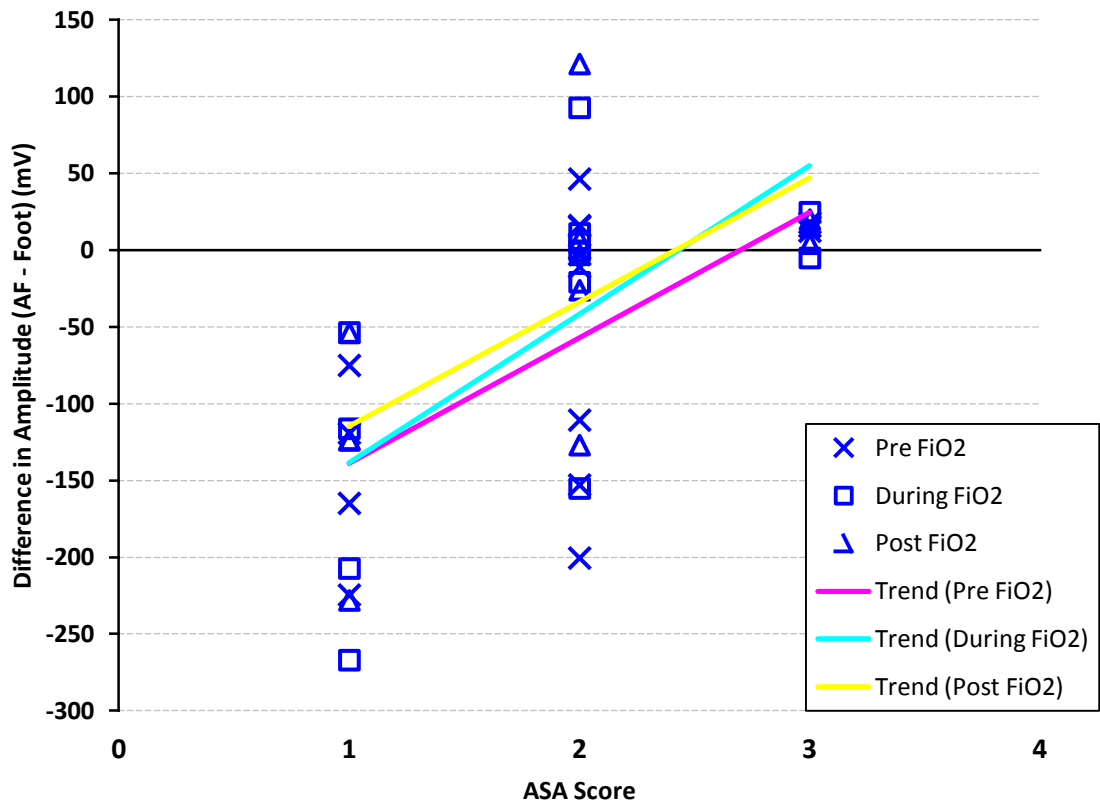


Figure 10.8: Mean IR normalised PPG amplitudes vs ASA score.

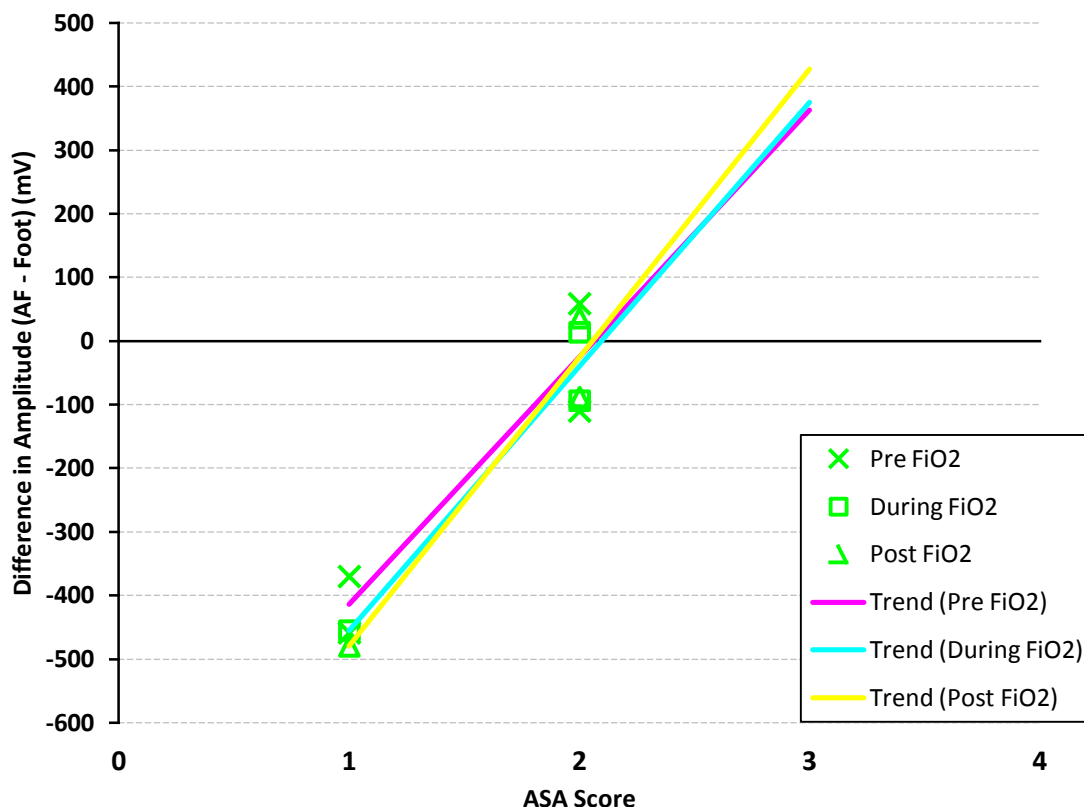


Figure 10.9: Mean GREEN normalised PPG amplitudes vs ASA score.

Correlation between the ASA score and the difference in amplitudes was calculated and is tabulated in table 10.7.

Table 10.7: Correlation (R) of amplitude differences and ASA scores.

Correlation (R)								
Pre FiO ₂ increase			During FiO ₂ increase			Post FiO ₂ increase		
RED	IR	GREEN	RED	IR	GREEN	RED	IR	GREEN
0.599	0.627	0.945	0.792	0.653	0.976	0.668	0.635	0.973
n = 15	n = 15	n = 4	n = 12	n = 12	n = 3	n = 11	n = 11	n = 3

10.4 Amplitude Analysis Summary

Initial results indicate a strong correlation between sensors at times of known oxygen concentration change; suggesting that PPG monitoring from the AF may be a viable option to calculate SpO₂. What effect the negativity of the correlation has on the calculated SpO₂ values is the subject of the next chapter, although since SpO₂ calculation is essentially a derivative process (Chapter 9, section 9.4) the expected outcome for SpO₂ calculation

would also be expected to be a negative correlation between the foot and AF, to what degree this affects the accuracy of SpO₂ calculation when compared to the commercial devices and gold standard values from blood gas analysis is also covered in the next chapter.

Tests for normality in section 10.2 reveal that the amplitude analysis data fits normal distributions for most samples, where the tests fail the deviation from the normal was very small, for this reason a parametric test method, paired t-test, was used to look for significant differences between monitoring periods, as opposed to a non-parametric method. However it is observed that although a visible change in the amplitudes of PPGs can be directly observed (as in figures 10.3a – 10.3c), the paired t-test does not always reveal a significant change ($P < 0.05$). The significant changes (according to the paired t-test) are observed from the DC portion of the signal, and only at the red and infrared wavelengths.

Correlation of PPG amplitudes with the age and size (weight) of the patient reveals relatively little correlation with only weak to medium positive correlation at best. Other factors affecting the observed PPGs may be a contributor and will be discussed in *Chapter 13 - Discussions, Conclusions and Future Work*.

The final analysis of differences in amplitudes versus the ASA score for each patient was designed in an attempt to reveal that the sickest of patients (i.e. those more at risk of peripheral supply compromise) would have smaller normalised peripheral PPG amplitudes than those who are assessed to be in a healthier condition. In other words as the relative health of the patient diminishes (ASA score increases) then the AF sensor detects increasing normalised PPG amplitudes when compared to the peripheral sensor amplitude. At the point of peripheral supply compromise the AF sensor therefore should still be able to detect the AC PPG. The results obtained do indeed show an increase in amplitude difference with increasing ASA score for all wavelengths, and the correlation results are positively strong to very strong ($R > 0.5$), supporting this assumption.

Chapter Eleven

Anterior Fontanelle and Foot SpO₂ Analysis

Chapter ten presented the analysis of raw PPG waveforms from the anterior fontanelle (AF) and a reference sensor placed on the foot of the neonate. Analysis revealed that changes in blood oxygen saturation (SpO₂), artificially brought about by changing delivered oxygen concentration (FiO₂), correlated strongly with changes in the amplitude of the raw PPG waveforms. This suggests that the PPG waveforms at the AF may well be suitable for SpO₂ monitoring. To test this hypothesis the normalised amplitudes from the AF and the foot, calculated in the previous chapter, have been utilised in the estimation of SpO₂ and compared against the actual SpO₂ values from a commercial monitor (Com) (Philips Intelliview with HP Merlin Sensors and Modules, Netherlands). Comparison with blood gas analysis arterial oxygen saturation (SaO₂) (Abbott POC i-STAT Handheld, NJ, USA) has also been made.

11.1 Estimation of SpO₂ during FiO₂ increase and decrease.

SpO₂ has been calculated using the method described in section 9.4 (Chapter 9). To make a comparison with actual SpO₂ readings, as recorded by the clinical monitors, time stamps were marked into the raw data files using the time stamping function of the virtual instrument (VI) across all trials, coinciding with specific clinical events and/or observations (e.g. feeding, drug administration and readings from clinical monitors). These values were then compared against the computed SpO₂ values. Figure 11.1 shows an example from one patient of the SpO₂ values from the commercial monitor against those computed from the custom sensors.

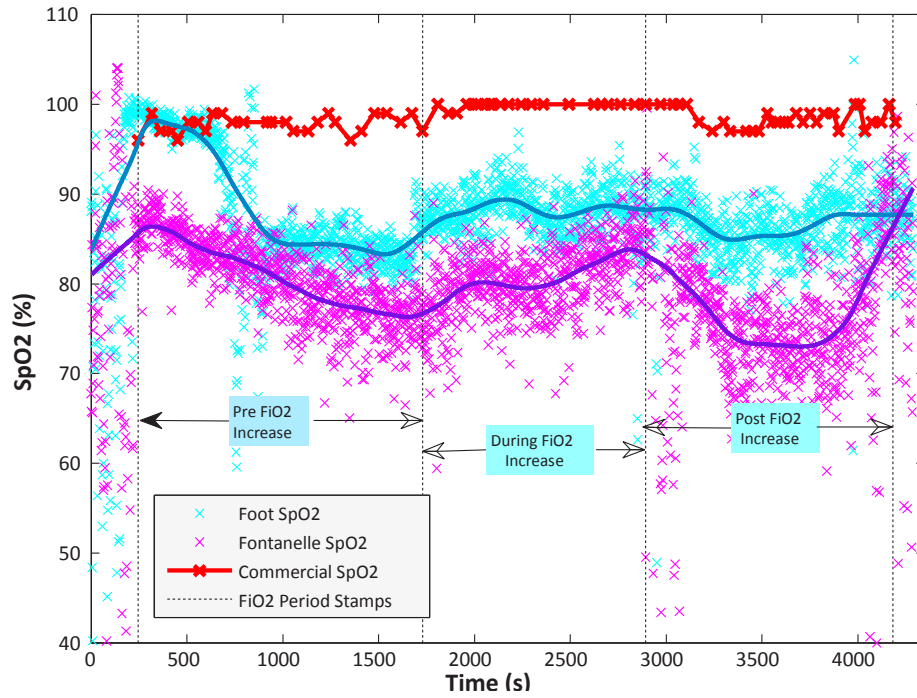


Figure 11.1: Custom SpO₂ sensor readings against commercial sensor readings from one patient with trend-lines during FiO₂ change. Commercial SpO₂ time stamps (n) = 78.

The method described in section 9.5 (chapter 9) was utilised to eliminate unwanted SpO₂ values from 759 recorded time stamps. Mean and standard deviation was computed for each period for each sensor and is tabulated in table 11.1. Figure 11.2 is a bar-graph of this data.

Table 11.1: Mean SpO₂ Values in each period for each patient

#	SpO ₂ (%)								
	Pre FiO ₂ increase			During FiO ₂ increase			Post FiO ₂ increase		
	Foot	AF	Com	Foot	AF	Com	Foot	AF	Com
1	98.5	92.6	100.0	99.1	96.8	100.0	99.4	97.0	99.3
2	96.1	101.6	95.0	99.3	100.5	98.5	96.7	102.8	93.5
4	84.4	92.3	77.6	-	-	95.8	-	-	-
5	96.9	104.1	93.2	97.8	103.4	98.7	97.0	103.5	95.6
6	94.0	79.5	96.7	97.5	73.7	99.8	94.5	73.9	96.3
7	84.0	78.1	97.9	88.4	80.9	99.1	86.9	81.4	98.5
8	89.3	91.5	96.5	93.8	91.8	98.1	89.1	93.6	97.6
9	87.3	96.9	99.1	99.9	89.1	99.8	93.5	93.4	99.3
10	99.1	100.6	99.6	100.8	97.5	96.5	98.9	97.9	99.9
11	87.6	97.4	91.6	91.3	99.2	98.5	90.4	97.3	93.0
12	92.7	97.6	98.2	93.3	91.7	100.0	-	-	-
13	99.4	97.8	100.0	98.8	100.3	100.0	99.3	99.4	99.9
14	91.4	87.8	100.0	90.9	95.9	95.8	88.8	97.6	98.6
15	81.5	98.3	98.0	-	-	-	-	-	-
16	97.2	95.5	93.7	-	-	-	-	-	-
Mean	92.0	94.1	95.8	95.9	93.4	98.7	94.0	94.3	97.4
SD	12.5	7.5	5.7	14.0	8.7	1.4	14.0	9.0	2.5
n	15	15	15	12	12	12	11	11	11

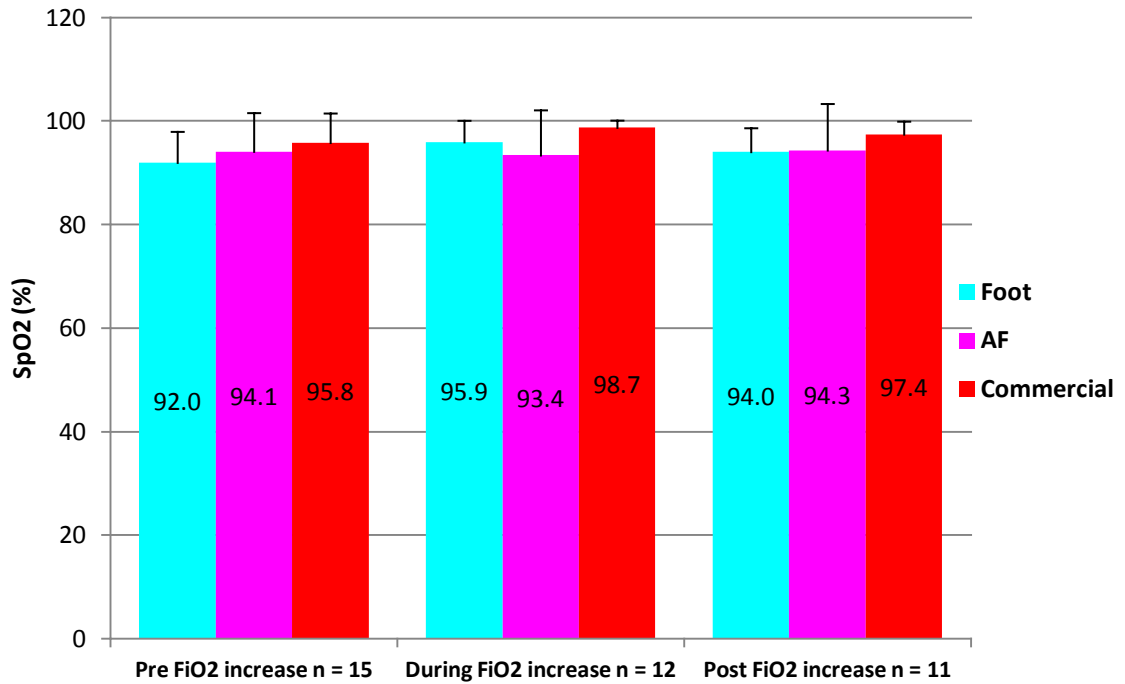


Figure 11.2: Mean bar-graph of SpO₂ change across the three monitoring periods for the three different sensors.

These values were then correlated with each other to look for similar trends (table 11.2).

Table 11.2: Correlation of SpO₂ values of the three sensors, computed with SpO₂ values from the mean values at each period (pre, during and post FiO₂ increase).

Correlation (R)	AF	Foot	Commercial
AF	-	-0.731	-0.696
Foot	-0.731	-	0.999
Commercial	-0.696	0.999	-

11.2 Fontanelle SpO₂ compared to Blood Gas SaO₂ Readings.

From the examination of the 759 time stamps taken, a total of 26 arterial blood tests were conducted as part of routine clinical procedure, including the 15 tests used to time the start of the trial. The time the blood was drawn from the arterial cannula it was marked into the raw data file via the time stamping function of the data-acquisition VI. These time stamps were then matched against the corresponding commercial SpO₂ reading and the SpO₂ reading calculated from the foot and AF at those times.

A linear regression scatter plot has been constructed from the blood gas analysis versus the various SpO₂ sensor data and is shown in figure 11.3.

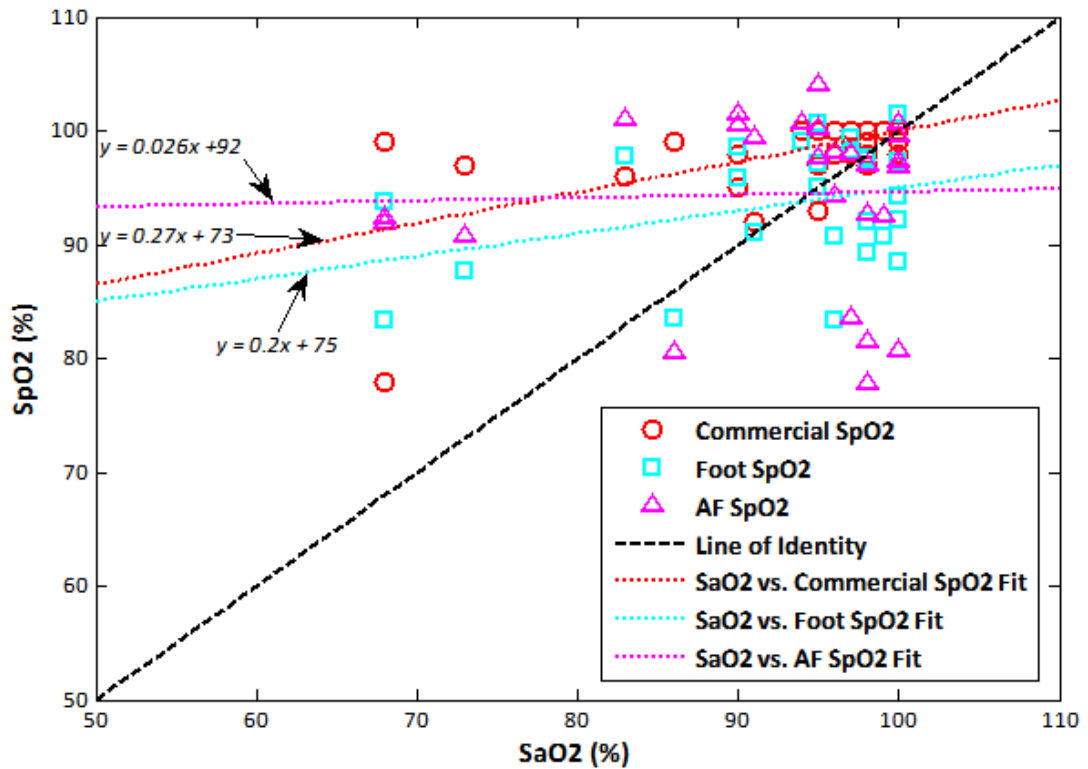


Figure 11.3: Linear regression scatter plot of blood gas analysis (x-axis) versus the various SpO₂ sensors (y-axis), $n = 26$.

The Linear regression analysis is a good indicator of how well one method agrees with another method, where the ideal agreement lies along the line of identity, i.e. where measurement $x =$ measurement y . The Bland and Altman test for accuracy between two different measurement techniques (Bland and Altman, 1986), or “differences-between-methods” has been utilised to help identify the relative accuracy of these three measurements. Commercial SpO₂, reference foot SpO₂ and AF SpO₂ have all been individually compared with the 26 blood gas samples taken. Figures 11.4 – 11.6 are the three sensors comparison with the blood gas test results.

The “gold standard” blood gas test values have been plotted in figure 11.7 as a distribution on a histogram against a normal distribution curve and a measurement of the skewness. This was done to investigate the normality of the SaO₂ values, and to compare later on the distribution of SpO₂ values computed using the custom sensors.

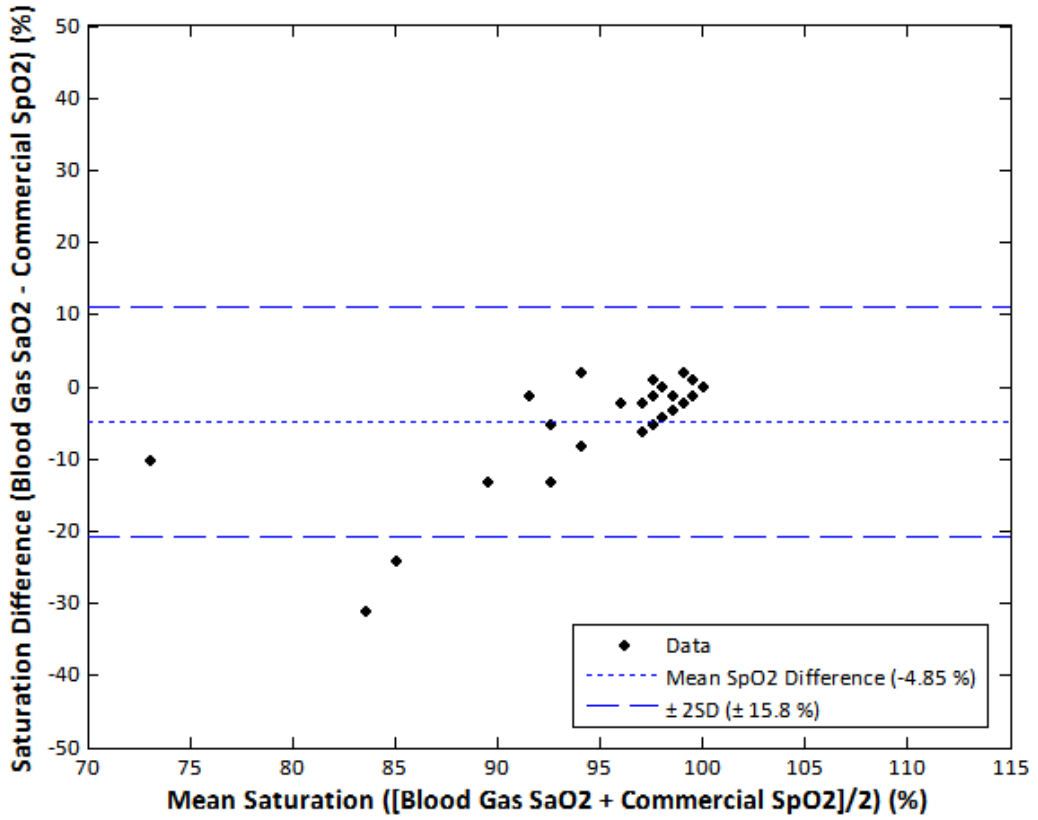


Figure 11.4: Blood Gas SaO₂ verses Commercial SpO₂ readings.

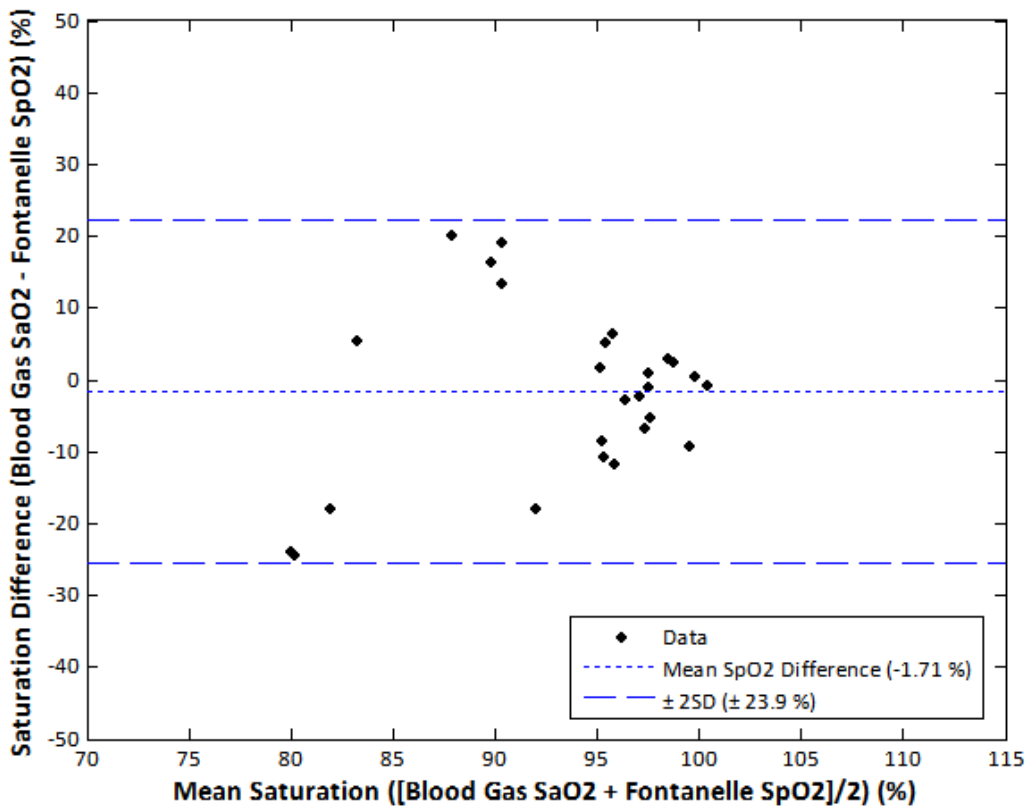


Figure 11.5: Blood Gas SaO₂ verses AF SpO₂ readings.

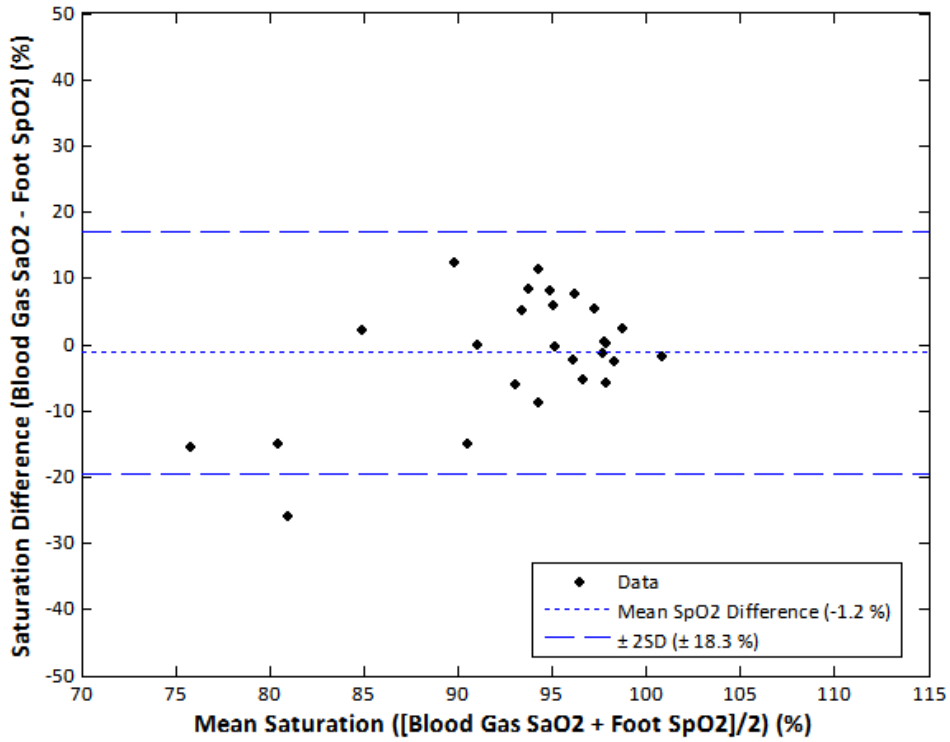


Figure 11.6: Blood Gas SaO₂ versus Foot SpO₂ readings.

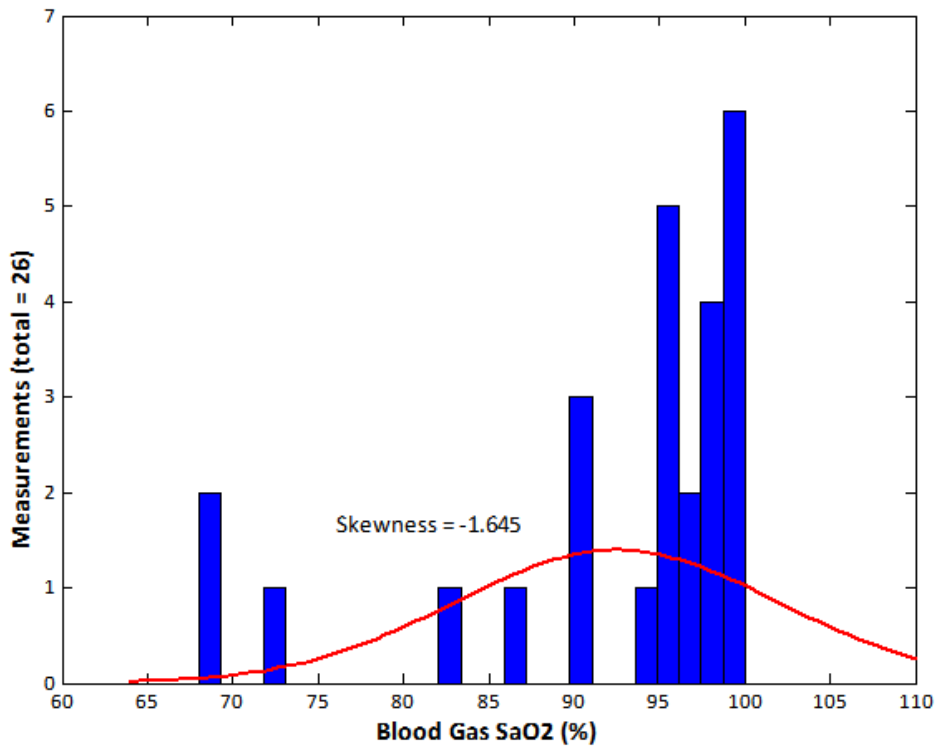


Figure 11.7: Histogram of blood gas SaO₂ readings with superimposed normal distribution function (mean = 92.5 %) with skewness measurement.

11.3 Anterior Fontanelle SpO₂ compared to Reference Foot and Commercial SpO₂ Sensors.

After the elimination process described in section 9.5 (Chapter 9) the 759 time stamps revealed 621 time stamps suitable for SpO₂ comparison. A second difference-between-methods analysis has been carried out to compare the three SpO₂ sensors used in the trial (figure 11.8 – 11.10).

The last three figures (figure 11.11 – 11.13) are histogram distributions of the measured SpO₂ values (621 values) from the three monitors with their measurement of skewness included as an indicator of how far from a normal distribution each set of measurements deviates.

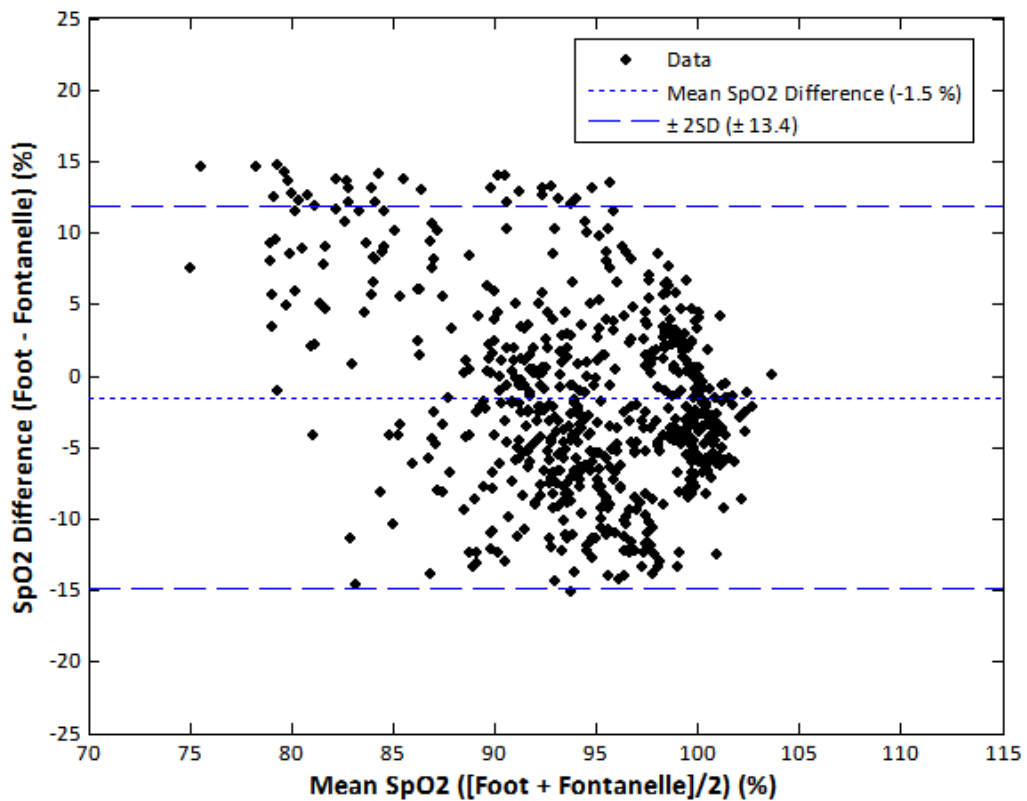


Figure 11.8: AF and foot SpO₂/PPG sensor accuracy relative to each other.

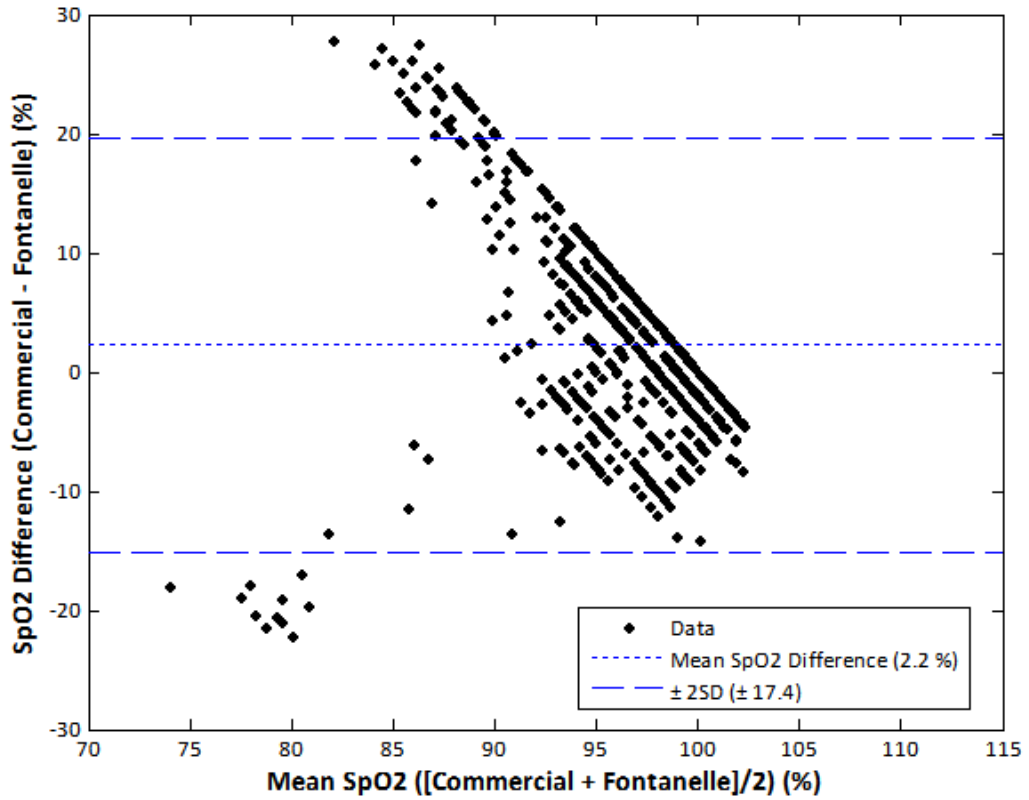


Figure 11.9: AF and commercial sensor accuracy relative to each other.

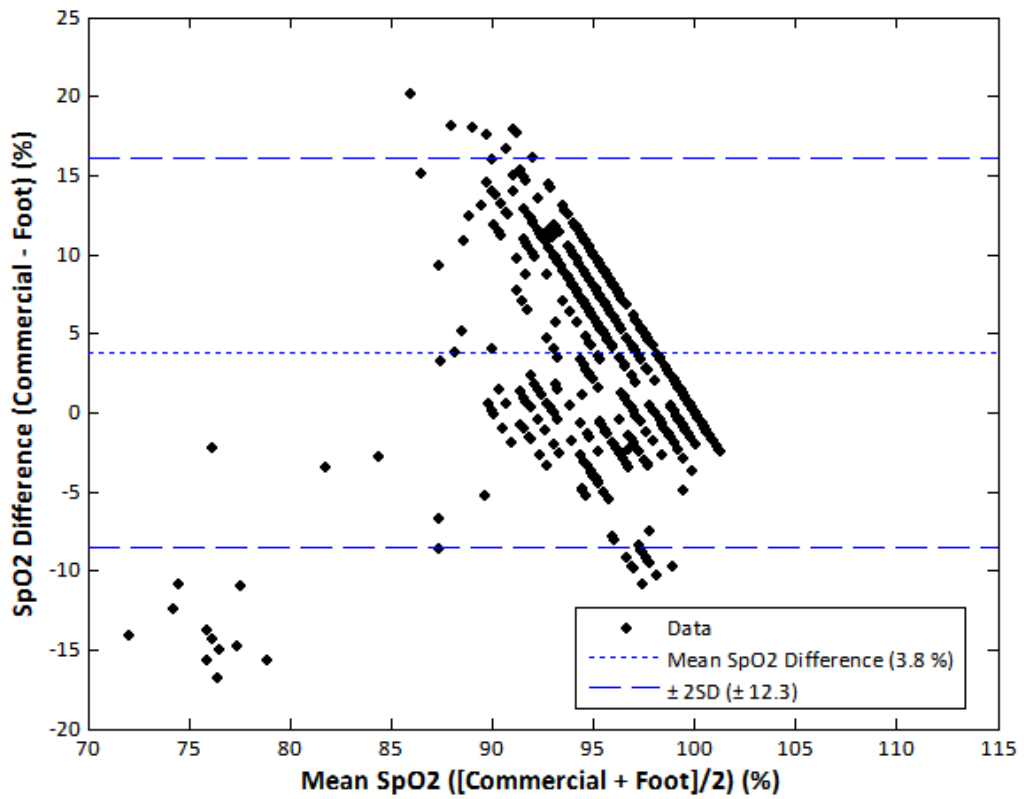


Figure 11.10: Reference foot and commercial sensor accuracy relative to each other.

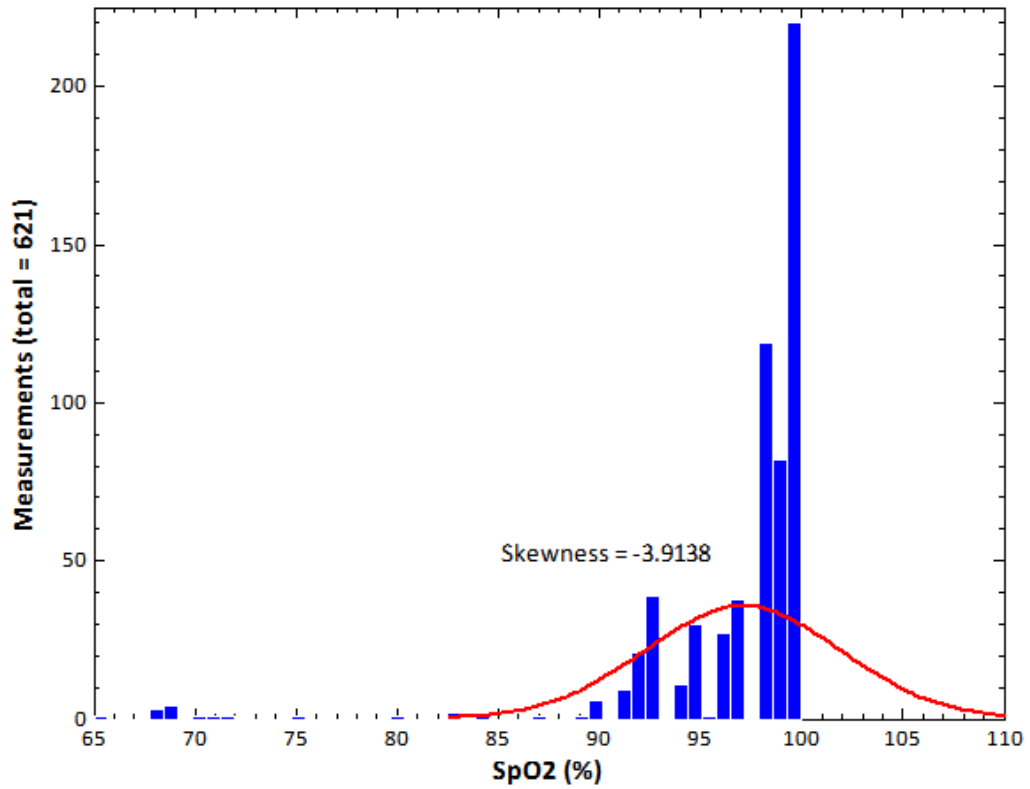


Figure 11.11: Histogram of commercial SpO₂ readings with superimposed normal distribution function (mean = 97.1 %) and skewness measurement (-3.91).

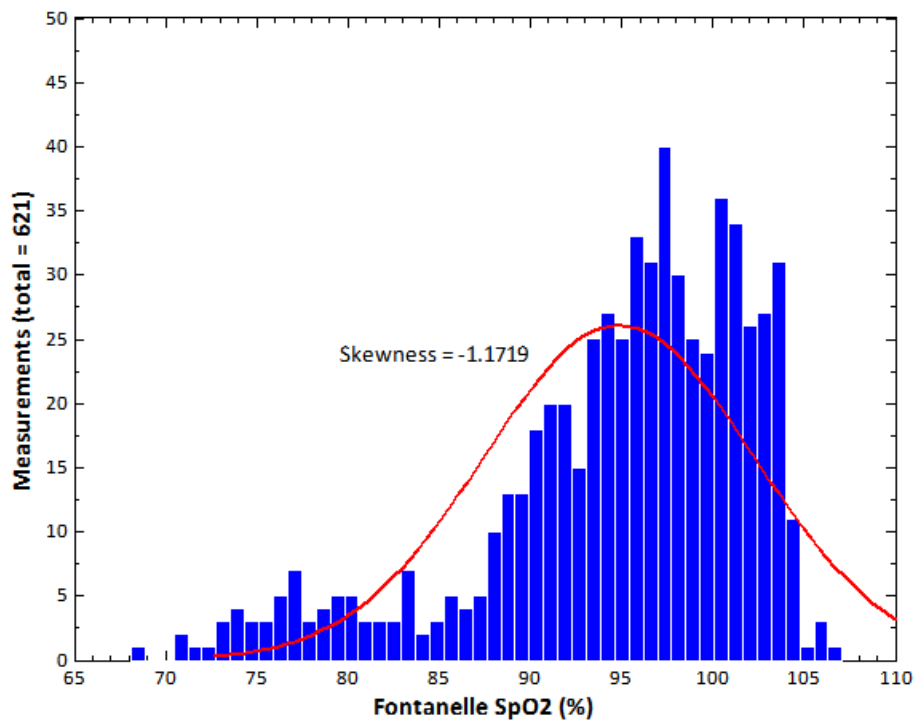


Figure 11.12: Histogram of fontanelle SpO₂ readings with superimposed normal distribution function (mean = 94.9 %) and skewness measurement (-1.17).

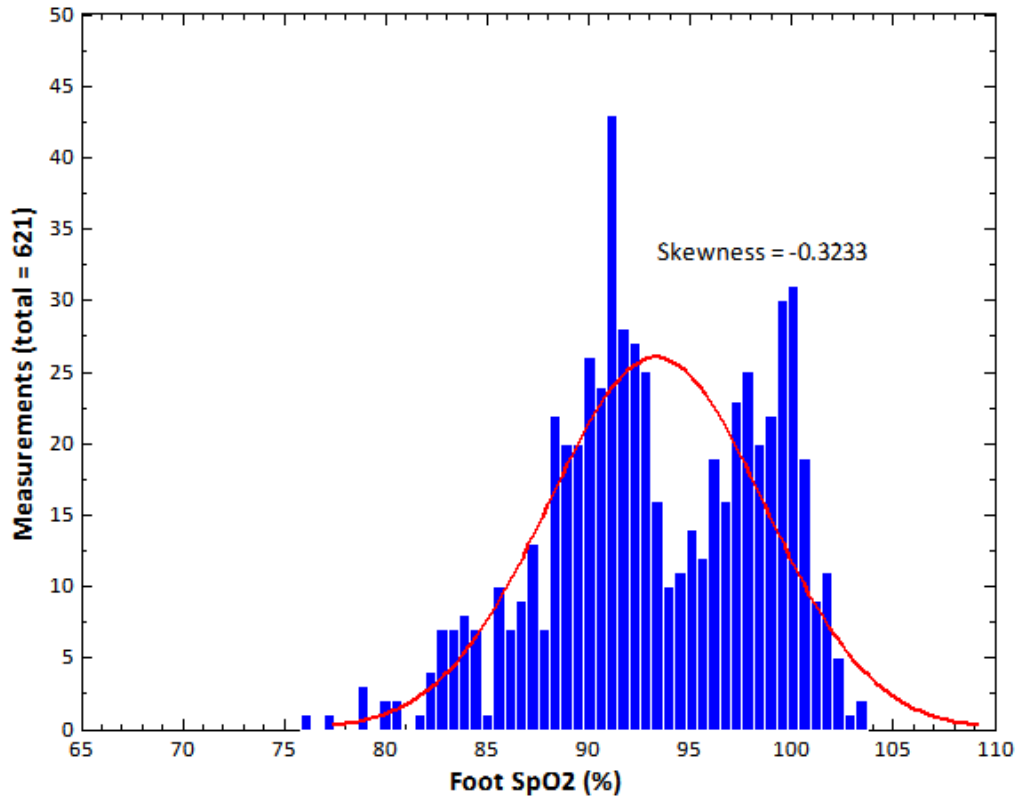


Figure 11.13: Histogram of foot SpO₂ readings with superimposed normal distribution function (mean = 93.3 %) and skewness measurement (-0.32).

11.4 Fontanelle SpO₂ Analysis Summary

Comparisons of SpO₂s from both custom sensors have been made with gold standard measurements (blood gas analysis) and the bedside SpO₂ monitor. These analysis reveal a strong correlation ($R > 0.5$ | $R < -0.5$) between conventional transmission commercial sensors and both custom reflective sensors (-0.696 for the AF sensor and 0.999 for the reference foot sensor) when the amount of delivered oxygen is altered. Correlation between the custom sensors ($R = -0.731$) also demonstrates strong correlation between periods. This suggests that the AF sensor may be used as an alternative to sensors placed on the foot or other peripheral locations.

The histogram plot of the “gold standard” SaO₂s (figure 11.7) from the commercial blood gas analyser reveals that the expected distribution of blood oxygen values for the group of neonates studied is negatively skewed, a result repeated when looking at the histograms of SpO₂ values from the commercial pulse oximeter and the SpO₂ values computed using both custom sensors (figures 11.11 – 11.13). This would indicate that the AF sensor is in

relatively broad agreement with the commercial sensor and the results from blood gas analysis.

The linear regression plot in figure 11.3 suggests that no method of calculating blood oxygenation (commercial, custom foot sensor or AF sensor) is accurate for SaO₂s below about 90 %. Interestingly it is observed that a direct comparison of the commercial SpO₂ values with the blood gas tests reveal a large mean difference (figure 11.4) of nearly 5 %, whilst the SpO₂ values computed from the custom sensors show better agreement with the blood gas tests (less than 2% for both sensors). However the limits of agreement for the custom sensors are observed to be larger than the commercial sensor.

Possible reasons and explanations for the discrepancies observed are discussed in Chapter 13 – *Discussions, Conclusions and Future Work*.

Chapter Twelve

Oesophageal Photoplethysmographs and SpO₂ Analysis, Proof of Concept Demonstrations *In-vivo*

It has been previously discussed (Chapter 5) that the oesophagus (OES) may be an alternative monitoring location for SpO₂ at times of peripheral compromise in the paediatric population. This chapter presents the findings from two ASA-3 Patients who were enrolled for a study of the comparison of PPGs simultaneously from a peripheral location and the oesophagus, SpO₂s from a commercial device (COM) (Philips Intelliview with HP Merlin Sensors and Modules, Netherlands) and the custom sensors; and blood gas results (SaO₂) (Abbott POC i-STAT Handheld, NJ, USA).

12.1 Clinical Methods

Candidates for OES PPG/SpO₂ monitoring were selected on ward rounds by the lead clinician against the list of inclusion/exclusion criteria specified in the protocol (Appendix E). Two patients were successfully recruited for the procedure; both patients were classed as ASA-3, on an oscillator for respiratory support and under adequate sedation. Patient 1 was a 7 year-old, 23 kg female admitted to the paediatric ICU with breathing complications related to other medical conditions. Patient 2 was a 9 month-old female burns patient admitted with 1st degree burns to 40 % of her body.

Following informed consent from parents the procedure to compare PPG signals for the estimation of SpO₂ commenced; A routine blood gas test was scheduled and both sensors (peripheral and OES) were cleaned with alcohol wipes. The peripheral sensor (REF) was placed into a clear adhesive sterile pocket constructed from clear dressing sheets (Tegaderm™, 3M, MN, USA). The reference PPGs were established by placing and securing the peripheral sensor with standard medical tape. Patient 1 had the peripheral sensor placed on the palm of the hand, and Patient 2 (due to the extent of dressings used for the treatment of the burns) had the sensor placed on the right temple. The OES sensor was placed into a disposable size 12 nasogastric tube sealed with a fast-acting sterile skin

adhesive (Dermabond, Johnson & Johnson, NJ, USA). The OES sensor was then inserted into the mouth to a depth pre-determined by the lead clinician that would situate the sensor approximately at the same level as the aorta. As part of clinical procedure Patient 1 had a chest x-ray scheduled that coincided with the trial. Figure 12.1 is the chest x-ray with the OES sensor clearly visible. Photographic consent was obtained from the parents for the use of all images (including x-rays) in publications related to this work. Photoplethysmograph signals were confirmed before the sensor was secured in place by the end of the tube being taped to the bed.

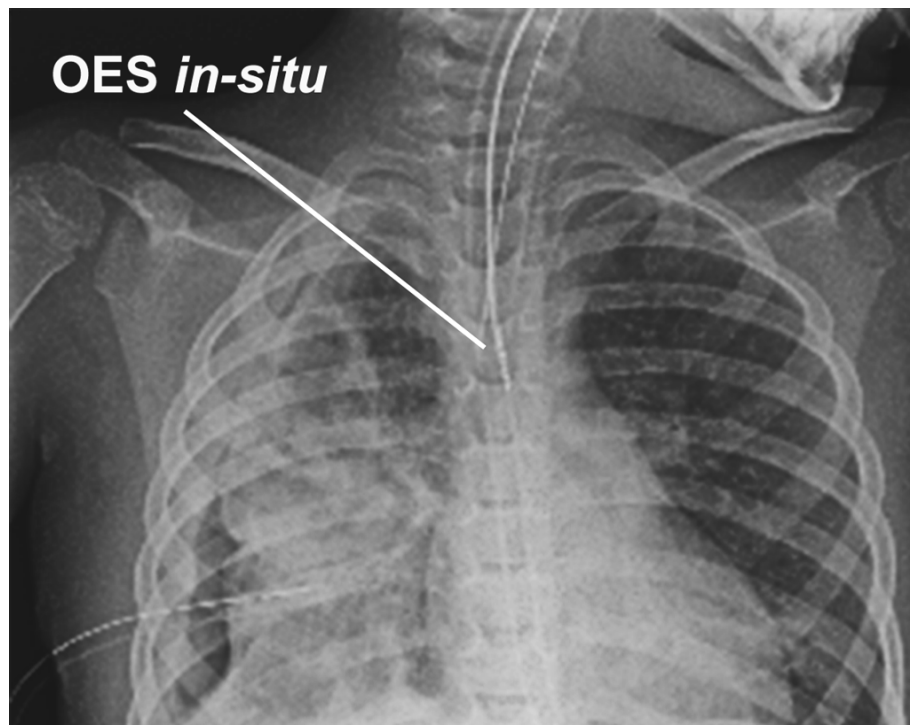


Figure 12.1: Chest X-ray of the OES sensor in-situ of Patient 1. The head of the sensor is sitting approximately 15 cm into the oesophagus, just behind the aorta of the heart.

At this time the routine blood sample was taken for blood-gas analysis, and marked as a time stamp in the data file with the time-stamp function of the virtual instrument (VI). Recording of PPGs was continued for a maximum length of 30 minutes before the baseline of delivered oxygen concentration (FiO₂) was increased by 50 %, .e.g. 30 % to 45 %. The time of FiO₂ changes were marked as time stamps. Continued monitoring was maintained for a maximum time of one hour before the FiO₂ was decreased back to the initial baseline value and PPGs were further monitored for 30 minutes before the trial ended. The commercial sensor for Patient 1 was a transmission type SpO₂ sensor on the index finger of the left hand. The commercial sensor for Patient 2 was a disposable transmission type paediatric SpO₂ sensor placed on the left ear (see figure 12.2).



Figure 12.2: Paediatric burns Patient, Patient 2, with commercial disposable ear sensor.

12.2 Oesophageal and Periphery Photoplethysmographs

Recording of PPGs from Patient 1 totalled a length of 61 minutes 13 seconds, recordings from Patient 2 totalled 59 minutes 46 seconds. The monitoring periods are defined by the condition of FiO₂ delivery; pre FiO₂ increase, during FiO₂ increase and post FiO₂ increase. By direct observation of the PPG recordings Patient 1 had 4 sets of pre FiO₂ stable PPG periods (total = 21 minutes 40 seconds), 4 sets of during FiO₂ stable PPG periods (total = 10 minutes 15 seconds) and 1 continuous set of post FiO₂ stable PPGs (12 minutes 58 seconds). Patient 2 had 1 continuous set of pre FiO₂ stable PPGs (24 minutes 26 seconds), one continuous set of during FiO₂ increase stable PPGs (12 minutes 48 seconds) and 1 continuous set of post FiO₂ stable PPGs (19 minutes 16 seconds). Figures 12.3 and 12.4 are the complete recorded length of both sets of PPGs from the two patients from the OES and peripheral sensors. Marked are the FiO₂ monitoring periods; these PPGs have been normalised and filtered (oscillator noise removed) by the methods in section 9.1 and 9.2 (Chapter 9). Figure 12.5 and 12.6 are zoomed-in views (10 second samples) of the PPGs in figures 12.3 and 12.4.

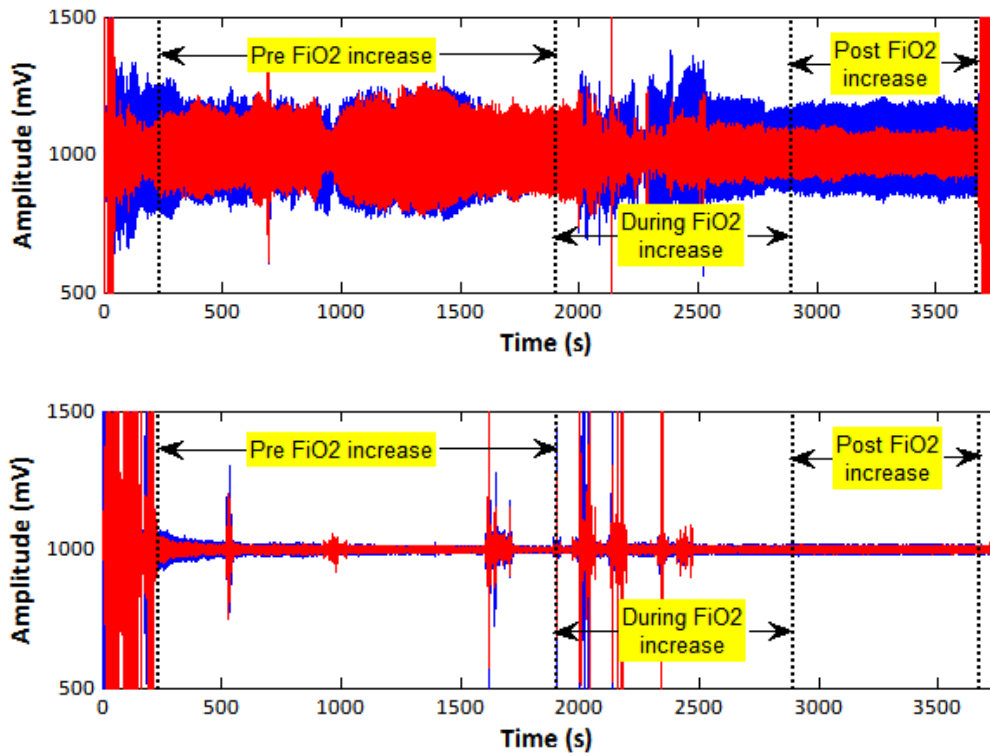


Figure 12.3: Normalised PPG recording from Patient 1, top = OES sensor, bottom = periphery sensor on hand. Red PPGs shown in red, Infrared PPGs shown in blue.

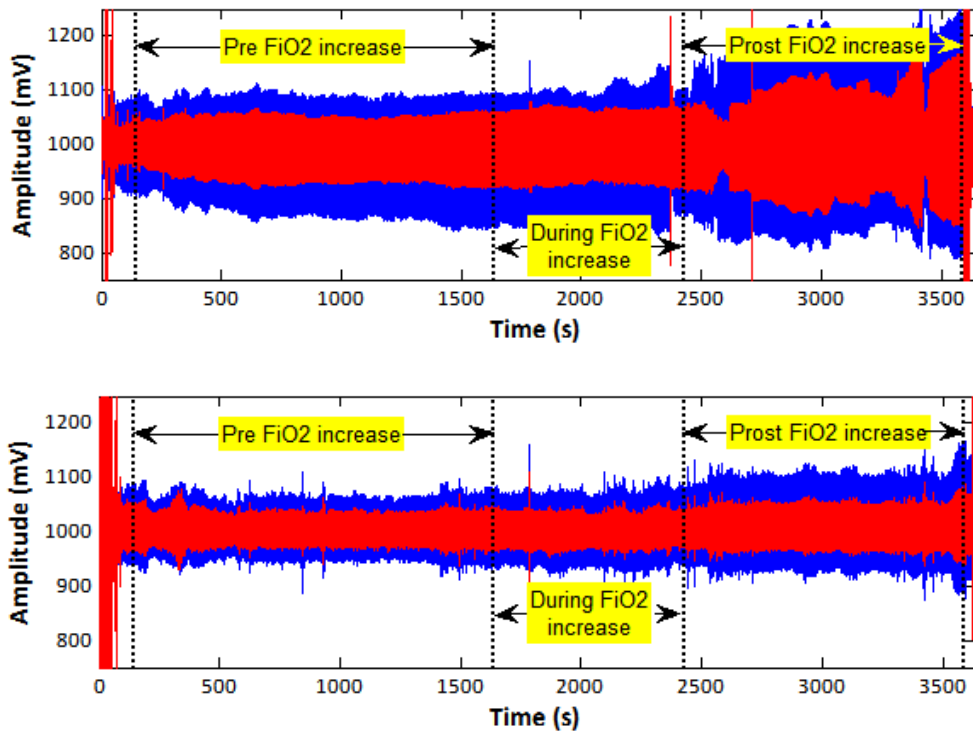


Figure 12.4: Normalised PPG recording from Patient 2, top = OES sensor, bottom = periphery sensor on temple. Red PPGs shown in red, Infrared PPGs shown in blue.

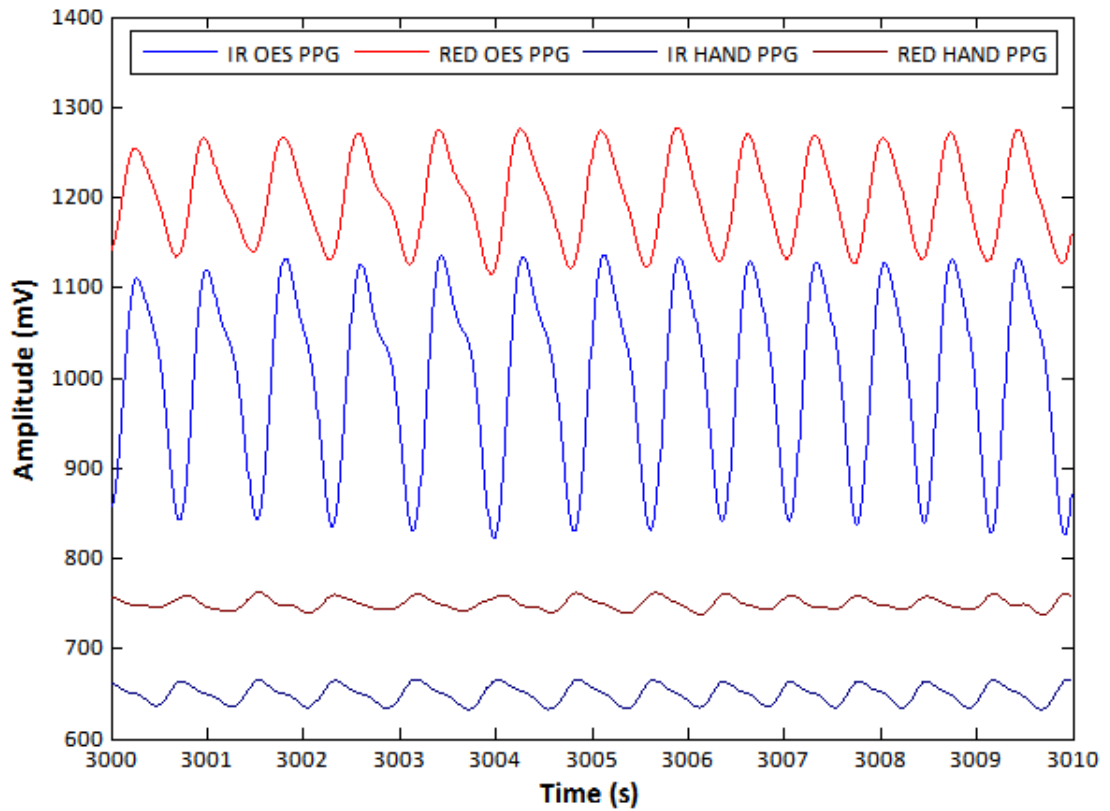


Figure 12.5: Normalised and filtered PPG sample (10 seconds) from Patient 1, HR \approx 78 – 80 BPM

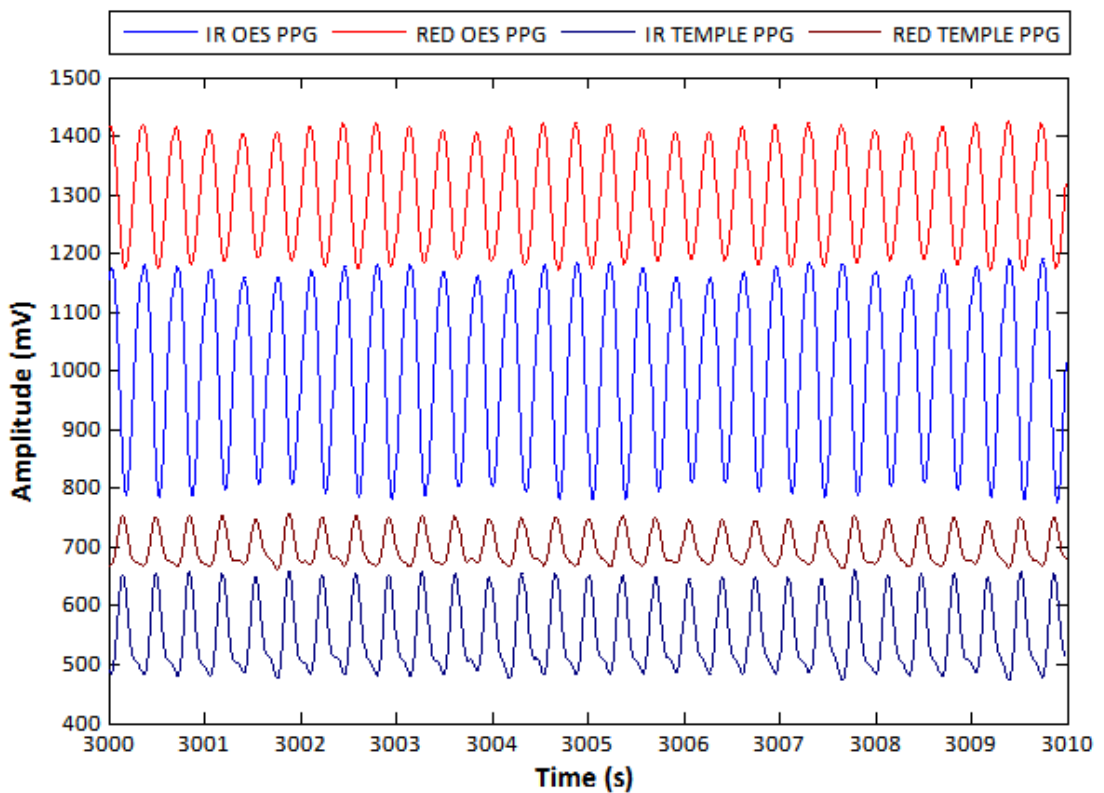


Figure 12.6: Normalised and filtered PPG sample (10 seconds) from Patient 2, HR \approx 165 – 168 BPM.

12.3 Oesophageal and Periphery Normalised Amplitude Analysis

Amplitudes were calculated by the method described in section 9.3 (Chapter 9), and erroneous readings identified and removed from further calculations by the method given in section 9.5 (Chapter 9). Normalised amplitude results for both patients are tabulated in tables 12.1a and 12.1b. No test for normality was performed on the amplitudes due to the small data set of two patients. The tabulated data has been plotted graphically on the line graphs in figures 12.7 and 12.8, and computed for correlation in table 12.2.

Table 12.1a: Mean red (660 nm) normalised AC amplitudes for each period per patient.

Patient #	RED Normalised Amplitudes (mV)					
	Pre FiO ₂ increase		During FiO ₂ increase		Post FiO ₂ increase	
	REF	OES	REF	OES	REF	OES
1	26.6	310.6	27.6	218.7	22.1	153.3
2	69.3	119.9	71.0	138.9	89.1	208.4
Mean	48.0	215.3	49.3	178.8	55.6	180.8
SD	30.2	134.8	30.7	56.4	47.3	38.9

Table 12.1b: Mean infrared (940 nm) normalised amplitudes for each period per patient.

Patient #	IR Normalised Amplitudes (mV)					
	Pre FiO ₂ increase		During FiO ₂ increase		Post FiO ₂ increase	
	REF	OES	REF	OES	REF	OES
1	40.3	336.1	42.6	314.5	32.3	317.8
2	121.8	217.6	141.5	248.6	181.4	356.4
Mean	81.0	276.9	92.1	281.6	106.9	337.1
SD	57.6	83.8	70.0	46.6	105.4	27.3

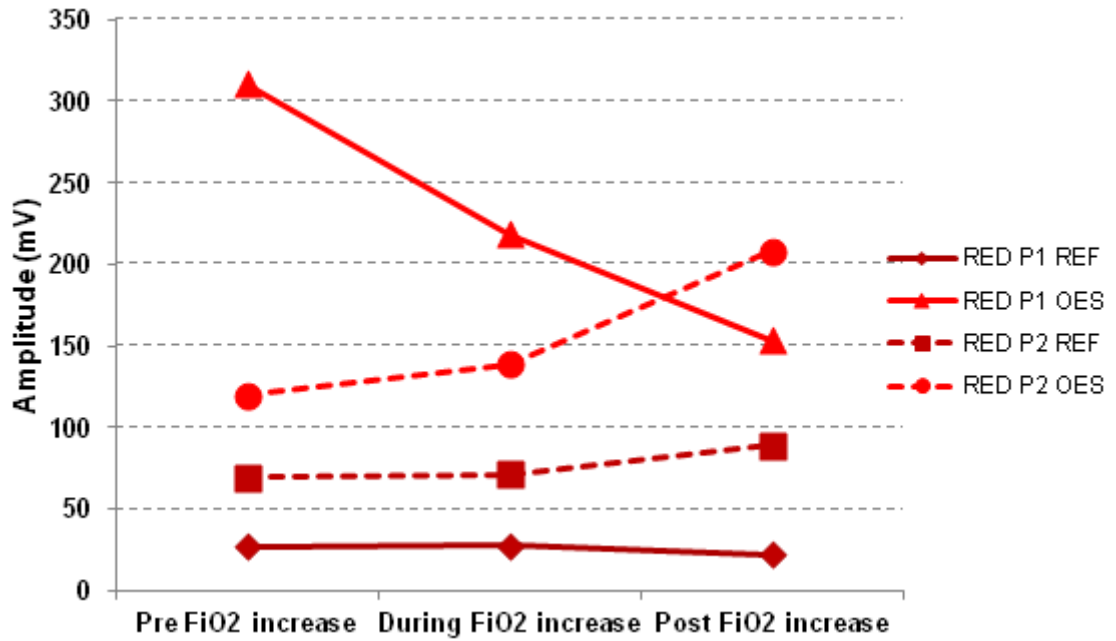


Figure 12.7: Red PPG amplitude changes across the monitoring periods for each patient. Patient 1 is represented by the solid lines, Patient 2 by the dashed lines.

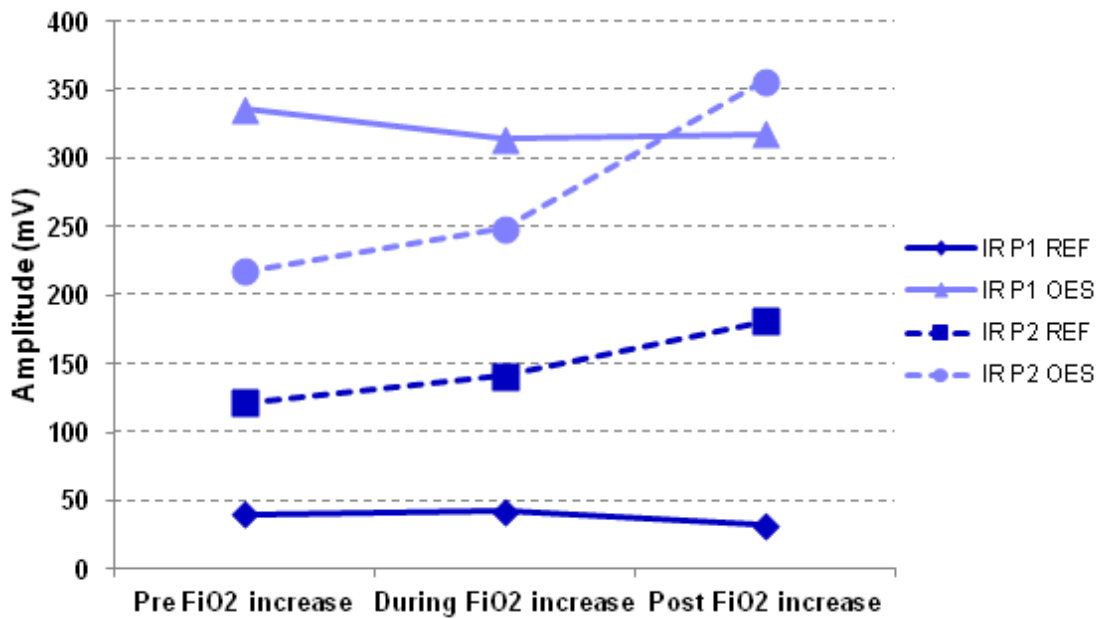


Figure 12.8: Infrared PPG amplitude changes across the monitoring periods for each patient. Patient 1 is represented by the solid lines, Patient 2 by the dashed lines.

Table 12.2: Correlation of PPGs across the periods between sensors, strong correlation = $R > 0.5$.

Correlation (R)	Red PPGs	IR PPGs
Patient 1	0.702	0.166
Patient 2	0.991	0.993

12.4 Estimation of SpO₂ during FiO₂ Increase and Decrease

To make a comparison with actual SpO₂ readings, as recorded by the clinical monitors, time stamps were marked into the raw data files using the time stamping function of the virtual instrument (VI) for both trials, coinciding with specific clinical events and/or observations (e.g. feeding, drug administration and readings from clinical monitors). These values were then compared against the computed SpO₂ values. SpO₂ was calculated by the methods set out in section 9.4 (Chapter 9). Table 12.3 is the computed mean SpO₂ values in each period against the commercial device. Figure 12.9 and 12.10 show the computed SpO₂ for each patient with the custom sensors against the clinical SpO₂ values in each monitoring period. Correlation was computed between the sensors and is tabulated in table 12.4.

Table 12.3: Mean SpO₂ values in each period for both patients.

#	SpO ₂ (%)								
	Pre FiO ₂ increase			During FiO ₂ increase			Post FiO ₂ increase		
	REF	OES	Com	REF	OES	Com	REF	OES	Com
1	92.4	86.7	96.8	93.5	91.5	99.4	92.9	97.8	97.5
2	95.9	96.2	98.1	97.5	96.0	99.8	97.8	95.4	99.1
Mean	94.2	91.4	97.5	95.5	93.8	99.6	95.3	96.6	98.3
SD	2.5	6.7	0.5	2.8	3.1	0.3	3.5	1.7	1.1

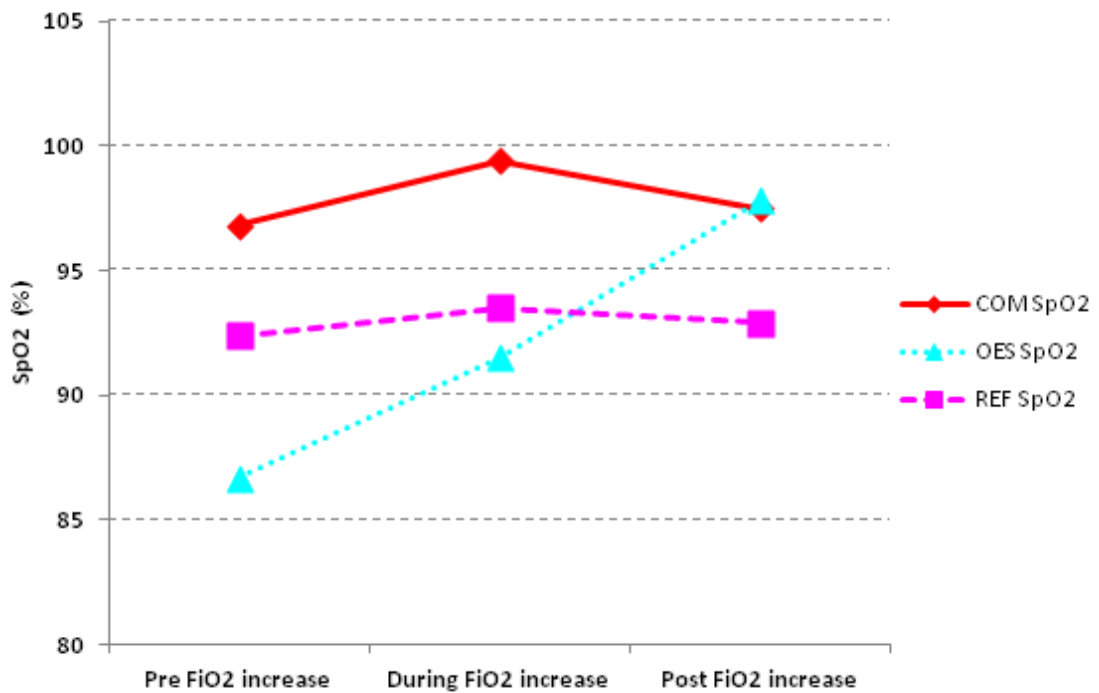


Figure 12.9: Mean SpO₂ values in each monitoring period for Patient 1 from all three sensors.

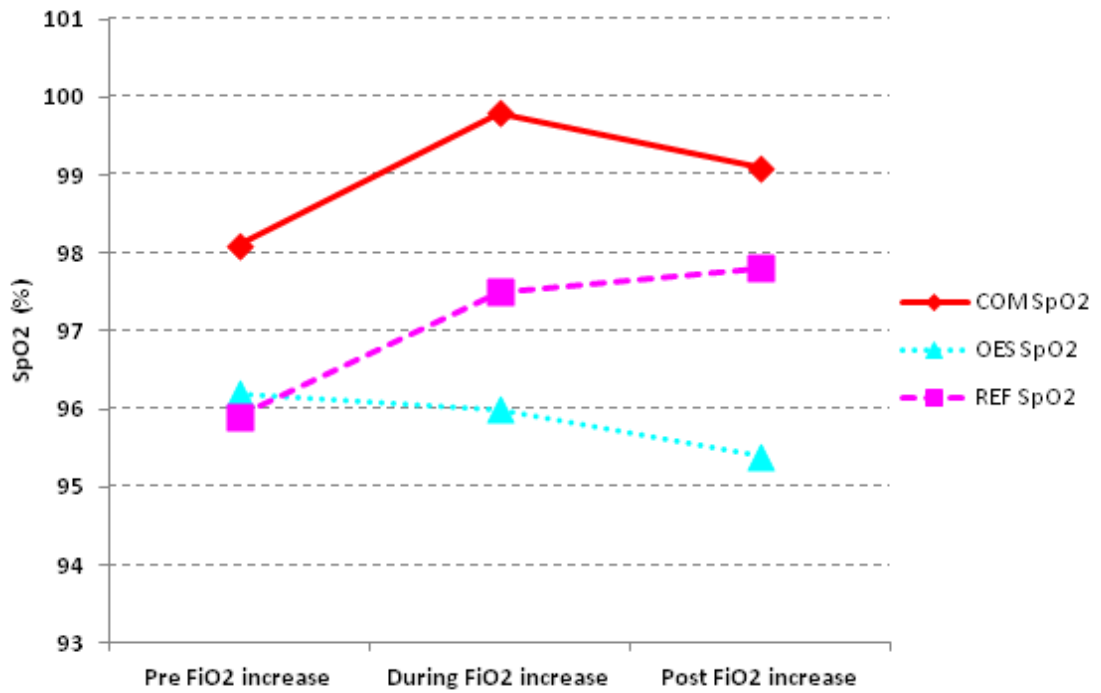


Figure 12.10: Mean SpO₂ values in each monitoring period for Patient 2 from all three sensors.

Table 12.4a: Correlation of SpO₂s between sensor locations for Patient 1

Correlation (R)	OES	REF	Commercial
OES	-	0.383	0.184
REF	0.383	-	0.978
Commercial	0.184	0.978	-

Table 12.4b: Correlation of SpO₂s between sensor locations for Patient 2.

Correlation (R)	OES	REF	Commercial
OES	-	-0.792	-0.337
REF	-0.792	-	0.842
Commercial	-0.337	0.842	-

12.5 Oesophageal SpO₂ Comparison with Commercial SpO₂ and Blood Gas SaO₂

Each trial was commenced with the timing of a routine blood-gas sample drawn from an arterial line. Over the time of the two studies a total of 5 samples were taken as part of routine care and are tabulated in table 12.5. A linear regression scatter plot was drawn and is shown in figure 12.11. A Bland and Altman test (Bland and Altman 1986) was then performed between each pairing of saturation values; SaO₂ vs. COM SpO₂; SaO₂ vs. OES SpO₂ and SaO₂ vs. REF SpO₂. These are shown in figures 12.12, 12.13 and 12.14 respectively.

Table 12.5: Blood gas samples (SaO₂) taken as part of routine clinical procedure during the time of study with corresponding SpO₂ from all three sensors.

Patient	SaO ₂ (%)	COM SpO ₂ (%)	OES SpO ₂ (%)	REF SpO ₂ (%)
1	93	96	96.0	91.0
1	94	98	81.5	91.4
1	99	100	95.8	94.6
2	95	98	96.7	94.6
2	97	100	95.3	97.7
Mean	95.6	98.4	93.1	93.9
SD	2.4	1.7	6.5	2.7

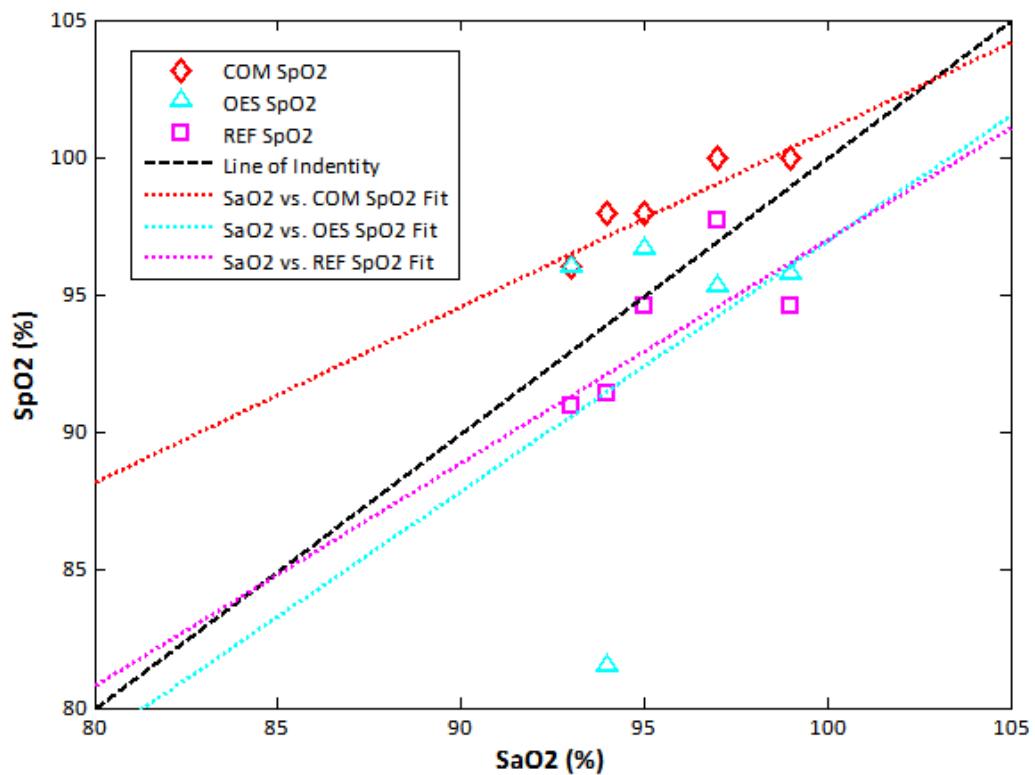


Figure 12.11: Linear regression plot of blood Gas SaO₂ vs all three SpO₂ sensors

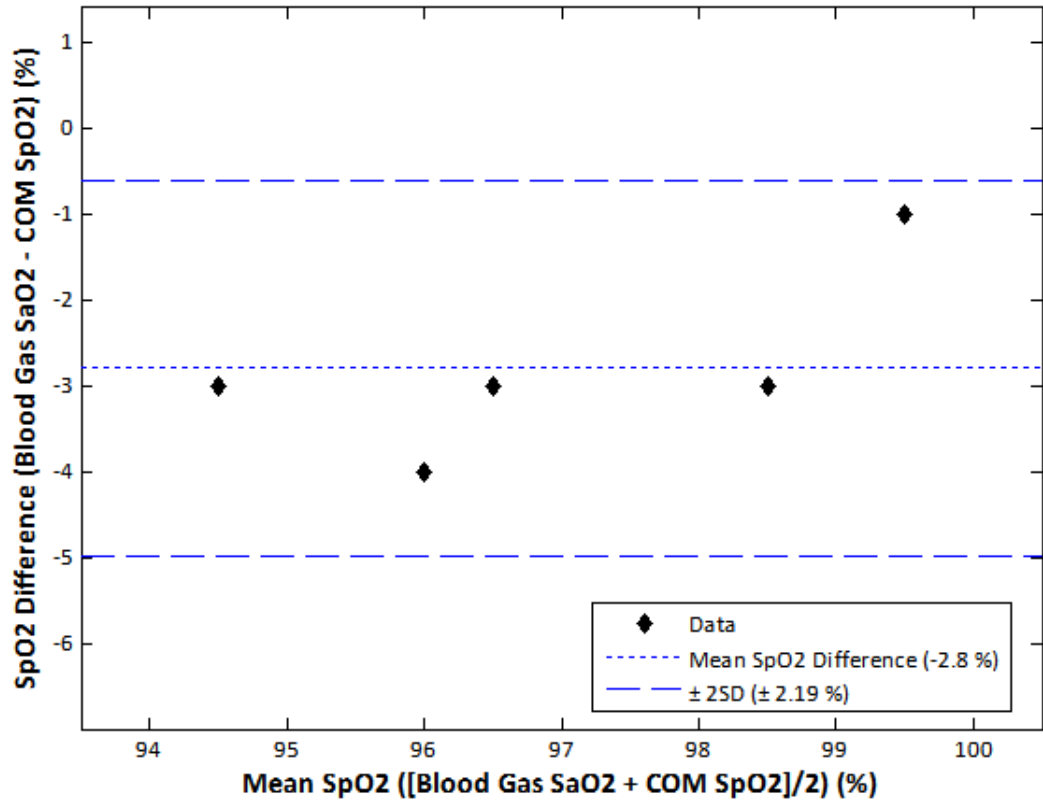


Figure 12.12: Blood Gas vs. Comercial SpO₂ readings.

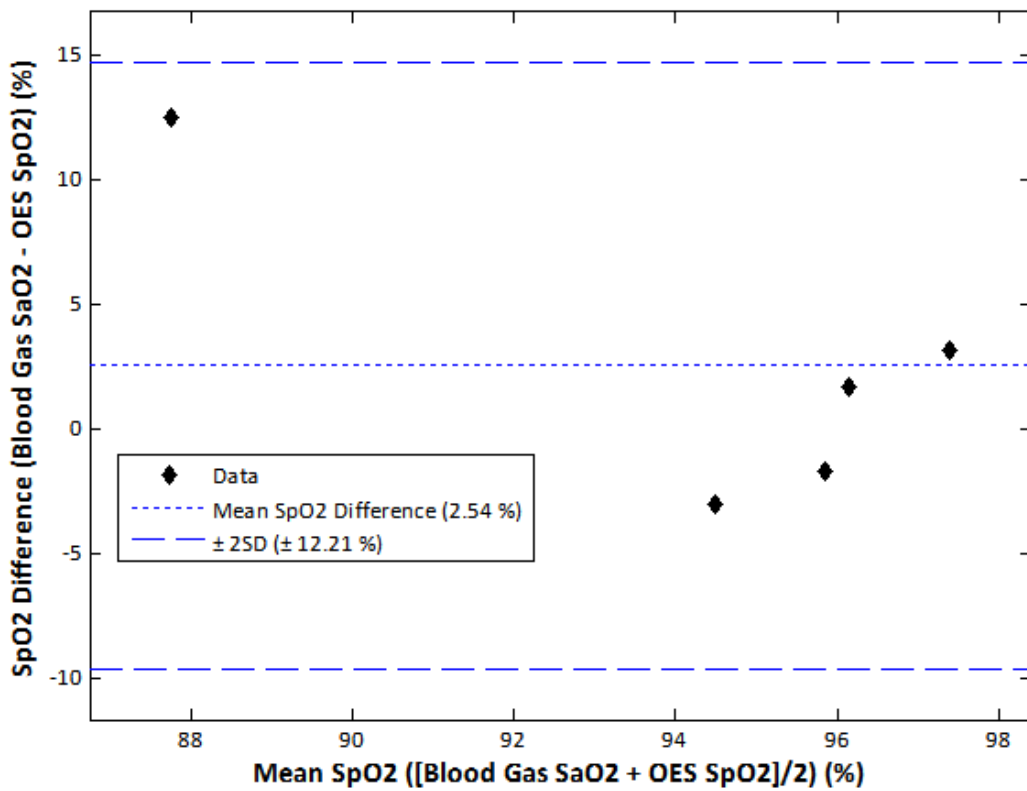


Figure 12.13: Blood Gas vs. Oesophageal readings

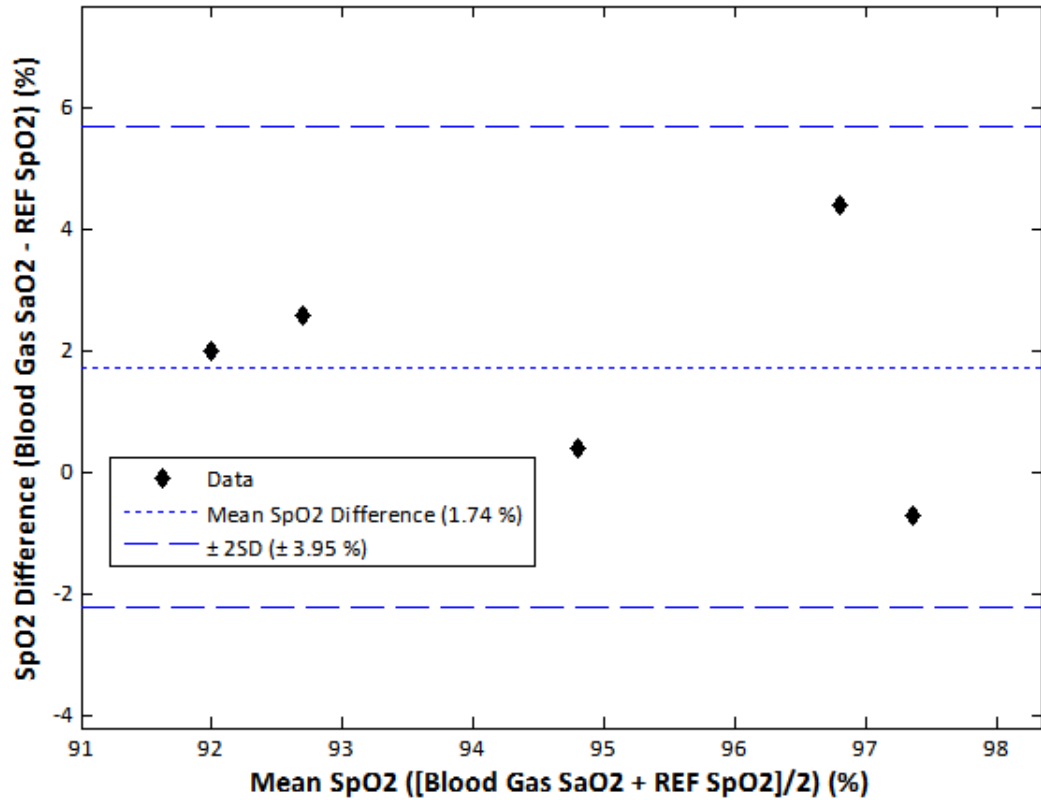


Figure 12.13: Blood Gas vs. reference sensor readings

12.6 Oesophageal PPG and SpO₂ Analysis Summary

Placement of the OES sensor and its' situation in the oesophagus has been confirmed by x-ray imaging. SpO₂ monitoring from those patients whom no other periphery location (hands or feet) is available has been successfully demonstrated on a patient with 1st degree burns to those areas, demonstrating its' attraction in the monitoring of neonates and children who have little or no peripheral blood supply, or who's peripheral location is inaccessible. These results are discussed in detail in the final chapter, *Discussions, Conclusions and Future Work*.

Chapter Thirteen

Discussions, Conclusions and Future Work

The goal of this research was to assess photoplethysmography (PPG) for the purpose of blood oxygen saturation (SpO_2) monitoring at alternative monitoring locations, in neonates and children, when periphery PPGs begin to become compromised by poor health, utilising custom-made miniature photometric sensors and instrumentation.

Reflective mode photometric sensors have been successfully designed, constructed and tested for thermal and electrical safety, that can be placed on peripheral location, such as the hand or foot, on the neonatal anterior fontanelle (AF) or into the infant oesophagus (OES) (Chapter 6). Acquisition of PPGs from these sensors utilising the instrumentation described in chapter 7 revealed good quality PPGs with large amplitudes. Custom instrumentation and software developed simultaneously (Chapter 7 and 8) has successfully operated the sensors and recorded the raw PPG signals, with time-stamping information, to a laptop computer.

Consultation with a clinical collaborator at Great Ormond Street Hospital for Children (GOSH), London, UK, helped to establish a protocol (Appendix E) for clinical trials that would utilise the developed sensors to look for changes in PPG amplitudes that coincide with blood oxygen saturation changes artificially induced by altering the delivered oxygen concentration (FiO_2). Two populations have been investigated, a neonatal population where the fontanelle sensor was tested, and an infant population where the oesophageal sensor was tested. Following instrumentation safety testing by the biomedical engineering department at GOSH, the protocol was approved by a local ethics committee and trials began.

13.1 Fontanelle PPG and SpO_2 Monitoring

The age and weight of the patients in these trials seems to have had little effect on the observed PPG amplitudes, with very weak correlation scores ($R < 0.3$) in nearly all correlation tests between the normalised amplitudes and each patient's age or weight. This suggests that the amplitudes obtained may be more dependent on the individuals' anatomy and physiology and what treatment was being given at the time.

Figures 10.5 and 10.6 demonstrate that for these trials the largest normalised amplitude for the AC component of a PPG occurs at 525 nm, the green LED light source. Infrared has the second largest and red has the lowest overall normalised amplitude. The AC component of the PPG waveform is thought to be solely attributed to the oxygenated arterial blood, (which appears bright red in colour when fully oxygenated). Red light is therefore reflected back and absorbed less, hence the small normalised amplitude, infrared light is more strongly absorbed by HbO₂, and both HbO₂ and Hb strongly absorb green light, hence the higher amplitudes.

Altering the amount of delivered oxygen to the patient results in more or less blood being successfully oxygenated during pulmonary blood circulation (mean increase in SpO₂ as reported by the clinical devices = 2.9 % during FiO₂ increase; mean decrease = 1.3% post FiO₂ increase).

Initial amplitude analysis from the bar graphs and tables suggests a correlation between FiO₂ increase and PPG amplitudes from the AF and foot simultaneously, and the amplitude trace from the AF in figure 10.4b visually demonstrates this for the infrared signal. The results in table 10.5 are highly suggestive of this strong correlation.

Across all wavelengths for every monitoring period the PPGs from the fontanelle were smaller when normalised than the PPGs from the foot. Difficulties during trials regarding the placement and securing of the fontanelle sensor may have lead to errors in capturing the PPG signal that were unobservable before PPG analysis. A difficulty with making the AF sensor lie flat and remain in position was a particular problem and this may have caused the light from the sensor to reflect off the top layer of skin and hair rather than penetrate through and into the tissue beneath. PPGs were observable for all neonates at the red and infrared wavelengths, even with a thick covering of hair, suggesting that the presence of hair does not affect light at these wavelengths enough to be of a concern when observing PPGs. However as the acquisition of green PPGs from the fontanelle was relatively rare, hair may have affected the green light PPGs. The anterior fontanelle is situated directly above a major venous reservoir in the skull (superior sagittal sinus), where a large amount of venous blood and other cerebral fluids are present. As Hb absorbs strongly in the red region this may count for the lower amplitudes observed.

Signals have been normalised for this analysis, the relative signal to noise ratio for each wavelength of light thus remains the same. In figure 10.4a it is clearly observable that whilst the green light PPG normalised amplitudes are higher than the red or infrared

amplitudes, they are far more spread out (have a larger variation in amplitude). This may be the cause of the poor green PPG amplitude results, however other contributing factors may have hindered green PPG acquisition from the AF; the photodiode sensitivity to green light is only around 40 % of the sensitivity to infrared light (see chapter 6), meaning that green light PPGs would initially be smaller before normalisation. This coupled with the fact that green light is more heavily absorbed by Hb and HbO₂ than red or infrared light would further reduce the initial relative amplitude before normalisation. The tiny amplitudes observed in the raw data file may have suffered a large quantization error during digitisation, hence the large variance in amplitudes.

Peripheral supply compromise cannot be induced in real patients ethically, so the method of FiO₂ change was introduced to show that the AF sensor could detect a change in PPG amplitude and SpO₂ during FiO₂ increase/decrease that was in line with the SpO₂ recorded on conventional sensors at conventional locations. There were no cases within the trial period where peripheral compromise occurred. However, an analysis of the difference between normalised amplitudes from the foot and the AF for the different classes of patients studied (ASA 1, 2 and 3) does show an decrease of the difference in amplitude of PPGs between the AF sensor and the foot sensor the more critical the individual child's ASA was. This is depicted in figures 10.7 to 10.9 as the trend lines for each set of PPG amplitude differences (pre, during and post FiO₂ increase) increase. Across all trials, across all monitoring periods 86 sets of amplitude differences (AF PPG amplitude minus Foot PPG amplitude) were computed (38 red, 38 infrared, 10 green). Correlation of the results for red and infrared PPGs is strong ($R \geq 0.6$) in all cases. Due to the low success rate of green PPG acquisition it cannot be determined significantly if the very strong correlation of amplitudes of green PPGs ($R > 0.9$) is represented by the larger population. The results for red and infrared PPGs, however, are highly suggestive that as the patient becomes more critical the smaller the difference in PPG amplitudes between the AF and foot becomes, demonstrating the autonomous function of the body to preserve blood supply in core locations, and hence the AF sensor could be a critical tool in measuring PPGs for the purpose of SpO₂ estimation.

The above amplitude analysis results of the PPGs and their overall corresponding strong correlations both with FiO₂ change and patient health (ASA score) is a positive indicator that the AF may be suitable in the monitoring of SpO₂ at times of periphery supply compromise. Computation of SpO₂ from the custom sensors and comparison with the commercial devices is discussed below.

From the step response in SpO_2 , seen in figure 11.1, it is clear that the AF sensor can respond to changes in oxygen in the same manner as the commercial sensor and reference sensor. For the example given in figure 11.1 there is an obvious discrepancy in the estimation of SpO_2 ; both the foot sensor and the AF sensor appear to be underestimating the value reported by the clinical device. Overall, across all the trials conducted, the mean SpO_2 values (as estimated by the AF and foot sensor) is below the SpO_2 reported by the clinical device (see figure 11.2), at all periods of monitoring. A larger standard deviation is also observed. These differences may arise from several sources; 1) The method described in section 9.4 (Chapter 9) for calculating SpO_2 from the custom sensors is not the same as the method utilised by the clinical monitors (which is unknown and may include additional routines that correct for movement and other errors) for this reason it is perhaps more beneficial to view SpO_2 values from the custom sensors only as an estimation of SpO_2 from the commercial devices, and looking for corresponding changes that correlate across the different sensors; 2) The custom sensors, instrumentation and software developed is un-calibrated for SpO_2 measurement, instead relying on the methods in section 9.4 to make an estimation, retrospectively. It was noted by Dassel *et al* (Dassel, et al. 1997), that different locations on the head reveal different compositions of tissues, and so the relationship between arterial oxygen saturation and the ratio between the red and infrared PPG signal would also differ, and thus new calibrations would have to be derived for the different positions on the head; 3) The instrumentation was primarily developed for PPG acquisition and was optimised for the accurate retrieval and recording of said PPGs.

Despite these limitations and differences and overall change in SpO_2 from the AF is seen to correlate well with both the foot sensor and commercial device (AF/Foot $R < -0.7$, AF/Commercial $R < -0.6$, Foot/Commercial $R \approx 1$). The negative correlations seen between sensors may be explained by; 1) Changes in the orientation of the sensor on the AF between studies may have resulted in the optical signals received to be absorbed and scattered by underlying tissue differently, i.e. small blood vessels in the scalp directly under the sensor may have affected the light from one LED light source but not the other, resulting in different red to infrared PPG ratios. Although an effort was made in trials to place the sensor in the same orientation for each patient it was sometimes impractical, either due to other clinical sensors, orientation of the child's head (if they were on a ventilator that required the head to be turned to the side) or if the physical size of the fontanelle meant that orientation of the sensor in the desired position resulted in a failure to acquire PPGs in the first place; 2) The anterior fontanelle sits directly over the sagittal

sinus, a large venous reservoir observed to periodically rise and fall, and have a measurable heart-beat synchronous pulses as detected with a Doppler ultrasound device (Dassel, et al. 1997). As described in chapter 4, pulse-oximetry assumes that it is only the arterial blood that is pulsatile, and it is this property that is the basis of estimation of SpO₂, however if the strongest pulsatile signal measured is venous in nature and getting mixed with the pulsatile signal from the arteries then the algorithms used would have no means to distinguish arterial blood from venous blood; 3) Finally it has also been reported that ventilator operation (Mark, 1989, Sami et al., 1991, Jørgensen et al., 1995) that causes changes in venous blood volume may also have an effect, 11 out of the 15 patients studied were on some form of mechanical ventilation, however since ventilator and respiratory noise were effectively removed in post-processing using the filters described in section 9.1 (Chapter 9) it is unlikely that this was a contributing cause

Comparison of SaO₂ with commercial SpO₂ reveals that there is a large mean difference and variance (-4.85 % with ± 15.8 % variance). Figure 11.4 demonstrates that the conventional SpO₂ estimation is most accurate where SaO₂ > 95%. In comparison the AF and reference foot sensor both have better mean differences in SpO₂ estimation (-1.71 % and -1.2 % respectively), but slightly larger variance (± 23.9 % and ± 18.3 %), again the most accurate estimations (figure 11.5 and 11.6) are when SaO₂ > 95 %. This result is clear and suggests that the AF foot sensor is measuring closer to the true SaO₂ than the pulse oximeter in the hospital, with the large variance also being of a similar magnitude; however for SaO₂ < 95% the accuracy declines also. It seems unusual that a calibrated device (commercial SpO₂) has less accuracy than an un-calibrated one, and one could argue that the smaller variance observed from the commercial device compensates by reducing overall erroneous readings (falsely high and low SpO₂s).

The above analysis is interesting at highlighting the inaccuracy of commercial SpO₂ monitors when compared to the gold standard, and although it may be desirable to not draw blood for any testing purposes, the demonstrated error in SpO₂ measurement compared to SaO₂ reveals that for the most critical testing of blood oxygen saturation, blood gas analysis cannot be replaced. However, a continuous measurement of SpO₂ at times of peripheral supply compromise would be highly beneficial as it would negate the need for frequent blood gas tests. The general low mean difference in SpO₂ (Figures 11.8 – 11.10) between custom and commercial sensors demonstrate good agreement with commercial SpO₂ and SaO₂, and with continued development the AF as a location for SpO₂ monitoring is a viable alternative.

13.2 Oesophageal PPG and SpO₂ Monitoring

Paediatric oesophageal monitoring has been previously reported (Kyriacou, Jones et al. 2008). In this study five neonates were monitored for SpO₂ that were compared against a commercial sensor placed on the toe. This thesis aimed at developing the OES sensor study in paediatrics further by making comparisons of PPGs from a reference location, comparing SpO₂s with blood gas test results and make an effort at attempting to acquire PPGs from the oesophagus in children who's periphery circulation was failing or inaccessible.

The oesophageal SpO₂ study was carried out only on two patients. This was due to considerable difficulty in recruiting patients who met the required approved criteria in the time allowed for the study. Results and observations from the trials conducted are, however, of note. Firstly, confirmed location of the OES in the oesophagus by x-ray imaging has been carried out; pre-scheduled chest x-ray imaging for the monitoring of a collapsed lung clearly shows the OES sensor *in-situ* (Figure 12.1). Secondly, a burns-patient with inaccessible digits due to medical dressings (Figure 12.2) for the treatment of burns was successfully monitored using the OES sensor for approximately one hour.

Amplitude analysis reveals that PPG signals in the oesophagus are of larger relative amplitude than PPGs from a reference location, either on the periphery (hand, Patient 1) or on the head (temple, Patient 2). This suggests that the oesophagus may be well-suited to SpO₂ monitoring.

Correlation between the amplitudes of PPGs at both wavelengths during FiO₂ change between the reference sensor and the OES sensor is very strongly positive ($R > 0.7$) for Patient 2, and strongly positive for Patient 1 at the red wavelength. In Patient 2 there is strong evidence that changes in SpO₂, artificially altered by changing FiO₂, does correspond to a change in amplitudes detected by both sensors. This suggests that the oesophagus is just as sensitive to changes in delivered oxygen as any other location. Amplitudes from Patient 1 at the red wavelength exhibit this same behaviour, however at the infrared wavelength the correlation is weak ($R < 0.2$), and in this case the oesophagus may be unsuitable at detecting the level of change required for accurate SpO₂ monitoring, however this is speculative as there was noticeable movement noise in the PPG signals at some stages in the trial due to other clinical procedures, and this may have had an effect.

Analysis of SpO₂ is in general agreement with the SpO₂ reported by the clinical devices, although generally lower in estimation. These preliminary results suggest that the OES sensor is sensitive to changes in oxygen and may well be suited, with further development, as an alternative location for SpO₂ monitoring. Correlation at times of FiO₂ change is very strong between the commercial sensor and the reference sensor ($R > 0.8$), but only weak when compared to the OES sensor ($R < 0.4$ | $R > -0.4$). Correlation between the custom sensors varies from weak to strong.

Finally a comparison of the gold standard SaO₂ and the SpO₂ readings reveals that there is relatively little mean difference in accuracy (mean difference $< \pm 3\%$) in all of the sensors. It is interesting to note that the largest mean difference between any sensor and the SaO₂ value was from the commercial device, as reported also in the fontanelle study, and the best accuracy was from the reference sensor. The commercial sensor reported higher values than actual SaO₂ for all samples, whilst the oesophageal sensor, for all but one blood sample reported closer SpO₂ values to the true SaO₂ value than the commercial device. The one erroneous SpO₂ reading from the OES sensor was noted to happen at the same moment as a movement in the OES tube, caused by other routine clinical care being administered.

13.3 Future Work

The effects observed in these investigations, and the limitations encountered, need to be further addressed in future investigations in order to develop the technology to the point where it is a viable alternative. The future work is suggested:

1. To see the effect of age and weight on paediatric PPGs a controlled study on a group of healthy individuals is suggested, perhaps within the setting of postnatal check-ups, commonly performed regularly a number of months after birth.
2. Sensor geometry and the effect of different LED/photodiode arrangements is suggested, as well as studying what effect different colourings/thicknesses of hair have on the signals being received
3. Further technical improvements to the sensor could be made, primarily a new sensor with multiple photodiodes (each tailored specifically to the wavelengths of light being used) could be implemented, this would in theory improve signal amplitude and signal to noise ratio, and the chances of obtaining green light PPGs from the AF may improve.

4. A larger population would need to be studied to confirm the behaviour of green PPGs in patients whose periphery blood supply may be at risk of failure.
5. More effort needs to be made to look for patients who are more prone to periphery failure, and hence PPGs observed at such times.
6. A larger study done to confirm the observation of the diminishing peripheral PPG in sicker patients is also needed as a PPG-based monitoring system could be developed to assess a patients' relative health as an index of PPG amplitude difference between two monitoring locations (e.g. head and foot).
7. Further studies into the effect of the vasculature of the head at the site of the sensor is needed in order to better understand the processes involved, especially the pulsation of the sagittal sinus synchronous with heart rate as observed with Doppler ultrasound imaging.
8. The successful acquisition of oesophageal PPGs from a patient with no accessible peripheral pulse confirms the clinical usefulness of paediatric oesophageal SpO₂ monitoring. A study conducted looking at SpO₂ monitoring from the tongue (Coté et al., 1992) in similar circumstances noted that although their method was successful it was limited to those patients who were intubated; already the developed oesophageal sensor is small enough to be placed nasally, however due to the relatively large nasal-gastric tubing used to protect the prototype sensor during trials this was not a viable method of placement, but with little effort to make the device completely bio-inert the tubing could be omitted entirely and it would be possible to place the OES sensor nasally, rather than orally, into the oesophagus, thus eliminating the prerequisite of intubated patients only. Further study is also needed, with data gathered from larger populations, with greater diversity in health.

Appendices

Appendix A

Microcontroller Source Code

```
#include <avr\io.h>
#include <util\delay.h>

int main (void)
{
    DDRB = 0x07; //Sets Channels 0,1,2 & 3 as output

    const float freq = 101.2; //freq Hz of Main LED Clock, DEMUX clock
    3 times higher

    const float time = 6*freq; // Math to calculate delay time
    const float delay = 1/time; // for required frequency
    const float delayus = delay*1000000;
    // const float delayus2 = delayus/2;

    while (1) //Clock Cycles
    {
        PORTB = 0b00000001;
        _delay_us(delayus);
        PORTB = 0b00000000;
        _delay_us(delayus);
        PORTB = 0b00000010;
        _delay_us(delayus);
        PORTB = 0b00000000;
        _delay_us(delayus);
        PORTB = 0b00000100;
        _delay_us(delayus);
        PORTB = 0b00000000;
        _delay_us(delayus);
    }
}
```

Appendix B

Frequency Response data of Filter Circuit

B.1 Low-pass Frequency Response

Frequency (Hz)	Vin (V)	Vout (V)	Gain (Vout/Vin)	20*log(Gain) (dB)
0.05	10.60	10.11	0.95	-0.41
0.10	10.60	10.17	0.96	-0.36
0.20	10.60	10.17	0.96	-0.36
0.30	10.60	10.17	0.96	-0.36
0.40	10.60	10.17	0.96	-0.36
0.50	10.60	10.11	0.95	-0.41
0.60	10.60	10.17	0.96	-0.36
0.70	10.60	10.14	0.96	-0.39
0.80	10.60	10.17	0.96	-0.36
0.90	10.60	10.09	0.95	-0.43
1.00	10.60	10.14	0.96	-0.39
2.00	10.60	10.06	0.95	-0.45
3.00	10.60	9.91	0.93	-0.59
4.00	10.70	9.72	0.91	-0.83
5.00	10.60	9.46	0.89	-0.98
6.00	10.60	9.23	0.87	-1.20
7.00	10.60	8.94	0.84	-1.48
8.00	10.60	8.61	0.81	-1.81
9.00	10.60	8.21	0.77	-2.22
10.00	10.28	7.79	0.76	-2.41
11.00	10.27	7.45	0.73	-2.79
12.00	10.27	7.09	0.69	-3.22
13.00	10.27	6.73	0.65	-3.68
14.00	10.29	6.41	0.62	-4.12
15.00	10.21	6.08	0.60	-4.50
16.00	10.28	5.75	0.56	-5.05
17.00	10.26	5.48	0.53	-5.45
18.00	10.29	5.18	0.50	-5.97
19.00	10.29	4.90	0.48	-6.44
20.00	10.32	4.66	0.45	-6.91
25.00	10.26	3.57	0.35	-9.17
30.00	10.27	2.79	0.27	-11.33
40.00	10.24	1.78	0.17	-15.19
50.00	10.27	1.22	0.12	-18.50
60.00	10.26	0.88	0.09	-21.29
70.00	10.27	0.67	0.06	-23.76
80.00	10.27	0.52	0.05	-25.94
90.00	10.28	0.42	0.04	-27.81
100.00	10.25	0.34	0.03	-29.54
200.00	10.15	0.09	0.01	-41.02

B.2 Band-pass Frequency Response

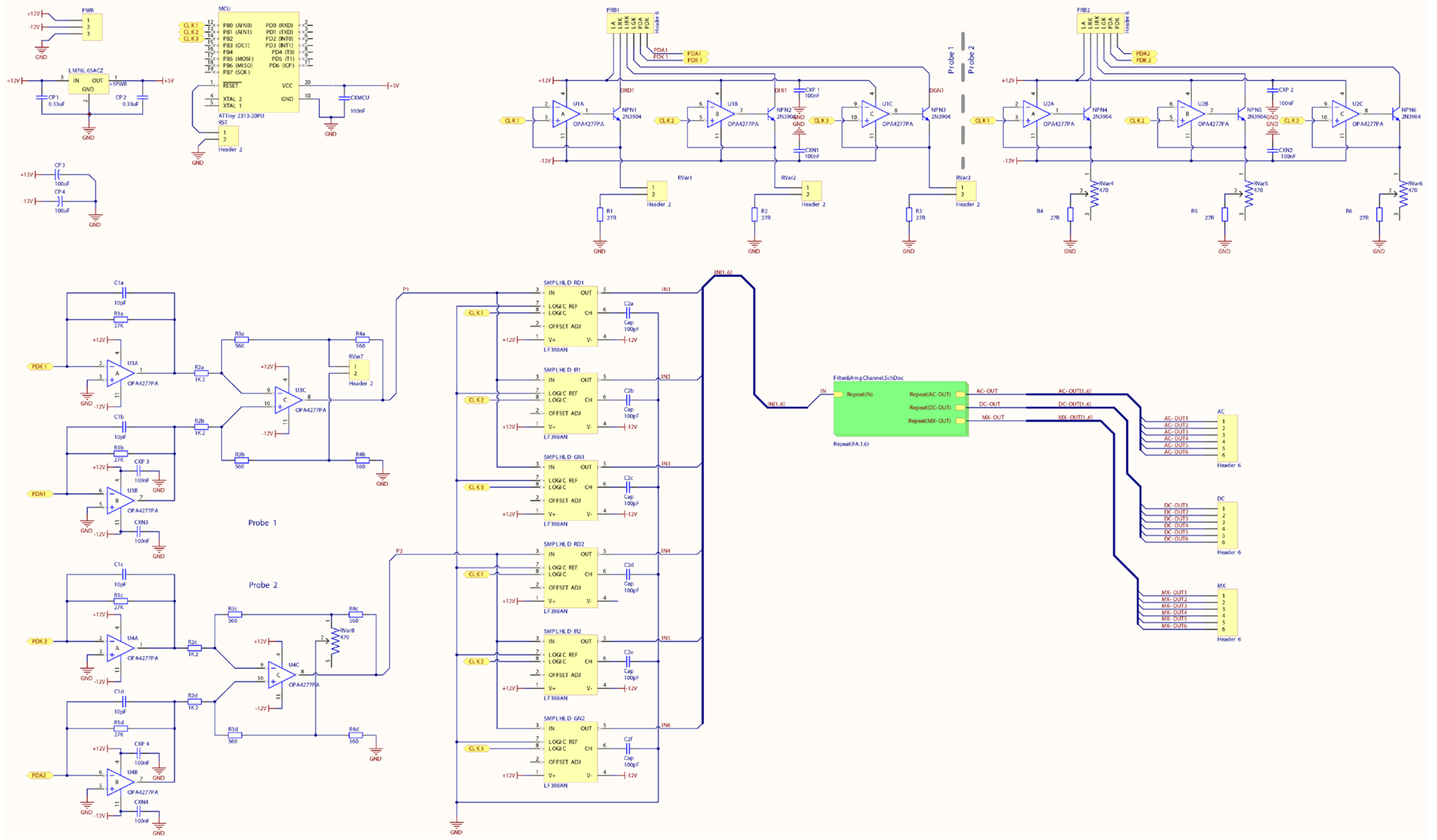
Frequency (Hz)	Vin (V)	Vout (V)	Gain (Vout/Vin)	20*log(Gain) (dB)
0.05	10.60	0.25	0.02	-32.55
0.06	10.60	0.35	0.03	-29.75
0.07	10.50	0.44	0.04	-27.48
0.08	10.60	0.56	0.05	-25.48
0.09	10.60	0.68	0.06	-23.84
0.10	10.60	0.82	0.08	-22.21
0.15	10.60	1.66	0.16	-16.12
0.20	10.70	2.59	0.24	-12.32
0.25	10.70	3.51	0.33	-9.68
0.30	10.60	4.40	0.42	-7.64
0.35	10.60	5.16	0.49	-6.25
0.40	10.60	5.82	0.55	-5.21
0.45	10.70	6.40	0.60	-4.46
0.50	10.50	6.89	0.66	-3.65
0.55	10.50	7.32	0.70	-3.13
0.60	10.60	7.62	0.72	-2.87
0.65	10.60	7.96	0.75	-2.49
0.70	10.60	8.21	0.77	-2.22
0.75	10.60	8.38	0.79	-2.04
0.80	10.60	8.59	0.81	-1.82
0.85	10.60	8.69	0.82	-1.73
0.90	10.60	8.86	0.84	-1.56
0.95	10.70	8.98	0.84	-1.53
1.00	10.60	9.07	0.86	-1.35
1.50	10.60	9.62	0.91	-0.84
2.00	10.60	9.80	0.92	-0.68
2.50	10.60	9.80	0.92	-0.68
3.00	10.60	9.75	0.92	-0.73
3.50	10.60	9.72	0.92	-0.75
4.00	10.60	9.62	0.91	-0.84
5.00	10.60	9.44	0.89	-1.01
6.00	10.60	9.15	0.86	-1.28
7.00	10.60	8.89	0.84	-1.53
8.00	10.60	8.58	0.81	-1.84
9.00	10.60	8.24	0.78	-2.19
10.00	10.60	7.88	0.74	-2.58
10.50	10.60	7.70	0.73	-2.78
11.00	10.60	7.52	0.71	-2.98
11.50	10.60	7.35	0.69	-3.18
12.00	10.60	7.17	0.68	-3.39
12.50	10.60	6.92	0.65	-3.70
13.00	10.60	6.84	0.65	-3.81
13.50	10.60	6.64	0.63	-4.06
14.00	10.70	6.50	0.61	-4.33
15.00	10.60	6.16	0.58	-4.71
16.00	10.60	5.84	0.55	-5.18
17.00	10.60	5.56	0.52	-5.60
18.00	10.28	5.19	0.51	-5.93
19.00	10.30	4.91	0.48	-6.44
20.00	10.24	4.65	0.45	-6.86
25.00	10.28	3.58	0.35	-9.15
30.00	10.29	2.80	0.27	-11.31
40.00	10.26	1.78	0.17	-15.20
50.00	10.27	1.22	0.12	-18.53
60.00	10.25	0.88	0.09	-21.31
70.00	10.26	0.67	0.07	-23.75
80.00	10.28	0.52	0.05	-25.91
90.00	10.28	0.42	0.04	-27.74
100.00	10.24	0.34	0.03	-29.53
200.00	10.18	0.09	0.01	-40.72

Appendix C

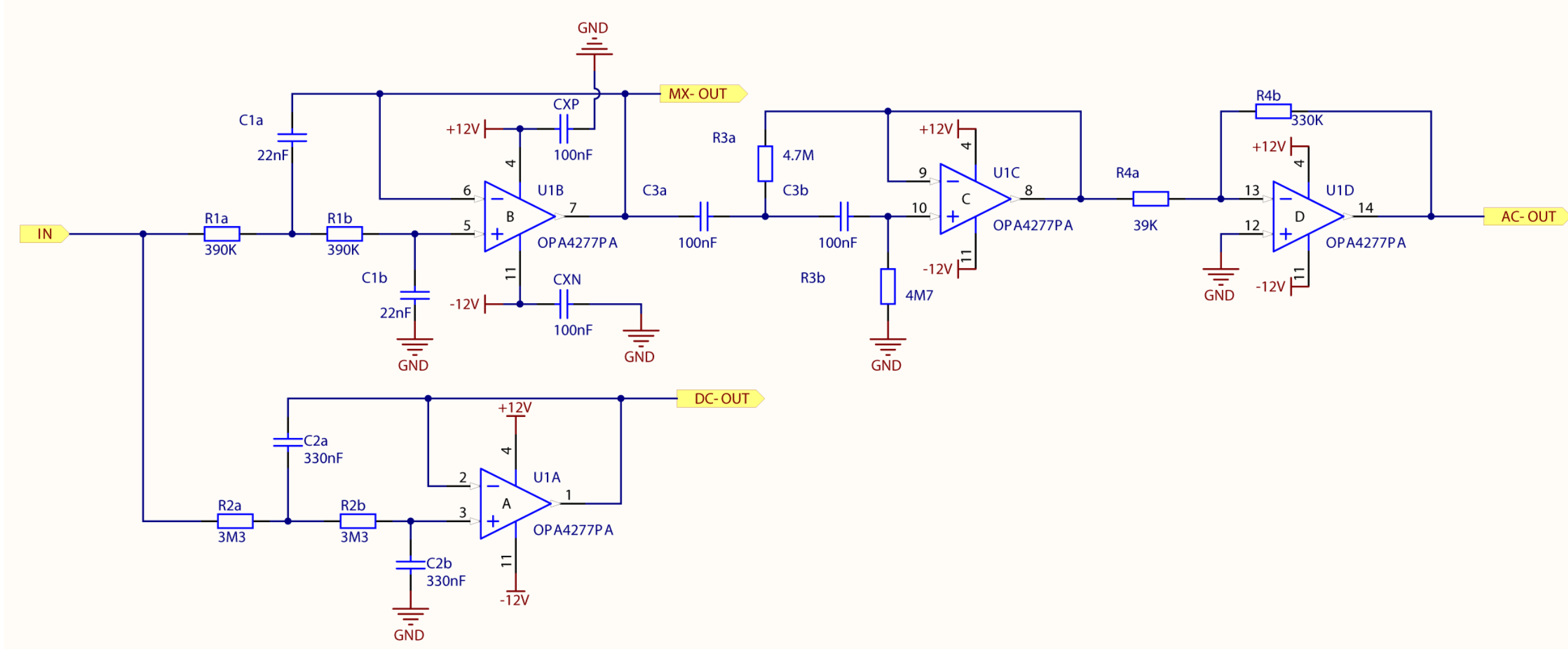
Final Printed Circuit Board Design

C.1 Final Circuit Schematics with Component Values

(PTO).

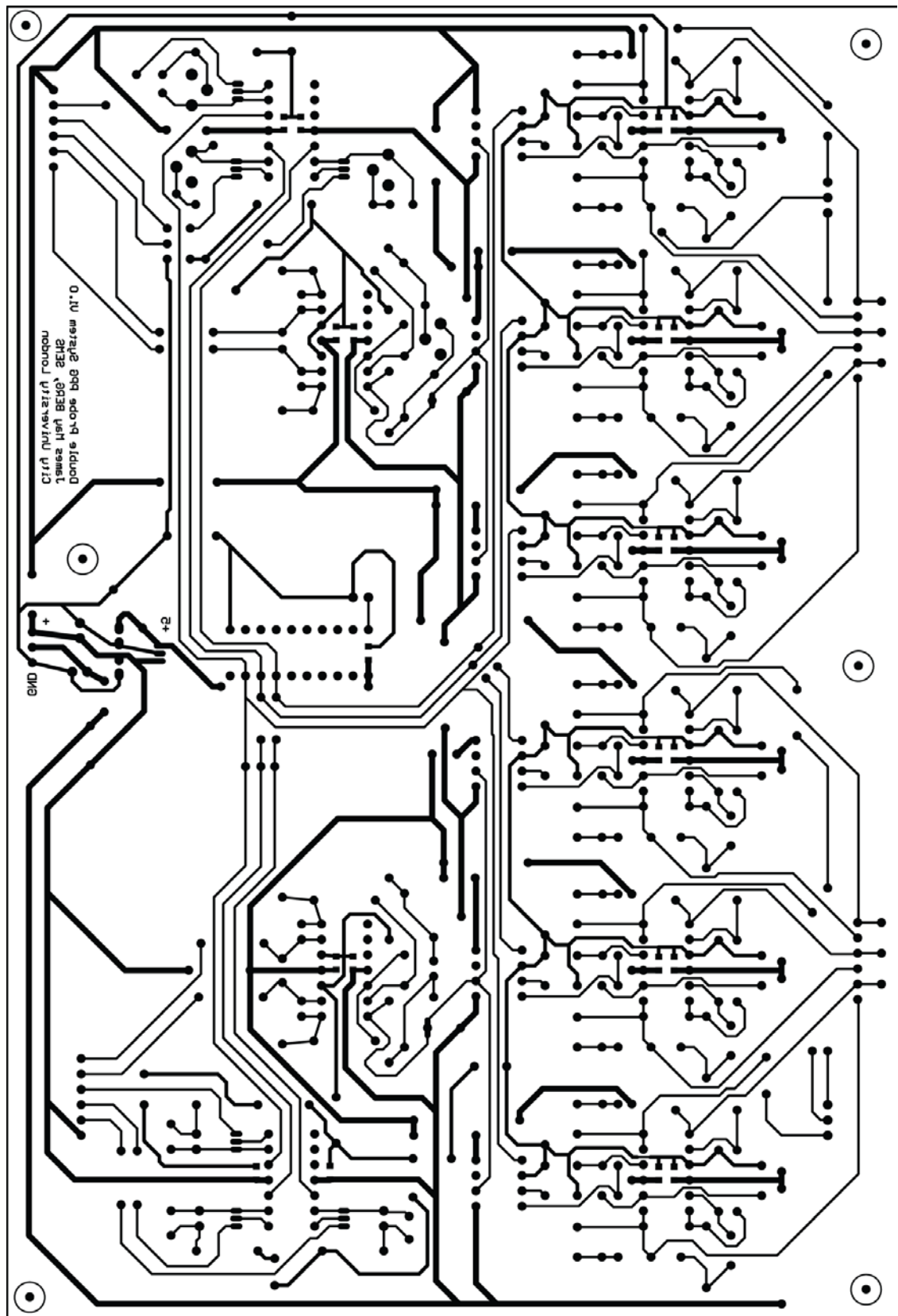


Main Schematic



Filter Section

C.2 Printed Circuit Board Layout / Photo-template



Appendix D

PPG data file output sample

(PTO)

```

=datetime                                     %Header Information
14/02/2013 09:42:58                          %Date + Time
=patID                                        %
sytemtest0123                                %Patient ID
=fs                                           %
200.00                                       %Sampling Rate
=ProbLocs                                    %
P1      P2                                    %Location of Probes
Toe/FootAnterior Fontanel
=events                                       %Event Markers successfully merged with raw data
Event 1 122.4700                             %
Event 2 128.4700                             %
Event 3 132.4710                             %
Event 4 136.4730                             %
Event 5 138.4690                             %
Event 6 142.4690                             %
Event 7 146.4720                             %
Event 8 150.4710                             %
Event 9 154.4720                             %
Event 10160.4720                             %

=Start of Raw Data: data =                  %Raw Data Starts here, each channel is a column separated by tabs, channel names included at top of
                                             %column
p1GNac p1GNmxp1IRac p1IRmx p1RDac p1RDmx p2GNac p2GNmxp2IRac p2IRmx p2RDac p2RDmx
-5.3228 5.4604 5.4604 5.4604 5.4604 5.4604 -1.4710 -1.7785 -2.1565 -1.8075 -7.2266 -5.0919 -0.6978
-5.3228 5.4604 5.4604 5.4604 5.4604 5.4604 -1.4835 -1.7910 -2.1696 -1.8200 -7.2437 -5.1044 -1.3066
-5.3228 5.4604 5.4604 5.4604 5.4604 5.4604 -1.4743 -1.7756 -2.1522 -1.8035 -7.2243 -5.0808 -1.3467
-5.3228 5.4604 5.4604 5.4604 5.4604 5.4604 -1.4842 -1.7884 -2.1670 -1.8200 -7.2414 -5.0913 -1.2990
-5.3228 5.4604 5.4604 5.4604 5.4604 5.4604 -1.4687 -1.7733 -2.1456 -1.8039 -7.2203 -5.0627 -1.2592
-5.1553 5.4604 5.4604 5.4604 5.4604 5.4604 -1.4723 -1.7684 -2.1361 -1.8016 -7.2108 -5.0492 -1.2375
-4.9335 5.4604 5.4604 5.4604 5.4604 5.4604 -1.4937 -1.7927 -2.1644 -1.8276 -7.2259 -5.0712 -1.2197
-4.6747 5.4604 5.4604 5.4604 5.4604 5.4604 -1.4723 -1.7657 -2.1361 -1.8052 -7.1927 -5.0360 -1.2388
-4.3932 5.4604 5.4604 5.4604 5.4604 5.4604 -1.4977 -1.7910 -2.1630 -1.8381 -7.2170 -5.0666 -1.2056
-4.0970 5.4604 5.4604 5.4604 5.4604 5.4604 -1.4760 -1.7621 -2.1364 -1.8174 -7.1818 -5.0347 -1.2003
-3.9611 5.4604 5.4604 5.4604 5.4604 5.4604 -1.4931 -1.7825 -2.1565 -1.8443 -7.1966 -5.0548 -1.2260
-3.8882 5.4604 5.4604 5.4604 5.4604 5.4604 -1.5023 -1.7858 -2.1653 -1.8578 -7.2068 -5.0666 -1.1776
-3.9512 5.4604 5.4604 5.4604 5.4604 5.4604 -1.4917 -1.7756 -2.1594 -1.8473 -7.1927 -5.0597 -1.2306
-3.9206 5.4604 5.4604 5.4604 5.4604 5.4604 -1.4996 -1.7838 -2.1696 -1.8614 -7.1983 -5.0762 -1.2151
-3.8153 5.4604 5.4604 5.4604 5.4604 5.4604 -1.4931 -1.7772 -2.1597 -1.8562 -7.1855 -5.0748 -1.2082
-3.7962 5.4604 5.4604 5.4604 5.4604 5.4604 -1.4885 -1.7703 -2.1584 -1.8473 -7.1782 -5.0729 -1.2046
-3.8546 5.4604 5.4604 5.4604 5.4604 5.4604 -1.5026 -1.7828 -2.1742 -1.8687 -7.1930 -5.0985 -1.2010
-5.3228 5.4604 5.4604 5.4604 5.4604 5.4604 -1.4710 -1.7785 -2.1565 -1.8075 -7.2266 -5.0919 -0.6978
-5.3228 5.4604 5.4604 5.4604 5.4604 5.4604 -1.4835 -1.7910 -2.1696 -1.8200 -7.2437 -5.1044 -1.3066
-5.3228 5.4604 5.4604 5.4604 5.4604 5.4604 -1.4743 -1.7756 -2.1522 -1.8035 -7.2243 -5.0808 -1.3467
-5.3228 5.4604 5.4604 5.4604 5.4604 5.4604 -1.4842 -1.7884 -2.1670 -1.8200 -7.2414 -5.0913 -1.2990
-5.3228 5.4604 5.4604 5.4604 5.4604 5.4604 -1.4687 -1.7733 -2.1456 -1.8039 -7.2203 -5.0627 -1.2592
-5.1553 5.4604 5.4604 5.4604 5.4604 5.4604 -1.4723 -1.7684 -2.1361 -1.8016 -7.2108 -5.0492 -1.2375
-4.9335 5.4604 5.4604 5.4604 5.4604 5.4604 -1.4937 -1.7927 -2.1644 -1.8276 -7.2259 -5.0712 -1.2197
-4.6747 5.4604 5.4604 5.4604 5.4604 5.4604 -1.4723 -1.7657 -2.1361 -1.8052 -7.1927 -5.0360 -1.2388
-4.3932 5.4604 5.4604 5.4604 5.4604 5.4604 -1.4977 -1.7910 -2.1630 -1.8381 -7.2170 -5.0666 -1.2056
-4.0970 5.4604 5.4604 5.4604 5.4604 5.4604 -1.4760 -1.7621 -2.1364 -1.8174 -7.1818 -5.0347 -1.2003
-3.9611 5.4604 5.4604 5.4604 5.4604 5.4604 -1.4931 -1.7825 -2.1565 -1.8443 -7.1966 -5.0548 -1.2260
-3.8882 5.4604 5.4604 5.4604 5.4604 5.4604 -1.5023 -1.7858 -2.1653 -1.8578 -7.2068 -5.0666 -1.1776
-3.9512 5.4604 5.4604 5.4604 5.4604 5.4604 -1.4917 -1.7756 -2.1594 -1.8473 -7.1927 -5.0597 -1.2306
-3.9206 5.4604 5.4604 5.4604 5.4604 5.4604 -1.4996 -1.7838 -2.1696 -1.8614 -7.1983 -5.0762 -1.2151
-3.8153 5.4604 5.4604 5.4604 5.4604 5.4604 -1.4931 -1.7772 -2.1597 -1.8562 -7.1855 -5.0748 -1.2082
-3.7962 5.4604 5.4604 5.4604 5.4604 5.4604 -1.4885 -1.7703 -2.1584 -1.8473 -7.1782 -5.0729 -1.2046
-3.8546 5.4604 5.4604 5.4604 5.4604 5.4604 -1.5026 -1.7828 -2.1742 -1.8687 -7.1930 -5.0985 -1.2010
-5.3228 5.4604 5.4604 5.4604 5.4604 5.4604 -1.4710 -1.7785 -2.1565 -1.8075 -7.2266 -5.0919 -0.6978
-5.3228 5.4604 5.4604 5.4604 5.4604 5.4604 -1.4835 -1.7910 -2.1696 -1.8200 -7.2437 -5.1044 -1.3066
-5.3228 5.4604 5.4604 5.4604 5.4604 5.4604 -1.4743 -1.7756 -2.1522 -1.8035 -7.2243 -5.0808 -1.3467
-5.3228 5.4604 5.4604 5.4604 5.4604 5.4604 -1.4842 -1.7884 -2.1670 -1.8200 -7.2414 -5.0913 -1.2990
-5.3228 5.4604 5.4604 5.4604 5.4604 5.4604 -1.4687 -1.7733 -2.1456 -1.8039 -7.2203 -5.0627 -1.2592
-5.1553 5.4604 5.4604 5.4604 5.4604 5.4604 -1.4723 -1.7684 -2.1361 -1.8016 -7.2108 -5.0492 -1.2375
-4.9335 5.4604 5.4604 5.4604 5.4604 5.4604 -1.4937 -1.7927 -2.1644 -1.8276 -7.2259 -5.0712 -1.2197
-4.6747 5.4604 5.4604 5.4604 5.4604 5.4604 -1.4723 -1.7657 -2.1361 -1.8052 -7.1927 -5.0360 -1.2388
-4.3932 5.4604 5.4604 5.4604 5.4604 5.4604 -1.4977 -1.7910 -2.1630 -1.8381 -7.2170 -5.0666 -1.2056
-4.0970 5.4604 5.4604 5.4604 5.4604 5.4604 -1.4760 -1.7621 -2.1364 -1.8174 -7.1818 -5.0347 -1.2003
-3.9611 5.4604 5.4604 5.4604 5.4604 5.4604 -1.4931 -1.7825 -2.1565 -1.8443 -7.1966 -5.0548 -1.2260
-3.8882 5.4604 5.4604 5.4604 5.4604 5.4604 -1.5023 -1.7858 -2.1653 -1.8578 -7.2068 -5.0666 -1.1776

```

Appendix E

Approved Clinical Trials Protocol and Ethical Approval Confirmation



National Research Ethics Service

NRES Committee London - City & East

South West REC Centre

Whitefriars

Level 3, Block B

Lewins Mead

Bristol

BS1 2NT

Telephone: 01173421386

Facsimile: 01173420445

07 October 2011

Professor Panayiotis Kyriacou
City University London
SEMS, City University London
Northampton Square
EC1V OHB

Dear Professor Kyriacou

Study title: A Pilot Investigation of Oesophageal and Fontanelle Arterial and Venous Oxygen Saturations in Neonates and Infants Utilising Miniature Optical Photometric Sensors

REC reference: 11/LO/1431

Thank you for your letter of 26 September 2011, responding to the Committee's request for further information on the above research and submitting revised documentation.

The further information was considered at the meeting of the Committee held on 06 October 2011. A list of the members who were present at the meeting is attached.

Confirmation of ethical opinion

On behalf of the Committee, I am pleased to confirm a favourable ethical opinion for the above research on the basis described in the application form, protocol and supporting documentation as revised, subject to the conditions specified below.

The Committee noted that you have done what was requested in the provisional opinion letter. The Committee agreed that the researchers involved in the study are experienced in performing similar procedures in adults and the study can potentially benefit the infants and children in future.

The Committee therefore gave a favourable opinion for the study but the Committee again strongly advised that in the event of any adverse event (serious or not) the study should be immediately stopped and the Committee should be immediately notified.

Ethical review of research sites

NHS sites

The favourable opinion applies to all NHS sites taking part in the study, subject to management permission being obtained from the NHS/HSC R&D office prior to the start of the study (see "Conditions of the favourable opinion" below).

Non-NHS sites

Conditions of the favourable opinion

The favourable opinion is subject to the following conditions being met prior to the start of the study.

Management permission or approval must be obtained from each host organisation prior to the start of the study at the site concerned.

Management permission ("R&D approval") should be sought from all NHS organisations involved in the study in accordance with NHS research governance arrangements.

Guidance on applying for NHS permission for research is available in the Integrated Research Application System or at <http://www.rdforum.nhs.uk>.

Where a NHS organisation's role in the study is limited to identifying and referring potential participants to research sites ("participant identification centre"), guidance should be sought from the R&D office on the information it requires to give permission for this activity.

For non-NHS sites, site management permission should be obtained in accordance with the procedures of the relevant host organisation.

Sponsors are not required to notify the Committee of approvals from host organisations

It is the responsibility of the sponsor to ensure that all the conditions are complied with before the start of the study or its initiation at a particular site (as applicable).

Approved documents

The final list of documents reviewed and approved by the Committee is as follows:

Document	Version	Date
Covering Letter		15 August 2011
Covering Letter		26 September 2011
Evidence of insurance or indemnity		01 December 2010
Investigator CV		15 August 2011
Other: Student CV - James May		15 August 2011
Other: CV for Lead Clinician - Andy Petros		15 August 2011
Other: Unfavourable Opinion Letter - South West London REC 3		14 February 2011
Other: Unfavourable Opinion Letter - London City and East REC		14 June 2011
Participant Consent Form: Participant Consent Form - Oesophageal Study	3	15 August 2011
Participant Consent Form: Participant Consent Form - Fontanelle Study	3	15 August 2011
Participant Information Sheet: Participant Information Sheet - Oesophageal Study	3	15 August 2011
Participant Information Sheet: Participant Information Sheet - Fontanelle Study	3	15 August 2011
Participant Information Sheet: Parent/Guardian Information Leaflet-Fontanelle Sensor for Babies	4	16 September 2011
Participant Information Sheet: Parent/Guardian Information Leaflet-Oesophageal Sensor for Infants	4	16 September 2011
Protocol	4	15 August 2011

REC application	3.3	16 August 2011
Referees or other scientific critique report		16 August 2011
Response to Request for Further Information		26 September 2011

Statement of compliance

The Committee is constituted in accordance with the Governance Arrangements for Research Ethics Committees (July 2001) and complies fully with the Standard Operating Procedures for Research Ethics Committees in the UK.

After ethical review

Reporting requirements

The attached document “*After ethical review – guidance for researchers*” gives detailed guidance on reporting requirements for studies with a favourable opinion, including:

- Notifying substantial amendments
- Adding new sites and investigators
- Notification of serious breaches of the protocol
- Progress and safety reports
- Notifying the end of the study

The NRES website also provides guidance on these topics, which is updated in the light of changes in reporting requirements or procedures.

Feedback

You are invited to give your view of the service that you have received from the National Research Ethics Service and the application procedure. If you wish to make your views known please use the feedback form available on the website.

Further information is available at National Research Ethics Service website > After Review

11/LO/1431	Please quote this number on all correspondence
-------------------	---

With the Committee’s best wishes for the success of this project

Yours sincerely,



pp Dr Arthur T. Tucker
Chair

Email: Ubh-tr.CityandEastREC@nhs.net

Enclosures: List of names and professions of members who were present at the meeting and those who submitted written comments

“After ethical review – guidance for researchers”

*Copy to: Mr James M May
Ms Tracy Assari, Great Ormond Street*

NRES Committee London - City & East

Attendance at Committee meeting on 06 October 2011

Committee Members:

Name	Profession	Present	Notes
Dr Louise Abrams	Pharmacology (Vice Chair)	Yes	
Dr Chandan Alam	Experimental Pathology	No	
Dr Marie E Bardsley	Director	No	
Dr Ayse Baxter	Independent Consultant Pharmaceutical Physician	Yes	
Mr Frank Cross	Consultant General and Vascular Surgeon	No	
Ms Stephanie Ellis		No	
Dr Miran Epstein	Senior Lecturer Medical Ethics	Yes	
Mrs Janelle Hill	Non-medical lay member	Yes	
Professor Atholl Johnston	Professor of Clinical Pharmacology	Yes	
Professor Malcolm Law	Epidemiologist	No	
Mr John Lynch	Lay Member	Yes	
Dr Eleni Palazidou	Consultant Psychiatrist & Honorary Senior Lecturer	Yes	
Dr Kim Piper	Consultant Histopathologist/Hon Sen Lecturer in Oral Pathology	Yes	
Dr Melanie Powell	Consultant Clinical Oncologist	Yes	
Dr Arthur T. Tucker	Principal Clinical Scientist & Senior Lecturer (REC Chairman)	Yes	
Ms Brigid Tucker	Non-Medical Lay Member	Yes	
Professor David Wingate	Gastroenterologist	Yes	
Dr Ariel Zosmer	Consultant, Associate Specialist	Yes	

Also in attendance:

Name	Position (or reason for attending)
Mr Rajat Khullar	Committee Coordinator
Mr Roger Maran	Observer

1. Introduction

1.1 Background

About twenty-five years ago most Neonatal Intensive Care Units (NICU) only had the ability to routinely monitor a baby's ECG and respiration rate [1]. Times have changed dramatically and a typical NICU bedside monitor will incorporate ECG, heart-rate, respiration, temperature, non-invasive blood-pressure, oxygen saturation (SpO₂) and invasive blood-pressure [2].

Pulse oximetry is a non-invasive photometric technique (pulse oximeter sensors are usually placed on the finger, earlobe or toe) that provides information about the arterial blood oxygen saturation (SpO₂) and heart rate, and has widespread clinical applications. Pulse oximeters estimate arterial oxygen saturation by shining light at two

different wavelengths, red and infrared, through vascular tissue. In this method the pulsatile PPG (ac PPG) signal associated with cardiac contraction is assumed to be attributable solely to the arterial blood component. The amplitudes of the red and infrared ac PPG signals are sensitive to changes in arterial oxygen saturation because of differences in the light absorption of oxygenated and deoxygenated haemoglobin at these two wavelengths. From the ratios of these amplitudes, and the corresponding dc photoplethysmographic components, arterial blood oxygen saturation (SpO_2) is estimated. Hence, the technique of pulse oximetry relies on the presence of adequate peripheral arterial pulsations, which are detected as PPG signals.

In neonatal and paediatric monitoring, when peripheral perfusion is poor, as in states of hypovolaemia, hypothermia, vasoconstriction, low cardiac output and low mean arterial pressure, pulse oximeter readings become unreliable or cease altogether [3, 4]. The oxygenation readings become unreliable in these circumstances because conventional pulse oximeter sensors that are usually placed on the most peripheral parts of the body such as the finger or toe, where pulsatile flow is most vulnerable, as it is compromised by diversion of blood flow to more vital organs. Hence, pulse oximetry becomes unreliable in a significant group of patients at just the time when the measurement of blood oxygen saturation would be clinically of most value.

A previous pilot study [5] investigated PPG signals in the neonatal oesophagus based on the hypothesis that such a central site might provide better quality PPG signals and therefore enable the continuous monitoring of SpO_2 when the peripheral sites fail [3- 4, 6 - 13]. This pilot study was only applied to a very small population plus the monitoring of oesophageal PPGs was only brief and therefore did not allow a more rigorous investigation of PPG signals and oxygen saturation values from the infant oesophagus. The proposed study aims to investigate PPG signals from the infant oesophagus more rigorously in a larger sample size, and for this reason a new miniaturised custom made oesophageal reflective PPG sensor, which fits in a 12F feeding tube (3.6mm diameter), will be used. This new physiological measurement study will also give us the opportunity to compare the oesophageal oxygen saturation values with CE-marked commercial peripheral pulse oximetry devices, especially at times when the peripheral perfusion is compromised.

This study will also investigate PPG signals from another monitoring site; the Anterior Fontanelle (AF) on the scalp of the neonate utilising a custom made non-invasive PPG sensor. Fontanelle PPG signals and SpO_2 values will be compared with toe or finger PPGs and SpO_2 s, and where possible with oesophageal PPGs and SpO_2 s. So far there are no known similar studies where the fontanelle was used as a measurement site in intensive care. The only reported study, of similar nature, made preliminary

measurements of PPGs from the fontanelle [14], however the results of this study were inconclusive. As well as direct brain oxygen saturation readings, our study aims to investigate what underlying anatomy may influence the readings we obtain, and whether there is a pulsatile venous signal that can be used to calculate venous oxygen saturation (SvO₂) in the newborn. Monitoring of the neonatal brain through the AF may also reveal information of other pathologies such as intracerebral bleeding and changes in intracranial pressure.

For comparison purposes (with the oesophageal or fontanelle PPGs) a custom made toe PPG sensor will also be used in these investigations.

[1] McIntosh, N., 1983. The Monitoring of Critically Ill Neonates. *Journal of Medical Engineering & Technology*, 7(3), 121-129.

[2] Murković, I., Steinberg, M.D. & Murković, B., 2004. Sensors in neonatal monitoring: current practice and future trends. *Technol. Health Care*, 11(6), 399-412.

[3] Poets, C.F. & Southall, D.P., 1994. Non-invasive monitoring of oxygenation in infants and children: practical considerations and areas of concern. *Pediatrics*, 93(5), 737-746.

[4] Poets, C.F., Urschitz, M.S. & Bohnhorst, B., 2002. Pulse oximetry in the neonatal intensive care unit (NICU): detection of hyperoxemia and false alarm rates. *Anesthesia and Analgesia*, 94(1 Suppl), S41-43.

[5] Kyriacou, P.A. et al., 2008. A Pilot Study of Neonatal and Paediatric Esophageal Pulse Oximetry. *Anesthesia and Analgesia*, 107(3), 905-908.

[6] Salyer, J.W., 2003. Neonatal and paediatric pulse oximetry. *Respiratory Care*, 48(4), 386-396; discussion 397-398.

[7] Fanconi, S., 1988. Reliability of pulse oximetry in hypoxic infants. *The Journal of Pediatrics*, 112(3), 424-427.

[8] Hay, W.W., Brockway, J.M. & Eyzaguirre, M., 1989. Neonatal pulse oximetry: accuracy and reliability. *Pediatrics*, 83(5), 717-722.

[9] Praud, J. et al., 1989. Accuracy of two wavelength pulse oximetry in neonates and infants. *Pediatric Pulmonology*, 6(3), 180-182.

[10] Miyasaka, K., 2002. Pulse oximetry in the management of children in the PICU. *Anesthesia and Analgesia*, 94(1 Suppl), S44-46.

[11] Hay, W.W. et al., 2002. Reliability of conventional and new pulse oximetry in neonatal patients. *Journal of Perinatology: Official Journal of the California Perinatal Association*, 22(5), 360-366.

[12] Malviya, S. et al., 2000. False alarms and sensitivity of conventional pulse oximetry versus the Masimo SET technology in the pediatric postanesthesia care unit. *Anesthesia and Analgesia*, 90(6), 1336-1340.

[13] Wilson, S., 1990. Conscious sedation and pulse oximetry: false alarms? *Pediatric Dentistry*, 12(4), 228-232.

[14] Dassel, A.C. et al., 1997. Effect of location of the sensor on reflectance pulse oximetry. *British Journal of Obstetrics and Gynaecology*, 104(8), 910-916.

1.2 Biomedical Engineering Research Group, City University London

The Biomedical Engineering research group at City University originated in the mid-90's with the aim of promoting research in the emerging field of Biomedical Engineering, a profession that applies the principles of the science of physics/engineering directly to the devices and operation of the complex medical devices used in the diagnosis and treatment of the sick and injured.

The main objectives of the group are:

to undertake theoretical and applied research in the broad area of biomedical engineering

to develop and exploit engineered solutions of the research

to provide a focus for multi-disciplinary based research in the School of Engineering

to provide advanced research training in the areas of its activities

to develop strong collaborative research links with Industry, Services and Academia

to work closely with the national health sector (NHS)

The core of the group's research activities lies in the application of electronic, optical and physical techniques to solve practical problems in surgery, anaesthesia and intensive care. The main research directions are focused upon the understanding, development and applications of instrumentation and measurements to facilitate the prognosis, diagnosis and treatment of disease or the rehabilitation of patients. Mathematical modelling and computed fluid dynamic (CFD) studies of various physiological and anatomical functions are also used as a basis for new instrumentation development. Challenges from various clinical specialities are being addressed, leading to interdisciplinary applications of advanced and novel technologies. Current areas of research are:

Non-invasive techniques for blood gas measurements

Electro-optical and fibre-optic medical sensors

Microprocessor-based medical instrumentation

Neonatal/paediatric monitoring

Respiration Techniques

Computer implemented virtual medical instruments
Physiological measurements
Mathematical modelling of light interaction with biological media
Medical Ultrasound
Bio-signal processing

The group has close collaborations with scientists and clinicians with world renowned clinical institutions and industries such as:

St Bartholomew's Hospital
Great Ormond Street Hospital for Children
The Royal London Hospital
St Andrew's Centre for Plastic Surgery & Burns
The Royal Brompton Hospital
Yale Medical School
GE Healthcare
Siemens Medical
 Draeger

One of the main research areas that make the group nationally and internationally known is the area of Photoplethysmography, where many studies have been conducted in different populations and in different anatomical areas utilising custom made peripheral or indwelling PPG sensors. These investigations have a main focus the understanding of the PPG signal both in the time and frequency domain. These investigations seek to also understand the underlying haemodynamics of the various areas/organs that are monitored with an aim to contribute to the further knowledge of perfusion. These studies are conducted using PPG systems/sensors customised to the different anatomical areas that are investigated (i.e. oesophagus, splanchnic organs, finger, toe, brain, etc). During these PPG investigations commercial technologies (pulse oximeter, blood gas analysers, co-oximeters) are also used as comparative tools.

Some of the studies that were undertaken in this area are summarised below:

04/Q0508/119 - Paediatric Oesophageal Pilot Study

06/Q0603/110 - Evaluation of a new optical method for measuring brain tissue oxygenation in intensive care patients being monitored via an intra-cranial bolt.

07/Q0603/41 - Evaluation of a fibre-optic technique for the measurement of arterial oxygen saturation in the oesophagus of anaesthetised patients undergoing routine surgery

08/H0703/22 - Custom made PPG sensor for assessing PPGs and SpO₂s from splanchnic organ during open laparotomy splanchnic Study

08/H0703/48 - Evaluation of a fibre-optic technique for the measurement of arterial oxygen saturation in the oesophagus of anaesthetised patients (Amendment of 07/Q0603/41 to include jejunal flaps)

10/H0703/39 – Non-invasive optical method for monitoring free flap perfusion in plastic surgery

11/LO/0048 - Investigation of a new non-invasive optical technique for measurement of local venous oxygen saturation

2 Study Aims and Objectives

The aim of this study is to investigate oesophageal and anterior fontanelle Photoplethysmographic (PPG) signals in two study groups (critically ill neonates and infants) accordingly. For this purpose two custom made optical PPG sensors (one for the oesophagus (OES) and one for the anterior fontanelle (AF)) and an in-house designed processing system (see Appendix A) have been developed. The hypothesis underlying this project is that a more central site, such as the OES or the AF might remain adequately perfused in cases of compromised peripheral perfusion, giving the possibility of monitoring blood oxygen saturation (SpO₂) at the oesophagus or the AF when conventional peripheral (finger or toe) oximetry fails. The work program will be carried out through experimental and clinical measurements in vivo encompassing the following objectives:

To investigate PPG signals from nonconventional (finger and toe) anatomical locations and identify if such signals are reliable for the estimation of blood oxygen saturation by comparing them with commercial pulse oximeters and results from “gold standard” techniques, such as blood gas analysis.

To determine if the fontanelle PPG signals obtained from the neonate can be used as a more reliable reading (compared with the periphery, i.e. toe) for arterial blood oxygen saturation in cases of low perfusion.

To determine if the oesophageal PPG signals obtained from the infant can be used as a more reliable reading (compared with the periphery, i.e. toe) for arterial blood oxygen saturation in cases of low perfusion.

Investigate if either site yields signals that may contain a venous component that could be used to calculate venous oxygen saturation.

To determine whether fontanelle PPG signals can be used to detect other pathologies associated with neonates in intensive care, i.e. intracerebral bleeds, change in intracranial pressure, etc.

3 Study Design

3.1. Outline

Studies will be performed using two custom, in-house made, non-invasive optical reflectance PPG sensors for each study group. The infant study will utilise a custom, in-house made, reflectance PPG/pulse oximeter sensor for the monitoring of PPGs and oxygen saturation in the oesophagus. The neonatal study will exploit a custom, in-house made, reflectance sensor with geometry adapted to the AF for the non-invasive monitoring of brain PPGs. For each group a second custom, in-house made, periphery toe PPG/SpO₂ sensor, identical in geometry of a commercial sensor and electrically and optically identical to the oesophageal and fontanelle sensor will also be used. This is to facilitate comparison of PPG signals from the periphery and the oesophagus or the fontanelle.

3.2 Patient Selection and Location

Following Ethical Committee approval and approved consent from the parent or guardian, 30 (maximum) neonates (Fontanelle study) and 30 (maximum) infants (Oesophageal study) on the intensive care unit at Great Ormond Street Hospital for Children, and who meet the inclusion criteria (section 4.1), will be recruited for this study.

3.3 Study Procedure

3.3.1 Oesophageal study

The oesophageal PPG probe will be inserted into a sealed 12 French gauge stomach tube (used routinely in clinical practice). The tube will then be inserted by the lead clinician through the mouth into the oesophagus under direct vision. The stomach tube will be advanced into the oesophagus until the end of the probe itself is at a depth of 3-5 cm into the oesophagus. Depth will be assessed outside the body prior to insertion and measured to sit in a mid-thoracic position.

The toe sensor will also be placed by the lead clinician around the foot of the neonate. PPG traces and SpO₂ values from the oesophagus and the toe (using the custom made toe PPG sensor), along with ECG traces, will be recorded simultaneously. During the trial values of blood oxygen saturation from a commercial toe pulse oximeter will also be recorded. The Oesophageal and toe SpO₂ values will also be compared

with any routine blood gas analysis measurements that will take place during this investigation.

Oesophageal and toe PPG measurements will be recorded up to a period of 30 minutes as a baseline. After the initial period, oxygen concentration delivered will be increased by a factor of 50% above the baseline. Continuous monitoring will continue for a period of up to 1 hour. Delivered Oxygen concentration will be decreased back down to the baseline level and monitoring will continue for up to 30 minutes before termination of the trial. The total maximum study time for each recruited subject will be 2 hours unless otherwise stopped by the lead clinician (see section 4.4). All signals will be further analysed offline using the statistical methods described in section 5.

3.3.2 Fontanelle Study

The fontanelle sensor will be placed by the lead clinician on the anterior fontanelle (soft spot) of the neonate's scalp. The fontanelle sensor will adhere to the skin surface utilising a commercially available sterile reflectance oximeter adhesive patches/tape (Appendix A).

The toe sensor will also be placed by the lead clinician around the foot of the neonate. PPG traces and SpO₂ values from the fontanelle and the toe (using the custom made toe PPG sensor), along with ECG traces, will be recorded simultaneously. During the trial values of blood oxygen saturation from a commercial toe pulse oximeter will also be recorded. The fontanelle and toe SpO₂ values will also be compared with any routine blood gas analysis measurements that will take place during this investigation.

Fontanelle and toe PPG measurements will be recorded for a period of up to 30 minutes as a baseline. After the initial period oxygen concentration delivered will be increased by a factor of 50% above the baseline. Continuous monitoring will continue for a period of up to 1 hour. Delivered Oxygen concentration will be decreased back down to the baseline level and monitoring will continue for up to 30 minutes before termination of the trial. The total maximum study time for each recruited subject will be 2 hours unless otherwise stopped by the lead clinician (see section 4.4). All signals will be further analysed offline using the statistical methods described in section 5.

3.4 Study endpoints (applies to both studies)

After 2 hours of monitoring or earlier if the lead clinician responsible for the subject requests that we stop the study, or if the parent or guardian who is present requests that we stop the study (see section 4.4)

4 Subject Selection and Withdrawal

4.1 Inclusion Criteria

Parental/Guardian consent given

Normal oesophageal anatomy

Normal fontanelle anatomy (Neonates)

Over 3Kg

Greater than 36 weeks gestational age (Neonates)

Ventilated

Sedated

4.2 Exclusion Criteria

No Parental/Guardian consent given

Abnormal oesophageal anatomy/oesophageal procedures previously carried out

Abnormal fontanelle anatomy/closed fontanelle (Neonates)

Less than 3 Kg

Less than 36 weeks gestational age (Neonates)

Not ventilated

Not sedated

4.3 Subject Recruitment and Screening

Subjects will be assessed using the inclusion and exclusion criteria from available patient lists within the ICU. The screening will be carried out by a researcher acting under arrangements with the responsible care organisation. The researcher will have medical qualifications (e.g. medical research fellow).

Once a subject has been identified the parent/guardian will be approached at a time before the intended study. If they agree they will be handed an information sheet, given adequate time to reflect and consider and then they will be asked to sign a form of consent for the patient if they agree.

4.4 Withdrawal of Subjects

If the lead clinician responsible for the subject requests that we stop the study

If the parent or guardian who is present requests that we stop the study

5 Statistical Plan

5.1 Sample Size Determination

This pilot study is not intended to provide information for medical decisions affecting the direct care of the patients under examination, it is however intended that this study be used to inform further studies. Following discussion with the clinical experts it is suggested that the number of patients proposed for this investigation will yield enough data to allow comparative analysis between the proposed monitoring sites, and provide meaningful information about the sites under investigation.

5.2 Statistical Methods

Tests for normality.

Demographic statistics will be presented, mean, median, confidence intervals.

Non-parametric test for significant difference.

5.3 Recording of Adverse Events

Documented in full as per GCP guidelines

5.4 Study Stopping Rules

If the lead clinician responsible for the subject requests that we stop the study or if the parent or guardian who is present requests that we stop the study. This will be documented with reasons explaining why.

6 Data Handling and Record Keeping

6.1 Confidentiality

The personal data and measurements recorded will be kept locked in the office of the Principal Investigator. All study data will be anonymised and kept in electronic format in a password protected file on a personal computer. The computer will be kept in a locked office.

6.2 Study Documents

Parental information sheet.

Consent form.

Case Report Forms.

6.3 Records Retention

Following the publication of the study results, the database will be stored on a CD-ROM and filed in a locked filing cabinet. The Research Group will act as custodians for this data.

7 Study Monitoring, Auditing, and Inspecting

7.1 Study Monitoring Plan

The study will be conducted according to ICH/GCP standards. The chief investigator and members of the study research group will be responsible for monitoring the conduct of the study.

8 Ethical Considerations

8.1 Local Regulations

The local Investigator will ensure that this study is conducted in accordance with the Principles of the "Declaration of Helsinki" (as amended in Tokyo (1975), Venice (1983), Hong Kong (1989), South Africa (1996) and Edinburgh (2000)). <http://www.wma.net/e/policy/b3.htm> or with the laws of the country in which the research is conducted, whichever accords greater protection to the individual. The study will fully adhere to the principles outlined in the Guidelines for Good Clinical Practice" ICH Tripartite Guideline (January 1997)

8.2 Informed Consent

The investigators will obtain written informed consent from the parent/guardian of each patient prior to participation in the study, following adequate explanation of the aims, methods, anticipated benefits and potential hazards of the study.

8.3 Independent Ethics Committee/Institutional Review Board

This protocol and the accompanying material given to a potential patient (Patient Information Sheet, Consent form) as well as any advertising material will be submitted by the Investigator to an Independent Ethics Committee in the UK. Full approval by the Committee will be obtained prior to starting the study and will be fully documented by letter to the Chief Investigator naming the study site, local PI (who may also be the Chief Investigator) and date the Committee deemed the study as permissible at that site.

9 Study Finances

9.1 Funding Source

The study will be financed by the Engineering and Physical Sciences Research Council (EPSRC).

9.2 Indemnity for the performance of the study

The Chief Investigator and PhD Researcher have indemnity from City University London for clinical trials.

The Lead Clinician has indemnity from the NHS trust for clinical trials

9.3 Subject Payments

None

10 Publication Plan

The results of the study will be presented in international and national conferences and published in peer-reviewed journals

11 Attachments

This section should contain all pertinent documents associated with the management of the study. The following is a list of attachments, those with an asterisk* must be submitted to the Ethics Committee with the protocol.

Consent Form*

Information Sheet*

Appendix F

Pre-Normalised AC and DC Amplitudes

Patient #	RED AC Amplitudes (mV)					
	Pre FiO ₂ increase		During FiO ₂ increase		Post FiO ₂ increase	
	Foot	AF	Foot	AF	Foot	AF
1	93.1	118.2	91.1	131.7	86.8	152.2
2	194.3	64.0	150.7	54.4	159.5	43.2
4	136.5	86.4				
5	510.9	70.8	458.5	70.0	371.2	98.7
6	896.1	50.3	432.4	70.5	485.0	123.9
7	205.3	56.2	165.8	47.3	148.2	53.5
8	63.5	127.1	49.4	134.5	71.4	116.5
9	140.5	110.1	75.7	107.4	197.1	93.0
10	421.4	148.6	372.9	124.2	256.7	133.4
11	417.6	157.4	401.8	205.7	429.6	179.5
12	66.2	60.9	69.4	53.6		
13	57.5	97.0	46.3	64.5	53.3	64.4
14	553.9	130.5	775.9	86.7	1016.9	116.6
15	864.2	56.3				
16	421.4	45.2				
Mean	336.2	91.9	206.0	76.7	218.4	78.3
SD	279.1	37.7	229.4	57.4	273.1	60.3
Measurements (n)	15	15	12	12	11	11

Patient #	IR AC Amplitudes (mV)					
	Pre FiO ₂ increase		During FiO ₂ increase		Post FiO ₂ increase	
	Foot	AF	Foot	AF	Foot	AF
1	324.2	233.8	309.2	341.2	299.1	412.5
2	348.0	350.8	332.8	260.6	307.1	261.2
4	171.2	283.0				
5	1917.0	734.0	1790.7	643.6	1440.9	665.3
6	1544.5	89.6	1493.7	104.5	1922.5	235.6
7	308.1	130.5	224.1	105.8	202.3	88.7
8	75.3	296.9	84.4	354.9	100.0	352.3
9	160.5	370.5	158.0	189.8	197.4	238.3
10	982.9	618.8	943.6	395.8	539.8	438.7
11	592.3	562.5	690.8	641.7	648.2	495.0
12	144.0	178.7	164.4	127.6		
13	152.5	281.1	146.4	216.6	141.9	215.2
14	1559.5	218.2	1991.5	236.2	2277.2	358.1
15	1285.8	162.0				
16	707.3	150.4				
Mean	684.9	310.7	555.3	241.2	538.4	250.7
SD	618.3	190.0	680.5	206.5	737.5	206.0
Measurements (n)	15	15	12	12	11	11

GREEN AC Amplitudes (mV)						
Patient #	Pre FiO ₂ increase		During FiO ₂ increase		Post FiO ₂ increase	
	Foot	Font	Foot	Font	Foot	Font
1	29.8		28.5		27.9	
2	80.0		74.9		72.7	
4	59.7					
5	460.8	16.2	441.4	15.2	397.1	18.5
6	897.5		729.6		734.7	
7	178.4	26.9	212.4	21.2	182.7	21.7
8	64.3		70.6		79.3	
9	78.1		59.7		100.1	
10	624.4	19.4	521.0		318.4	
11	386.6		385.1		340.4	
12	159.8		186.1			
13	60.8	38.6	60.7	26.1	59.1	30.4
14	669.7		848.0		901.0	
15	746.2					
16	84.4					
Mean	305.4	6.7	241.2	4.2	214.2	4.7
SD	299.2	12.5	279.2	8.9	280.0	10.0
Measurements (n)	15	4	12	3	11	3

RED DC Amplitudes (mV)						
Patient #	Pre FiO ₂ increase		During FiO ₂ increase		Post FiO ₂ increase	
	Foot	AF	Foot	AF	Foot	AF
1	758.6	1771.1	786.8	1771.9	783.2	1750.5
2	3965.6	1896.6	4092.1	1891.2	3989.7	1903.2
4	5303.1	2820.7				
5	3583.9	1956.3	3740.7	1950.1	3787.8	1901.7
6	4351.4	1988.0	4795.5	1906.0	4953.3	1917.2
7	6115.0	1448.5	6504.7	1400.1	6260.5	2068.6
8	2924.6	3700.0	2991.5	3687.9	3009.7	3663.8
9	2585.8	3686.0	2616.5	3553.8	2689.4	3560.4
10	3066.8	4317.3	3115.9	4276.9	3061.7	4271.6
11	4013.1	3983.1	4095.2	3948.1	4022.8	3978.9
12	3848.3	2886.8	4019.5	2685.0		
13	3846.1	3932.1	3881.5	3938.9	3887.4	3912.9
14	3745.7	3277.0	3947.4	3084.4	3923.2	3048.6
15	3955.4	3209.5				
16	6387.0	4542.2				
Mean	3896.7	3027.7	2972.5	2273.0	2691.2	2131.8
SD	1379.8	1011.1	1949.5	1487.2	2040.9	1578.2
Measurements (n)	15	15	12	12	11	11

Patient #	IR DC Amplitudes (mV)					
	Pre FiO ₂ increase		During FiO ₂ increase		Post FiO ₂ increase	
	Foot	AF	Foot	AF	Foot	AF
1	6501.4	2432.2	6511.1	2425.2	6538.6	2471.3
2	3967.3	3509.7	4069.4	3495.0	4165.6	3499.9
4	7101.8	6568.4				
5	7057.8	4812.6	7096.0	4737.7	7072.8	4525.4
6	6144.9	4233.3	8299.3	4117.8	8664.4	4077.2
7	7022.1	3715.0	7623.0	3647.0	7910.9	3913.5
8	3206.7	7093.4	3320.8	7087.3	3363.6	7119.7
9	2706.2	6268.8	2659.5	5997.7	2745.5	6017.7
10	3129.4	6772.3	2928.0	6802.0	2872.2	6791.6
11	4331.4	6067.5	4306.0	5933.1	4294.2	5986.1
12	5962.7	3261.7	5921.5	3163.7		
13	4312.9	5548.4	4374.9	5643.9	4446.4	5512.2
14	7862.9	4941.4	7749.0	4742.0	7468.3	4653.2
15	6708.3	4335.8				
16	5566.6	8767.5				
Mean	5438.8	5221.9	4323.9	3852.8	3969.5	3637.9
SD	1684.9	1712.2	2870.1	2392.8	3076.6	2579.6
Measurements (n)	15	15	12	12	11	11

Patient #	GREEN DC Amplitudes (mV)					
	Pre FiO ₂ increase		During FiO ₂ increase		Post FiO ₂ increase	
	Foot	Font	Foot	Font	Foot	Font
1	80.5		82.5		83.8	
2	1479.5		1490.6		1491.1	
4	1192.8					
5	820.8	155.6	799.4	155.1	799.4	149.3
6	1345.1		1280.9	0.0	1266.4	
7	1389.9	428.1	1469.4	413.9	1445.7	563.7
8	1505.8		1472.3		1470.6	
9	1094.0		1111.6		1118.2	
10	1260.4	155.1	1325.1		1333.2	
11	1030.1		1021.6		1011.8	
12	1018.4		1016.7			
13	1532.9	395.2	1541.8	415.5	1536.6	405.7
14	1118.2		1052.6		1018.6	
15	1200.0		0.0			
16	1680.0		0.0			
Mean	1183.2	75.6	911.0	65.6	838.4	74.6
SD	382.3	146.9	594.1	147.2	634.3	173.5
Measurements (n)	15	4	12	3	11	3

Appendix G

Fontanelle Study Patient Statistics.

Patient #	Age (Days)	Weight (Kg)	Gender	ASA
1	5	2.8	m	2
2	115	3.3	m	3
3	7	3	f	1
4	4	3.2	f	3
5	7	3.2	m	1
6	30	1.14	f	2
7	3	2.8	m	2
8	36	3	m	3
9	88	2.3	m	2
10	56	3.7	f	1
11	161	4.95	f	1
12	3	3.99	m	2
13	6	3.1	m	2
14	24	3.9	m	1
15	4	3.45	f	2
16	35	1.39	f	2
Mean	36.5	3.07		
SD	46.8	0.93		

References

- ALLEN, J. 2007. Photoplethysmography and its application in clinical physiological measurement. *Physiological Measurement*, 28, R1-39.
- ADLER, J. N., HUGHES, L. A., VIVILECCHIA, R. & CAMARGO, C. A. 1998. Effect of skin pigmentation on pulse oximetry accuracy in the emergency department. *Academic Emergency Medicine: Official Journal of the Society for Academic Emergency Medicine*, 5, 965-970.
- AOYAGI, T. 2003. Pulse oximetry: its invention, theory, and future. *Journal of Anesthesia*, 17, 259-266.
- BARKER, S. J. & BADAL, J. J. 2008. The measurement of dyshemoglobins and total hemoglobin by pulse oximetry. *Current Opinion in Anaesthesiology*, 21, 805-810.
- BARKER, S. J. 2006. Problems with forehead reflectance pulse oximetry. *Respiratory Care*, 51, 715-716 %U <http://www.ncbi.nlm.nih.gov/pubmed/16800901>.
- BEBOUT, B. L., MANNHEIMER, P. & WUN, C. C. 2001. Site-dependent differences in the time to detect changes in saturation during low perfusion. *Critical Care Medicine*, 29, A115 (abstract).
- BERKENBOSCH, J. W. & TOBIAS, J. D. 2006. Comparison of a new forehead reflectance pulse oximeter sensor with a conventional digit sensor in pediatric patients. *Respiratory Care*, 51, 726-731.
- BLAND, J. M. & ALTMAN, D. G. 1986. Statistical methods for assessing agreement between two methods of clinical measurement. *Lancet*, 1, 307-310.
- CARLSON, B. M. 2004. *Human embryology and developmental biology*, Mosby %@ 9780323014878.
- COTÉ, C. J., DANIELS, A. L., CONNOLLY, M., SZYFELBEIN, S. K. & WICKENS, C. D. 1992. Tongue oximetry in children with extensive thermal injury: comparison with peripheral oximetry. *Canadian journal of anaesthesia = Journal canadien d'anesthésie*, 39, 454-457.

- D'AGROSA, L. S. & HERTZMAN, A. B. 1967. Opacity pulse of individual minute arteries. *Journal of Applied Physiology*, 23, 613-620.
- DASSEL, A. C., GRAAFF, R., AARDEMA, M., ZIJLSTRA, W. G. & AARNOUDSE, J. G. 1997. Effect of location of the sensor on reflectance pulse oximetry. *British Journal of Obstetrics and Gynaecology*, 104, 910-916.
- DAVIES, D. P., ANSARI, B. M. & COOKE, T. J. 1975. Anterior fontanelle size in the neonate. *Archives of Disease in Childhood*, 50, 81-83.
- DECKARDT, R. & STEWARD, D. J. 1984. Noninvasive arterial hemoglobin oxygen saturation versus transcutaneous oxygen tension monitoring in the preterm infant. *Critical Care Medicine*, 12, 935-939.
- DERRICKSON, G. J. & TORTORA, B. H. 2008. *Principles of Anatomy and Physiology* 12th Edition, Wiley.
- EDSALL, J. T. 1972. Blood and hemoglobin: the evolution of knowledge of functional adaptation in a biochemical system, part I: The adaptation of chemical structure to function in hemoglobin. *Journal of the History of Biology*, 5, 205-257.
- EISENKRAFT, J. B. 1988. Pulse oximeter desaturation due to methemoglobinemia. *Anesthesiology*, 68, 279-282.
- FAISST, K., HANNON, W., JØRGENSEN, J. S., KÖNIG, V., BUCHER, H. U., HUCH, A. & HUCH, R. 1995. Reflectance pulse oximetry in neonates. *European Journal of Obstetrics, Gynecology, and Reproductive Biology*, 61, 117-122.
- FAISST, K., KIRKINEN, P., KÖNIG, V., HUCH, A. & HUCH, R. 1997. Intrapartum reflectance pulse oximetry: effects of sensor location and fixation duration on oxygen saturation readings. *Journal of Clinical Monitoring and Computing*, 13, 299-302.
- FALLER, A. 2004. *The Human Body: An Introduction to Structure and Function*, Thieme.
- FANCONI, S., DOHERTY, P., EDMONDS, J. F., BARKER, G. A. & BOHN, D. J. 1985. Pulse oximetry in pediatric intensive care: comparison with measured saturations and transcutaneous oxygen tension. *The Journal of Pediatrics*, 107, 362-366.

- FEINER, J. R., SEVERINGHAUS, J. W. & BICKLER, P. E. 2007. Dark Skin Decreases the Accuracy of Pulse Oximeters at Low Oxygen Saturation: The Effects of Oximeter Probe Type and Gender. *Anesthesia & Analgesia*, 105, S18 -S23.
- FLUCK, R. R., SCHROEDER, C., FRANI, G., KROPF, B. & ENGBRETSON, B. 2003. Does ambient light affect the accuracy of pulse oximetry? *Respiratory Care*, 48, 677-680.
- FUTRAN, N. D., STACK, B. C., HOLLENBEAK, C. & SCHARF, J. E. 2000. Green light photoplethysmography monitoring of free flaps. *Archives of Otolaryngology--Head & Neck Surgery*, 126, 659-662.
- GLOOR, F. 1953. [Vascularization of the esophagus]. *Thoraxchirurgie*, 1, 146-67.
- GRAAFF, K. V. D., RHEES, R. W. & PALMER, S. L. 2009. *Schaum's Outline of Human Anatomy and Physiology, Third Edition*, Schaum's Outlines.
- GRAY, H. 2008. *Gray's Anatomy*, Arcturus Publishing.
- HANSEN, J. T. & LAMBERT, D. R. 2005. *Netter's Clinical Anatomy*, Saunders.
- HAY, W. W. 2005. History of Pulse Oximetry in Neonatal Medicine. *NeoReviews*, 6, e533-e538.
- HAY, W. W., BROCKWAY, J. M. & EYZAGUIRRE, M. 1989. Neonatal pulse oximetry: accuracy and reliability. *Pediatrics*, 83, 717-722.
- HERTZMAN, A. B. & DILLON, J. B. 1940. Distinction between arterial, venous and flow components in photoelectric plethysmography in man. *American Journal of Physiology -- Legacy Content*, 130, 177 -185.
- HERTZMAN, A. B. & FLATH, F. 1963. The Continuous Simultaneous Registration of Sweating and Blood Flow in a Small Skin Area. *Aerospace Medicine*, 34, 710-713.
- HERTZMAN, A. B. 1937. Photoelectric Plethysmography of the Nasal Septum in Man. *Proceedings of the Society for Experimental Biology and Medicine. Society for Experimental Biology and Medicine (New York, N.Y.)*, 37, 290-292.
- HICKEY, M., SAMUELS, N., RANDIVE, N., LANGFORD, R. M. & KYRIACOU, P. A. 2011. Investigation of photoplethysmographic signals and blood oxygen saturation values obtained from human splanchnic organs using a fiber optic sensor. *Journal of Clinical Monitoring and Computing*.

- HOPPE-SEYLER, F. 1864. Über die chemischen und optischen Eigenschafter des Blutfarbstoffs. Arch Pathol Anat Physiol 29, 233-251.
- IYER, P., MCDUGALL, P., LOUGHNAN, P., MEE, R. B., AL-TAWIL, K. & CARLIN, J. 1996. Accuracy of pulse oximetry in hypothermic neonates and infants undergoing cardiac surgery. Critical Care Medicine, 24, 507-511.
- JACKSON, C. L. 1950. Bronchoesophagology, Philadelphia,, Saunders.
- JAMES, E. S. 1999. Pulse oximetry: Principles and limitations. The American Journal of Emergency Medicine, 17, 59-66.
- JENNIS, M. S. & PEABODY, J. L. 1987. Pulse oximetry: an alternative method for the assessment of oxygenation in newborn infants. Pediatrics, 79, 524-528.
- JØRGENSEN, J. S., SCHMID, E. R., KÖNIG, V., FAISST, K., HUCH, A. & HUCH, R. 1995. Limitations of forehead pulse oximetry. Journal of Clinical Monitoring, 11, 253-256.
- KRAMER, K. 1934. Bestimmung des Sauerstoffgehaltes und der Himoglobin Konzentration in Himoglobinlungen und himolysierten Blut auf lichtelektrischen Wege. Z Biol, 95, 126-134.
- KUGELMAN, A., WASSERMAN, Y., MOR, F., GOLDINOV, L., GELLER, Y. & BADER, D. 2004. Reflectance pulse oximetry from core body in neonates and infants: comparison to arterial blood oxygen saturation and to transmission pulse oximetry. Journal of Perinatology: Official Journal of the California Perinatal Association, 24, 366-371.
- KYRIACOU, P. A. 2006. Pulse oximetry in the oesophagus. Physiological Measurement, 27, R1-35.
- KYRIACOU, P. A., JONES, D. P., LANGFORD, R. M. & PETROS, A. J. 2008. A pilot study of neonatal and pediatric esophageal pulse oximetry. Anesthesia and Analgesia, 107, 905-908.
- KYRIACOU, P. A., MOYE, A. R., CHOI, D. M., LANGFORD, R. M. & JONES, D. P. 2001. Investigation of the human oesophagus as a new monitoring site for blood oxygen saturation. Physiological Measurement, 22, 223-232.

- KYRIACOU, P. A., MOYE, A. R., GREGG, A., CHOI, D. M., LANGFORD, R. M. & JONES, D. P. 1999. A system for investigating oesophageal photoplethysmographic signals in anaesthetised patients. *Medical & Biological Engineering & Computing*, 37, 639-643.
- KYRIACOU, P. A., POWELL, S., LANGFORD, R. M. & JONES, D. P. 2002a. Esophageal pulse oximetry utilizing reflectance photoplethysmography. *IEEE Transactions on Bio-Medical Engineering*, 49, 1360-1368.
- KYRIACOU, P. A., POWELL, S., LANGFORD, R. M. & JONES, D. P. 2002b. Investigation of oesophageal photoplethysmographic signals and blood oxygen saturation measurements in cardiothoracic surgery patients. *Physiological Measurement*, 23, 533-545.
- LAWSON, D., NORLEY, I., KORBON, G., LOEB, R. & ELLIS, J. 1987. Blood flow limits and pulse oximeter signal detection. *Anesthesiology*, 67, 599-603.
- LIEBERMANN-MEFFERT, D. M., LUESCHER, U., NEFF, U., RUEDI, T. P. & ALLGOWER, M. 1987. Esophagectomy without thoracotomy: is there a risk of intramediastinal bleeding? A study on blood supply of the esophagus. *Ann Surg*, 206, 184-92.
- LUNDERQUIST, A., ALWMARK, A., GULLSTRAND, P., HALL-ANGERAS, M., JOELSSON, B., OWMAN, T., PETTERSSON, K. I. & TRANBERG, K. G. 1983. Pharmacologic influence on esophageal varices: a preliminary report. *Cardiovasc Intervent Radiol*, 6, 65-71.
- MACLEOD, D. B., CORTINEZ, L. I., KEIFER, J. C., CAMERON, D., WRIGHT, D. R., WHITE, W. D., MORETTI, E. W., RADULESCU, L. R. & SOMMA, J. 2005. The desaturation response time of finger pulse oximeters during mild hypothermia. *Anaesthesia*, 60, 65-71.
- MAEDA, Y., SEKINE, M. & TAMURA, T. 2010. The Advantages of Wearable Green Reflected Photoplethysmography. *Journal of Medical Systems*.
- MAEDA, Y., SEKINE, M., TAMURA, T., MORIYA, A., SUZUKI, T. & KAMEYAMA, K. 2008. Comparison of reflected green light and infrared photoplethysmography. *Conference Proceedings: ... Annual International Conference of the IEEE*

- Engineering in Medicine and Biology Society. IEEE Engineering in Medicine and Biology Society. Conference, 2008, 2270-2272.
- MARK, J. B. 1989. Systolic venous waves cause spurious signs of arterial hemoglobin desaturation. *Anesthesiology*, 71, 158-160.
- MASIMO 2006. Radical 7(TM) signal extraction pulse oximeter: Operator's Manual. Masimo: Masimo.
- MASIMO 2007. Demystifying Methemoglobinemia: A Clinically Pervasive Disorder with Ambiguous Symptoms Masking Prevalence, Morbidity, and Mortality. <http://www.masimo.co.uk/Rainbow/pdf/LAB4280B%20-%20met.pdf>: Masimo Corporation.
- MASIMO 2008. Carbon Monoxide Lurking Within: The Danger of Carboxyhemoglobinemia in Acute Care. <http://www.masimo.co.uk/Rainbow/pdf/LAB4427B%20-%20spco%20acute.pdf>: Masimo Corporation.
- MENDELSON, Y. & OCHS, B. D. 1988. Noninvasive pulse oximetry utilizing skin reflectance photoplethysmography. *IEEE Transactions on Bio-Medical Engineering*, 35, 798-805.
- MENDELSON, Y., DUCKWORTH, R. J. & COMTOIS, G. 2006. A wearable reflectance pulse oximeter for remote physiological monitoring. Conference Proceedings: ... Annual International Conference of the IEEE Engineering in Medicine and Biology Society. IEEE Engineering in Medicine and Biology Society. Conference, 1, 912-915.
- MERRICK, E. B. & HAYES, T. J. 1976. Continuous, Non-Invasive Measurements of Arterial Blood Oxygen Levels. *Hewlett-Packard Journal*.
- MILLIKAN, G. A. 1933. A simple photoelectric colorimeter. *The Journal of Physiology*, 79, 152-157.
- MORGAN, M. E. & DURBIN, G. M. 1986. Pulse oximetry in neonatal care. *Archives of disease in childhood*, 61, 1247-1247.

- MORRIS, R. W., NAIRN, M. & TORDA, T. A. 1989. A comparison of fifteen pulse oximeters. Part I: A clinical comparison; Part II: A test of performance under conditions of poor perfusion. *Anaesthesia and Intensive Care*, 17, 62-73.
- MOWER, W. R., SACHS, C., NICKLIN, E. L. & BARAFF, L. J. 1997. Pulse Oximetry as a Fifth Pediatric Vital Sign. *Pediatrics*, 99, 681-686.
- MOYLE, J. T. B. 2002. Pulse Oximetry, *BMJ*.
- NÄSLUND, J., PETTERSSON, J., LUNDEBERG, T., LINNARSSON, D. & LINDBERG, L.-G. 2006. Non-invasive continuous estimation of blood flow changes in human patellar bone. *Medical & Biological Engineering & Computing*, 44, 501-509.
- NICOLAI, L. 1932. Über Sichtbarmachung, Verlauf und chemische Kinetik der Oxyhemoglobinreduktion im ebenen Gewebe, besonders in der menschlichen *Arch Ges Physiol*, 229, 372-389.
- NIJBOER, J. A., DORLAS, J. C. & MAHIEU, H. F. 1981. Photoelectric plethysmography--some fundamental aspects of the reflection and transmission method. *Clinical Physics and Physiological Measurement: An Official Journal of the Hospital Physicists' Association, Deutsche Gesellschaft Für Medizinische Physik and the European Federation of Organisations for Medical Physics*, 2, 205-215.
- NIJLAND, R., JONGSMA, H. W., VAN DEN BERG, P. P., NIJHUIS, J. G. & OESEBURG, B. 1995. The effect of pulsating arteries on reflectance pulse oximetry: measurements in adults and neonates. *Journal of Clinical Monitoring*, 11, 118-122.
- PAL, S. K., KYRIACOU, P. A., KUMARAN, S., FADHEEL, S., EMAMDEE, R., LANGFORD, R. M. & JONES, D. P. 2005. Evaluation of oesophageal reflectance pulse oximetry in major burns patients. *Burns: Journal of the International Society for Burn Injuries*, 31, 337-341.
- PETERS, A. 2007. *BMA Illustrated Medical Dictionary* 2nd edition, Dorling Kindersley.
- PETTERSON, M. T., BEGNOCHE, V. L. & GRAYBEAL, J. M. 2007. The effect of motion on pulse oximetry and its clinical significance. *Anesthesia and Analgesia*, 105, S78-84.

- PHILLIPS, J. P., GEORGE, K. J., KYRIACOU, P. A. & LANGFORD, R. M. 2009. Investigation of photoplethysmographic changes using a static compression model of spinal cord injury. Conference Proceedings: ... Annual International Conference of the IEEE Engineering in Medicine and Biology Society. IEEE Engineering in Medicine and Biology Society. Conference, 2009, 1493-1496.
- PHILLIPS, J. P., LANGFORD, R. M., CHANG, S. H., MANEY, K., KYRIACOU, P. A. & JONES, D. P. 2010. Cerebral arterial oxygen saturation measurements using a fiber-optic pulse oximeter. *Neurocritical Care*, 13, 278-285.
- POETS, C. F. & SOUTHALL, D. P. 1994. Noninvasive monitoring of oxygenation in infants and children: practical considerations and areas of concern. *Pediatrics*, 93, 737-746.
- POLLARD, J. A. 1968. A new photoelectric plethysmograph. *Anesthesia and Analgesia*, 47, 310-319.
- PRAHL, S. 1998. Available: <http://omlc.ogi.edu/spectra/hemoglobin/summary.html> [Accessed].
- RALSTON, A. C., WEBB, R. K. & RUNCIMAN, W. B. 1991. Potential errors in pulse oximetry. III: Effects of interferences, dyes, dyshaemoglobins and other pigments. *Anaesthesia*, 46, 291-295.
- REYNOLDS, K., PALAYIWA, E., MOYLE, J., SYKES, M. & HAHN, C. 1993. The effect of dyshemoglobins on pulse oximetry: Part I, theoretical approach and part II, experimental results using an in vitro test system. *Journal of Clinical Monitoring and Computing*, 9, 81-90.
- ROLFE, P. 1979. *Non-invasive physiological measurements*, Academic Press.
- SAMI, H. M., KLEINMAN, B. S. & LONCHYNA, V. A. 1991. Central venous pulsations associated with a falsely low oxygen saturation measured by pulse oximetry. *Journal of Clinical Monitoring*, 7, 309-312.
- SANDBERG, M., ZHANG, Q., STYF, J., GERDLE, B. & LINDBERG, L. G. 2005. Non-invasive monitoring of muscle blood perfusion by photoplethysmography: evaluation of a new application. *Acta Physiol Scand*, 183, 335-43.

- SCANLON, V. C. & SANDERS, T. 2007. Essentials of anatomy and physiology, F.A. Davis Co.
- SEDAGHAT-YAZDI, F., TORRES, A., JR., FORTUNA, R. & GEISS, D. M. 2008. Pulse oximeter accuracy and precision affected by sensor location in cyanotic children. *Pediatric Critical Care Medicine: A Journal of the Society of Critical Care Medicine and the World Federation of Pediatric Intensive and Critical Care Societies*, 9, 393-397.
- SENAY, L. C., CHRISTENSEN, M. & HERTZMAN, A. B. 1960. Cutaneous vascular responses in finger and forearm during rising ambient temperatures. *Journal of Applied Physiology*, 15, 611 -618.
- SEVERINGHAUS, J. W. & ASTRUP, P. B. 1986. History of blood gas analysis. VI. Oximetry. *Journal of Clinical Monitoring*, 2, 270-288.
- SEVERINGHAUS, J. W. & KOH, S. O. 1990. Effect of anemia on pulse oximeter accuracy at low saturation. *Journal of Clinical Monitoring*, 6, 85-88.
- SEVERINGHAUS, J. W. & SPELLMAN, M. J. 1990. Pulse oximeter failure thresholds in hypotension and vasoconstriction. *Anesthesiology*, 73, 532-537.
- SEVERINGHAUS, J. W. 2007. Takuo Aoyagi: Discovery of Pulse Oximetry. *Anesthesia & Analgesia*, 105, S1 -S4.
- SHAPIRO, A. L. & ROBILLARD, G. L. 1950. The esophageal arteries their configurational anatomy and variations in relation to surgery. *Ann Surg*, 131, 171-85, illust.
- SHELLEY, K. H., TAMAI, D., JABLONKA, D., GESQUIERE, M., STOUT, R. G. & SILVERMAN, D. G. 2005. The effect of venous pulsation on the forehead pulse oximeter wave form as a possible source of error in Spo₂ calculation. *Anesthesia and Analgesia*, 100, 743-747.
- SINEX, J. E. 1999. Pulse oximetry: Principles and limitations. *The American Journal of Emergency Medicine*, 17, 59-66.
- STACK, B. C., FUTRAN, N. D., SHOHE'T, M. J. & SCHARF, J. E. 1998. Spectral analysis of photoplethysmograms from radial forearm free flaps. *The Laryngoscope*, 108, 1329-1333.

- STOKES, G. G. 1864. On the reduction and oxygenation of the colouring matter of the blood. *philos Mag*, 28, 391.
- SWIGART, L. L., SIEKERT, R. G. & ET AL. 1950. The esophageal arteries; an anatomic study of 150 specimens. *Surg Gynecol Obstet*, 90, 234-43, illust.
- TOMPSETT, D. H. 1969. Anatomical injections. *Ann R Coll Surg Engl*, 45, 108-15.
- TRAINING.SEER.CANCER.GOV. 2010. Esophagus.
- TRIVEDI, N. S., GHOURI, A. F., SHAH, N. K., LAI, E. & BARKER, S. J. 1997. Effects of motion, ambient light, and hypoperfusion on pulse oximeter function. *Journal of Clinical Anesthesia*, 9, 179-183.
- VILLANUEVA, R., BELL, C., KAIN, Z. N. & COLINGO, K. A. 1999. Effect of peripheral perfusion on accuracy of pulse oximetry in children. *Journal of Clinical Anesthesia*, 11, 317-322.
- WEBSTER, J. G. 1997. Design of pulse oximeters, Institute of Physics Pub.
- WEINMAN, J., BEN-YAAKOV, S. & SAPOZNIKOV, D. 1969. The application of photoplethysmography to the recording of Valsalva maneuver responses. *Israel Journal of Medical Sciences*, 5, 534-536.
- WILLIAMS, D. B. & PAYNE, W. S. 1982. Observations on esophageal blood supply. *Mayo Clinic Proceedings*. Mayo Clinic, 57.
- WOOD, E. & GERACI, J. E. 1949. Photoelectric determination of arterial oxygen saturation in man. *J Lab Clin Med*, 34, 387-401.
- WWW.STUDENT.LORETTO.ORG/ANATOMYPHYS/. 2013 (downloaded). The Respiratory System [Online]. Available: <http://www.student.loretto.org/anatomyphys/Key%20diagram--Respiratory%20System.htm> [Accessed January 2013 2013].

Own Publications

- MAY, J. M., KYRIACOU, P. A. & PETROS, A. J. 2011. Development of an optoelectronic sensor for the investigation of photoplethysmographic signals from the anterior fontanel of the newborn. *Conference Proceedings: ... Annual International Conference of the IEEE Engineering in Medicine and Biology Society. IEEE Engineering in Medicine and Biology Society. Conference*, 2011, 18-21.
- MAY, J. M., KYRIACOU, P. A., HONSEL, M. & PETROS, A. J. 2012. Photoplethysmographic and SpO₂ readings from the neonatal anterior fontanelle: a case study. *Conf Proc IEEE Eng Med Biol Soc*, 2012, 1619-22.